**The Dissertation Committee for Mayank Malik Certifies that this is the approved version of the following dissertation:**

# Numerical Simulation and Interpretation of Formation-Tester Measurements Acquired in the Presence of Mud-Filtrate Invasion

**Committee:**

Carlos Torres-Verdín, Supervisor

Kamy Sepehrnoori, Co-Supervisor

David G. Hull

Gary A. Pope

Steven L. Bryant

# Numerical Simulation and Interpretation of Formation-Tester Measurements Acquired in the Presence of Mud-Filtrate Invasion

**by**

**Mayank Malik, B.E.; M.A.Sc.**

**Dissertation**

Presented to the Faculty of the Graduate School of
The University of Texas at Austin
in Partial Fulfillment
of the Requirements
for the Degree of

**Doctor of Philosophy**

**The University of Texas at Austin**

**May, 2008**

# Dedication

To my mother Kanchan Malik, my father Dev Raj Malik, and my grandmother Sudarshan Bhalla with all my love and affection.

# Acknowledgements

I would like to express my deepest gratitude to my supervising professors, Dr. Carlos Torres-Verdín and Dr. Kamy Sepehrnoori. I thank them for their valuable advice and guidance with their wisdom, knowledge and experience. Their patience to help me through difficult times as well as giving me the freedom to learn and explore on my own has been invaluable.

I would also like to acknowledge the support of many people who contributed their time and energy to this project: Dr. Roger Terzian and Joanna Castillo for computer support and for installing various software; and Bob Brugman from Computer Modelling Group Limited (CMGL) for his guidance in implementing simulation cases with CMG-GEM. Many simulator-related numerical problems would not have been solved without their deep understanding and extensive experience.

I would like to thank my colleagues and friends from CPE 5.146: Renzo Angeles, Hee Jae Lee, Zhipeng Lu, Robert Mallan, Dr. David Wolf, and Luis Javier Miranda for making the lab a positive working environment that is very conducive for research. Special thanks go to my former fellow graduate students Dr. Faruk O. Alpak, Dr. Jesús M. Salazar, and Dr. Emmanuel Toumelin for their mentoring in the area of inversion and petrophysics. I would like to extend my most sincere appreciation to the members of my dissertation committee: Dr. Steven L. Bryant, Dr. David G. Hull, and Dr. Gary A. Pope for taking the time to review my dissertation. A note of gratitude is also extended to Reynaldo Casanova for handing university paperwork of my appointment.

This project would not have been possible without the funding of the Formation Evaluation Joint Industry Consortium at The University of Texas at Austin. Anadarko,

Aramco, Baker Atlas, BHP Billiton, BP, British Gas, ConocoPhillips, Chevron, ENI E&P, ExxonMobil, Halliburton Energy Services, Hydro, Marathon Oil Corporation, Mexican Institute for Petroleum, Occidental Petroleum Corporation, Petrobras, Schlumberger, Shell International E&P, Statoil, TOTAL and Weatherford have jointly sponsored this consortium over the years.

# Numerical Simulation and Interpretation of Formation-Tester Measurements Acquired in the Presence of Mud-Filtrate Invasion

Publication No._____________

Mayank Malik, Ph.D.
The University of Texas at Austin, 2008

Supervisor: Carlos Torres-Verdín
Co-supervisor: Kamy Sepehrnoori

Wireline formation testers (WFT) are widely used to measure fluid pressure, to perform downhole fluid analysis in real-time, and for estimating permeability through pressure transient testing. Formation testers can measure a range of fluid properties such as color, viscosity, density, composition, pH, optical refractive index, pressure, salinity, fractional flow, and gas-oil ratio (GOR). However, WFT measurements are influenced by the process of mud-filtrate invasion because overbalanced drilling promotes radial displacement of in-situ fluids by mud filtrate. Oil-base mud (OBM) is first-contact miscible with native oil and can lead to contaminated fluid samples, erroneous estimates of petrophysical properties, and changes of composition, viscosity, compressibility, GOR, and fluid density.

The objective of this dissertation is three-fold: (1) to quantify the effect of OBM-filtrate invasion on WFT measurements, (2) to estimate in-situ petrophysical properties concomitantly from transient measurements of pressure, flow rate and GOR acquired with formation testers, and (3) to quantify petrophysical, geometrical, and fluid properties that can minimize the time of withdrawal of uncontaminated fluid samples.

In order to quantify the effect OBM-filtrate invasion on WFT measurements, we develop a two-dimensional axial-symmetric compositional simulator and subsequently use a commercial adaptive-implicit compositional simulator, CMG-GEM[1]. History matching of three field data sets acquired with probe-type formation testers in light-oil formations accurately reproduces measurements of sandface pressure, observation-probe pressure, GOR, and flow rate. Further, we demonstrate that history matching enables the detection and diagnosis of adverse data-acquisition conditions such as plugging, noisy data, and presence of OBM-filtrate invasion. We introduce a dimensionless fluid contamination function that relates GOR to fluid-sample quality. Sensitivity analysis of simulated fluid-sample quality to petrophysical properties clearly indicates that sample quality improves in the presence of anisotropy and impermeable shale boundaries.

A computationally efficient dual-grid inversion algorithm is developed and tested on both synthetic and field data sets to estimate in-situ petrophysical properties from WFT measurements. These tests confirm the reliability and accuracy of the inversion technique. Results indicate that permeability estimates can be biased by noisy measurements as well as by uncertainty in flow rate, relative permeability, radial invasion length, formation damage, and location of bed boundaries.

To quantify petrophysical and geometrical factors that can optimize the time of withdrawal of uncontaminated fluid samples, we compare the performance of focused and conventional probe-type WFT in the presence of mud-filtrate invasion. Simulations indicate a significant reduction in fluid-cleanup time when using a focused probe. The

---

[1] Trademark of Computer Modelling Group Limited

specific amount of improvement depends on probe geometry, fluid composition, and petrophysical properties of the probed formation.

Finally, we develop an inversion method to estimate Brooks-Corey parametric saturation-dependent functions jointly from transient measurements of fractional flow and probe pressure. Results show that estimating Brooks-Corey parameters can be non-unique if the a-priori information about fluid and petrophysical properties is uncertain. However, we show that focused fluid sampling consistently improves both the accuracy and reliability of the estimated relative permeability and capillary pressure parametric functions with respect to estimates obtained with conventional-probe measurements.

# Table of Contents

# List of Tables

# List of Figures

# Chapter 1: Introduction

This chapter outlines the scope, method, and organization of the dissertation. Current interpretation methods of formation-tester measurements with analytical expressions of spherical and linear single-phase flow give incorrect estimates of petrophysical properties in miscible flow regimes. We develop a compositional reservoir simulator to accurately model the process of mud-filtrate invasion and formation-tester measurements. Analysis of transient measurements of pressure and fractional flow shows that early-time measurements can be used to reliably estimate petrophysical properties and to diagnose adverse field-operating conditions.

Recent advances in wireline fluid sampling include the introduction of the focused sampling probe, which comprises two fluid channels with the intent of achieving higher-purity fluid samples in a shorter period of time than with a conventional probe. To the best of our knowledge, this is the first study that models both focused and conventional wireline formation-tester (WFT) measurements, thereby assessing geometrical, fluid, and petrophysical factors that can enhance fluid sample quality and improve the estimation of petrophysical properties in situ.

## 1.1 BACKGROUND

Formation testers are widely used to perform downhole fluid analysis (Dong et al., 2007) by measuring fluid properties (in real-time), estimating permeability, and detecting spatial variations of absolute permeability through pressure transient testing (Ayan et al., 2001; Wu et al., 2002). Current-generation formation testers can measure a range of fluid properties such as color, viscosity, density, composition, pH, optical refractive index, pressure, salinity, fractional flow, and GOR (volumetric gas-to-liquid ratio of crude oil measured at standard conditions of 1 atm and 60 $^{o}$F). To that end, formation testing is akin to performing several downhole experiments in an adverse high-pressure, high-temperature environment.

Wireline formation-tester measurements are commonly influenced by the process of mud-filtrate invasion that takes place prior to measurement acquisition. Mud-filtrate invasion occurs in porous and permeable rock formations penetrated by a well that is hydraulically overbalanced by mud circulation. Water-base mud (WBM) and oil-base mud (OBM) are alternatively used in field applications depending on the drilling environment. In the case of WBM, the invading mud is immiscible with formation hydrocarbons. By contrast, OBM is partially or fully miscible with native hydrocarbons (Mullins et al., 2000; Chin et al., 2005). Miscibility is responsible for changes of fluid viscosity, compressibility, GOR, and fluid density that can lead to contaminated fluid samples and erroneous estimates of petrophysical properties (Alpak et al., 2006).

Oil-base mud is increasingly being used in deep drilling operations around the world, including the Gulf of Mexico (Cheung et al., 2001), due to faster penetration, inhibition of chemical alteration with shale sections, and good wellbore stability (Andrew et al., 2001). Early-time fluid sampling in general gives non-representative fluid samples due to the process of mud-filtrate invasion under overbalanced drilling conditions. At the same time, extended duration of the formation test to render clean fluid samples can escalate the rig cost and lead to greater chances of the tool being stuck in the wellbore.

Recently, Schlumberger commercially introduced the Quicksilver[2] focused-sampling probe, which includes two fluid channels with the intent of achieving higher-purity fluid samples in a shorter period of time than with a conventional probe (Weinheber and Vasques, 2006). However, it is imperative to compare the performance of focused and conventional probe-type formation testers under a variety of

---

[2] Trademark of Schlumberger

petrophysical, fluid, and field conditions to quantify the improvement in fluid cleanup time. To the best of our knowledge, this dissertation is the first study that compares the performance of the probes in the presence of mud-filtrate invasion. By modeling both focused and conventional WFT measurements, we are able to assess optimum WFT configurations that can enhance fluid cleanup and provide additional degrees of freedom for the estimation of petrophysical properties.

The objective of this dissertation is three-fold: (1) to quantify the effect of oil-base mud-filtrate invasion on WFT measurements, (2) to estimate in-situ petrophysical properties concomitantly from transient measurements of pressure, flow rate and GOR acquired with formation testers, and (3) to quantify petrophysical, geometrical, and fluid factors that can optimize the time of withdrawal of uncontaminated fluid samples. The physics of mud-filtrate invasion is included in the simulation of WFT measurements and estimation of petrophysical properties. On the other hand, comparison of numerical simulations to field measurements helps to diagnose and quantify adverse data-acquisition conditions such as plugging, noisy data, and presence of mud-filtrate invasion.

## 1.2 PROBLEM STATEMENT

Throughout the sampling process, varying concentrations of OBM contained in the sampled fluid will lead to changes in observed (apparent) fluid properties (Austad et al., 2001; McCalmont et al., 2005). Similarly, sandface transient pressure measurements are affected by OBM invasion as the invasion process modifies both fluid viscosity and density in the near-wellbore region due to mixing between different hydrocarbon components (Wu et al., 2002). Therefore, it is important to (a) identify the impact of petrophysical and fluid properties that affect fluid sample quality in the presence of invasion, (b) develop suitable guidelines for fluid sampling, and (c) history match field measurements to diagnose and quantify adverse data-acquisition conditions.

Probe-type formation testers are often used to estimate permeability and anisotropy from pressure transient measurements (Ayan et al., 2001). The interpretation of these measurements is non trivial in the presence of OBM-filtrate invasion due to its partial or full miscibility with formation gas and oil, respectively (Goode et al., 1996; Hashem et al., 1999). Analytical expressions of spherical and linear single-phase flow may not give correct estimates of permeability in miscible or partially miscible flow regimes. A three-dimensional (3D) numerical model is required to provide accurate and reliable estimates of formation properties.

Optimizing the time required to acquire clean fluid samples can be challenging due to a variety of circumstances, including the drilling environment, formation properties, and radial extent of mud-filtrate invasion. Alternatively, focused probe-type formation testers can be used to secure clean fluid samples faster than with a conventional probe. Because there is a rubber sealing between the guard and sample regions of a focused probe, OBM- contaminated fluid tends to flow toward the guard region whereas native formation fluids tend to preferentially flow toward the sample probe (Akkurt et al., 2006; Kumar et al., 2006; O'Keefe et al, 2006). Ideally, the guard flow line withdraws OBM filtrate whereas the sample flow line withdraws clean formation fluids. In theory, the physical design of the focused fluid-sampling probe should help to acquire cleaner fluid samples faster especially in the presence of deep OBM-filtrate invasion. If an appropriate pressure differential is maintained, diversion of the fluid stream to different channels can lead to faster cleanup thereby reducing fluid sampling time. However, it is critical to compare the performance of conventional and focused probes under a variety of petrophysical, fluid, and field conditions to quantify the improvement in fluid cleanup time. Numerical modeling provides a general, efficient, and consistent method to assess different fluid probes under the same sampling conditions.

Early-time fractional flow is typically ignored in the estimation of petrophysical properties from fluid-sampling measurements. However, fractional-flow measurements can provide valuable information to estimate relative permeability and capillary pressure. (Gok et al., 2006; Zeybek et al., 2004). Previous studies have explored the possibility of using both fluid-sampling measurements acquired with dual-packer formation testers and borehole resistivity measurements to estimate saturation-dependent petrophysical properties (Alpak et al., 2004). However, no previous work has been done to estimate petrophysical properties from measurements acquired with a focused-probe WFT. It is our hypothesis that the additional fluid channel in the focused probe should increase the redundancy of input data available for the estimation of saturation-dependent petrophysical properties.

### 1.3 RESEARCH OBJECTIVES

The focus of this dissertation is to quantify the effect of OBM-filtrate invasion on WFT measurements, estimate in-situ petrophysical properties, and identify factors that can enhance fluid cleanup. Specifically, the goals pursued by the dissertation are as follows:

- Develop a two-dimensional (2D) compositional simulator for modeling multi-component OBM-filtrate invasion in a vertical well, simulate packer-type WFT measurements, and assess fluid-sample quality from transient measurements of pressure and fluid density.
- Develop a binary-component formulation of the 2D compositional simulator to model array-induction resistivity (AIT) measurements from spatial distributions of water saturation in the presence of OBM-filtrate invasion.

- Apply a 3D commercial compositional reservoir algorithm to simulate OBM-filtrate invasion, probe-type WFT fluid production, and to perform history matching of field measurements to detect and diagnose adverse data-acquisition conditions.
- Develop a hybrid inversion technique for fast estimation of permeability and anisotropy from probe-type WFT measurements.
- Quantify the operating differences between focused and conventional probe-type WFT measurements acquired in the presence of mud-filtrate invasion, and assess sample quality from transient measurements of GOR and fractional flow.
- Estimate parametric models of saturation-dependent capillary pressure and relative permeability from focused and conventional probe-type WFT measurements acquired in the presence of WBM-filtrate invasion.

### 1.4 OUTLINE OF METHOD AND APPROACH

The dissertation is sub-divided into three sections: (1) Development of a 2D axial-symmetric compositional simulator for OBM-filtrate invasion to quantify packer-type formation-tester and borehole resistivity measurements; (2) Application of a 3D commercial compositional reservoir method to simulate OBM-filtrate invasion, fluid production with a probe-type formation tester, and for fast estimation of underlying petrophysical properties; (3) Comparison of the performance of focused and conventional probe-type formation testers in the presence of water-base and oil-base mud-filtrate invasion.

### 1.4.1 Development of a 2D axial-symmetric compositional simulator for OBM-filtrate invasion to quantify the impact on packer-type formation tester fluid-production and borehole resistivity measurements

We simulate fluid flow in porous media of multi-component OBM with dynamic changes of fluid density, compressibility, and viscosity due to changes of hydrocarbon concentration and pressure. The invasion process is modeled with a volume-averaged flow rate. Simulations of packer-type WFT measurements relate oil density to fluid-sample quality to study the time evolution of fluid cleanup. Hydrocarbon phase compositions are tracked using the Peng-Robinson (Peng and Robinson, 1976) equation-of-state (EOS). Phase density is calculated from the EOS to account for variations of fluid density due to changes of pressure and composition. In so doing, we enforce a quarter-power mixing rule to describe the changes in fluid viscosity due to time-space variations of fluid composition.

We also quantify the influence of petrophysical and fluid properties on array-induction resistivity measurements acquired in the presence of oil-base mud-filtrate invasion. A simple binary-component formulation for the oil phase (OBM and reservoir oil) is considered wherein the components are first-contact miscible. The simulated spatial distributions of water saturation are transformed into spatial distributions of electrical resistivity using Waxman-Smits' formulations. Subsequently, AIT measurements are simulated with a numerical mode-matching method to reproduce induction-resistivity measurements acquired in a deepwater turbidite reservoir.

### 1.4.2 Application of a 3D commercial compositional reservoir method to simulate OBM-filtrate invasion, probe-type formation tester fluid-production, and to perform fast estimation of petrophysical properties

We use a commercial adaptive-implicit compositional numerical simulator (CMG-GEM[3]) to model the filtrate cleanup process during fluid sampling with a probe-type formation tester and to compare the predicted pressure and apparent fluid properties against observed field measurements. A history-matching approach is used to estimate permeability and anisotropy from field measurements. We apply the estimation workflow to three sets of field measurements acquired with a formation tester in light-oil formations. Measurements consist of sink-probe pressure, observation-probe pressure, GOR, and flow rate. The invasion process is modeled with a piston-like displacement front. Since the formation is invaded with OBM filtrate that is assumed free of gas, GOR is used to discriminate between fluids. A dimensionless fluid-contamination function relates transient GOR measurements to fluid-sample quality. Sensitivity analyses identify the dominant parameters that affect the fluid sampling operation, such as formation properties, formation-tester flow rates, and radial extent of mud-filtrate invasion. In order to accurately model the time evolution of miscible flow properties, the compositional model includes eight pseudo-components: five formation oil components and three oil-base mud-filtrate components. Hydrocarbon phase compositions are tracked using the Peng-Robinson EOS (Peng and Robinson, 1976) with a Peneloux correction for the volume-shift parameter. We use the Lohrenz-Bray-Clark (LBC) correlation to compute fluid viscosity of the hydrocarbon phase (Lohrenz et al., 1964).

A new inversion method is developed to efficiently estimate permeability and anisotropy with a cascade sequence of least-squares minimizations. Measurements consist of pressure transients acquired at the sand face with a probe-type WFT. The new

---

[3] Generalized Equation of State Simulator, Computer Modeling Group Limited

inversion method executes the forward 3D problem only in an outer loop. In the inner loop, we perform fast minimizations with a 2D cylindrical grid. Transient measurements of pressure at the sand face simulated with the 2D cylindrical grid are correlated to the corresponding measurements simulated with the 3D grid. Once the 2D minimization is completed, we perform a 3D simulation of transient pressure to update the 2D-3D correlation parameter and a new 2D minimization is performed until convergence is reached. The process repeats itself until the simulated 3D pressure transients reproduce the field measurements within pre-stipulated error bounds.

### 1.4.3 Comparison of the performance of focused and conventional probe-type formation testers in the presence of water- and oil-base mud-filtrate invasion

We simulate the process of fluid sampling with a focused probe in a vertical well and compare its performance to that of a one-inch diameter conventional probe in the presence of mud-filtrate invasion. Fluid cleanup is a function of the transient GOR and fractional flow measured in the sampled fluid stream. The process of mud-filtrate invasion is modeled with a volume-averaged flow rate across the borehole wall prior to simulating WFT measurements. A commercial adaptive-implicit compositional reservoir simulator is used to model both invasion and filtrate cleanup processes. Comparison between fluid sampling with focused and conventional probes identifies cases in which focused fluid sampling leads to improved sample quality in a shorter period of time.

We model OBM-filtrate invasion and perform inversion jointly from transient measurements of GOR and probe pressures to estimate formation permeability, anisotropy, and rate of mud-filtrate invasion. In the first loop of inversion, we estimate the rate of mud-filtrate invasion from GOR measurements. In the second loop of inversion, we estimate permeability and anisotropy from probe pressure measurements. Lastly, we model WBM-filtrate invasion and perform inversion jointly from transient measurements of fractional flow and probe pressures to estimate absolute permeability, relative permeability, irreducible phase saturations, and capillary pressure. In the first loop, we estimate Brooks-Corey's (Brooks and Corey, 1964) saturation-dependent parameters from fractional flow measurements. In the second loop, we estimate only absolute permeability from probe pressure measurements. Inversion results are performed in three synthetic rock formations that cover a wide spectrum of petrophysical properties.

## 1.5 ORGANIZATION OF THE DISSERTATION

The dissertation consists of seven additional chapters following this introductory chapter. Chapter 2 defines the numerical formulation of a compositional method for the simulation of oil-base mud-filtrate invasion and WFT measurements. An implicit-pressure-explicit-concentration (IMPEC) scheme is implemented to model the measurements acquired with a packer-type formation tester. The simulation model assumes axial-symmetric variations of petrophysical properties as well as axially symmetric flow rate sources and boundary conditions.

Chapter 3 introduces a binary-component compositional formulation to model the impact of OBM-filtrate invasion on array-induction resistivity measurements. The relative mobility of the oil phase varies during the process of invasion. This behavior in turn affects the spatial distribution of electrical resistivity in a transition zone and, consequently, the borehole array-induction measurements. The combined simulation of OBM-filtrate invasion and array-induction resistivity measurements provides reliable estimates of water saturation to improve the assessment of in-place hydrocarbon reserves.

In Chapter 4, we study the effect of OBM-filtrate invasion on probe-type WFT measurements. A commercial reservoir simulator, CMG-GEM is employed to model compositional flow. We implement a history-matching technique to reproduce field measurements of sandface pressure, observation probe pressure, GOR, and flow rate acquired with a formation tester in light-oil formations. A dimensionless fluid contamination function is used to relate transient GOR measurements to sample fluid quality. The successful comparison to field measurements validates our simulation model, and enables the detection and diagnosis of adverse data-acquisition conditions such as plugging, noisy data, and presence of mud-filtrate invasion.

Chapter 5 develops a fast and automated estimation method based on a dual-grid minimization technique. The inversion method efficiently estimates permeability and anisotropy with a cascade sequence of least-squares minimizations. Measurements consist of pressure transients acquired at the probes. The new inversion method simulates the forward 3D problem only in an outer loop. In the inner loop, we perform fast minimizations with a 2D cylindrical grid. We perform tests of the new inversion algorithm on synthetic data sets acquired in the presence of oil-base mud-filtrate invasion and one field data set. Results confirm that our coupled 2D/3D hybrid inversion approach enables significant savings in computer time and provides reliable and accurate estimates of permeability and anisotropy.

Chapter 6 extends our simulation technique to model probe-type formation testers. We simulate the process of fluid sampling with a focused probe in a vertical well and compare its performance to that of a one-inch diameter conventional probe in the presence of OBM-filtrate invasion. Comparison between fluid sampling with focused and conventional probes identifies cases in which focused fluid sampling leads to improved sample quality in a shorter period of time.

In Chapter 7, we introduce a new method to estimate Brooks-Corey saturation-dependent functions jointly from transient measurements of fractional flow and probe pressures. The process of fluid sampling with a focused probe in a vertical well is compared to that of a one-inch diameter conventional probe in the presence of WBM-filtrate invasion. We observe that the estimation of Brooks-Corey parameters can be non-unique depending on the specific range of petrophysical properties of the formation and the rate of mud-filtrate invasion. However, we show that focused fluid sampling consistently improves both the accuracy and reliability of the estimated relative permeability and capillary pressure parametric functions with respect to estimates obtained with conventional-probe measurements.

Lastly, Chapter 8 summarizes the general conclusions of the dissertation and provides recommendations for future research.

### 1.6 LIST OF PUBLICATIONS

Several journal and conference papers have been published or submitted for review as a result of the research projects described in this dissertation:

- **Refereed Conference Proceedings**

Malik, M., Torres-Verdín, C., and Sepehrnoori, K., "Robust and efficient simulation of formation tester measurements with a rigorous compositional simulation code," paper SPE 102151, presented at the SPE Annual Technical Conference and Exhibition, San Antonio, September 2006.

Malik, M., Torres-Verdín, C., Sepehrnoori, K., Dindoruk, B., Elshahawi, H., and Hashem, M., "Field examples of history matching of formation-tester data in the presence of oil-base mud-filtrate invasion," paper KK, presented at the SPWLA Annual Symposium, Austin, June 2007.

Malik, M., Salazar, J.M., Torres-Verdín, C., Wang, G.L., Lee, H.J., and Sepehrnoori, K., "Influence of petrophysical and fluid properties on array-induction measurements acquired in the presence of oil-base mud-filtrate invasion," paper AAA, presented at the SPWLA Annual Symposium, Austin, June 2007.

Malik, M., Torres-Verdín, C., and Sepehrnoori, K., "A dual grid automatic history matching technique with applications to 3D formation testing in the presence of oil-base muds," paper SPE 109956, presented at the SPE Annual Technical Conference and Exhibition, Anaheim, November 2007.

Salazar, J.M., Malik, M., Torres-Verdín, C., Wang, G.L., and Duan, H., "Fluid density and viscosity effects on resistivity measurements acquired in the presence of oil-base mud-filtrate invasion," paper SPE 109946, presented at the SPE Annual Technical Conference and Exhibition, Anaheim, November 2007.

Malik, M., Torres-Verdín, C., Sepehrnoori, K., Jackson, R., Weinheber, P., Mullins, O.C., Elshahawi, H., Dindoruk, B., and Hashem, M., "Comparison of wireline formation-tester sampling with focused and conventional probes in the presence of oil-base mud-filtrate invasion," submitted to the SPWLA Annual Logging Symposium, Edinburgh, Scotland, May 25-28, 2008.

- **Refereed Journal Publications**

Malik, M., Torres-Verdín, C., and Sepehrnoori, K., "Axially symmetric compositional simulation of formation tester measurements," *Journal of Petroleum Science and Engineering*, v. 59, no. 3-4, pp. 333-349, 2007.

Malik, M., Torres-Verdín, C., Sepehrnoori, K., Dindoruk, B., Elshahawi, H., and Hashem, M., "History matching and sensitivity analysis of probe-type formation-tester measurements acquired in the presence of oil-base mud-filtrate invasion," *Petrophysics*, v. 48, no. 6, 2007.

Malik, M., Salazar, J.M., Torres-Verdín, C., Wang, G.L., Lee, H.J., and Sepehrnoori, K., "Effects of petrophysical properties on array-induction measurements acquired in the presence of oil-base mud-filtrate invasion," *Petrophysics*, v.49, no. 1, 2008.

# Chapter 2: Axially Symmetric Compositional Simulation of Formation Tester Measurements

This chapter describes the development, testing, and successful application of a new compositional code for the numerical simulation of oil-based mud invasion and formation tester measurements that involve arbitrary miscibility between oil-based mud and native oil. The simulator assumes axially symmetric variations of petrophysical properties as well as axially symmetric flow rate sources and boundary conditions. However, there are no restricting assumptions to the degree of miscibility between the fluids involved in the simulations. We solve the time-space evolution of component concentration with a time-marching implicit pressure explicit concentration (IMPEC) scheme. This method of solution considers the complete equations of state and implements flash calculations to describe the thermo-dynamical evolution of the various compositional phases due to space-time variations of pressure and concentration.

Simulations described in this chapter consider the process of oil-based mud-filtrate invasion into reservoirs containing mixtures of connate water and oil. Subsequently, we simulate formation tester measurements by enforcing fluid withdrawal through the dual-packer section of the tester. Measurements consist of fluid pressure, fractional flow rates, fluid density, and fluid viscosity. Examples of application include homogenous and multi-layer formations as well as a capillary transition zone. Comparison of simulation results against those obtained with a commercial code confirms the efficiency, accuracy, and reliability of our method of solution.

Sensitivity analysis indicate that time evolution of fractional flow rates, fluid density, and fluid viscosity measured with the formation tester remain influenced by the petrophysical properties of the formation, volume of mud-filtrate invasion, and by saturation-dependent rock-fluid properties (relative permeability and capillary pressure).

The simulations provide suitable guidelines for the acquisition of clean samples of in-situ formation fluids in the presence of invasion and heterogeneous conditions of petrophysical and rock-fluid properties.

## 2.1 INTRODUCTION

Formation testers are widely used to measure pressure, estimate reservoir permeability and permeability anisotropy, and to detect spatial variation of hydraulic connectivity through pressure transient testing (Ayan et al., 2001; Wu et al., 2002). Often, formation tester measurements remain influenced by the process of mud-filtrate invasion that takes place prior to measurement acquisition. Mud-filtrate invasion occurs in reservoirs penetrated by a well that is hydraulically overbalanced by mud circulation. In the case of WBM, the invading mud is immiscible with respect to the formation hydrocarbons. However, in the case of OBM, the invading mud is miscible with the formation oil. In addition, OBM is responsible for changes in fluid viscosity, compressibility, and fluid density that can lead to erroneous estimates of permeability. Oil-base muds are increasingly being used in deep drilling operations around the world, including the Gulf of Mexico (Cheung et al., 2001), due to faster penetration, inhibition of chemical alteration with shale sections, and good wellbore stability. Thus, it becomes imperative to accurately model the effect of OBM on the invasion process and, subsequently, on formation tester measurements.

Previous work on formation testing has been focused to simulating immiscible flow (Goode and Thambynayagam, 1996; Kuchuk and Onur, 2003; Dubost et al., 2004). Due to the complexity of miscible flow (Mullins et al., 2000), limited work has been advanced to simulate invasion by OBM. Chin et al. (2005) presented a strategy to quantify clean fluid sampling times in miscible flow. However, their algorithm was based on the assumption of only one hydrocarbon component in the oil phase and did not take into account changes of density or viscosity due to changes of pressure. Wu et al. (2002) modeled single component OBM using an immiscible mud-filtrate invasion model and a commercial compositional algorithm to simulate formation tester measurements and to estimate permeability, relative permeability, and capillary pressure. Proett et al. (2002) quantified optimal clean fluid sampling times in the presence of OBM invasion based on the component concentration of a single-component OBM. Alpak et al. (2006) used a miscible flow approach with a commercial equation-of-state (EOS) simulator to simulate formation-tester measurements in the presence of OBM. In addition, they described examples of field measurements acquired with a probe-type formation tester, and compared measurements of GOR to those obtained with their compositional simulator. However, they did not include comparisons of field measurements of probe pressure against numerical simulations.

In this chapter, we simulate fluid flow in porous media of multi-component OBM including component PVT properties and mud-filtrate invasion together with dynamic changes of fluid density, compressibility, and viscosity due to changes of hydrocarbon concentration and pressure. In addition, we describe simulations of transient measurements of sand face pressure and oil density. Simulations of formation-tester measurements relate oil density to fluid-sample quality in order to study the time evolution of fluid cleanup.

Our simulations assume axially symmetric variations of both petrophysical properties and flow-rate sources. These assumptions are not restrictive to quantify fundamental properties of formation tester measurements including the time evolution of fluid sampling at the sand face. We consider five different hydrocarbon components in the formation and use field data to assign specific PVT properties of OBM invading the formation. Hydrocarbon phase compositions are tracked using the Peng-Robinson EOS

(Peng and Robinson, 1976). Phase density is calculated from the EOS to account for variations of fluid density due to changes of pressure and composition. In so doing, we enforce a quarter-power mixing rule to describe the changes in fluid viscosity due to time-space variations of fluid composition.

In the sections to follow, we describe the simulation method and introduce a base case of formation properties to quantify the accuracy, reliability, and performance of our simulation code. Subsequently, we consider cases of multi-layer and capillary transition zones to assess the impact of formation petrophysical properties on the time evolution of fluid properties due to fluid pumpout with a dual-packer formation tester.

### 2.2 METHOD

We use an IMPEC technique to solve for the time-space evolution of primitive unknowns in the porous and permeable medium, namely oil pressure and component compositions. Upon obtaining the overall composition of each component, we perform a phase equilibrium calculation to determine the phase composition of each component and the corresponding phase saturation. Subsequently, we carry out flash calculations in order to determine the phase density. The formulation and the algorithm used in this simulator are similar to those of UTCOMP (Chang et al., 1990); however, our algorithmic formulation is specifically designed to approach the case of azimuthal symmetry in formation properties with respect to the axis of a vertical borehole. In addition, our formulation enforces boundary and source flow-rate conditions on specific depth segments along the wellbore. The outer limits of the reservoir consist of impermeable zones with no-flow boundary conditions.

In the formulation, we assume $n_c$ hydrocarbon components and one water component in the aqueous phase hence resulting in a total of $n_c+1$ components. There are $n_p$ phases, with negligible mass fluxes (dispersion and mutual solubility) between water and other phases. Moreover, given that, in general, heat capacity of formation rocks is much larger than that of fluids present, we assume that space-time variations of temperature are negligible. Finally, we assume that there are no chemical reactions between the OBM and the native formation oil.

Darcy's law for multiphase flow in porous media governs the time-space evolution of pressure and concentration. Based on the above-described assumptions, the partial differential equation for pressure is given by

$$\left(V_p c_f - \frac{\partial V_t}{\partial P}\right)\frac{\partial P}{\partial t} + V_b \sum_{i=1}^{n_c+1} \overline{V}_{ti} \vec{\nabla} \cdot \sum_{j=1}^{n_p} (\xi_j x_{ij} \vec{u}_j) - \sum_{i=1}^{n_c+1} \overline{V}_{ti} q_i = 0, \quad \text{... (2.1)}$$

where:

$V_p$ is the pore volume,

$c_f$ is the formation compressibility,

$\frac{\partial V_t}{\partial P}$ is the partial derivative of total fluid volume with respect to pressure,

$P$ is fluid pressure,

$t$ is time,

$V_b$ is bulk volume,

$\xi_j$ is the molar density of phase $j$,

$x_{ij}$ is the mole fraction of component $i$ in phase $j$,

$\vec{u}_j$ is the macroscopic Darcy velocity of fluid phase $j$,

$\overline{V}_{ti}$ is the partial derivative of total fluid volume with respect to molar concentration of component *i*, and $q_i$ is the molar flow rate of component *i*.

Analytical expression for $\overline{V}_{ti}$ are given by Chang (1990). In addition, the mass conservation equation for the net change of component *i* is expressed in moles as

$$\frac{\partial N_i}{\partial t} + V_b \sum_{j=1}^{n_p} \vec{\nabla} \cdot (\xi_j x_{ij} \vec{u}_j) - q_i = 0 \;\; for \;\; i = 1, \ldots, n_c + 1 \quad \text{... (2.2)}$$

where $N_i$ is the number of moles of component *i* per unit pore volume and is given by

$$N_i = \sum_{j=1}^{n_p} (S_j x_{ij} \xi_j), \qquad \text{... (2.3)}$$

where $S_j$ is saturation of phase $j$. In the above equations, molar density is calculated from the compressibility factor ($Z_j$) obtained from the Peng-Robinson-EOS, namely,

$$\xi_j = \frac{P}{Z_j RT}, \qquad \text{...(2.4)}$$

where $R$ is universal gas constant and $T$ is the reservoir temperature. On the other hand, mass density is computed from the molar density as

$$\rho_j = \xi_j \sum_{i=1}^{n_c} x_{ij} M_i, \qquad \text{...(2.5)}$$

where $M_i$ is the molecular weight of the hydrocarbon component. Thus, hydrocarbon mass density depends on the component concentrations as well as on reservoir pressure.

We calculate oil viscosity of phase $j$, $\mu_o$, by enforcing a quarter-power mixing rule (Todd and Longstaff, 1972) applied to the sum of concentration of component $i$ in the oil phase, i.e.

$$\mu_o = \left[ \sum_{i=1}^{Nc} x_{io} \cdot \mu_i^{1/4} \right]^4. \qquad \text{...(2.6)}$$

The component viscosities $\mu_i$ are initialized at specific values of formation temperature and pressure. Finally, we enforce mass conservation with the volume constraint

$$\sum_{j=1}^{3} \left\{ \frac{N_j}{\xi_j} \right\} = 1.0 \qquad \text{...(2.7)}$$

where the subscript $j$ designates water and oil phases, respectively.

We use a finite-difference discretization in radial geometry to solve numerically the pressure and concentration equations (**Eqs. 2.1** and **2.2**). The formulation does not consider azimuthal variations in pressure, concentration, or petrophysical properties and makes use of one-point upstream discretization in space and time. We solve the ensuing implicit pressure equation with a bi-conjugate stabilized (Van Der Vorst, 1992) iterative algorithm. Convergence of the matrix solver is diagnosed with the relative magnitude of the residual. According to this formulation, we solve **Eqs. 2.4-2.7** at each node of the discretization grid and at every time step with concomitant updates of fluid properties based on flash calculations.

## 2.3 NUMERICAL SIMULATION OF MUD-FILTRATE INVASION AND FLUID PUMPOUT

We simulate the process of OBM-filtrate invasion with flow rates of invasion calculated based on specific formation and mud properties. The process of invasion gives rise to an initial spatial distribution of phase concentrations and pressure in the invaded formation. Subsequently, these spatial distributions are taken as initial condition to simulate formation tester measurements. **Figure 2.1** shows the finite-difference grid (vertical and radial directions) used in the simulations for the case of a homogeneous and isotropic formation together with the location of the formation tester in a vertical well. The wellbore radius is equal to 0.35 ft. For the numerical simulations, we use a finite-difference grid consisting of 50 nodes in the radial direction and 45 nodes in the vertical direction. In keeping with the rapid space-time variations of pressure and concentration in the near-borehole region, radial nodes are logarithmically spaced from the wellbore to the outer grid boundary (located 1000 ft away from the axis of the borehole); along the vertical direction, grid nodes are spaced uniformly. As described in **Fig. 2.2**, the assumed dual-packer formation tester consists of one pressure-monitoring probe located 4 ft above the dual-packer module. The vertical opening of the dual packer is equal to 2.5 ft. Pressure and fluid sampling are simulated at the sand face of the center point of the dual-packer opening.  We use a constant time step size of $10^{-4}$ days to perform all the simulations described in this chapter.

We consider a volume-averaged flow-rate of mud-filtrate invasion across the borehole wall prior to simulating formation tester measurements. As shown in **Fig. 2.3**, mud-filtrate invasion continues for 36 hours with a flow rate of 5 $ft^3$/day, followed by fluid drawdown (pumpout) imposed with the dual-packer module for 58 minutes with a flow rate of 75 $ft^3$/day. The drawdown is followed by a shut-in stage of 1.63 hours. Invasion rate is equivalent to a filtration rate of 0.0198 $cm^3$/min/100 $cm^2$ calculated with respect to the wellbore radius. Our model assumes that the volume of fluid invading the formation during sampling is negligible compared to the volume of fluids that have previously entered the formation. Therefore, invasion and fluid withdrawal processes do not occur simultaneously.

We assume that the formation consists of light-oil with density equal to 37.2 $lbf/ft^3$ and viscosity equal to 0.3 cp. The gas-oil ratio of in-situ fluids is 142 SCF/STB. Hydrocarbon components in the formation range from $C_1$ to $C_{19+}$. These hydrocarbons are lumped into five different components ($C_{1-5}$, $C_{6-9}$, $C_{10-13}$, $C_{14-18}$, and $C_{19+}$) using their pseudo properties summarized in **Table 2.1**. In this chapter, we adopt the convention of describing component concentration in molar units. The binary-interaction parameter between the hydrocarbon components is assumed null. We use field data to assign component concentrations for the OBM that mixes with the assumed hydrocarbon formation components thereby changing the oil density and viscosity.

Specific numerical simulations considered in this chapter include the following formation models:

1. Homogeneous and isotropic formation at irreducible water saturation (Base Case formation model).
2. Multi-layer formation at irreducible water saturation.
3. Homogeneous and isotropic formation at variable fluid saturation within a capillary transition zone.

**Figure 2.4** shows the assumed oil-water relative permeability and capillary pressure curves. Capillary pressure is defined as the difference between the pressures of oil and water phases. In our simulations, relative permeability and capillary pressure curves are based on laboratory measurements performed on rock-core samples acquired in the deepwater Gulf of Mexico, and the assumed irreducible water saturation is equal to 0.06. The OBM and the formation oil are first-contact miscible under reservoir temperature and pressure, whereupon no capillary pressure or relative permeability effects exist within the hydrocarbon phase.

## 2.4 HOMOGENEOUS FORMATION AT IRREDUCIBLE WATER SATURATION (BASE CASE)

**Tables 2.1** through **2.3** summarize the PVT, geometrical, and petrophysical parameters, respectively, assumed in the simulations of the Base Case formation model (isotropic and homogenous formation). The objective of this simple model example is to quantify the accuracy, reliability, and physical consistency of the simulations of OBM-filtrate invasion and dual-packer formation tester measurements.

**Figure 2.5** displays the radial profile of $C_{14-18}$ fraction with respect to radial distance in the formation for different invasion times and at uniform time intervals of 1.44 hours. The dominant component in the OBM is $C_{14-18}$ and is used to assess radial extent of invasion in the formation. We observe that the radial length of invasion of that component is approximately 1.1 feet at 1.5 days after the onset of invasion. The extent of invasion is consistent with previous documented studies on the subject of mud-filtrate invasion (Wu et al., 2002; Dubost et al., 2004; Alpak et al., 2006). The radial length of invasion depends on formation petrophysical properties, such as permeability, anisotropy, and porosity. Due to miscibility between OBM and formation oil, the invasion front appears dispersed. If the fluids were immiscible, the invasion front will appear as a piston-like displacement in the absence of capillary forces.

**Figures 2.6-2.9** compare the time evolutions of pressure, oil viscosity, component concentrations, and fluid density, respectively, calculated with our simulator (identified as Near Wellbore Compositional Simulator, or NWCS, in the plots) against those calculated with the commercial simulator CMG-GEM[4]. Results indicate a good match between the two sets of simulations.

**Figure 2.6** shows that the pressure differential at the sand face is relatively high at the start of fluid withdrawal and gradually decreases with time. This behavior is due to the higher viscosity of mud filtrate that alters phase mobility. Oil phase mobility is defined as

$$\lambda_o(t) = \frac{k_{ro}}{\mu_o(t)} \qquad \text{...(2.8)}$$

where $k_{ro}$ is the relative permeability of the oil phase, $\mu_o(t)$ is time-dependent oil viscosity, and $\lambda_o(t)$ is the transient mobility of the oil phase. Oil viscosity varies at the sand face during fluid withdrawal due to the variation of component concentrations when the near-packer region is cleaned up of mud filtrate. In the case of a light-oil formation, formation oil viscosity is lower than mud-filtrate viscosity, hence transient oil viscosity decreases with time during cleanup. At early times, when mud-filtrate is being retrieved by the fluid-pumpout unit of the formation tester, oil mobility is relatively low because the viscosity is high. The lower mobility of the phase in turn causes a higher pressure differential. By contrast, at late times when low-viscosity formation oil is being produced, phase mobility increases and causes a lower pressure differential. Consequently, we observe a relatively high pressure differential in **Fig. 2.6** at early times

---

[4] Trademark of Computer Modelling Group Limited

of fluid withdrawal. Typical examples of this transient behavior in sandface pressure measurements occur in cases of light-oil and gas formations when the viscosity of mud filtrate is higher than the viscosity of formation fluid.

For the simulations considered in this chapter, we define the time variations of sample quality as a function of the oil mass density via the expression

$$S(t) = \frac{\rho_{oi} - \rho_o(t)}{\rho_{oi} - \rho_{of}}, \qquad \ldots(2.9)$$

where:

*S(t)* is the sample quality during fluid pumpout as a function of time *t*,

$\rho_{oi}$ is the oil-base mud filtrate density,

$\rho_{of}$ is the native formation oil density, and

$\rho_o(t)$ is the oil density during fluid pumpout.

As shown in **Fig. 2.10,** initially OBM is produced at the sand face during fluid pumpout and the sample quality gradually increases toward 100% concentration of clean formation components. Ideally, we would like to obtain zero contamination in fluid samples to determine in-situ fluid compositions. Laboratory PVT testing techniques can clean contaminated fluid samples in order to estimate approximate in-situ composition. It is possible to obtain representative fluid composition in formations isolated with oil only if the contamination is less than 10% by mole fraction. However, fluid contamination higher than 10% renders the sample inappropriate to determine accurate in-situ fluid composition. Therefore, it becomes critical to assess the factors that influence fluid contamination and to determine formation properties and effective techniques that can potentially reduce fluid contamination.

**Figures 2.11-2.15** describe the spatial distribution of OBM concentration in the near wellbore region at different times between the onset of invasion process and the end of the formation testing. These plots indicate gradual time variations of component concentration starting from those of the OBM filtrate and asymptoting toward the concentration of native hydrocarbon components. Within approximately one hour of fluid pumpout all component concentrations have reached native component concentrations in the region around the packer location. Previous studies on the simulation of dual-packer measurements indicate that the time required to obtain clean fluid samples can vary anywhere from 30 minutes to a few hours.

### 2.4.1 Sensitivity to formation permeability and porosity

We perform a sensitivity analysis of sample quality by increasing the formation permeability and porosity to 100 mD and 0.35 respectively, based on the empirical correlation

$$\phi = 0.0567\log_e(k) + 0.08866, \qquad \ldots(2.10)$$

where porosity ($\phi$) is given in fraction and permeability (k) is expressed in millidarcies. Using the same total volume of mud-filtrate invasion, the radial length of invasion decreases due to the higher porosity (**Figure 2.16**). The pressure differential during fluid withdrawal in **Fig. 2.17** is lower for the higher permeability case. In turn, sample quality (shown in **Figure 2.18**) improves at early times due to both faster flow with high permeability and reduction of the radial length of invasion due to higher porosity.

### 2.4.2 Sensitivity to the rates of mud-filtrate invasion and formation-tester production

We perform two sensitivity analyses of transient pressure measurements and sample quality by altering the flow rates. In the first case, the flow rate mud-filtrate invasion is decreased to 2.5 $ft^3$/day and the formation tester production rate is kept equal to that of the base case (referred to as "$Q_{inv}$=2.5 $ft^3$/day" in the plots). In the second case, the flow rate of fluid withdrawal with the formation tester is decreased to 37.5 $ft^3$/day whereas the flow rate of mud-filtrate invasion is kept equal to that of the base case (referred to as "$Q_{prod}$=37.5 $ft^3$/day" in the plots). **Figure 2.19** shows that the pressure differential is larger for the base case and smaller for the case of low rate of fluid withdrawal. The decrease of rates has an opposing effect to each other when compared to the base case as indicated by both the concentration profile (**Fig. 2.20**) and sample quality (**Fig. 2.21**). By decreasing the rate of mud-filtrate invasion, the volume of mud filtrate invading the formation decreases and this expedites the acquisition of clean fluid samples. On the other hand, by decreasing the fluid production rate, the total volume of fluids sampled by the formation tester decreases, thereby increasing the time necessary to acquire clean samples. Sample quality at the end of fluid withdrawal is only 82% with the decreased production rate. Therefore, in order to obtain cleaner fluid samples that are representative of in-situ fluids, the operator can either increase the rate of fluid production or increase the sampling duration in order to increase the cumulative fluid produced by the formation tester.

### 2.4.3 Sensitivity to permeability anisotropy

We perform a sensitivity analysis of pressure, spatial distribution of OBM, and sample quality to permeability anisotropy by decreasing the vertical permeability of the Base Case to 1 mD thereby yielding an anisotropy ($k_h$ /$k_v$) equal to 5. Remaining simulation parameters were the same as those of the Base Case formation model. **Figure 2.22** displays the concentration map for the anisotropic case at the end of fluid sampling. We can observe deeper radial flow in the near-packer region during fluid withdrawal. **Figure 2.23** shows that the decreased vertical permeability caused the pressure differential to increase. Likewise, as shown in **Fig. 2.24**, sample quality improves by 1% when compared to the Base Case formation model because of the corresponding decrease of vertical cross flow.

### 2.4.4 Sensitivity to mud-filtrate viscosity

We perform a sensitivity analysis of pressure, oil viscosity, and sample quality to the viscosity of mud filtrate. In so doing, we assume four values of mud-filtrate viscosity in the range of 0.2 cp to 2 cp. **Figure 2.25** shows that decreasing the viscosity of mud filtrate leads to a corresponding decrease of pressure differential. The corresponding change of phase mobility due to the variation of fluid composition, as defined by **Eqn. 2.8**, causes a variation of pressure differential at early times. At late times, when the near-packer region is cleaned up from oil-base mud filtrate, sand-face transient pressure curves converge due to negligible variation of phase mobility from compositional contrasts (**Fig. 2.26**). **Figure 2.27** displays the sample quality simulated for different values of mud-filtrate viscosity. We observe a 2% improvement in sample quality between mud-filtrate viscosity of 2 cp and 0.2 cp. Higher filtrate viscosity causes faster fluid cleanup because the mobility of mud filtrate is much lower than the mobility of formation oil.

### 2.4.5 Sensitivity to relative permeability

We performed a sensitivity analysis of sample quality to relative permeability by perturbing the oil-phase relative permeability curve. In so doing, oil relative permeability was decreased by 20% while the water relative permeability was kept constant. The perturbed curves, shown in **Figure 2.28**, exhibit different end points for the oil-phase relative permeability thereby entailing a change of oil-phase relative mobility. All formation properties, including irreducible water saturation, were kept the same as those of the base case formation model. Simulations obtained with the perturbed relative permeability curve are identified with the label “kro”. **Figure 2.29** displays the pressure transient measurements at the sand face compared to those of the base case. Pressure differential curves are separated by 24 psi and are almost parallel to each other. This behavior indicates that uncertainty in relative permeability of the movable phase can play a marked influence in determining formation permeability and significantly affects the measured pressure transients.

### 2.5 MULTI-LAYER FORMATION AT IRREDUCIBLE WATER SATURATION

**Figure 2.30** describes the multi-layer formation model consisting of three hydraulically communicated layers that exhibit the same values of porosity but different values of permeability. We assume that the water-oil capillary pressure and relative permeability curves are the same for the three layers (**Fig. 2.4**). **Table 2.4** summarizes the geometrical and petrophysical properties assumed for the three layers. In the simulations, the dual-packer opening is situated at the center of each layer in the vertical well. The purpose of this formation model is to quantify the influence of porosity and permeability on the time evolution of pressure, fluid density, and fluid viscosity during fluid pumpout.

**Figure 2.31** displays the pressure measurements at the packer within the three layers. The pressure differential varies with the permeability of the formation. **Figure 2.32** shows the simulated sample quality as a function of fluid pumpout time at the sandface of the three layers. We remark that oil mass density varies as a function of hydrocarbon component concentrations (**Eqn. 2.5**). As fluid pumpout time increases, sample quality increases and oil mass density approaches that of formation oil density. Sample quality is slightly lower in the low-permeability layer due to slower flow.

We consider an additional case of the multi-layer formation model in which the three layers exhibit the same values of permeability but different values of porosity. The horizontal and vertical permeability for all layers is equal to 5 mD. **Table 2.5** summarizes the geometrical and petrophysical properties assumed for the three layers. **Figure 2.33** shows the OBM concentration map at the end of fluid withdrawal for the middle layer. We note that the radial extent of invasion extends to 1.75 feet in the low-porosity, bottom layer. **Figure 2.34** displays the pressure measurements at the packer within the three layers. The sample quality (**Fig. 2.35**) calculated from oil density is conditioned by the porosity of the layers. Sample quality increases with an increase of porosity due to relatively shallower invasion. In all cases, sample quality increases to reach over 95% at the end of fluid pumpout. These simulations indicate that the interplay between permeability, porosity, and sample quality is important to accurately predict the sampling time necessary to acquire a sufficiently clean and representative sample of native formation oil.

### 2.6 HOMOGENEOUS FORMATION WITH MOVABLE FLUIDS IN A CAPILLARY TRANSITION ZONE

In this case, we assume that the formation is in a capillary transition zone such that a portion of the water phase is mobile. We consider three cases of mobile water saturation such that the initial water saturation in the formation varies from 0.25 to 0.75. Remaining petrophysical properties are the same as those described in **Table 2.3**. The objective of this example is to quantify the influence of mobile water in the time evolution of component concentration during fluid pumpout. Presence of non-irreducible water saturation causes the water-oil capillary pressure and relative permeability curves to condition the mobility of native oil during both OBM-filtrate invasion and fluid pumpout.

**Figure 2.36** shows the simulated pressure variation during fluid pumpout. The pressure differential increases drastically as the initial water saturation in the formation increases. We note that the pressure differential is 1168 psi at the packer for the initial water saturation of 0.75 case compared to the pressure differential of 97 psi for the Base Case at the end of fluid withdrawal even though the assumed values of porosity and permeability are the same in the two cases. The variation of pressure differential is due to the lower relative mobility of the oil phase within the capillary transition zone. In addition, the influence of such a relatively large pressure differential is observed in the oil density measured at the sandface (**Fig. 2.37**). There is a small increase in oil density of 0.3 lbf/ft$^3$ at the end of fluid pumpout due to the drastic increase of pressure at the sandface that equilibrates with the formation pressure.

**Figure 2.38** displays the fractional flow of water during pumpout. At early times during fluid pumpout, OBM is produced and the fractional flow of water is relatively low. By contrast, at late times the fractional flow increases due to the presence of free water in the formation for cases of initial water saturation of 0.5 and 0.75. For both the base case and the case of initial water saturation equal to 0.25, we observe negligible fractional flow of water because the relative permeability of water (**Fig. 2.4**) is relatively low. **Figure 2.39** shows the time evolution of OBM concentration at the packer for different cases of mobile water. As the initial water saturation increases, the amount of oil in the formation decreases. Therefore, for the same volume of mud-filtrate invasion, fluid sample quality (**Fig. 2.40**) deteriorates with increasing water saturation. Sample quality is 85% in the case of initial water saturation of 0.75.

### 2.7 SUMMARY AND CONCLUSIONS

The following summary and concluding remarks stem from the developments and simulation examples considered in this chapter:

1. We presented simulations of OBM invasion and fluid pumpout in oil-bearing formations that make use of an axially-symmetric compositional formulation with multi-component hydrocarbons. Benchmarking exercises with a commercial simulator confirmed the accuracy and reliability of our predictions of dynamic behavior of pressure and fluid density during mud-filtrate invasion and fluid pumpout. We performed an extensive sensitivity analysis to quantify relative

influence of several petrophysical properties on the time evolution of fluid cleanup.

2. Simulation of packer-type formation-tester measurements indicate that the time required to acquire clean fluid samples of formation oil is governed by the petrophysical and fluid properties of the tested formation, by the radial length of invasion of OBM, and by the flow rates imposed during fluid pumpout. In addition, for reservoirs that are not at irreducible water saturation, the dynamic behavior of fractional flow of water is largely conditioned by both relative permeability and capillary pressure. The pressure differential is very sensitive to both formation permeability and relative mobility of fluids in the near-packer region.
3. Reliable assessment of petrophysical properties from pressure-transient measurements acquired during fluid pumpout requires quantitative understanding of the interplay between oil density, oil viscosity, component concentrations, phase mobility, and fractional flow of water on the space-time evolution of fluid component concentrations in the near-wellbore region.
4. Numerical simulations indicate that transient measurements of oil density and oil viscosity can be used to determine sample quality as both quantities are sensitive to component molar concentrations. The early-time behavior of pressure transients is largely governed by the mobility of mud filtrate.

Table 2.1: Summary of PVT properties of hydrocarbon components assumed in this chapter for the simulations of mud-filtrate invasion and fluid pumpout.

| | $C_{1-5}$ | $C_{6-9}$ | $C_{10-13}$ | $C_{14-18}$ | $C_{19-29}$ |
|---|---|---|---|---|---|
| Initial Concentration | 0.24 | 0.5 | 0.18 | 0.03 | 0.05 |
| Injecting Concentration | 0.005 | 0.005 | 0.005 | 0.98 | 0.005 |
| Tc (K) | 315 | 575 | 644 | 718 | 788 |
| Pc (psi) | 325 | 295 | 284.257 | 237.297 | 211.754 |
| Acentric Factor | 0.15 | 0.41409 | 0.55671 | 0.72593 | 0.87772 |
| Molar Weight (lbs/lb-moles) | 40 | 119 | 165.116 | 226.776 | 290.558 |
| Component Viscosity (cp) | 0.12 | 0.294 | 0.49 | 0.94 | 1.2 |

Table 2.2: Summary of geometrical and numerical simulation parameters assumed for the Base Case formation model described in Fig. 2.1.

| **Variable** | **Units** | **Value** |
|---|---|---|
| Wellbore radius ($r_w$) | ft | 0.35 |
| External radius ($r_e$) | ft | 1000 |
| Reservoir thickness | ft | 22.5 |
| Datum depth | ft | 6500 |
| Water-oil contact | ft | 7000 |
| Number of nodes - radial axis | -- | 50 |
| Number of nodes - vertical axis | -- | 45 |
| Grid cell size - radial axis | ft | Variable |
| Grid cell size - vertical axis | ft | 0.5 |

Table 2.3: Summary of reservoir rock and rock-fluid properties assumed for the Base Case formation model described in Fig. 2.1.

| **Variable** | **Units** | **Value** |
|---|---|---|
| Porosity | fraction | 0.18 |
| Radial permeability | mD | 5 |
| Vertical permeability | mD | 5 |
| Water density @ STP | $lbf/ft^3$ | 64 |
| Water compressibility | $psi^{-1}$ | $3x10^{-6}$ |
| Initial water saturation | fraction | 0.06 |
| Water viscosity | cp | 1.0 |
| Formation compressibility | $psi^{-1}$ | $10^{-7}$ |
| Production flow rate | $ft^3/day$ | 75 |
| Initial Reservoir Pressure | psi | 3900 |
| Reservoir Temperature | $^oF$ | 160 |

Table 2.4: Summary of reservoir rock properties assumed for the multi-layer formation model with different values of permeability (Fig. 2.30).

| **Layer** | **Variable** | **Units** | **Value** |
|---|---|---|---|
| **Upper Layer** | | | |
| | Radial permeability | mD | 5 |
| | Vertical permeability | mD | 5 |
| | Top location | ft | 6500 |
| | Bottom location | ft | 6507.5 |
| **Middle Layer** | | | |
| | Horizontal permeability | mD | 20 |
| | Vertical permeability | mD | 20 |
| | Top | ft | 6507.5 |
| | Bottom location | ft | 6515 |
| **Lower Layer** | | | |
| | Horizontal Permeability | mD | 100 |
| | Vertical Permeability | mD | 100 |
| | Top location | ft | 6515 |
| | Bottom location | ft | 6522.5 |

Table 2.5: Summary of reservoir rock properties assumed for the multi-layer formation model with different values of porosity.

| Layer | Variable | Units | Value |
|---|---|---|---|
| **Upper Layer** | | | |
| | Porosity | fraction | 0.25 |
| | Top location | ft | 6500 |
| | Bottom location | ft | 6507.5 |
| **Middle Layer** | | | |
| | Porosity | fraction | 0.15 |
| | Top location | ft | 6507.5 |
| | Bottom location | ft | 6515 |
| **Lower Layer** | | | |
| | Porosity | fraction | 0.05 |
| | Top location | ft | 6515 |
| | Bottom location | ft | 6522.5 |

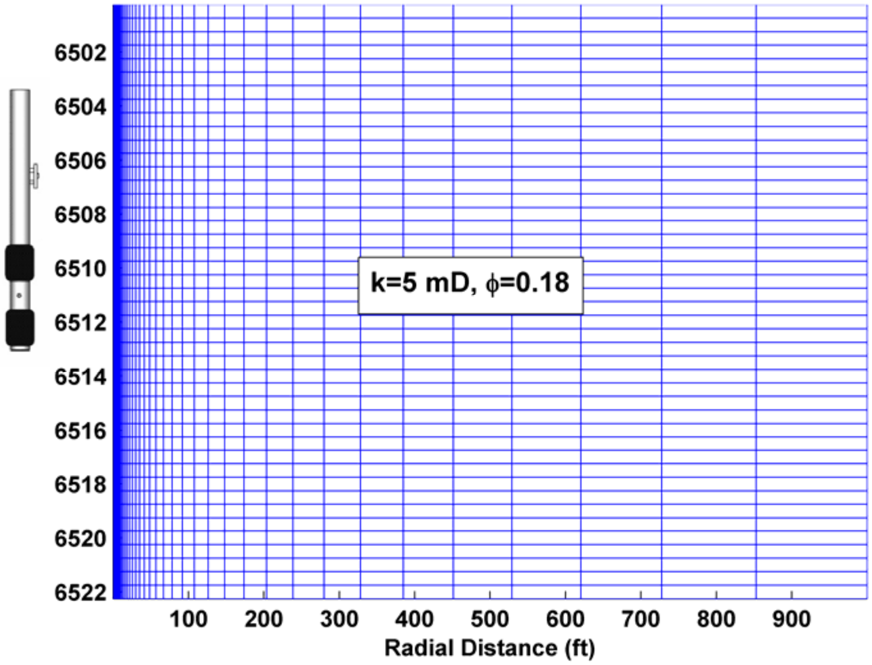

Figure 2.1: Description of the axially-symmetric finite-difference grid used in the simulations of OBM-filtrate invasion and dual-packer formation tester measurements. The values of permeability (k) and porosity ($\phi$) as well as the indicated depth range define the properties of the Base Case formation model.

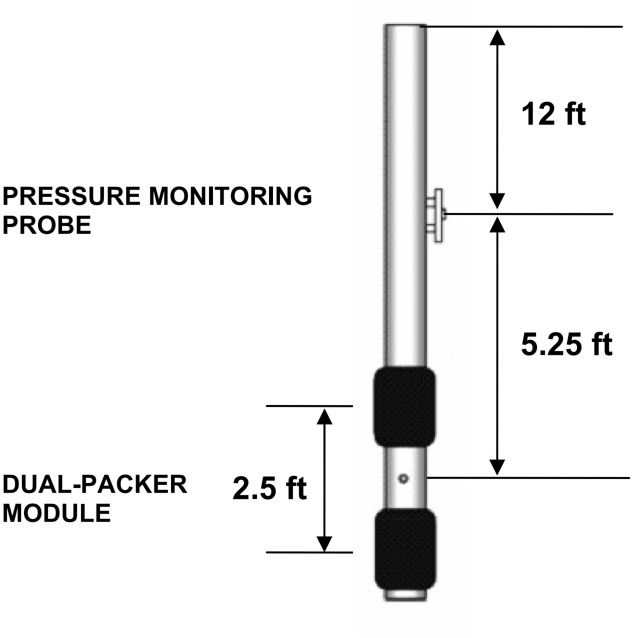

Figure 2.2: Configuration of the assumed dual-packer formation tester, consisting of a vertical pressure monitoring probe and a dual-packer module. Pressure and fluid sensors are included in the packer section of the formation tester.

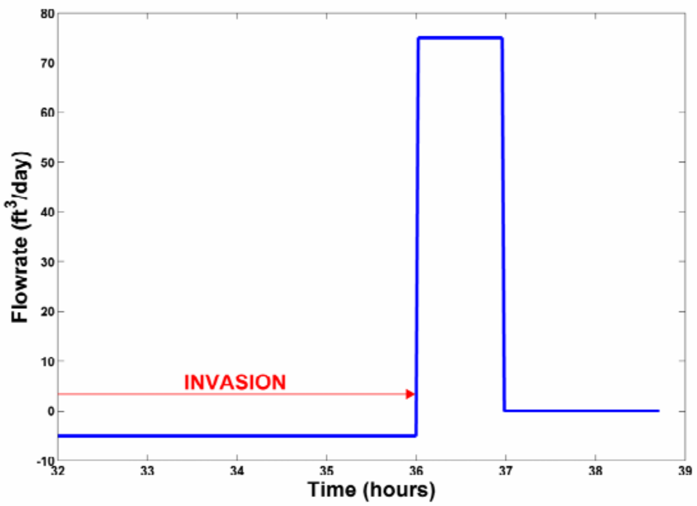

Figure 2.3: Flow rate assumed in the processes of mud-filtrate invasion and fluid pumpout (formation testing). Mud-filtrate invasion takes place during 36 hours followed by pumpout during 58 minutes. The total simulation time is 38.6 hours.

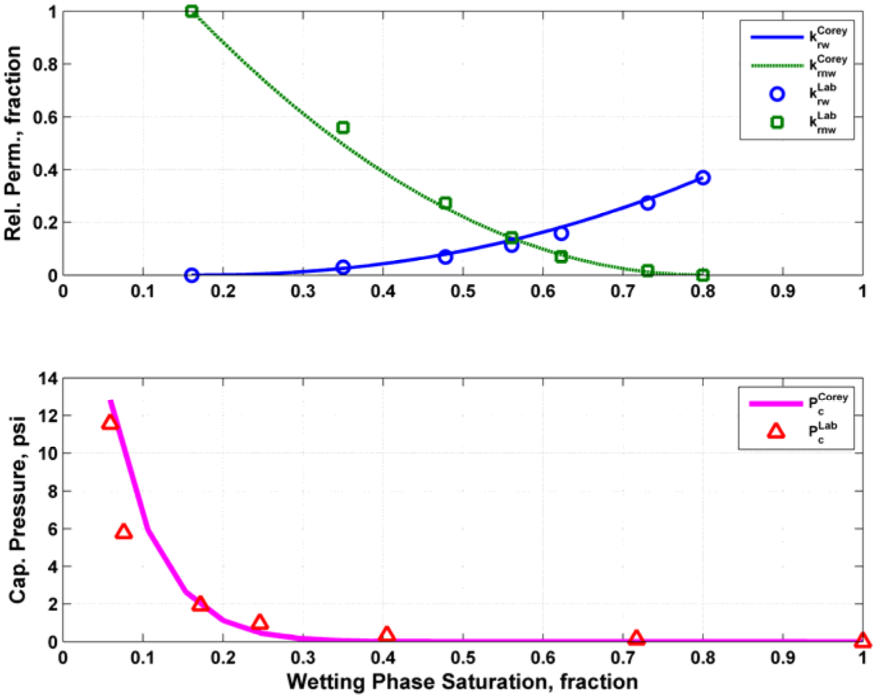

Figure 2.4: Water-oil relative permeability and capillary pressure curves assumed in the simulations of mud-filtrate invasion and fluid pumpout. Water and oil are the wetting and non-wetting fluid phases, respectively. The panels compare saturation-dependent properties measured in the laboratory on rock-core samples against properties calculated with a best-fit Brooks-Corey model.

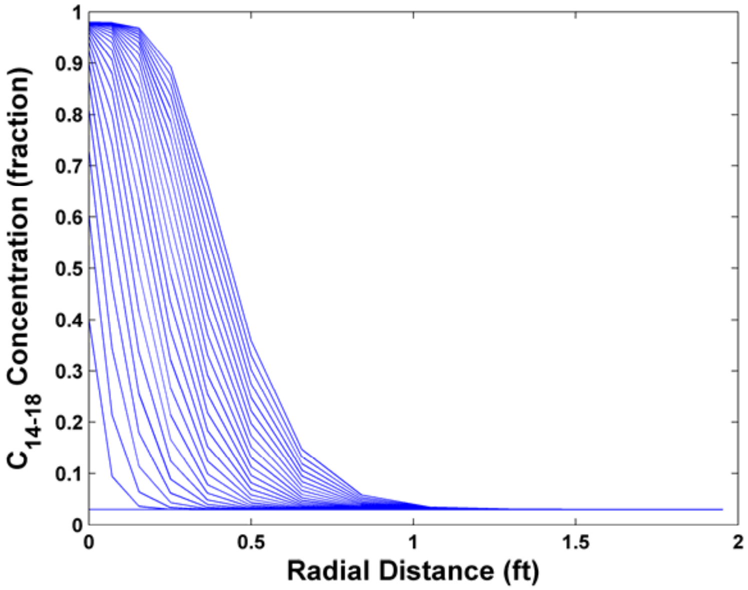

Figure 2.5: Variation of OBM $C_{14-18}$ component concentration during the process of mud-filtrate invasion for the Base Case formation model. Twenty-five curves are shown at time increments of 1.44 hours after the onset of invasion.

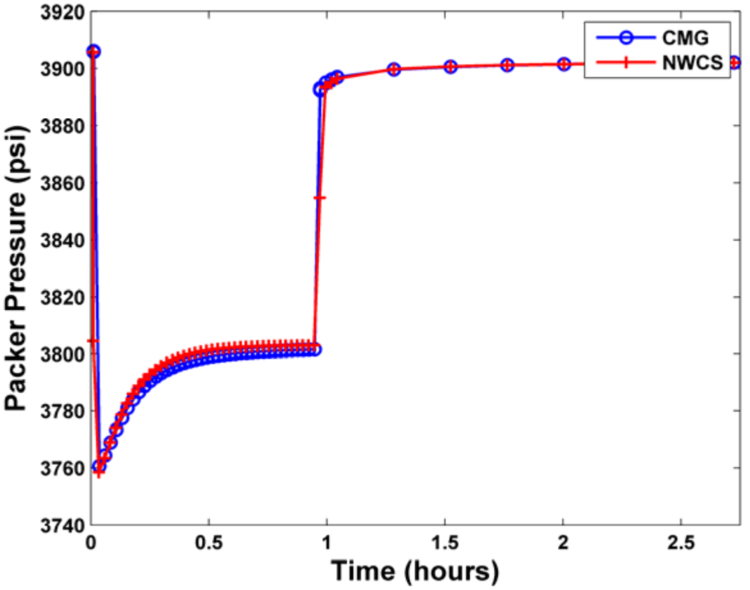

Figure 2.6: Comparison of pressure transient measurements at the packer calculated with CMG and the simulator developed in this chapter (NWCS) for the Base Case formation model.

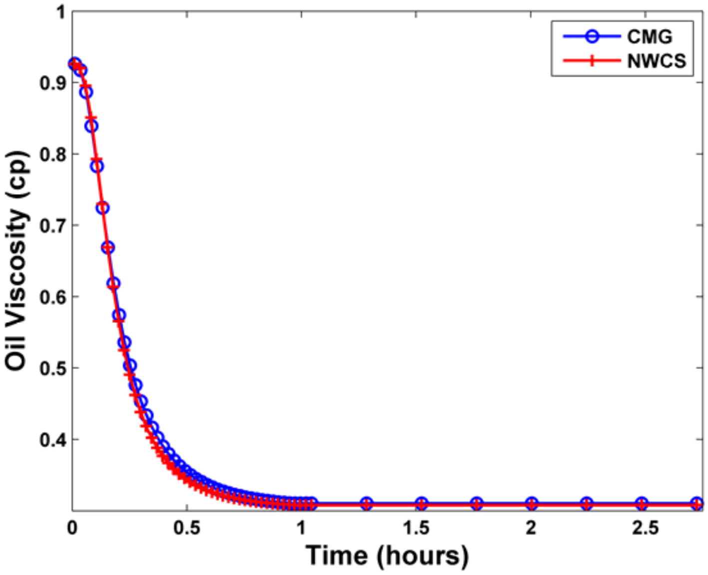

Figure 2.7: Comparison of the time evolution of oil viscosity at the packer during fluid pumpout calculated with CMG and the simulator developed in this chapter (NWCS) for the Base Case formation model.

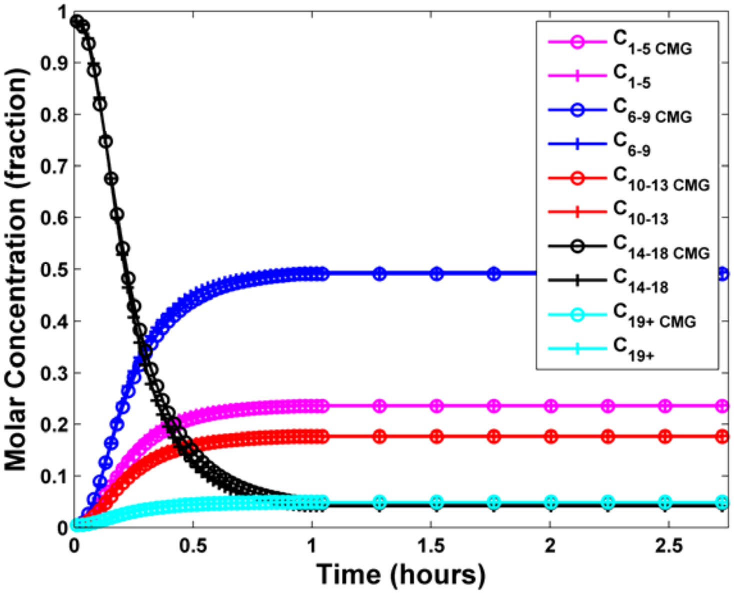

Figure 2.8: Comparison of the time evolution of hydrocarbon component concentrations at the sandface during the process of OBM pumpout calculated with CMG and the simulator developed in this chapter (NWCS) for the Base Case formation model. Concentrations reach the initial formation composition at the end of fluid pumpout.

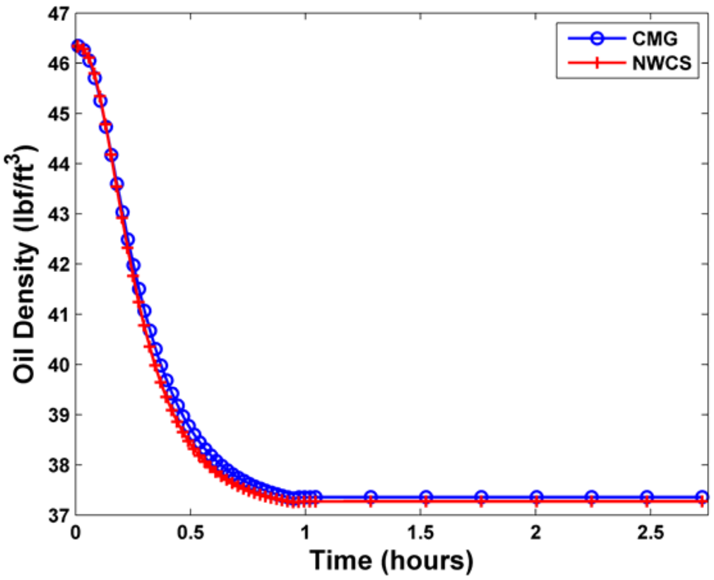

Figure 2.9: Comparison of the time evolution of oil density at the packer during fluid pumpout calculated with CMG and the simulator developed in this chapter (NWCS) for the Base Case formation model.

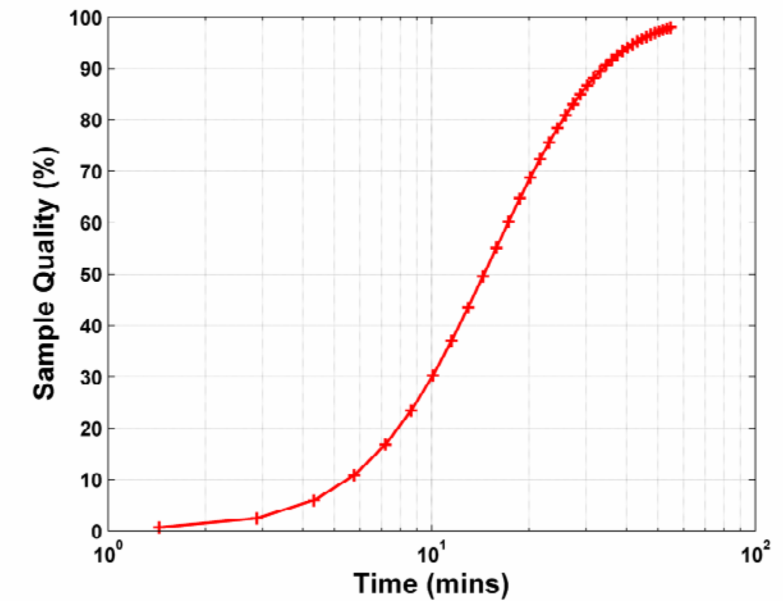

Figure 2.10: Time evolution of sample quality (calculated from the time evolution of oil density) at the packer during fluid pumpout for the Base Case formation model.

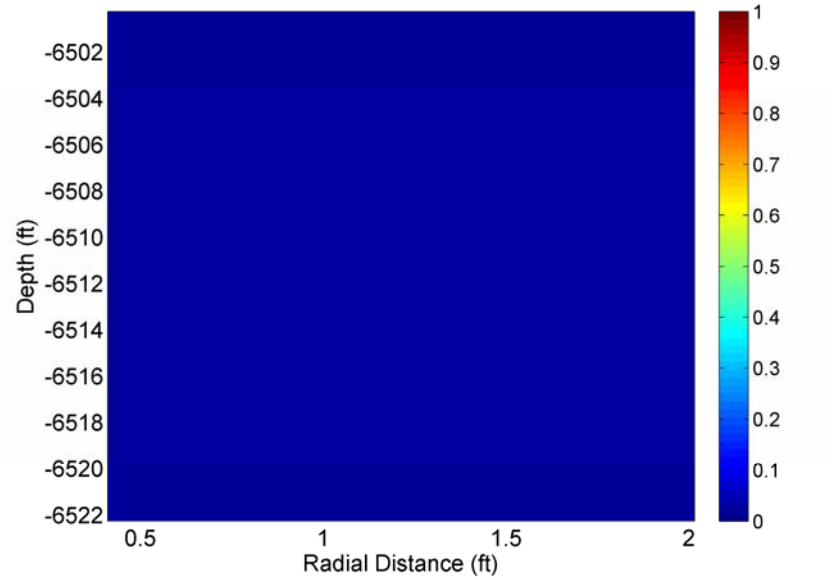

Figure 2.11: Spatial distribution (radial and vertical directions) of OBM concentration in the near wellbore region before the onset of invasion for the Base Case formation model.

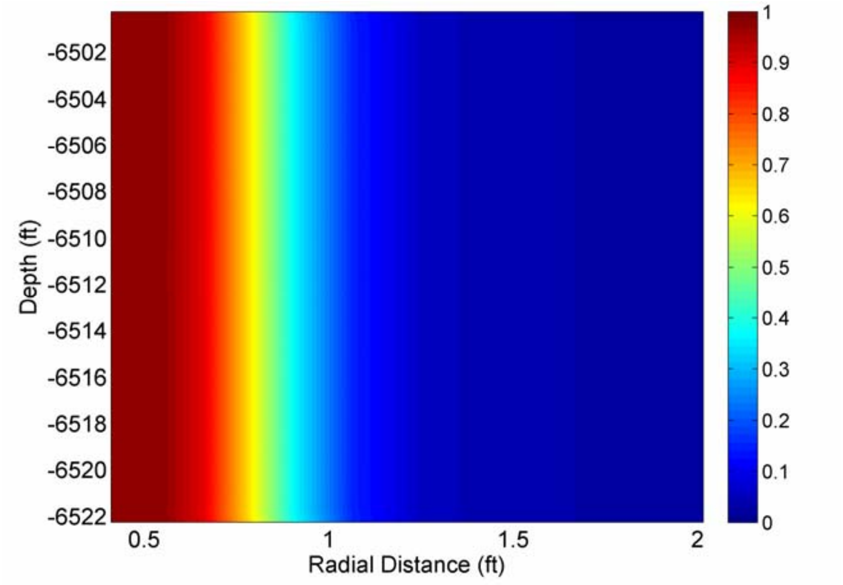

Figure 2.12: Spatial distribution (radial and vertical directions) of the OBM concentration in the near wellbore region at the end of mud-filtrate invasion for the Base Case formation model.

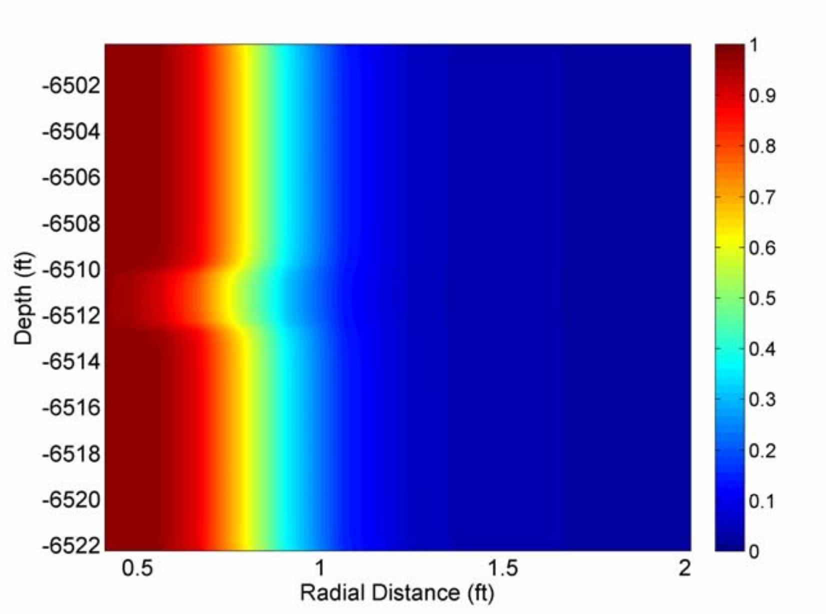

Figure 2.13: Spatial distribution (radial and vertical directions) of OBM concentration in the near wellbore region after 1.3 minutes of fluid pumpout for the Base Case formation model.

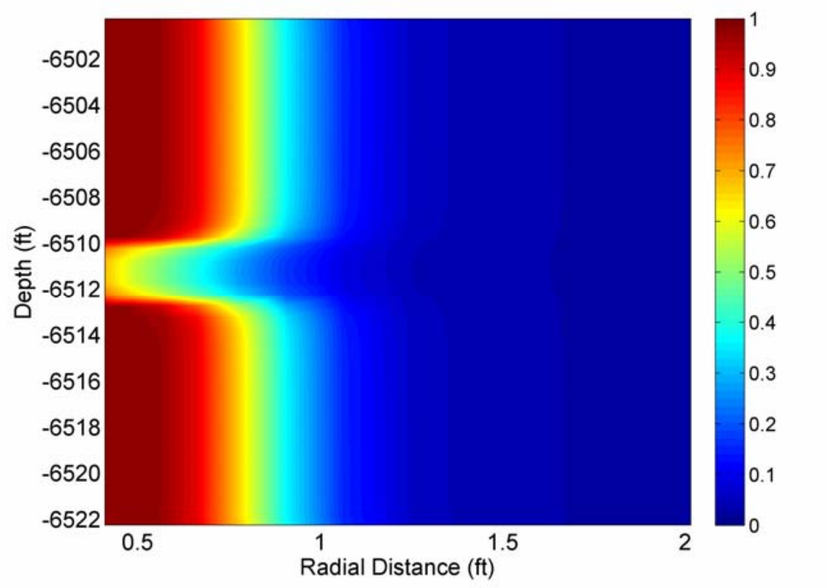

Figure 2.14: Spatial distribution (radial and vertical directions) of OBM concentration in the near wellbore region after 8.5 minutes of fluid pumpout for the Base Case formation model.

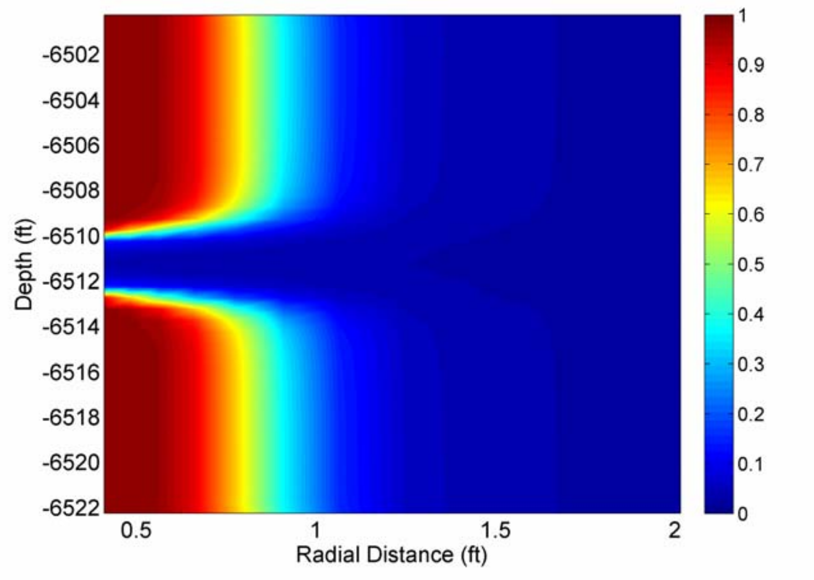

Figure 2.15: Spatial distribution (radial and vertical directions) of OBM concentration in the near wellbore region after 58 minutes of fluid pumpout for the Base Case formation model.

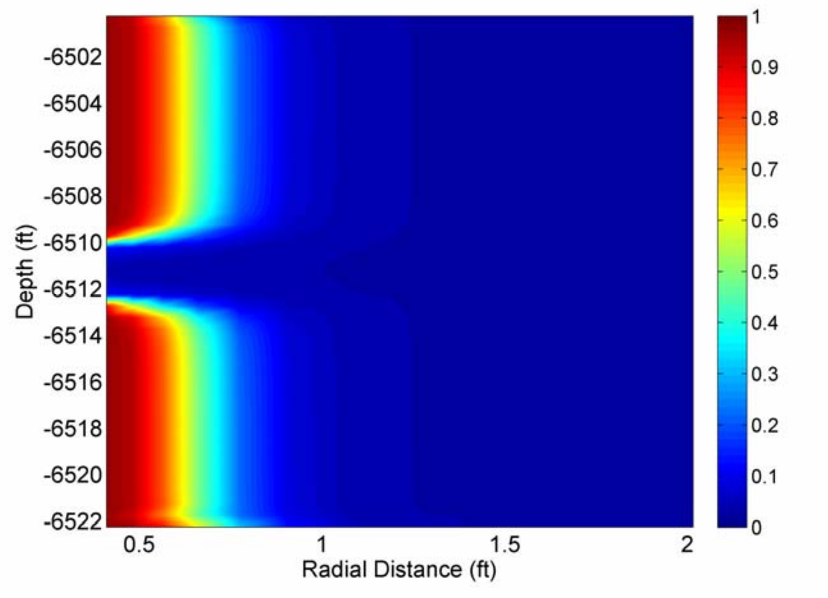

Figure 2.16: Spatial distribution (radial and vertical directions) of OBM concentration in the near wellbore region after 58 minutes of fluid pumpout for the high-permeability, high-porosity (k=100 mD, $\phi$=0.35) formation model.

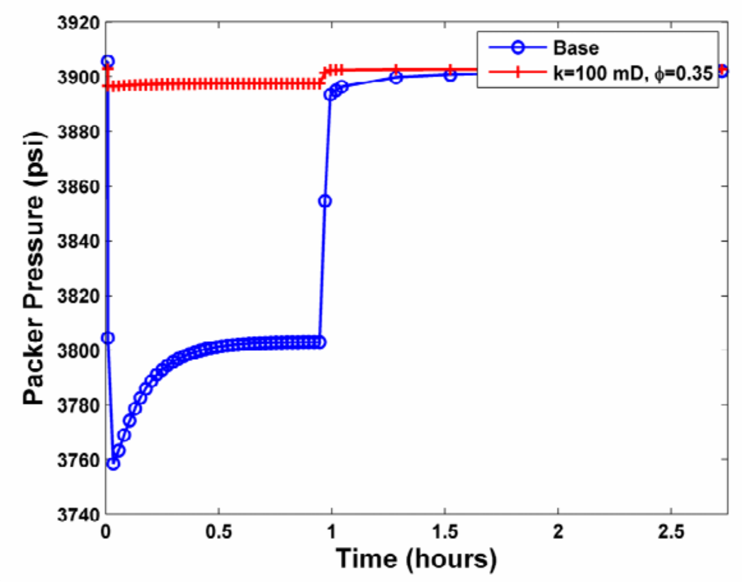

Figure 2.17: Pressure transient measurements simulated at the packer for the high-permeability, high-porosity formation model.

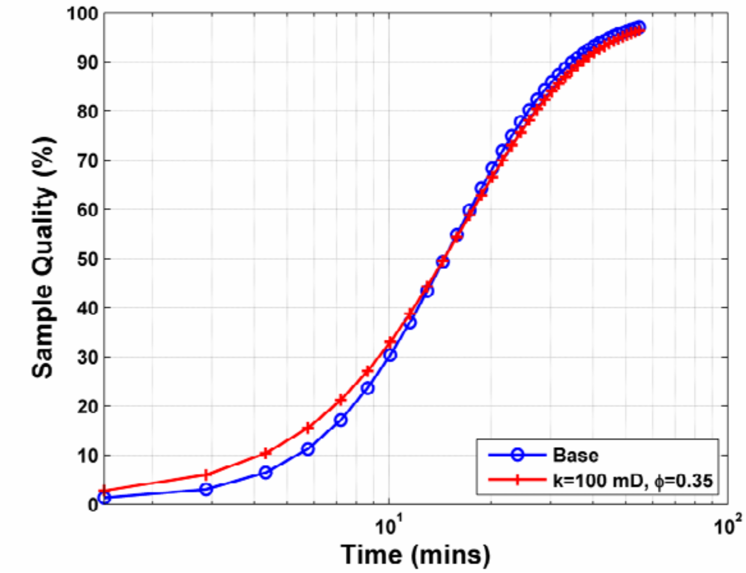

Figure 2.18: Sensitivity of the time evolution of sample quality to high values of permeability and porosity.

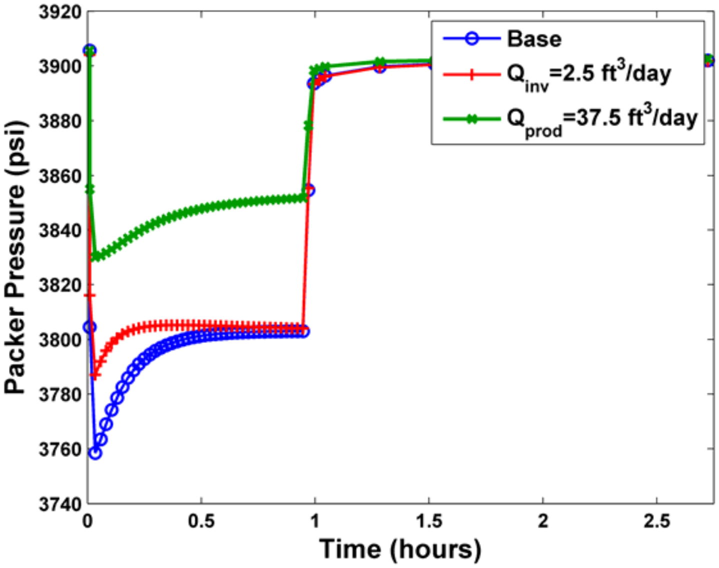

Figure 2.19: Pressure transient measurements simulated at the packer for different rates of mud-filtrate invasion and fluid withdrawal.

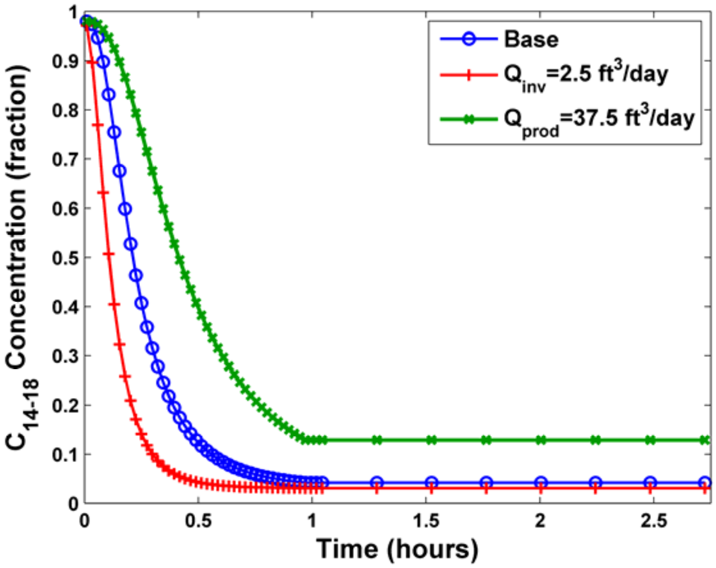

Figure 2.20: Simulated measurements of OBM component concentration at the packer for different rates of mud-filtrate invasion and fluid withdrawal.

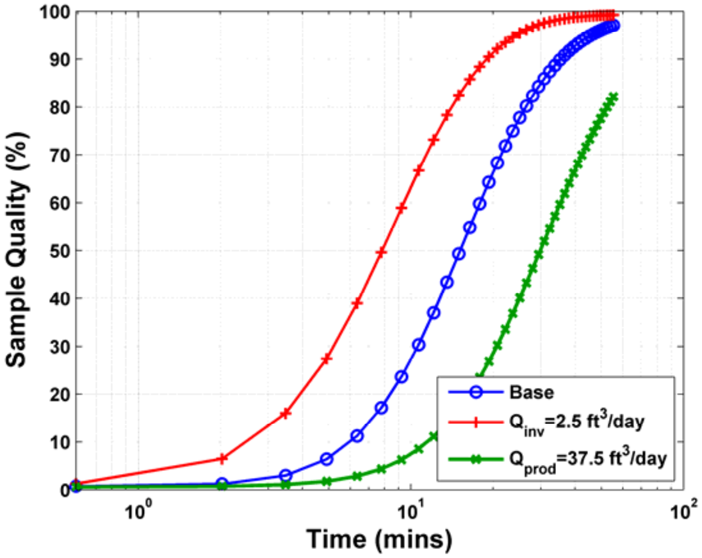

Figure 2.21: Sensitivity of the time evolution of sample quality to different rates of mud-filtrate invasion and fluid withdrawal.

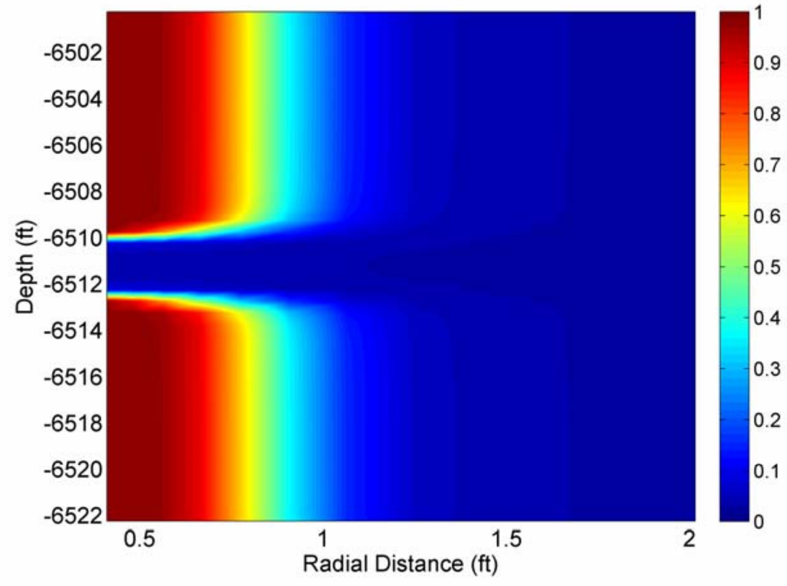

Figure 2.22: Spatial distribution (radial and vertical directions) of OBM concentration in the near wellbore region after 58 minutes of formation testing for the anisotropic formation model.

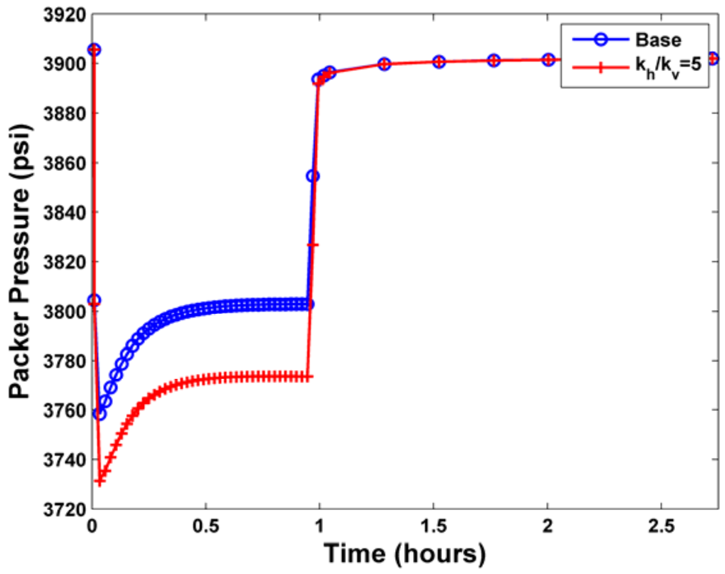

Figure 2.23: Pressure transient measurements simulated at the packer for the anisotropic formation model. Vertical permeability is 1 mD for the anisotropic formation model.

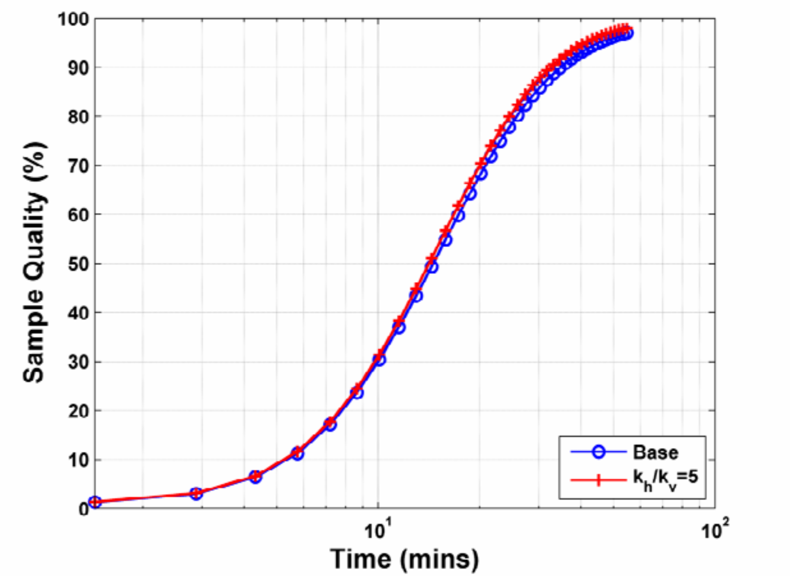

Figure 2.24: Sensitivity of the time evolution of sample quality to permeability anisotropy compared to that of the Base Case formation model.

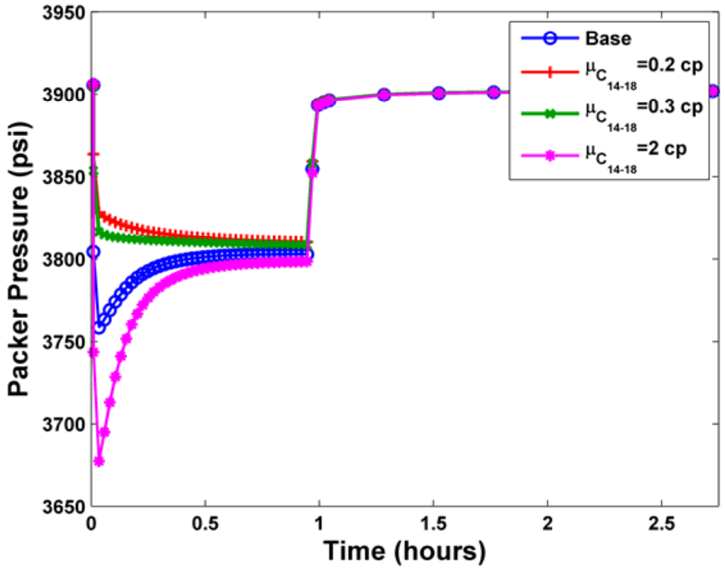

Figure 2.25: Pressure transient measurements simulated at the packer for different cases of OBM viscosity. Values of OBM viscosity vary from 0.2 cp to 2 cp.

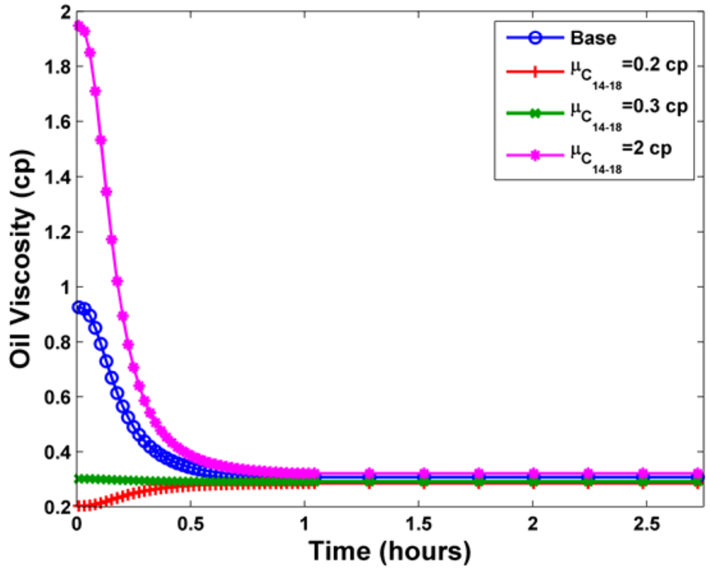

Figure 2.26: Sensitivity of the time evolution of oil phase viscosity to different values of OBM viscosity.

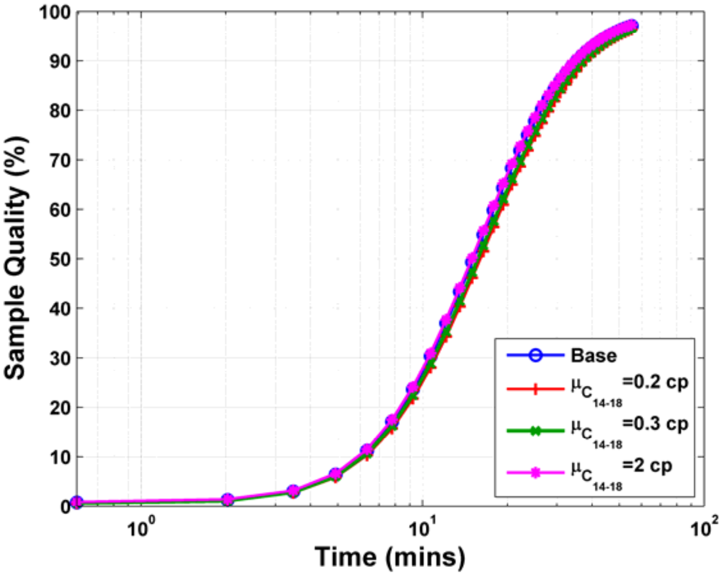

Figure 2.27: Sensitivity of the time evolution of sample quality to different values of OBM viscosity.

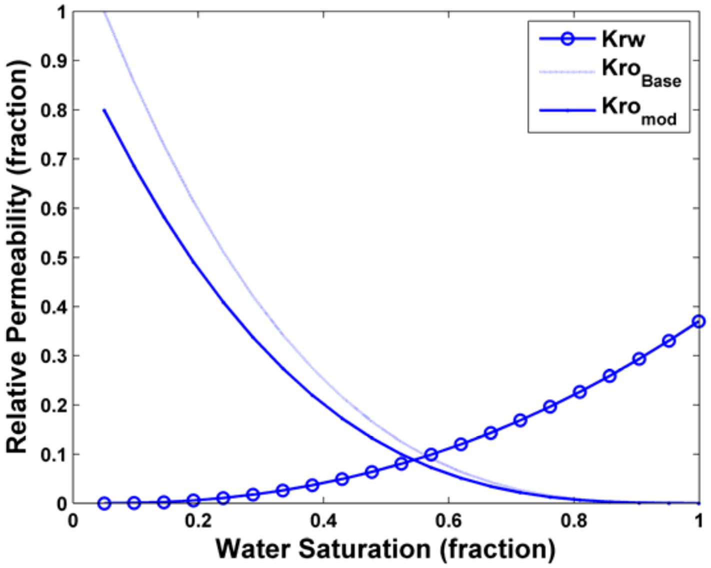

Figure 2.28: Sensitivity analysis to saturation-dependent relative permeability. The mobility of the oil phase is changed while the mobility of the water phase is kept constant.

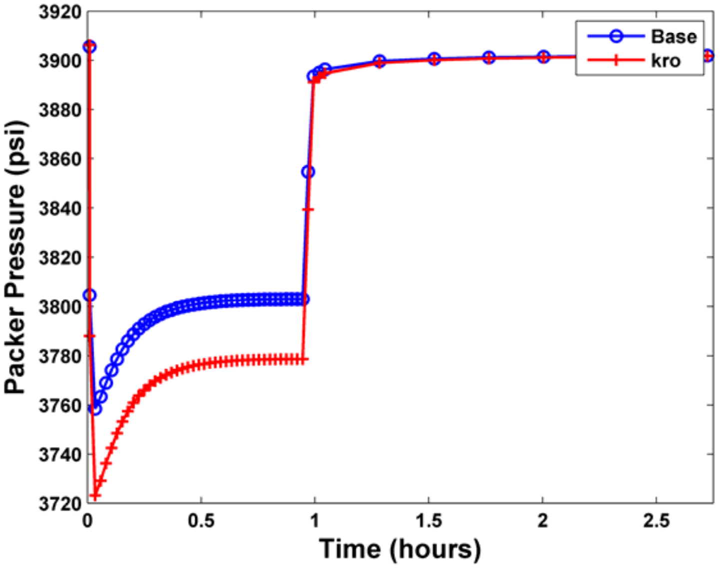

Figure 2.29: Pressure transient measurements simulated at the packer for the two cases of oil-phase relative permeability shown in Fig. 2.28.

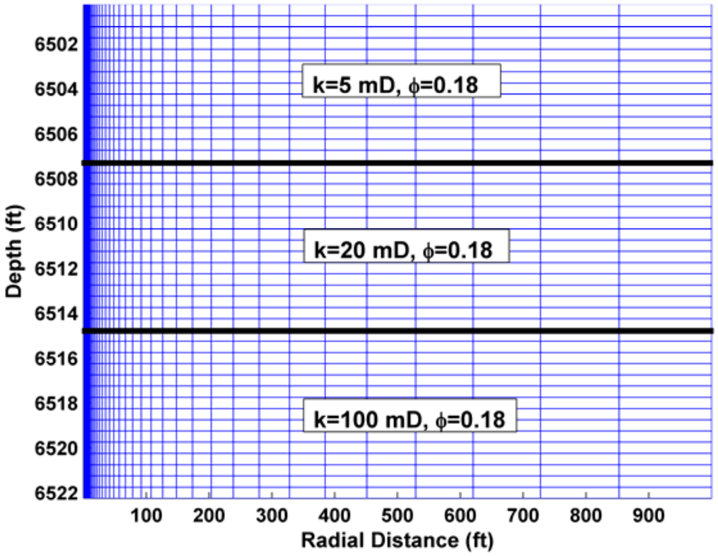

Figure 2.30: Three-layer reservoir model with different values of horizontal permeability ($k$ = absolute permeability, and $\phi$= porosity).

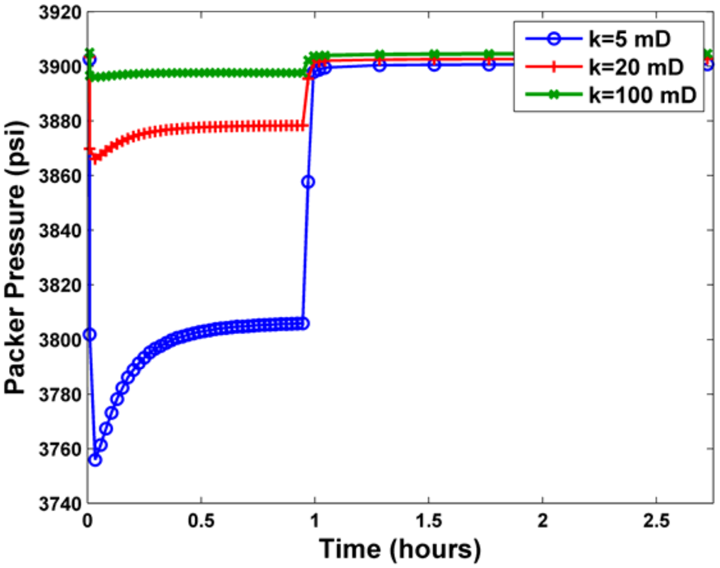

Figure 2.31: Simulated pressure transient measurements at packer locations centered with each of the three layers described in Fig. 2.30. Pressure differentials vary due to layer permeability.

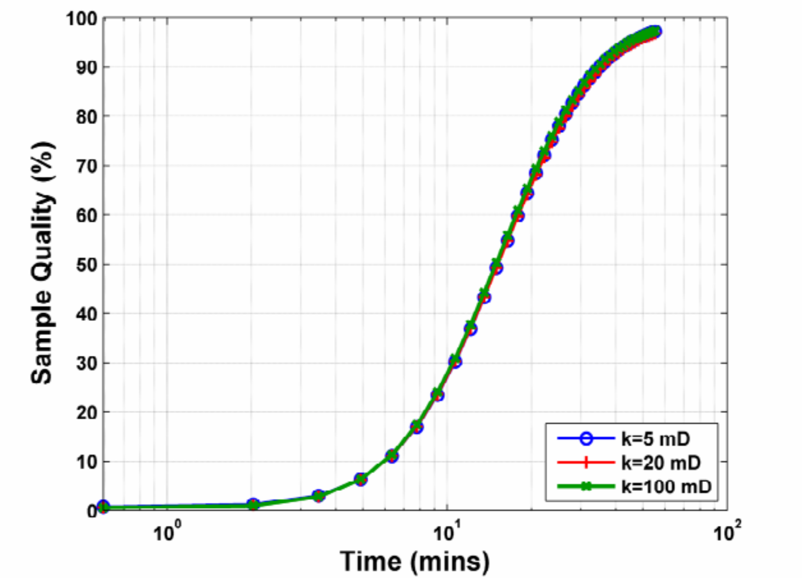

Figure 2.32: Time evolution of sample quality at the sand face during fluid pumpout as a function of layer permeability. The simulations were performed at packer locations centered with each of the three layers described in Fig. 2.30.

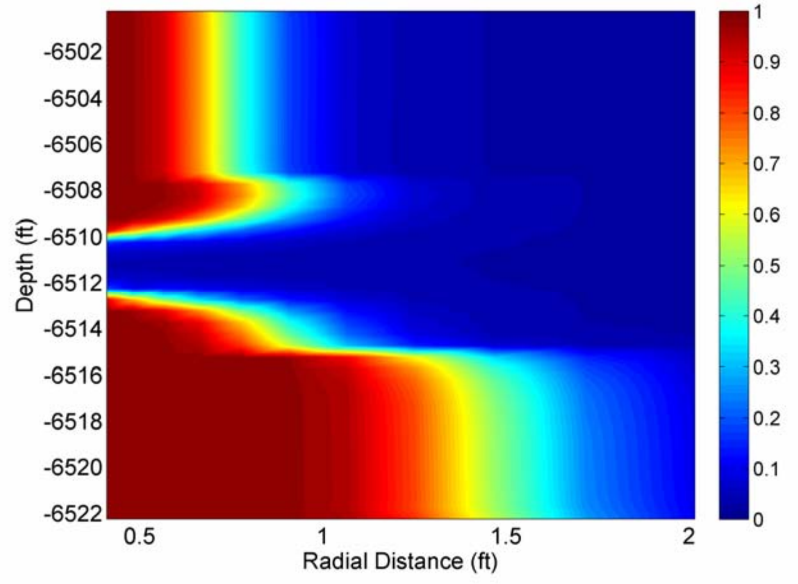

Figure 2.33: Spatial distribution (radial and vertical directions) of OBM concentration in the near wellbore region after 58 minutes of formation testing for the three-layer formation model described in Table 5. The radial extent of invasion varies in the layers due to different values of porosity. Invasion is roughly 1.75 ft for the lowest-porosity, bottom layer.

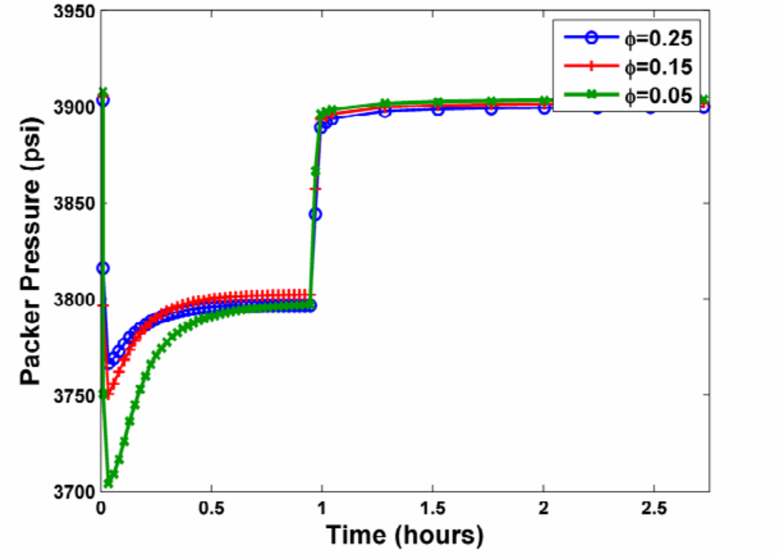

Figure 2.34: Simulated pressure transient measurements at packer locations centered with each of the three layers described in Table 2.5.

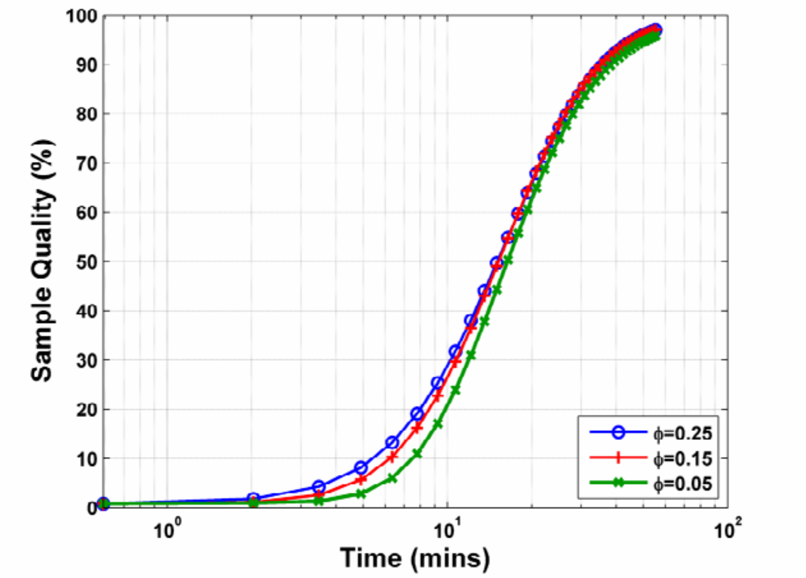

Figure 2.35: Sample quality at the sand face during fluid pumpout as a function of layer porosity. The simulations were performed at packer locations centered with each of the three layers described in Table 2.5.

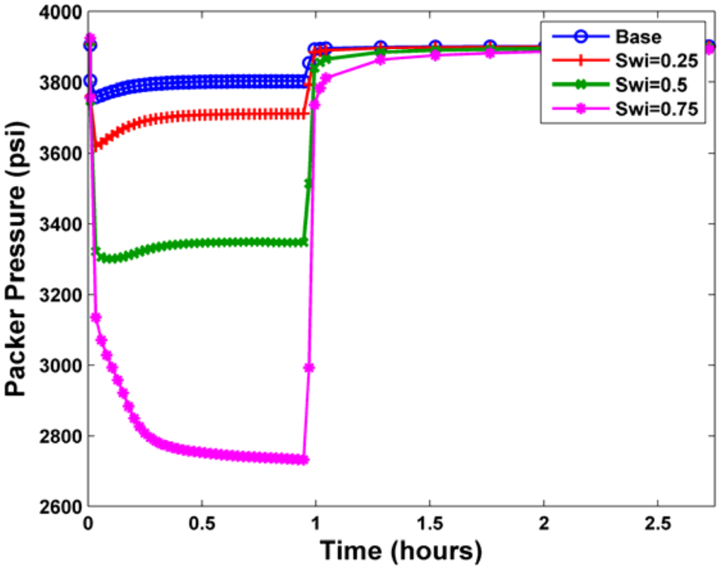

Figure 2.36: Pressure transient measurements simulated at the packer within a capillary transition zone for different values of initial water saturation.

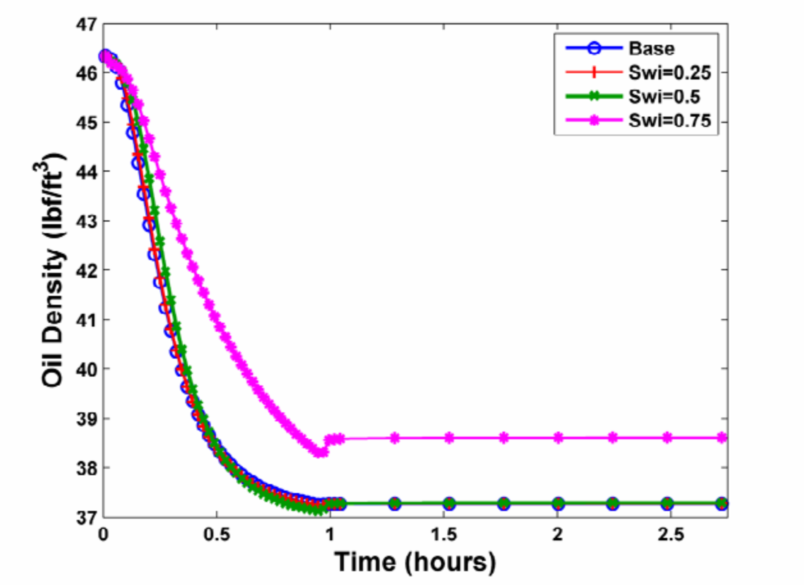

Figure 2.37: Time evolution of oil density during fluid pumpout within the capillary transition zone for different values of initial water saturation. Note the increase of oil density at the end of fluid pumpout. This behavior is attributed to the rise in pressure at the wellbore that in turn increases the oil density at the sandface.

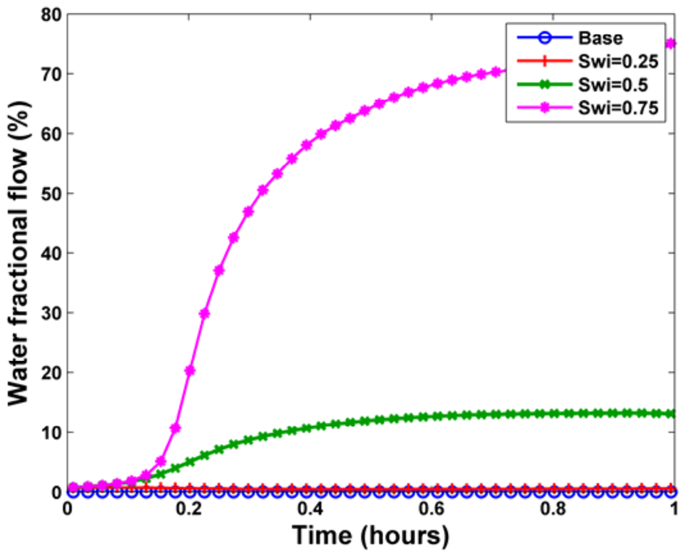

Figure 2.38: Time evolution of fractional flow of water at the sandface during fluid pumpout within the capillary transition zone for different values of initial water saturation.

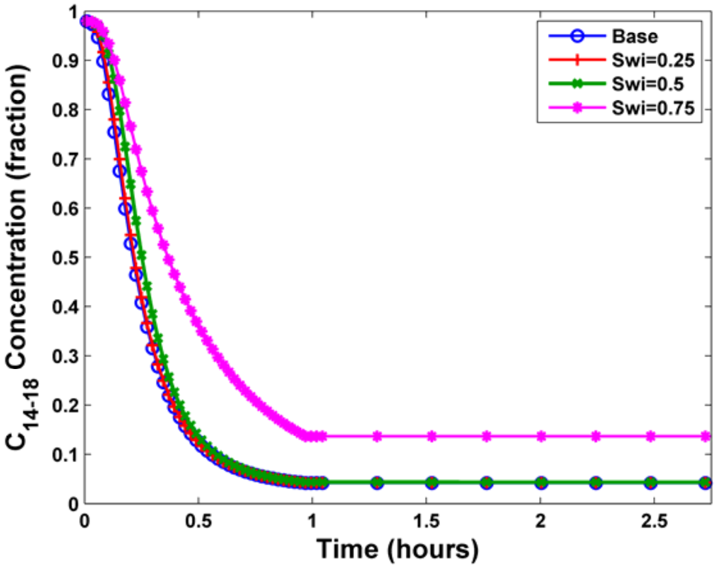

Figure 2.39: Simulated OBM component concentration measurements at the packer within the capillary transition zone for different values of initial water saturation.

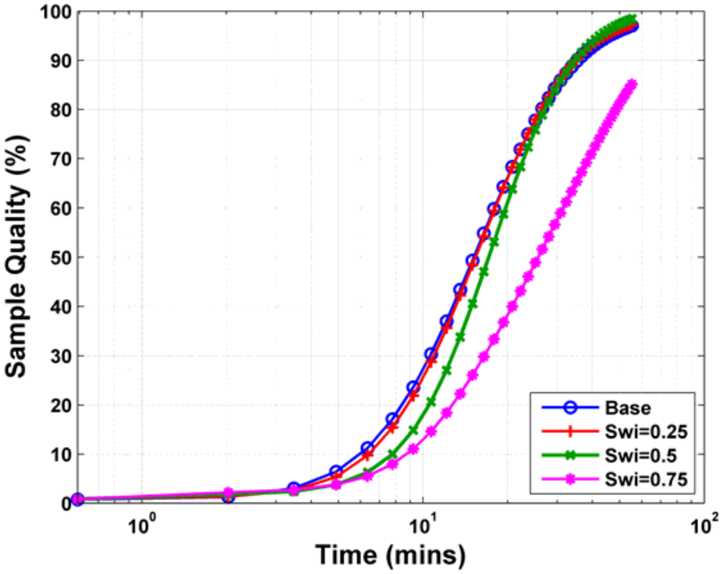

Figure 2.40: Sample quality at the sand face during fluid pumpout within the capillary transition zone for different values of initial water saturation.

# Chapter 3: Effects of Petrophysical Properties on Array-Induction Measurements acquired in the presence of Oil-Base Mud-Filtrate Invasion

In this chapter, we quantify the influence of petrophysical properties on array-induction resistivity measurements acquired in the presence of oil-base mud (OBM) filtrate invasion. To simulate OBM-filtrate invasion, we consider a simple two-component formulation for the oil phase (OBM and reservoir oil) wherein the components are first-contact miscible. Simulations also include the presence of irreducible, capillary-bound, and movable water. The dynamic process of OBM invasion causes the component concentrations to vary with space and time. In addition, the relative mobility of the oil phase varies during the process of invasion given that oil viscosity and oil density are both dependent on component concentrations. This behavior in turn affects the spatial distribution of electrical resistivity and, consequently, the borehole array-induction measurements.

We use an implicit pressure, explicit concentration (IMPEC) reservoir simulator with two-component formation fluids to reproduce the invasion process in axial-symmetric rock formations penetrated by a vertical well. Simulations of the process of OBM-filtrate invasion yield two-dimensional spatial distributions of water and oil saturation that are transformed into spatial distributions of electrical resistivity using Waxman-Smits' formulation. Subsequently, we simulate array-induction measurements with a numerical mode-matching method.

Simulation of induction measurements in the presence of OBM are compared against the corresponding measurements acquired in the presence of water-base mud (WBM) using field measurements acquired in a deepwater Gulf-of-Mexico reservoir. Sensitivity analyses are conducted to quantify the effect of OBM-filtrate invasion on array-induction logs, including different values of formation porosity-permeability, movable water zone, capillary pressure, relative permeability, mud-filtrate invasion rates, and fluid viscosity. In addition, we quantify the effect of changes of rock wettability due to OBM invasion on field measurements. Our study indicates that relative permeability, capillary pressure, and hence flow rate of invasion control the radial length of invasion of OBM and, consequently, the values and relative separation of apparent resistivity curves. Porous rock formations saturated with movable water entail smooth radial distributions of water saturation which, in turn, result in deep (1.5 ft - 2 ft) radial invasion profiles and relatively large separation of apparent resistivity curves. By contrast, null or marginal separation of apparent resistivity curves occurs when the invaded rock is at irreducible water saturation.

### 3.1 INTRODUCTION

The array-induction imager tool (AIT[5]) is widely used to measure formation resistivity in the presence of OBM. Resistivity measurements remain influenced by the process of mud-filtrate invasion that takes place under overbalanced drilling conditions. In the case of oil-base muds, invading mud-filtrate is miscible with formation oil. Such a fluid miscibility condition results in changes of bulk fluid density and fluid viscosity, thereby altering the apparent oil phase mobility in the near-wellbore region. Within a capillary transition zone, additional changes in the fluid saturation front due to invasion arise because of the presence of movable water. The fluid saturation front can also be altered because of variations of oil-phase mobility. Thus, it becomes imperative to accurately model the effect of OBM on the invasion process and, subsequently, on AIT measurements acquired some time after the onset of invasion.

---

[5] Trademark of Schlumberger

Oil-base muds contain a mixture of oil, water, and surfactants necessary to maintain the oil-water mixture as an emulsion (Bourgoyne Jr et al., 1986.; La Vigne et al., 1997), in which oil is the continuous phase and encapsulates the water (Proett et al. 2002). The continuous phase dominates the process of invasion and mixes with formation fluids. Proett et al. (2002) simulated the process of OBM invasion via Todd and Longstaff's (1972) miscible displacement algorithm in which the OBM was treated as a solvent. In this chapter, we assume oil as the main component of the OBM and neglect the effect of water and surfactants in the emulsion. Therefore, oil and water phases remain immiscible. This assumption is not restrictive in field applications, especially when the chemical activity of the OBM does not cause a separation of phases within the mud as the latter invades the formation.

We are interested in analyzing the time-space variability of AIT measurements in the presence of OBM-filtrate invasion. La Vigne et al. (1997) studied several field cases where such variability was attributed not only to invasion, but also to shale fracturing. While performing experiments using OBM invasion on sandstone cores, Yan and Sharma (1989) observed considerable changes on wettability as well as a reduction of permeability. The latter laboratory evidence provides solid footing upon which to analyze the effect of invasion observed in induction resistivity measurements acquired in wells drilled with OBM.

In this chapter, we first analyze the field measurements available to study the process of mud-filtrate invasion in a clastic formation. Subsequently, we explain the methodology to simulate the process of oil-base mud-filtrate invasion and array-induction resistivity measurements. Sensitivity analysis sheds insight to the petrophysical and fluid properties affecting the depth and shape of the invasion front. In addition, it provides a quantitative framework to interpret the resistivity measurements. Finally, we use the results of sensitivity analyses to reproduce induction resistivity measurements acquired in a deepwater turbidite reservoir.

### 3.2 GEOLOGICAL DESCRIPTION

The formation under analysis consists of unconsolidated shaly sands in a turbidite system formed mainly by channel levees located in the deepwater Gulf of Mexico. The sedimentary structure includes ripple stratification, clay laminations, and massive intervals with moderate to good grain sorting. Based on thin-section interpretations, it is known that cement of clinoptilolite and smectite are present in this system. Quartz concentration is between 85% and 95%, being clay minerals the remaining components of the rock. The latter minerals include illite/smectite, illite/mica, and kaolinite and chlorite in small amounts. In rare cases, it is possible to observe electrical conductive minerals like siderite and pyrite, as well as traces of calcite and dolomite. Porosity ranges between 20% and 34% while permeability varies from 10 md in low-porosity zones to 2,500 md in high-porosity intervals. **Figure 3.1** shows photographs of two core sections displaying both shale-laminated and massive sand intervals.

### 3.3 PETROPHYSICAL ASSESSMENT

We focus our attention to three intervals of the formation penetrated by a cored well. The first one is at the lower section of the formation and is a 100% water saturated interval that is assumed homogeneous (single layer). This interval is used to calibrate our synthetic base case where we perform sensitivity analyses to several petrophysical and fluid properties. The second and third intervals, located in the upper section of the formation, correspond to partially oil-saturated rocks containing movable water. These two intervals will be subsequently used to simulate the process of mud-filtrate invasion and to reproduce field measurements with numerical simulations.

### 3.3.1 Water Saturation

The formation is mainly composed of shaly sands and this prompts us to invoke Waxman-Smits' (1968) equations to calculate water saturation ($S_w$). However, since the connate water salt concentration is very high (>200 kppm), Archie's (1942) equation can also be applied to calculate $S_w$ in cases of low values of hydrocarbon saturation. Waxman-Smits' equation is given by

$$\frac{1}{R_t\left(r,z\right)} = S_w{}^{n^*}\left(r,z\right)\frac{\phi^{m^*}\left(z\right)}{a}\left[\frac{1}{R_w}+\frac{BQ_v}{S_w\left(r,z\right)}\right], \tag{3.1}$$

where $r$ is the radial distance from the wellbore, $z$ is the vertical distance with respect to the top of the formation, $R_t$ is true formation resistivity, $R_w$ is connate water resistivity, $a$ is the tortuosity factor, $m^*$ and $n^*$ are clay-corrected Archie's cementation and saturation exponents, respectively, $Q_v$ is the volumetric concentration of sodium exchange cations (CEC) associated with the clay, and $B$ designates the equivalent conductance of the counterions as a function of connate water resistivity. We use **Eq. 19** of Waxman and Smits' (1968) work to calculate $B$, whereas $m^*$, $n^*$ and $Q_v$ are obtained from laboratory measurements. **Equation 3.1** is solved iteratively for $S_w$ starting with Archie's $S_w$ as the initial-guess. **Table 3.1** describes the input parameters used to calculate initial water saturation using the Waxman-Smits model. Such parameters were obtained from laboratory measurements performed on cores and fluid samples withdrawn from the formation under consideration.

### 3.3.2 Porosity and Permeability

We followed the methodology applied by Salazar et al. (2006) to calculate porosity and permeability. Porosity is calculated from density and neutron measurements by accounting for the presence of two fluids (oil and water) and two minerals (quartz and clay) in the porous medium. Permeability is calculated via a modified Timur-Tixier equation from porosity and irreducible water saturation. The specific equation for permeability was obtained with calibration of porosity-permeability measurements, and is given by

$$k = 4.22 \times 10^{6} \frac{\phi^{7.5}}{S_{wir}^{\;0.09}}, \tag{3.2}$$

where $k$ (md) is permeability, $\phi$ (fraction) is porosity, and $S_{wir}$ (fraction) is irreducible water saturation. The coefficient and the exponents of the above equation were estimated with a multi-linear least-squares regression. **Figure 3.2** shows the results obtained from the petrophysical analysis in the water interval. **Figure 3.3** describes the results obtained from the petrophysical assessment in the two partially hydrocarbon-saturated zones.

## 3.4 SIMULATION OF BOREHOLE ARRAY-INDUCTION MEASUREMENTS

We describe the simulation of borehole AIT measurements in two stages. The first stage discusses our reservoir simulation methodology for oil-base mud-filtrate invasion in the formation. The second stage describes our resistivity simulation technique that uses spatial distributions of water saturation, calculated in the presence of OBM invasion, and transforms them into spatial distributions of electrical resistivity via **Eq. 3.1**.

### 3.4.1 Numerical Simulation of the Process of Mud-Filtrate Invasion with a Compositional Simulator

We use an IMPEC numerical formulation to calculate the spatial distribution of water saturation due to OBM-filtrate invasion. The formulation and the algorithm used in this simulation are similar to those described by Malik et al. (2007). We assume azimuthal symmetry in formation properties with respect to the axis of a vertical borehole. Our formulation enforces boundary and source flow-rate conditions on specific depth segments along the wellbore. The outer limits of the reservoir consist of impermeable zones with no-flow boundary conditions. Peng-Robinson (1976) equation of state is used to calculate the fluid compressibility factor and to solve for oil phase density. Since we assume that the OBM is water-free, salt concentration in the water phase is considered constant across the formation and equal to that of connate water.

In chapter 2, we simulated formation testing and pressure transient measurements using a multi-component formulation in the presence of OBM invasion. We described hydrocarbon phase components in the formation using four pseudo-components whereas mud filtrate was modeled with one pseudo-component. Increasing the number of pseudo-components can lead to longer computation times. In addition, due to the averaging of fluid component properties, we may not observe a significant difference in the saturation front (and, therefore on apparent resistivity measurements) by increasing the number of pseudo-components. Thus, in order to keep computational time to a minimum, we use a simpler binary formulation to describe both mud filtrate and formation oil. All components of OBM filtrate and formation oil are lumped into two pseudo-components.

**Table 3.2** summarizes the geometrical properties for the numerical grid used to simulate the base case. The wellbore radius is equal to 0.49 ft and the external radius is 1000 ft, with the grid consisting of 50 nodes in the radial direction and 60 nodes in the vertical direction. In keeping with the rapid space-time variations of pressure and component concentrations in the near-borehole region, radial nodes are logarithmically spaced from the wellbore toward the outer grid boundary (located 1000 ft away from the axis of the borehole). Along the vertical direction, grid nodes are spaced uniformly.

We simulate the process of OBM-filtrate invasion with flow rates of invasion calculated on the basis of specific formation and mud properties. The calculation of the invasion flow rate is based on the work by Wu et al. (2005), concerning WBM-filtrate invasion. At the onset of the mud-filtrate invasion process, the flow rate of filtrate is high due to the overbalance pressure in the wellbore. As the mudcake thickens, the filtrate flow rate gradually decreases with time. Although mudcake eventually becomes impermeable, invasion continues at a slow rate until the casing is set in the wellbore. Since OBM and formation oil are miscible, the invasion process in the presence of OBM differs from that involving WBM. In our work, we use a constant volume-averaged flow rate that was intended to simulate WBM-filtrate invasion as described by Wu et al., (2005). Rather than developing a new algorithm to quantify the mud-filtrate invasion process in the presence of OBMs, we use the theoretical WBM algorithm of Wu et al. (2005) and adjust it as necessary to reproduce borehole resistivity measurements and to calculate flow rates of invasion.

We assume that the original formation hydrocarbons consist of components in the range from $C_2$ to $C_{30+}$. These hydrocarbons are lumped into one component ($FHC_1$) using their pseudo properties summarized in **Table 3.3**. Oil-base mud filtrate is assumed to consist of components from $C_{14}$ to $C_{18}$ that are also lumped into one component ($MC_{16}$). Moreover, the binary-interaction parameter between the hydrocarbon components is assumed null. We calculate oil viscosity of the hydrocarbon phase, $\mu_o$, using a quarter-power mixing rule (Todd and Longstaff, 1972) that is widely used in the literature to describe well-mixed fluids (Koval, 1963). The mixing rule is applied to the sum of component concentrations of formation oil ($x_{fo}$) and OBM ($x_{OBM}$), given by

$$\mu_o = \left[ x_{fo} \cdot \mu_{fo}^{\ 1/4} + x_{OBM} \cdot \mu_{OBM}^{\ 1/4} \right]^4 .$$

In the above expression, component viscosities ($\mu_{fo}, \mu_{OBM}$) are initialized to specific values of formation temperature and pressure. Under dynamic drilling conditions, drilling mud mixes with the solid particulate matter and formation fluids. This can modify the composition and viscosity of the mud. In addition, due to the high cost of OBM compared to WBM, OBM is often recycled in field operations, thereby altering its original composition. Such an adverse situation leads to uncertainty in knowing the exact composition, PVT properties, and viscosity of the OBM. In our simulation model, we take into account uncertainty of mud-filtrate composition by simulating cases of different mud viscosity and by simulating the corresponding impact on AIT measurements.

Relative permeability and capillary pressure are two fundamental properties in the simulation of multiphase fluid flow. **Figure 3.4** shows laboratory measurements of oil-water relative permeability and capillary pressure curves, respectively, used for the simulations considered in this chapter. The same figure shows a fit to the Brooks-Corey (Corey, 1994) relation that is ultimately assumed in our analysis. **Table 3.4** summarizes the specific parameters used in conjunction with Brooks-Corey saturation-dependent properties. Oil-base mud and formation oil are first-contact miscible under reservoir pressure and temperature conditions, whereupon no capillary pressure or relative permeability effects exist within the hydrocarbon phase.

### 3.4.2 Resistivity Modeling

We simulate array-induction resistivity measurements from the spatial distribution of electrical resistivity. The simulation assumes 2D axial-symmetry, where current loop sources are located at the center of the borehole. We use the Numerical-Mode Matching Method (NMM) to perform the simulation (Chew et al., 1984; Zhang et al., 1999).

In summary, the algorithm is initialized with the fluid-flow simulation of OBM invading porous media. Inputs for the simulation include rock properties and fluid PVT properties obtained from *a priori* information. Water saturation, obtained from fluid flow simulation, is converted into electrical resistivity using Waxman-Smits' formulation. Subsequently, we use the spatial distribution of electrical resistivity to simulate the corresponding borehole array-induction resistivity measurements.

## 3.5 BASE CASE

We designate the rock formation shown in **Figure 3.2** as our base case for the simulation of mud-filtrate invasion. The formation under analysis is 100% water-saturated. Subsequently, we modify the initial water saturation of the same formation to carry out sensitivity analyses in a partially oil-saturated formation. **Table 3.5** summarizes the assumed average petrophysical properties for the formation under consideration.

### 3.5.1 History Matching of Apparent Resistivity Measurements to Estimate the Flow Rate of OBM

Because the simulation of oil-base mud-filtrate invasion requires knowledge of the flow rate, we invoked the well-established concept of water-base mud-filtrate invasion to estimate the flow rate of invasion. To that end, we used the University of Texas' Formation Evaluation ToolBox (UTFET), which allows one to calculate the flow rate of mud-filtrate invasion based on mudcake, rock, and fluid properties (Alpak et al., 2003; Wu et al., 2005). The process begins with a model that assumes standard mudcake properties for water-base mud (Dewan and Chenevert, 2001). After multiple simulations with varying mudcake properties (permeability, porosity, and maximum thickness), we secured a good match between measured and simulated apparent resistivity measurements. The average flow rate necessary to reproduce the apparent resistivity curves was approximately 0.027 $ft^3$/d/ft. **Table 3.6** describes the mudcake properties used to calculate the initial flow rate of mud-filtrate invasion. The same table describes the formation and fluid properties to be used in the analysis of the base case.

**Figure 3.5** describes the spatial distributions of water saturation and electrical resistivity calculated after three days of WBM-filtrate invasion. As expected, the low mudcake permeability causes shallow invasion similar to the case of OBM that is subsequently described in this chapter. This procedure is performed to calculate an initial guess of the flow-rate of OBM-filtrate invasion. However, we note that such a low permeability value for mudcake is not common in practical applications.

### 3.5.2 Simulation of OBM-filtrate Invasion

The calculated average flow rate for the WBM case is used as input to the simulation of OBM-filtrate invasion together with the properties described in the lower section of **Table 3.6**. **Figure 3.6** shows spatial distributions of water saturation and electrical resistivity calculated after three days of invasion. We note the similarity of the spatial distribution of electrical resistivity with those shown in **Figure 3.5**. **Figure 3.7** compares the simulated AIT measurements against field data for the cases of invasion with WBM and OBM.

**Figure 3.8** shows the time evolution of the radial distribution of OBM-filtrate saturation into the wet formation. Given that the spatial distribution of formation fluids due to invasion varies with time, formation resistivity in the near-wellbore region will also remain a function of time. At the end of three days, the radial length of invasion is 0.3 ft into the formation. This observation is consistent with previous studies (Proett et al. 2002) about the simulation of OBM invasion, which suggested that the radial extent of OBM invasion was shallower than for the case of WBM invasion for the same rock-formation properties.

## 3.6 SENSITIVITY ANALYSIS

We performed sensitivity analyses to appraise the effects of several petrophysical and fluid properties on the simulated array-induction resistivity logs. To that end, we slightly modified the base case to study the effect of OBM-filtrate invading a partially oil saturated formation. In this case, initial water saturation was assumed equal to 42% (hereafter referred as oil-base-case). Therefore, the formation under consideration is located within a capillary transition with presence of movable water together with gravity forces and vertical cross flow. With the intent of emphasizing the spatial variability of array-induction resistivity curves, the average flow rate was increased to 0.1667 $ft^3$/day/ft, which is approximately six times higher than the one used for the WBM case.

**Figure 3.9** shows the calculated spatial distributions of water saturation and electrical resistivity for this new case. We note low water saturation at the top of the formation and high water saturation toward the bottom of the formation due to gravity forces. Since the density of water phase is higher than the density of oil phase, water tends to flow toward the lower part of the formation.

**Figure 3.10** shows the corresponding simulated AIT measurements. Mud filtrate displaces the movable water in the near-wellbore region thereby causing separation among the array-induction apparent resistivity curves. **Figure 3.11** shows the time evolution of the radial distribution of oil saturation and oil viscosity that is miscible with formation oil. Mud filtrate reaches 0.9 ft into the formation due to the increased rate of invasion. Owing to the miscibility between OBM and formation oil, the concentration of OBM varies radially in the formation. The variation of OBM concentration in turn affects both oil-phase density and viscosity. As shown in **Figure 3.11**, oil-base mud viscosity is higher than the formation oil viscosity. The mobility of the oil phase ($\lambda_o$) is defined as

$$\lambda_o(S_o,t) = \frac{k_{ro}(S_o)}{\mu_o(t)},$$

where $k_{ro}$ is relative permeability of oil-phase as a function of oil saturation ($S_o$), and $\mu_o$ is oil-phase viscosity that varies spatially with time ($t$) due to invasion. Therefore, oil-phase mobility also varies spatially in the presence of mud-filtrate invasion. This behavior in turn affects the saturation front, which not only depends on the rate of mud-filtrate invasion, but also on the contrast between OBM and formation oil.

### 3.6.1 Sensitivity to the Relationship between Porosity and Permeability

We consolidated this analysis using **Eq. 3.2**. To that end, we honored the dependency of permeability on porosity when dealing with extreme perturbations of the two properties. Moreover, for this analysis we kept the ratio of vertical to horizontal permeability equal to 0.30. We remark that for each set of porosity and permeability values, capillary pressure was also modified via Brooks-Corey's equations. Changes in capillary pressure entail changes in the radial distribution of fluid properties. **Figure 3.12** shows the corresponding array-induction measurements simulated for three values of porosity and permeability. In high-porosity, high-permeability zones, the effect of gravity forces and cross-flow is remarkable as observed in the right-most track of **Figure 3.12**. Low-porosity low-permeability rocks entail marked radial variability of electrical resistivity, hence deep invasion profiles. The separation between apparent resistivity curves is largely governed by porosity. Accordingly, **Figure 3.13** shows that invasion is relatively shallow for the case of high-porosity and high-permeability rocks.

### 3.6.2 Sensitivity to Capillary Pressure

For this analysis, we modified the parameters included in Brooks-Corey's equation for capillary pressure in two stages. The first stage consists of modifying the capillary pressure coefficient ($P_c^0$) to render extreme values of the maximum capillary pressure but keeping the same shape of the base-case capillary pressure curve. We perform the sensitivity for the case of no capillarity ($P_c^0=0$) and very high capillarity ($P_c^0=150$ psi·D$^{1/2}$). The effect of this parameter is almost negligible. However, for high values of capillary pressure the variability of resistivity curves is null. In the absence of capillary forces, it becomes easier to displace the water phase, and hence oil saturation increases in the near-wellbore region.

The second stage consists of modifying the capillary pressure exponent ($e_p$) to produce different shapes of the curves but keeping the same value of capillary-pressure coefficient. This approach is equivalent to either changing the height of the capillary transition zone or changing the grain-size distribution of the rock under analysis. **Figure 3.14** shows three capillary pressure curves for three different values of $e_p$. **Figure 3.15** shows the corresponding apparent resistivity curves for each capillary pressure curve. The variation of capillary-pressure exponent leads to a large pressure differential between the oil and water phases and makes it more difficult to displace water from the pore space. Therefore, as the exponent decreases, capillary pressure increases, leading to a decrease in the separation among apparent resistivity curves. **Figure 3.16** shows that, for an exponent equal to 2, there is negligible displacement of the water phase by mud filtrate and, consequently, we do not observe separation among apparent resistivity curves.

### 3.6.3 Sensitivity to Residual Water Saturation

We modified the residual saturation to change the amount of movable water in the transition zone. The base case with $S_{wr} = 0.07$ was taken as the lower-bound value, whereas $S_{wr} = 0.40$ was the upper bound, which resulted in only 2% of movable water. **Figure 3.17** shows the Brooks-Corey relative permeability and capillary pressure curves for both cases; the two curves are affected by changes of residual water saturation. **Figure 3.18** shows the corresponding simulated apparent resistivity curves for three values of $S_{wr}$. From the plot, we observe that high movable water (low $S_{wr}$) causes a large variation of array-induction apparent resistivity curves compared to the small variation observed for the case of low movable water (high $S_{wr}$). **Figure 3.19** displays the radial distribution of oil saturation at the end of three days of invasion. Increasing the residual water saturation makes it difficult to displace water from the pores and hence there is no significant separation between the simulated apparent resistivity curves.

### 3.6.4 Sensitivity to Relative Permeability (Wettability)

In this analysis, we modified the critical water saturation ($S_{wcr}$: water saturation when the relative permeabilities of wetting and non-wetting phases are the same) by changing the exponents of the Brooks-Corey equation for relative permeability. The critical water saturation of the oil-base case is equal to 59%, which is considered a mixed-wet condition. **Figure 3.20** shows extreme cases of relative permeability with low-$S_{wcr}$ indicating a preferentially oil-wet rock, and high-$S_{wcr}$ indicating a preferentially water-wet rock. **Figure 3.21** shows the simulated apparent resistivity curves for the three values of wettability, from left to right, oil-, mixed-, and water-wet, respectively. Preferentially oil-wet rocks cause the invading oil to penetrate deeper in the formation, thereby resulting in more variability of the array-induction apparent resistivity curves. Highly water-wet rocks cause water to adhere to the grains, thereby preventing the invading oil from moving freely into the formation and, consequently, the radial length of invasion becomes relatively shallow.

The latter situation is similar to the case of irreducible water saturation. A similar conclusion stems from the radial distribution of oil saturation shown in **Figure 3.22**. In that figure, the radial length of invasion extends to 1.9 ft into the formation for a value of critical water saturation equal to 0.32. If the wettability of the rock is altered during the process of OBM-filtrate invasion, Archie's saturation exponent is no longer constant in the radial direction, and effectively becomes a function of wettability (Donaldson and Siddiqui, 1989), hence variable with time depending on invasion rate. Such effect is difficult to quantify; it suffices to state that we have found that changes in the wettability state of the rock are the most dominant in controlling the variability of apparent resistivity curves.

### 3.6.5 Sensitivity to the Rate of Mud-Filtrate Invasion

We perform an additional sensitivity analysis by changing the rate of mud-filtrate invasion associated with the oil base case. Two cases of perturbations of flow rate were considered in which the rates were changed by 50%. **Figure 3.23** shows the simulated apparent resistivity curves that resulted from this analysis. We note that as the flow rate increases the variability of the apparent resistivity curves also increases. **Figure 3.24** indicates that high invasion rates lead to relatively deep radial invasion. Uncertainty in both the flow rate of invasion and the elapsed time from the onset of drilling can drastically influence apparent resistivity measurements, as the latter are highly sensitive to the time evolution of fluid saturation. Therefore, this sensitivity analysis shows that it is important to quantify both the mud loss and the maximum time of invasion for a given formation in order to assess the impact of mud-filtrate invasion on borehole resistivity measurements.

### 3.6.6 Sensitivity to OBM Viscosity

In order to quantify the uncertainty of mud-filtrate composition on borehole resistivity measurements, we performed a sensitivity analysis by modifying the value of mud viscosity. Two cases of OBM viscosity were analyzed (0.9 cp and 2.5 cp) and compared to the oil base case. **Figure 3.25** shows the radial distribution of oil viscosity resulting from this analysis. Even though we decreased the OBM-filtrate viscosity by 24% and increased it by 40% with respect to the oil base case, there are negligible differences between the simulated apparent resistivity curves for each value of viscosity. Therefore, for the case of low uncertainty (±25%) in the viscosity of mud filtrate, the corresponding impact on simulated apparent array-resistivity measurements will be low in oil-bearing formations. However, if the formation is gas-bearing or heavy oil-saturated, where the viscosity contrast between mud and formation fluids is much higher, uncertainty in OBM viscosity can considerably affect the resistivity measurements.

## 3.7 REPRODUCING THE FIELD MEASUREMENTS

For the purpose of resistivity matching, we performed multiple simulations of the process of two-phase flow of oil-base mud filtrate invading a partially oil-saturated formation and compared the results to field measurements. As previously explained, the rock is also saturated with movable water whereas both formation and invading oil are fully miscible. The objective is to perform multiple simulations of induction resistivity by modifying the most dominant petrophysical and fluid parameters (as elicited from the sensitivity analysis) on invasion of OBM-filtrate, namely, relative permeability and flow rate of mud filtrate.

### 3.7.1 Field Data

**Figure 3.3** shows the formation under analysis. The lower interval is a 7.5 ft-thick, fairly homogeneous sandstone, and the upper interval is a highly heterogeneous 48.5 ft-thick clastic sequence. Both intervals exhibit high values of porosity and permeability. Previously, we described the algorithm used to perform the petrophysical assessment of field measurements. The lower formation was subdivided into 4 petrophysical layers, whereas the upper formation was subdivided into 12 petrophysical layers. Layer selection was based on observed changes of porosity-permeability and resistivity (Salazar et al, 2006). By dividing the formation into several layers, we are honoring the vertical heterogeneities included in the flow units. **Table 3.7** shows layer values of petrophysical properties for the two depth intervals. These properties are assumed constant in the radial direction, but distinct for each petrophysical layer. Based on **Eq. 3.2**, permeability was averaged within each layer and the ratio of vertical to horizontal permeability (anisotropy) was kept equal to that of the base case (0.3). Additional fluid, formation, and simulation grid properties are described in **Tables 3.2-3.7**.

### 3.7.2 History Matching

Once the layered model has been defined, we simulate array-induction measurements from the spatial distribution of electrical resistivity. At the end of resistivity modeling, field apparent resistivities are compared to those obtained from the simulation. The initial stage consists of matching the deepest-sensing resistivity curve (R90). This is accomplished by adjusting both porosity and initial water saturation. In the second stage, we attempt to match both the shallow-sensing resistivity curve (R10) and the separation of the intermediate-sensing curves (R20, R30, and R60). In the sensitivity analysis, we found that increasing the flow rate of invasion increased the maximum radial length of invasion. A similar situation occurred when we modified the value of critical water saturation in the relative permeability curves. The variability of the apparent resistivity curves increases when we assume that the rock is preferentially oil wet ($S_{wcr} < 50\%$).

The simulation is initialized with the flow rate and relative permeability curves for the oil-base case, namely, $q_{mf} = 0.1667$ ft$^3$/day/ft and $S_{wcr} = 59\%$. Subsequently, we change the average flow rate until securing a good match with the R10 curve. For the lower depth interval, the rate varies between 0.4 and 0.9 ft$^3$/day/ft whereas for the upper depth interval the value is between 0.3 and 0.9 ft$^3$/day/ft. Such values are 12 to 33 times higher than the ones calculated for the corresponding case of WBM-filtrate invasion. After multiple iterations, we were unable to reproduce the separation of the measured apparent resistivity curves. We realized that it was possible to secure a good match only if we modified the wettability of the rock. Because we did not have core flooding data to quantify the variation of rock wettability due to OBM-filtrate invasion, we implemented the simple approach of modifying the critical water saturation. This modification was performed layer by layer to secure the desired separation of apparent resistivity curves. Such separation also depended on the amount of movable water saturation within each layer. Assuming constant residual water saturation ($S_{wr}$ = 7%), for high values of initial water saturation the invading fluid will move more freely into the formation, thereby causing larger variability of the apparent resistivity curves. In order to secure a good match between measurements and simulations, $S_{wcr}$ was varied between 33% and 40%, with the lower values associated with those layers that exhibited low values of initial water saturation.

Previous studies of alkaline/surfactant/polymer (ASP) flooding validated some simulation models with laboratory measurements and showed that rock wettability depended on both formation and emulsion properties. Under uncertainty on the exact composition of OBM in the dynamic drilling environment, it is difficult to resort to an ASP model to simulate the process of mud-filtrate invasion. By modifying the critical water saturation to honor changes of rock wettability, we have introduced a simpler approach that can be used in conjunction with any reservoir simulator to match the measured apparent resistivities. Results from the simulation of mud-filtrate invasion consist of spatial distributions of water saturation and electrical resistivity, shown in **Figures 3.26** and **3.27** for the lower and upper depth formation intervals, respectively. Such distributions were input to the simulation of array-induction resistivity curves. **Figures 3.28** and **3.29** show the simulated apparent resistivities (2-foot vertical resolution) after manually changing both flow rate and critical water saturation. The same figures describe the field measurements, layer permeabilities, and average flow rate of mud filtrate. **Figures 3.30** and **3.31** compare simulated to measured apparent resistivity curves. For the lower depth interval, the simulated deepest- and shallowest-sensing apparent resistivity curves agree well with field measurements. However, measured and simulated intermediate-sensing curves do not match across the two middle layers, probably due to the transformation of raw conductivity measurements into apparent resistivities. In the field measurements, the R10 curve exhibits higher apparent resistivity values than the R20 curve, which indicates an anomalous behavior. In this case, our simulations show a more realistic variation between R10 and R20 apparent resistivity curves with R10>R20. As shown in **Figure 3.31**, for the upper depth interval, with the exception of a few layers, most of the simulated apparent resistivity curves agree well with field measurements.

## 3.8 DISCUSSION AND CONCLUSIONS

We studied the influence of OBM-filtrate invasion on array-induction resistivity measurements using a binary component formulation to describe the miscibility of the oil phase. Numerical simulations indicate that resistivity measurements are highly sensitive to porosity and permeability, rock wettability, and rate of mud-filtrate invasion. Alteration of rock wettability in the near-wellbore region increases the mobility of the water phase and influences the apparent resistivity measurements. Our simulations show that, to properly quantify the influence of the process of OBM-filtrate invasion on borehole resistivity measurements, it is important to quantify the mud loss in the invaded formation as well as the duration of the invasion process.

The well-documented physics of WBM-filtrate invasion can be used to estimate an initial value of flow rate of OBM-filtrate invasion. By performing multiple sensitivity analyses we were able to diagnose which petrophysical and fluid properties entailed the largest change on the spatial distribution of fluid properties resulting from OBM invasion. High rates of invasion cause radially deep invasion profiles. However, relative-permeability and capillary-pressure curves control the shape of the fluid invasion front. Thus, when simulating array-induction resistivity measurements, we found that the variability of apparent resistivity curves with various radial lengths of investigation remained controlled by the rock's relative permeability and capillary pressure. The separation of these curves is relatively large when the rock if preferentially oil wet, whereas the separation is negligible when the rock is preferentially water wet.

We simulated array-induction resistivity measurements using a history-matching approach in a partially oil-saturated turbidite reservoir. The formation consisted of dead oil and was invaded with OBM-filtrate. Simulation results indicate that it is possible to secure a good match with field measurements by simultaneously modifying both critical water saturation and rate of mud-filtrate invasion. However, uncertainty on the value of critical water saturation rendered our history-matching method difficult to adapt for automatic inversion.

Dead oil and OBM-filtrate are fully miscible under reservoir pressure and temperature conditions. In addition, we assumed that OBM did not include a water phase as part of emulsion, thereby neglecting salt mixing between the emulsion and movable water in the formation. Our binary component formulation limits the modeling of partial miscibility between formation gas and OBM as we need additional pseudo-components to accurately reproduce phase behavior effects. In this chapter, we focused our analysis to a high-porosity, high-permeability formation and concluded that flow rate of invasion and relative permeability dominated the radial length of invasion and variability of apparent resistivity curves. However, this conclusion may not hold true in low-porosity, low-permeability formations. As emphasized by the sensitivity analysis, low-porosity rocks entail deep invasion and hence result in significant variability of apparent resistivity curves. At irreducible water saturation conditions, we did not observe changes in the radial distribution of water saturation: the OBM-filtrate mixed with the native oil without entailing separation of apparent resistivity curves with various radial lengths of investigation. On the other hand, we showed that array-induction resistivity measurements can be highly affected by deep invasion (1.5 ft to 2ft) in zones with movable water. The larger the difference between irreducible and initial water saturation, the smoother the radial distribution of water saturation, and hence the larger the variability of apparent resistivity curves with different radial lengths of investigation.

Given the lack of laboratory measurements of wettability, we did not quantify the effect of wettability variations on the saturation exponent. Donaldson and Siddiqui (1989) performed laboratory experiments by flooding crude oil into core samples and measured different values of Archie's saturation exponent, *n*, for different values of oil saturation. As they injected oil, the rock became strongly oil-wet, thereby increasing the saturation exponent. Based on the comparisons between measurements and simulations, we found that resistivity measurements acquired in the lower-depth interval oil zone were difficult to match. One possible reason for the mismatch could be the processing of field raw conductivity measurements into apparent resistivities. Another reason may be an anomalous radial invasion profile due to the presence of surfactants on the emulsion forming the OBM, which was not studied in this chapter. Including the presence of surfactants in the OBM is still work in progress. History matching with field measurements helped us to diagnose adverse field conditions and led to improved interpretation of apparent resistivity measurements in the presence of invasion.

Table 3.1: Summary of Waxman-Smits' parameters and rock and fluid properties assumed in the calculation of water saturation and porosity.

| **Variable** | **Units** | **Value** |
|---|---|---|
| Archie's tortuosity factor *a* | - | 1.00 |
| Clay corrected *m*, *m** | | 1.92 |
| Clay corrected *n*, *n** | | 2.00 |
| Volumetric CEC, $Q_v$ | equiv/liters | 0.064 |
| Connate water resistivity @ 120 F | ohm.m | 0.02 |
| Matrix density | g/cm$^3$ | 2.65 |
| Shale density | g/cm$^3$ | 2.50 |
| Water density | g/cm$^3$ | 1.00 |
| Hydrocarbon density | g/cm$^3$ | 0.75 |

Table 3.2: Summary of geometrical and numerical simulation parameters assumed for all cases of study.

| **Variable** | **Units** | **Value** |
|---|---|---|
| Wellbore radius ($r_w$) | ft | 0.49 |
| External radius ($r_e$) | ft | 1000 |
| Reservoir thickness | ft | 30 |
| Number of nodes - *r* | -- | 50 |
| Number of nodes - *z* | -- | 60 |
| Grid cell size - *r* | ft | Variable |
| Grid cell size - *z* | ft | 0.5 |

Table 3.3: Summary of PVT properties of the assumed in-situ hydrocarbon components and mud filtrate.

| **Property** | **Units** | **$FHC_1$** | **$MC_{16}$** |
|---|---|---|---|
| Critical Temperature | $^o$F | 854.3 | 822.4 |
| Critical Pressure | psi | 280 | 245 |
| Acentric Factor | - | 0.405 | 0.7112 |
| Molar Weight | lb/lb-mol | 197 | 222 |
| Viscosity | cp | 0.84 | 1.5 |

Table 3.4: Summary of relative permeability and capillary pressure parameters used in Brooks-Corey's equations.

| **Variable** | **Value** |
|---|---|
| Empirical exponent for wetting phase, $e_w$ | 2.2 |
| Empirical exponent for non-wetting phase, $e_{nw}$ (water base case and oil base case) | 3.0 and 2.0 |
| End point for wetting phase, $k^o_{rw}$ | 0.37 |
| End point for non-wetting phase, $k^o_{rnw}$ | 0.99 |
| Empirical exponent for pore size distribution, $e_p$ | 25 |
| Capillary pressure coefficient, $P_c^o, [psi.D^{1/2}]$ | 15 |

Table 3.5: Summary of assumed petrophysical properties for the two cases of study.

| **Property** | **Units** | **Value** |
|---|---|---|
| Thickness | ft | 30 |
| Effective porosity | fraction | 0.27 |
| Water saturation | fraction | 1.0 |
| Shale concentration | fraction | 0.12 |
| Horizontal Permeability | md | 325 |
| Vertical Permeability | md | 100 |
| Formation compressibility | 1/psi | $10^{-8}$ |

Table 3.6: Summary of mudcake, fluid, and formation properties assumed in the simulation of the process of mud-filtrate invasion.

| ***Mudcake Parameters for WBM Only*** | | |
|---|---|---|
| **Variable** | **Units** | **Value** |
| Mudcake reference permeability | md | $5 \times 10^{-4}$ |
| Mudcake reference porosity | fraction | 0.50 |
| Mud Solid Fraction | fraction | 0.06 |
| Mudcake maximum thickness | in | 0.4 |
| Mudcake compressibility exponent | fraction | 0.30 |
| Mudcake exponent multiplier | fraction | 0.10 |
| Mud hydrostatic pressure | psi | 8,000 |

| ***Formation and Fluid Properties for All Cases of Study*** | | |
|---|---|---|
| **Variable** | **Units** | **Value** |
| Initial formation pressure | psi | 7,750 |
| Mud-filtrate viscosity | cp | 1.50 |
| Oil viscosity | cp | 0.85 |
| OBM-filtrate density | $lb/ft^3$ | 48.07 |
| Oil density | $lb/ft^3$ | 46.82 |
| Wellbore radius | ft | 0.49 |
| Maximum invasion time | days | 3.00 |
| Maximum invasion flow rate | $ft^3/d/ft$ | 0.027 |
| Temperature | $^oF$ | 139 |
| Formation outer boundary | ft | 1000 |
| Residual water saturation | fraction | 0.07 |
| Residual oil saturation | fraction | 0.10 |

Table 3.7: Summary of average petrophysical properties assumed for the formation under analysis.

| **Lower Interval** | | | |
|---|---|---|---|
| ***Thickness, ft*** | ***$\phi$, frac.*** | ***$S_w$, frac.*** | ***k, md*** |
| 1.5 | 0.260 | 0.470 | 198 |
| 2.0 | 0.250 | 0.220 | 782 |
| 2.0 | 0.305 | 0.245 | 527 |
| 2.0 | 0.273 | 0.338 | 250 |
| **Upper Interval** | | | |
| ***Thickness, ft*** | ***$\phi$, frac.*** | ***$S_w$, frac.*** | ***k, md*** |
| 5.5 | 0.230 | 0.230 | 409 |
| 3.5 | ***shale layer*** | | |
| 4.0 | 0.240 | 0.210 | 928 |
| 2.0 | 0.275 | 0.210 | 628 |
| 4.5 | 0.250 | 0.215 | 928 |
| 5.5 | 0.310 | 0.202 | 923 |
| 3.5 | ***shale layer*** | | |
| 5.0 | 0.250 | 0.250 | 1309 |
| 2.0 | ***shale layer*** | | |
| 6.0 | 0.280 | 0.230 | 1440 |
| 2.0 | 0.290 | 0.300 | 989 |
| 5.0 | 0.270 | 0.250 | 1153 |

Figure 3.1: Core photographs showing clay-laminated (left panel) and massive (right-most panel) sand intervals. The vertical scale is given in units of 1/10th of foot.

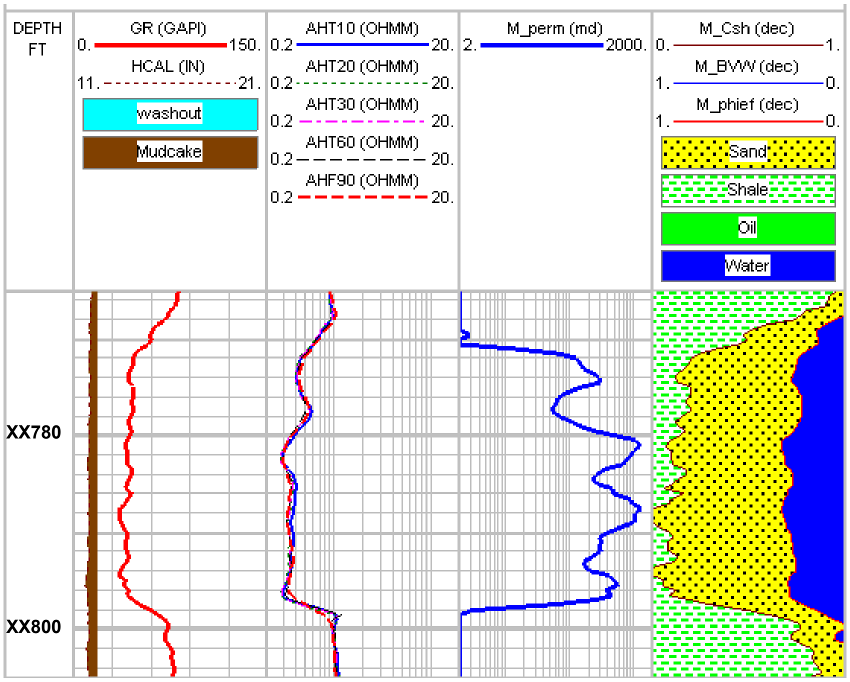

Figure 3.2: Petrophysical assessment within the water zone. Track 1 shows depth. Track 2 displays gamma-ray and caliper logs. Track 3 shows array-induction resistivity measurements (2-foot vertical resolution). Track 4 displays the estimated permeability. Track 5 describes the volumetric analysis with shale concentration, bulk volume water, and effective porosity. This depth interval is regarded as the base case for analysis.

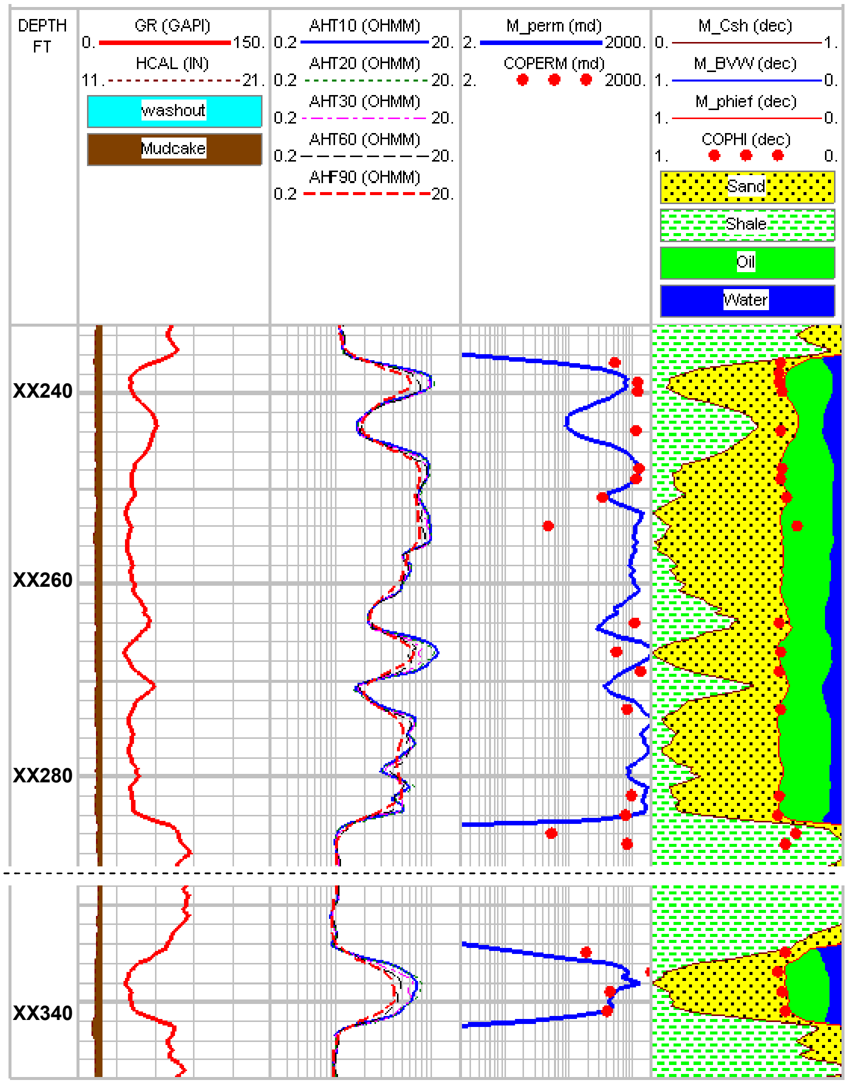

Figure 3.3: Petrophysical assessment of hydrocarbon zones. Track 1 shows depth. Track 2 displays gamma-ray and caliper logs. Track 3 shows array-induction resistivity measurements (2-foot vertical resolution). Track 4 displays log estimated and rock-core permeability. Track 5 describes the volumetric analysis with shale concentration, bulk volume water, and log estimated effective and rock-core porosity. The upper section is vertically heterogeneous while the lower depth interval is a fairly homogenous sand unit.

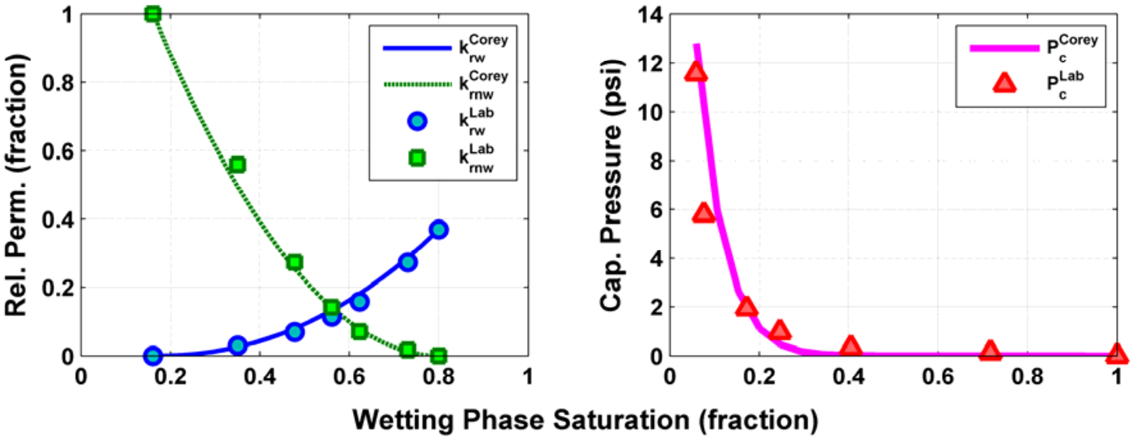

Figure 3.4: Water-oil relative permeability and capillary pressure curves assumed in the simulations of mud-filtrate invasion. Each panel compares Brooks-Corey's model to laboratory core measurements.

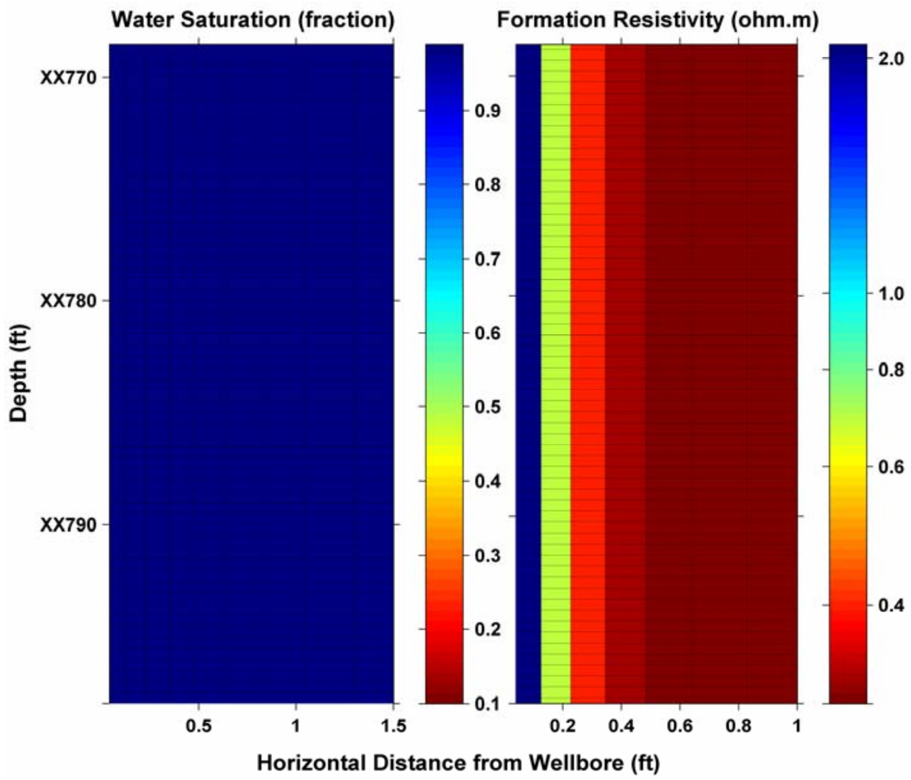

Figure 3.5: Spatial distributions of water saturation (left-hand panel) and electrical resistivity (right-hand panel) calculated after three days of water-base mud-filtrate invasion.

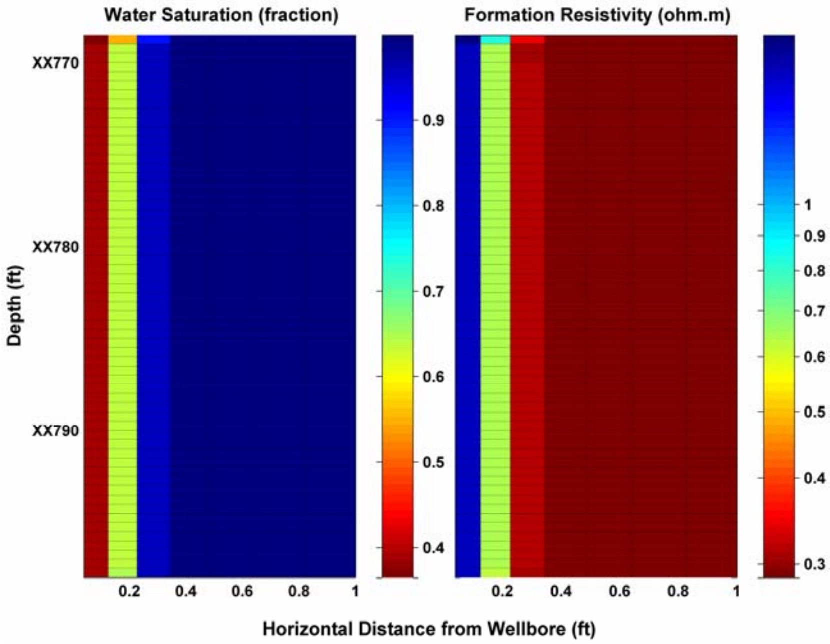

Figure 3.6: Spatial distributions of water saturation (left-hand panel) and electrical resistivity (right-hand panel) calculated after three days of oil-base mud-filtrate invasion into a water zone.

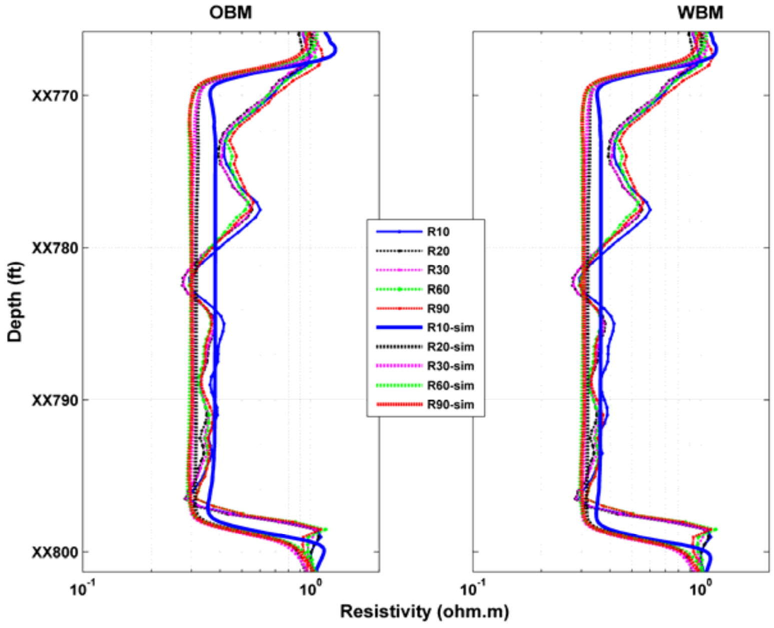

Figure 3.7: Field and simulated array-induction resistivity measurements after three days of oil-base (right-hand panel) and water-base (left-hand panel) mud-filtrate invasion into a water zone.

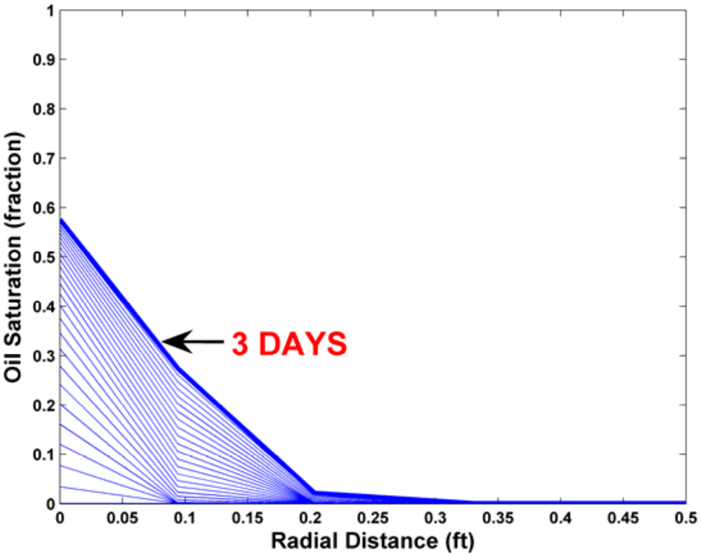

Figure 3.8: Time evolution of the radial distribution of oil saturation in the formation. Twenty five curves are plotted at time intervals of 0.12 days. At the end of three days of invasion, mud-filtrate extends to 0.3 ft into the formation.

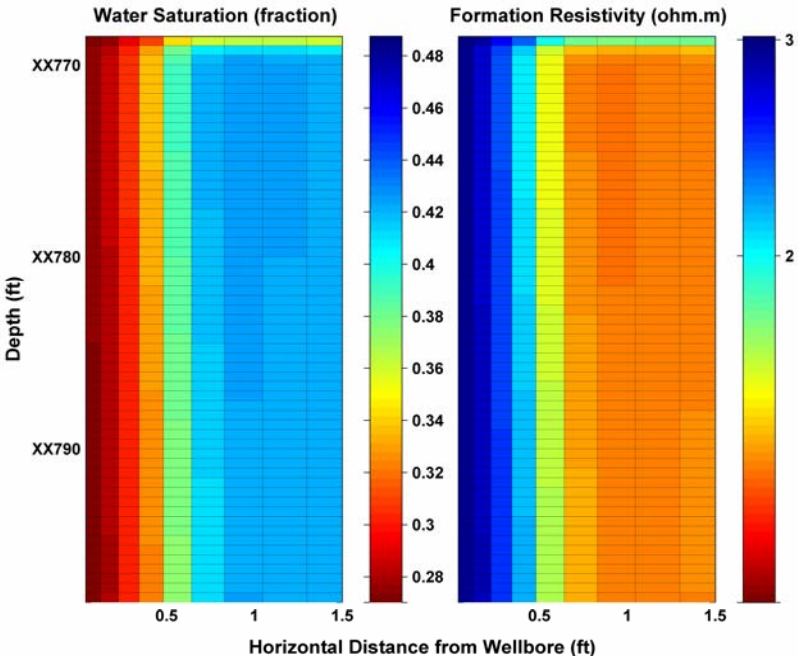

Figure 3.9: Spatial distributions of water saturation (left-hand panel) and electrical resistivity (right-hand panel) calculated after three days of oil-base mud-filtrate invasion into a partially oil-saturated formation.

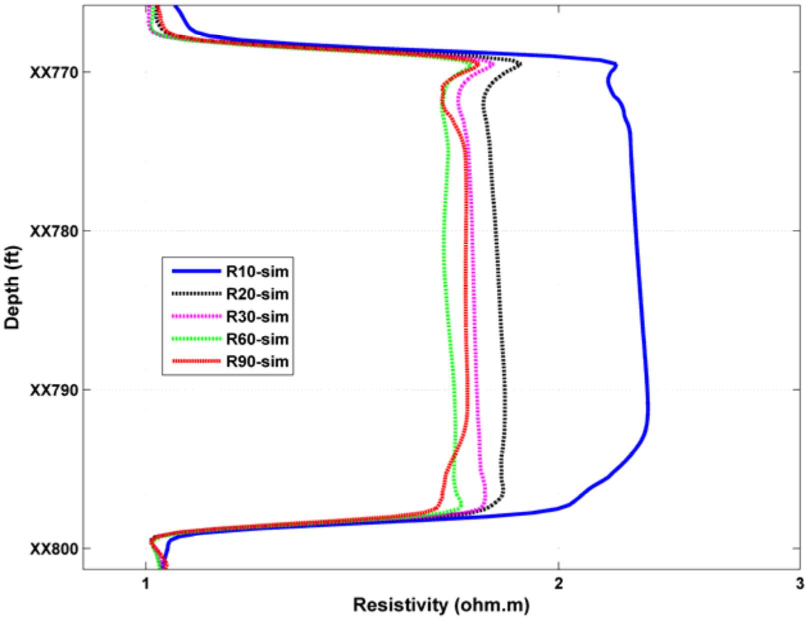

Figure 3.10: Array-induction resistivity measurements simulated after three days of oil-base mud-filtrate invasion into a partially oil-saturated formation.

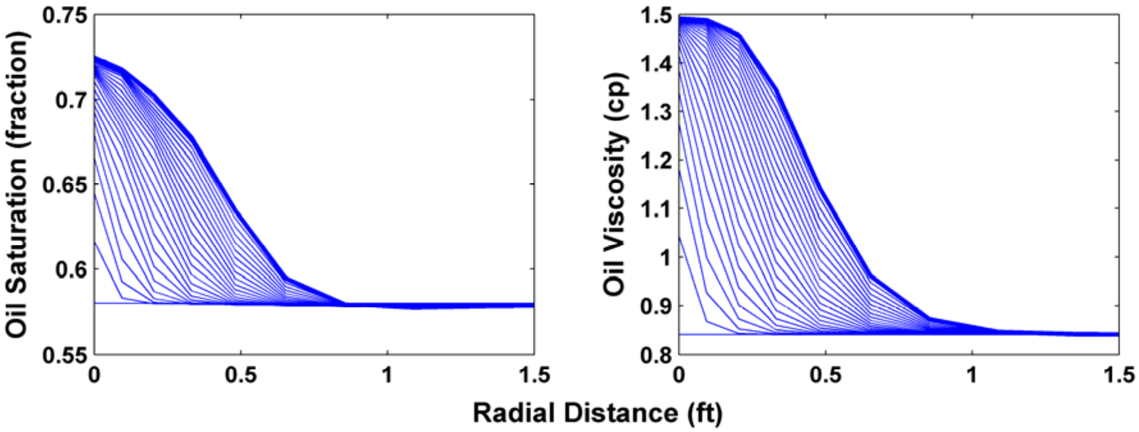

Figure 3.11: Time evolution of the radial distribution of oil saturation and oil viscosity in the formation in a transition zone. Twenty-five curves are shown at uniform time intervals of 0.12 days spanning three days of mud-filtrate invasion. At the end of invasion, mud filtrate extends to 0.9 ft into the formation.

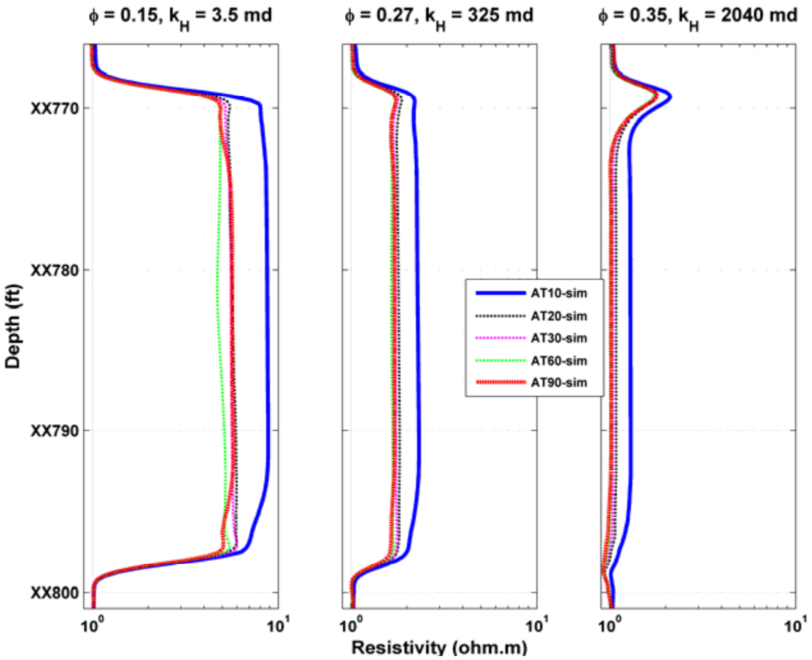

Figure 3.12: Sensitivity to porosity-permeability of array-induction resistivity measurements simulated after three days of oil-base mud-filtrate invasion into a partially oil-saturated formation. The center panel describes the oil base case.

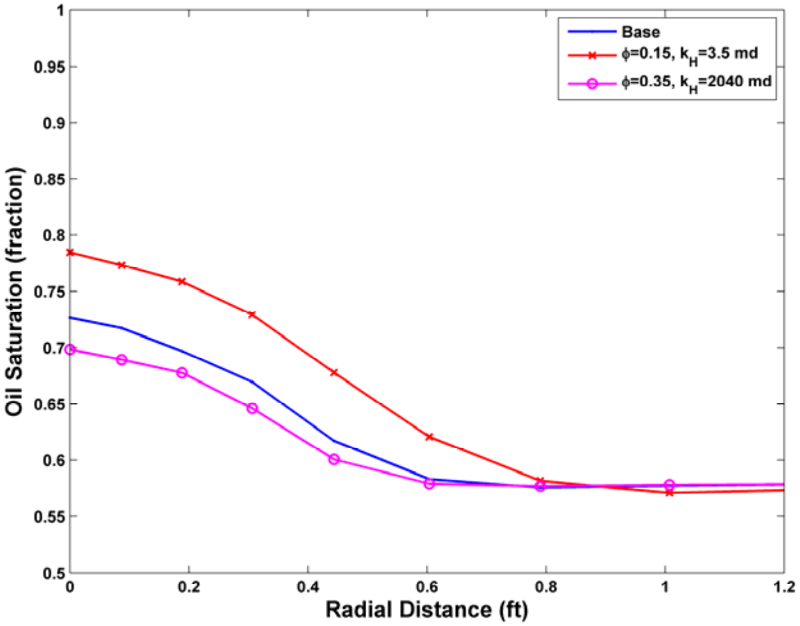

Figure 3.13: Radial distribution of oil saturation at the end of three days of invasion for different cases of formation porosity and permeability.

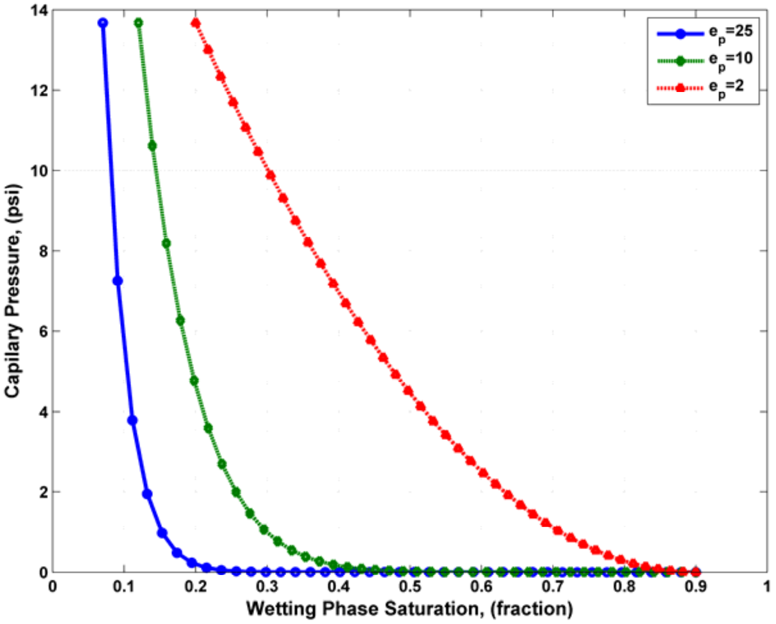

Figure 3.14: Water-oil capillary pressure curves for three different exponents of Brooks-Corey's equation. The changes of shape can also be interpreted as rock-quality (pore size), being the lowest $e_p$ the one associated with the poorest rock quality. The blue curve ($e_p = 25$) corresponds to the oil-base- case.

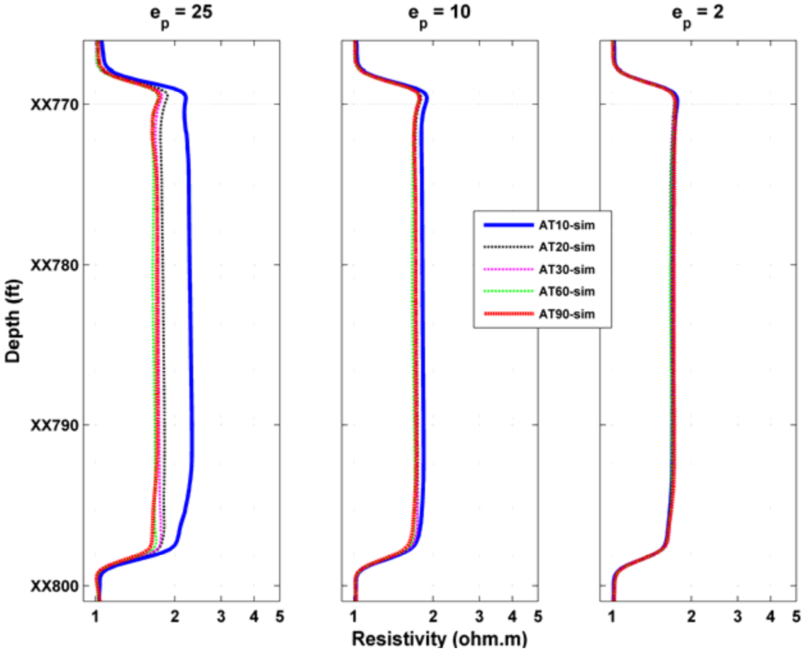

Figure 3.15: Sensitivity of the simulated array-induction resistivity measurements to the shape of capillary pressure curves after three days of oil-base mud-filtrate invasion into a partially oil-saturated formation. The left-most panel describes the oil base case.

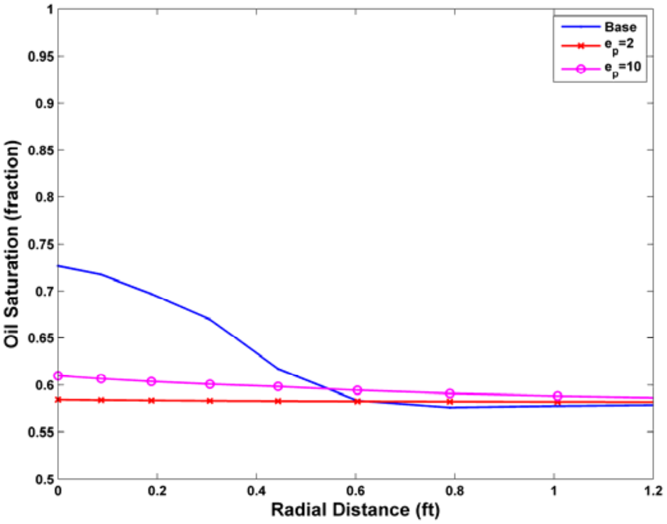

Figure 3.16: Radial distribution of oil saturation at the end of three days of invasion for different cases of capillary-pressure exponent.

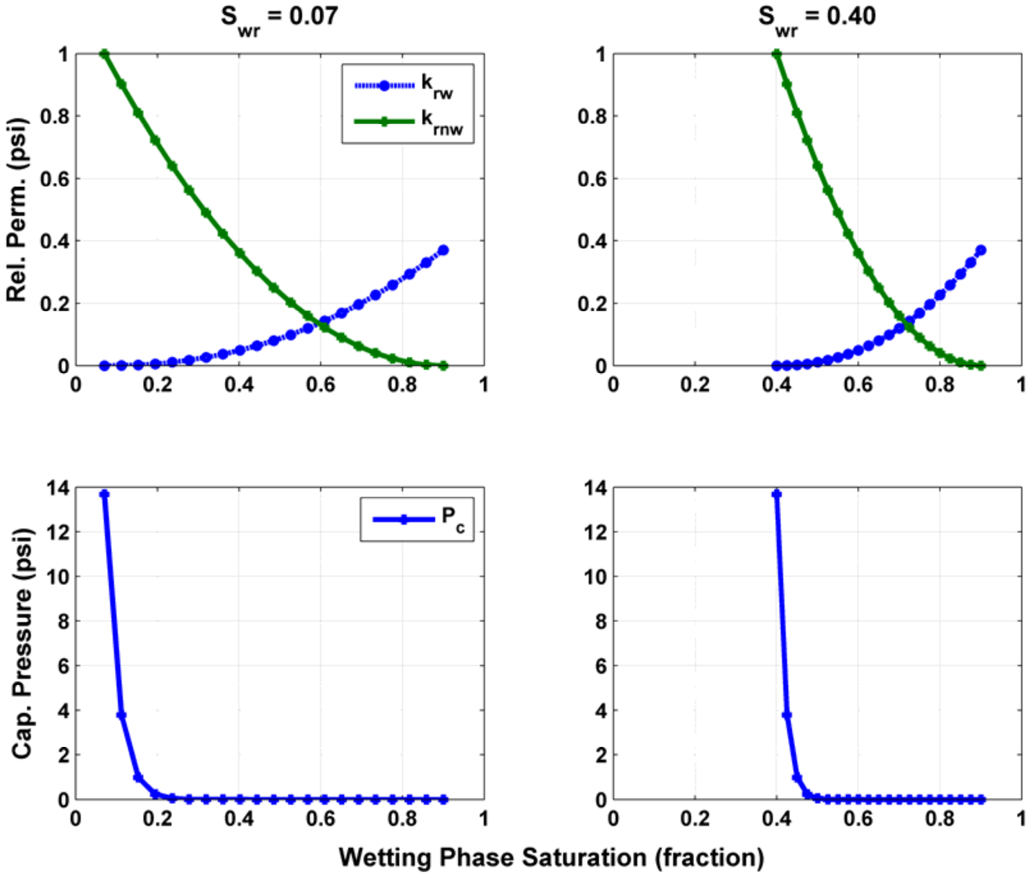

Figure 3.17: Water-oil capillary pressure and relative permeability curves for two different values of residual water saturation. Changes of $S_{wr}$ are equivalent to shifting the transition zone toward conditions of irreducible water saturation.

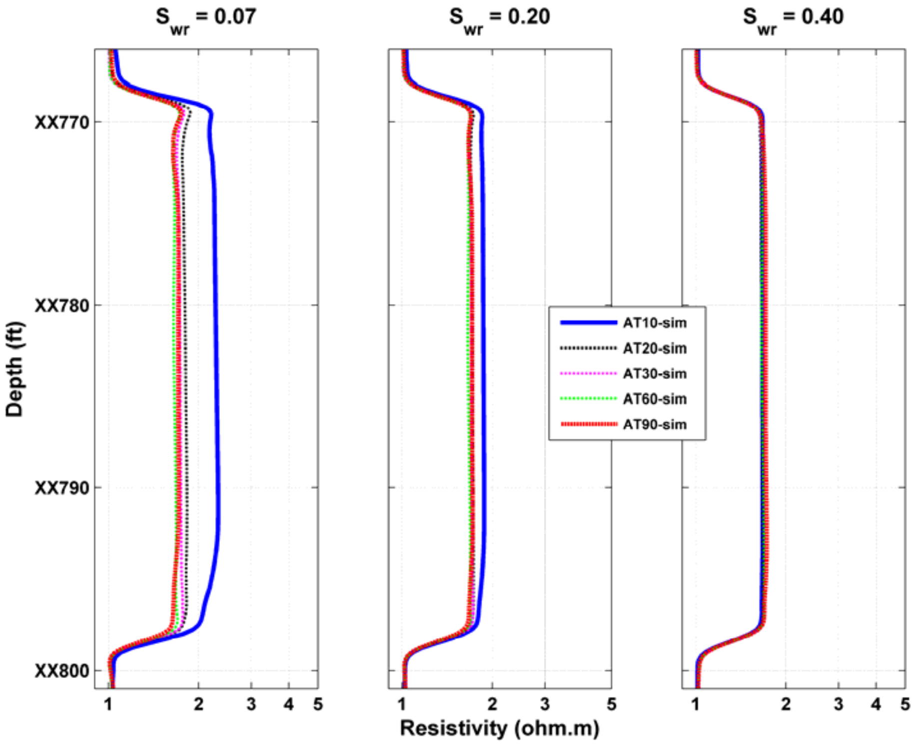

Figure 3.18: Sensitivity to residual water saturation of the array-induction resistivity measurements simulated after three days of oil-base mud-filtrate invasion into a partially oil-saturated formation. The left-most panel describes the oil base case.

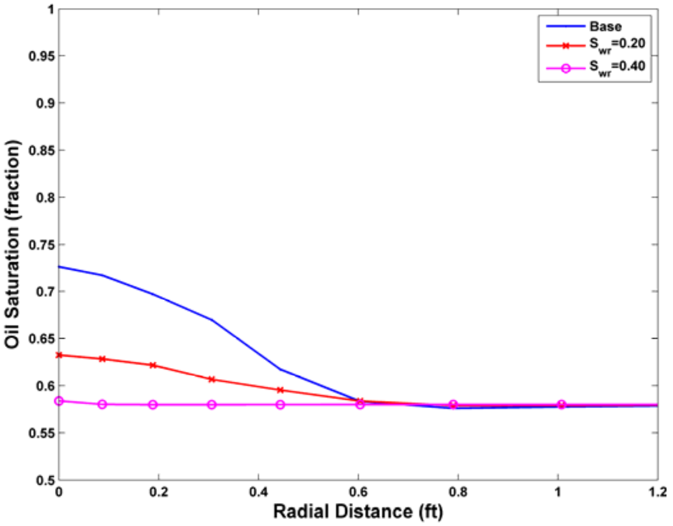

Figure 3.19: Radial distribution of oil saturation at the end of three days of invasion for different cases of residual water saturation.

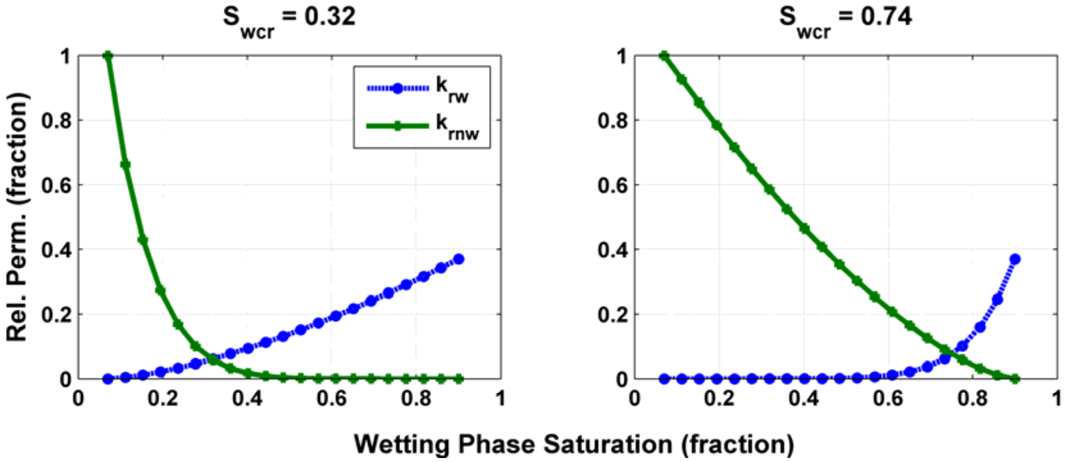

Figure 3.20: Water-oil relative permeability curves obtained by modifying Brooks-Corey's equation exponents. Location of critical water saturation indicates preferential wettability. The left-hand panel corresponds to a strongly oil-wet rock, whereas the right-hand panel represents a strongly water-wet rock.

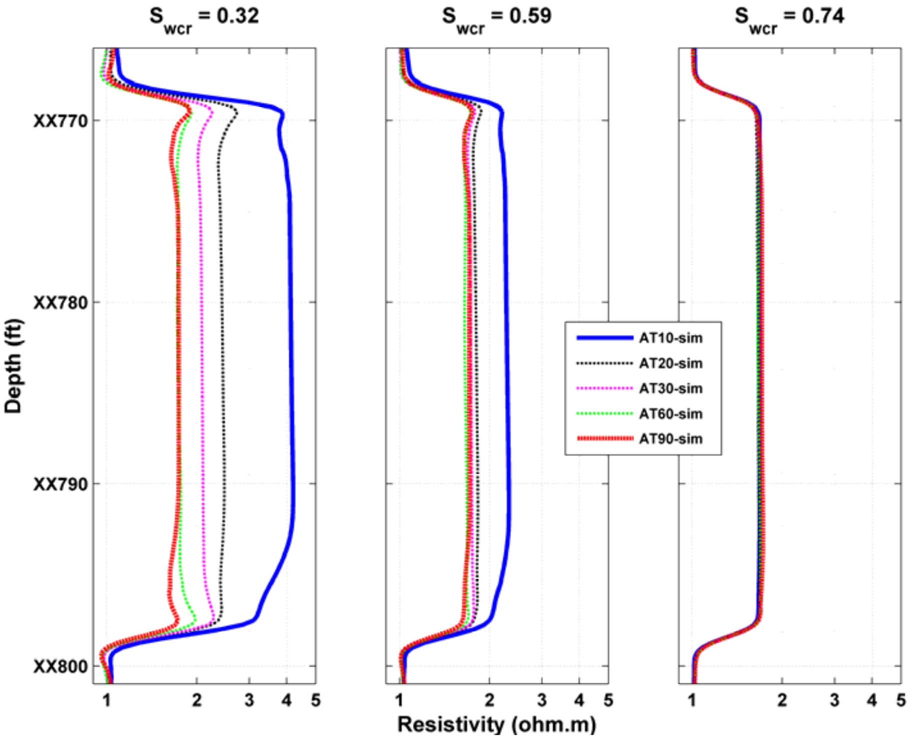

Figure 3.21: Sensitivity to relative permeability of array-induction resistivity measurements simulated after three days of oil-base mud-filtrate invasion into a partially oil-saturated formation. The center panel describes the oil base case.

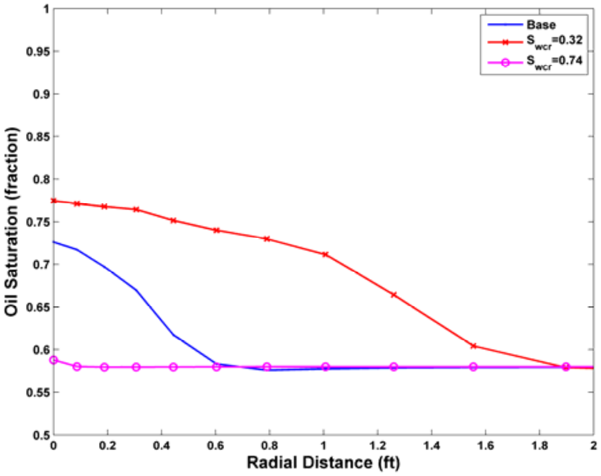

Figure 3.22: Radial distribution of oil saturation at the end of three days of invasion for different cases of critical water saturation. Low values $S_{wcr}$ causes smooth and deep invasion profiles.

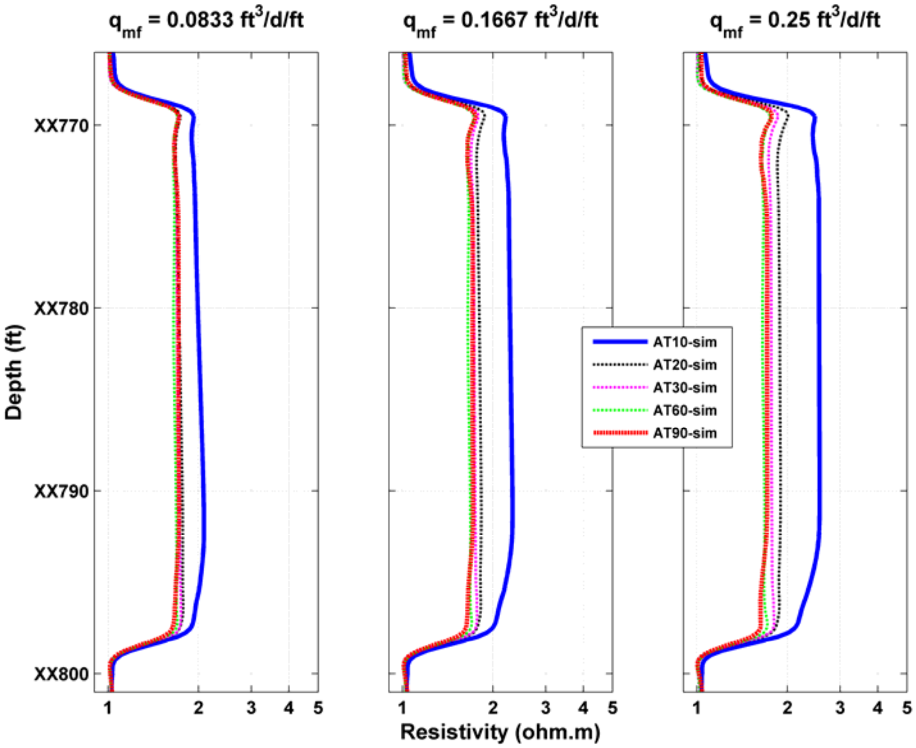

Figure 3.23: Sensitivity to average invasion flow rate of array-induction resistivity measurements simulated after three days of oil-base mud-filtrate invasion into a partially oil-saturated formation. The center panel describes the oil base case.

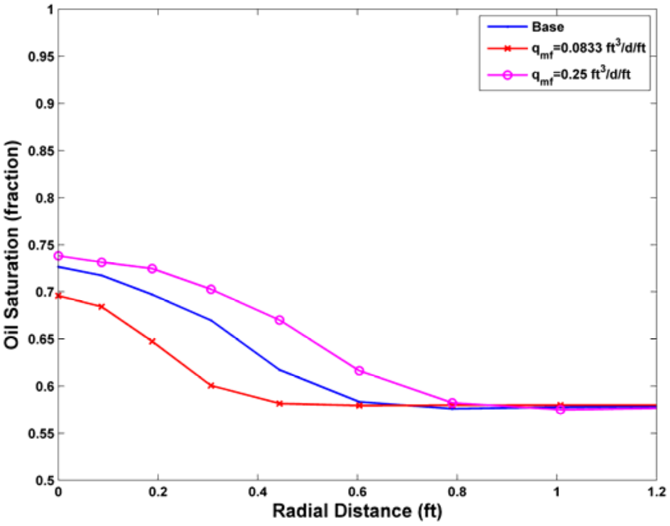

Figure 3.24: Radial distribution of oil saturation at the end of three days of invasion for different cases of flow rate of invasion.

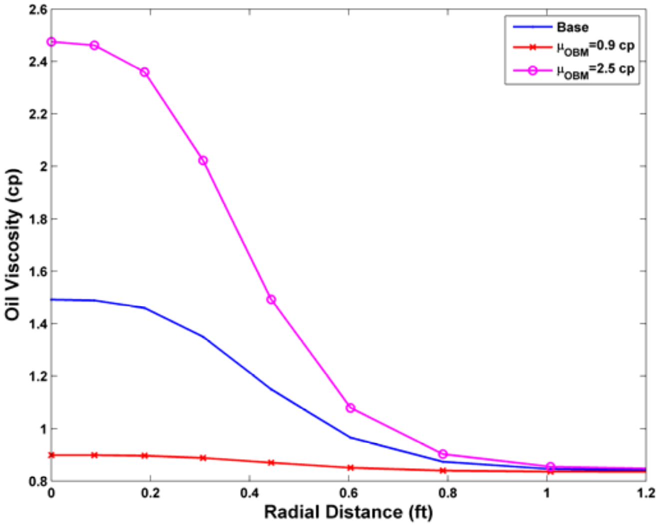

Figure 3.25: Radial distribution of oil viscosity at the end of three days of invasion for different cases of filtrate viscosity.

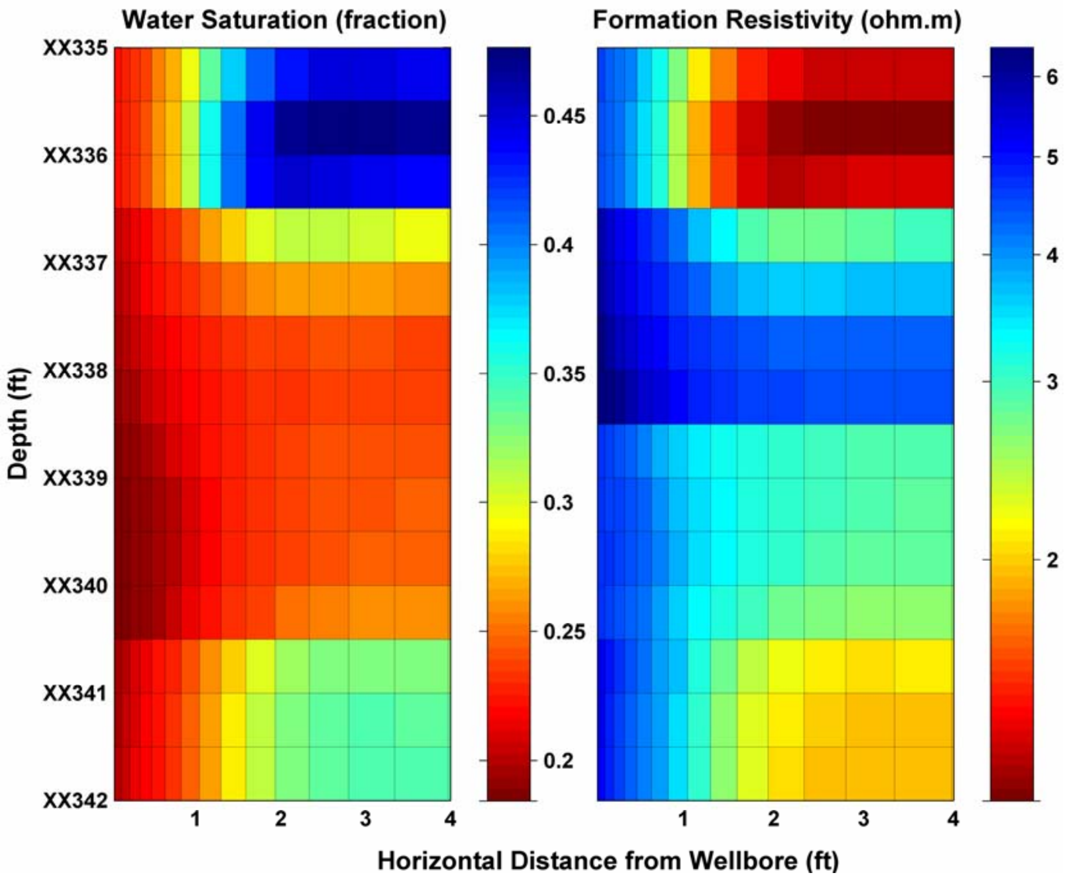

Figure 3.26: Lower depth interval of the oil-zone showing the spatial distributions of water saturation and electrical resistivity calculated after three days of oil-base mud-filtrate invasion. The spatial distributions were calculated after both flow rate of mud-filtrate invasion and relative permeability were adjusted multiple times to fit the available array-induction resistivity measurements.

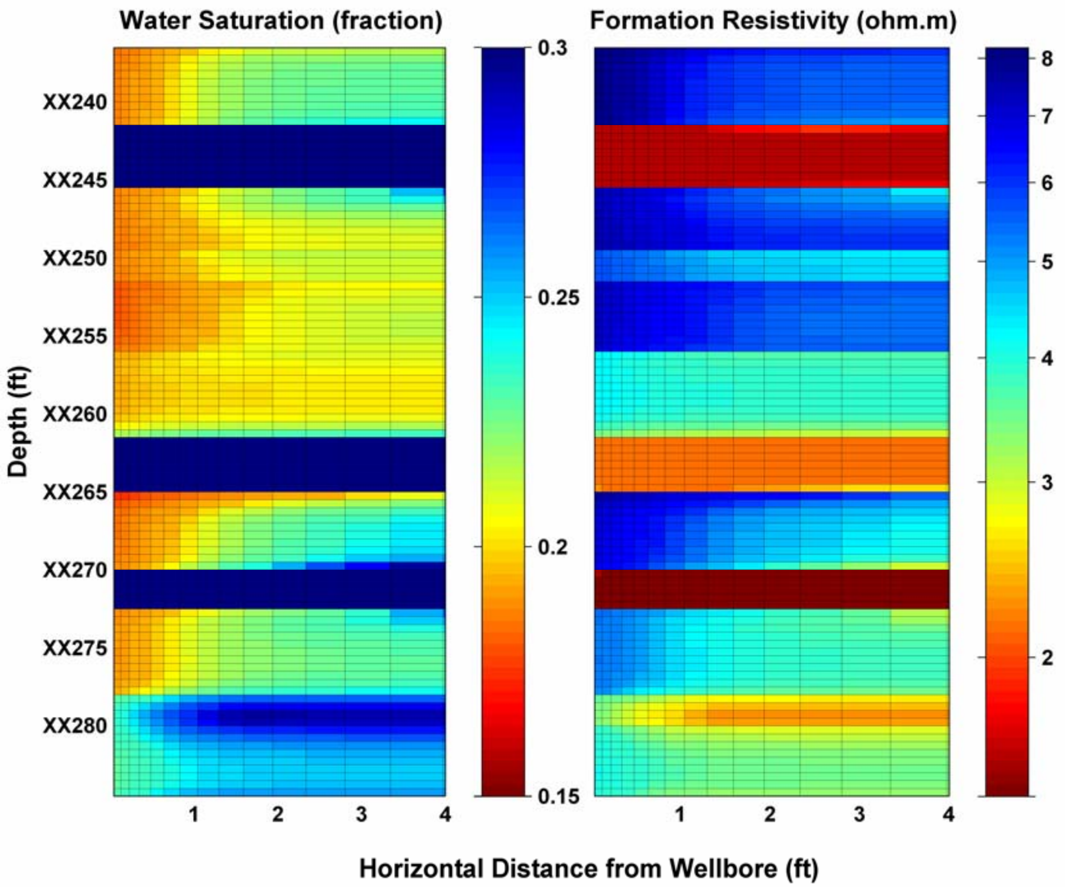

Figure 3.27: Upper depth interval of the oil-zone showing the spatial distributions of water saturation and electrical resistivity calculated after three days of oil-base mud-filtrate invasion. The spatial distributions were calculated after both flow rate of mud-filtrate invasion and relative permeability were adjusted multiple times to fit the available array-induction resistivity measurements.

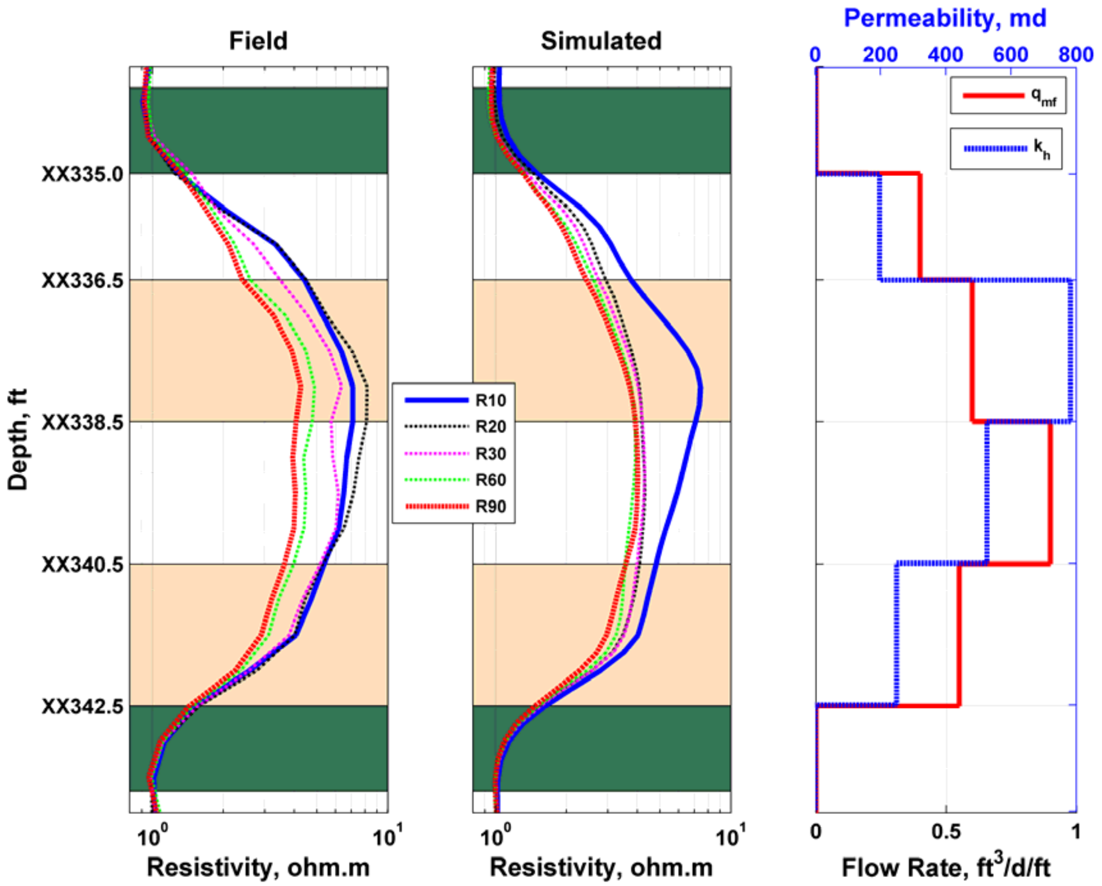

Figure 3.28: Lower depth interval: field (Track 1) 2-foot vertical resolution array-induction resistivity measurements compared to their simulated values after (Track 2) resistivity matching by manually changing both flow rate and relative permeability. The right-most tracks show the matching values of flow rate of mud-filtrate along with the assumed permeability for each layer. Shaded rectangles identify the various layers assumed in the simulation, where green zones identify shales.

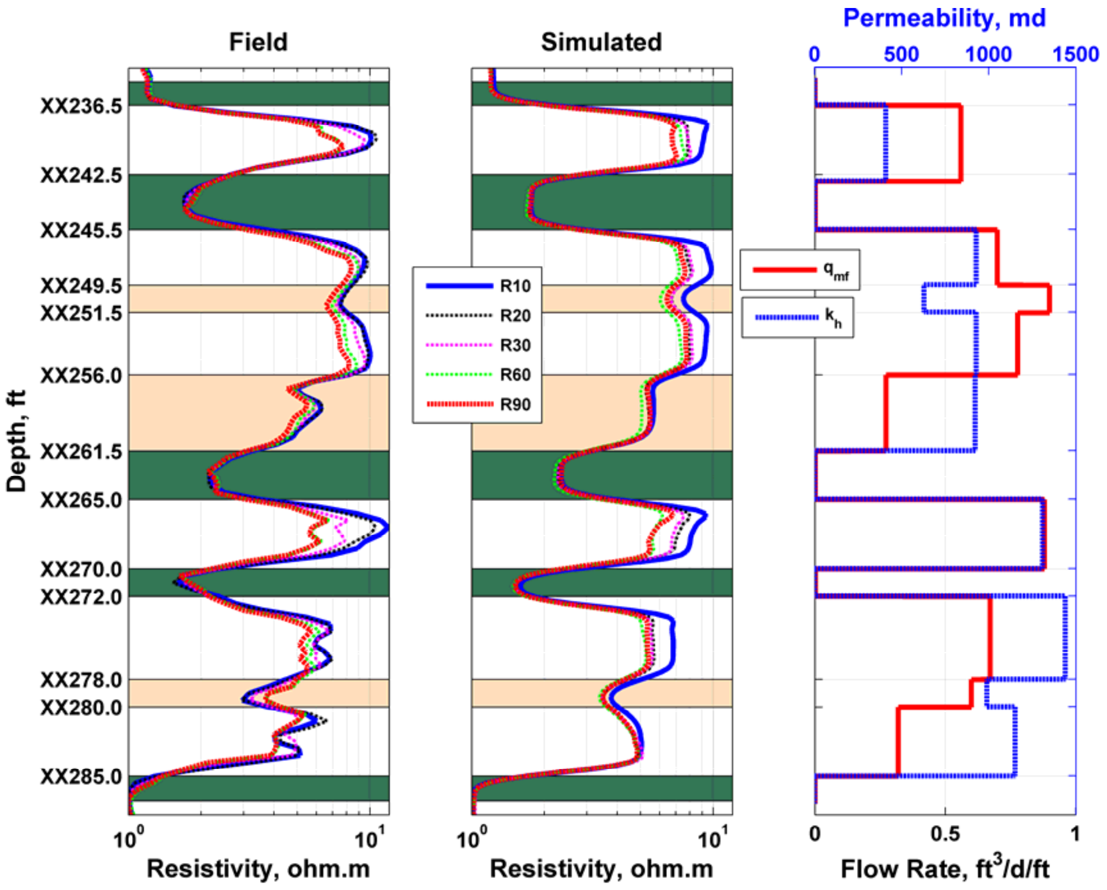

Figure 3.29: Upper depth interval: field (Track 1) 2-foot vertical resolution array-induction resistivity measurements compared to their simulated values after (Track 2) resistivity matching by manually changing both flow rate and relative permeability. The right-most tracks show the matching values of flow rate of mud-filtrate along with the assumed permeability for each layer. Shaded rectangles identify the various layers assumed in the simulation, where green zones identify shales.

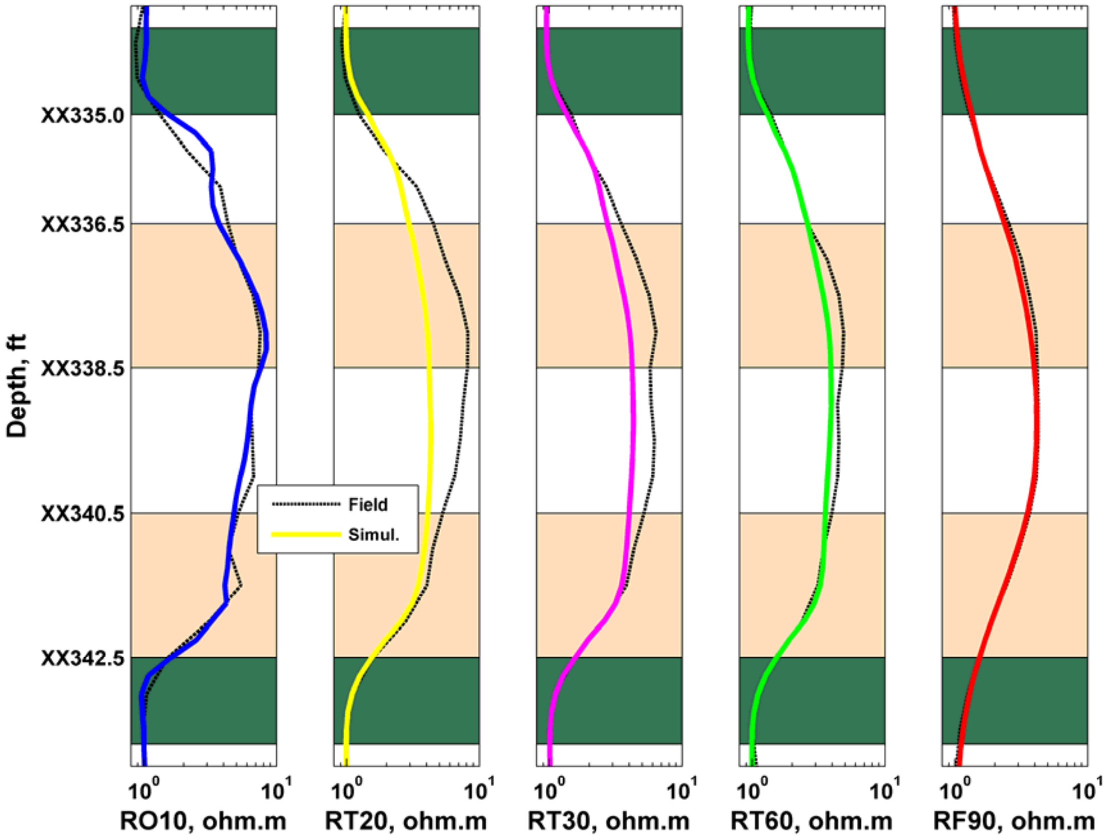

Figure 3.30: Lower depth interval: comparison of field and simulated array-induction resistivity curves after resistivity matching for five radial lengths of investigation. The right-most track shows the 1-foot resolution shallowest-sensing resistivity curves, the left-most-track displays the 4-foot resolution deepest-sensing curves, and the three center tracks show the 2-foot resolution intermediate-depth-of-investigation curves. Continuous thick curves identify simulated values and thin dashed curves identify field data.

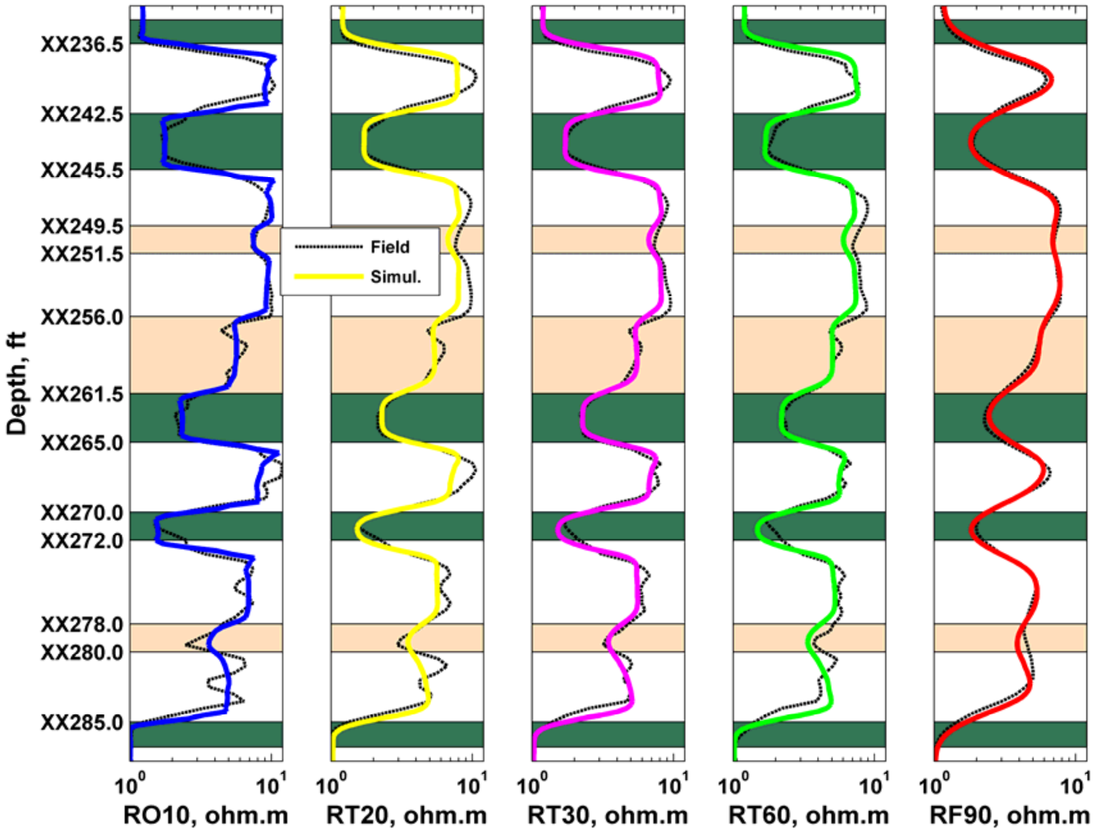

Figure 3.31: Upper depth interval: comparison of field and simulated array-induction resistivity curves after resistivity matching for five radial lengths of investigation. The right-most track shows the 1-foot resolution shallowest-sensing resistivity curves, the left-most-track displays the 4-foot resolution deepest-sensing curves, and the three center tracks show the 2-foot resolution intermediate-depth-of-investigation curves. Continuous thick curves identify simulated values and thin dashed curves identify field data.

# Chapter 4: History Matching and Sensitivity Analysis of Probe-Type Formation-Tester Measurements acquired in the presence of Oil-Base Mud-Filtrate Invasion

The acquisition of contamination-free fluid samples in hydrocarbon reservoirs drilled with OBM is challenging due to the presence of multiple fluid phases as well as partial-to-complete miscibility between reservoir fluids and OBM. Throughout the sampling process, varying concentrations of OBM contained in the sampled fluid will lead to changes in observed (apparent) fluid properties. Similarly, sand-face transient pressure measurements are affected by OBM invasion as the invasion process itself modifies both fluid viscosity and fluid density in the near-wellbore region due to mixing between different hydrocarbon components.

In this chapter, we use a commercial adaptive-implicit compositional numerical simulator to model the filtrate cleanup process during fluid sampling and to compare the predicted pressure and apparent fluid properties at the sand-face against observed field measurements. A history-matching approach is used to estimate formation permeability and permeability anisotropy.

We apply the proposed workflow to three sets of field measurements of sink probe pressure, observation probe pressure, GOR, and flow rate acquired with a formation tester in light-oil formations. Since the formation is invaded with oil-base mud filtrate that is assumed free of gas, GOR can be used to discriminate between fluids. We use a dimensionless fluid contamination function to relate transient GOR measurements to sample fluid quality. The successful comparison of simulations to field measurements helps us to diagnose and quantify adverse data-acquisition conditions such as plugging and noisy transient data. It is found that numerical simulations are a reliable way to verify the internal consistency of the transient measurements of flow rate, pressure, and GOR in the presence of biased acquisition problems.

We perform sensitivity analyses to identify the dominant governing parameters such as formation properties, formation tester flow rates, relative permeability, and radial extent of mud-filtrate invasion, on transient measurements of sand-face pressure and sampled fluid contamination. Our observation is that transient pressure, GOR, and density variations are sensitive to both the radial extent of mud-filtrate invasion and the rate of fluid cleanup. If the radial length of invasion is large, the total pumped volume must be increased in order to retrieve representative fluid samples. This can be achieved either by increasing the duration of the test, using higher rates of fluid withdrawal, or both.

## 4.1 INTRODUCTION

Wireline formation testers are widely used to measure reservoir pressure, estimate reservoir permeability and permeability anisotropy, and to collect representative reservoir fluid samples. Often, the process of mud-filtrate invasion that takes place under overbalanced drilling conditions influences WFT measurements of pressure and GOR. When wellbore pressure is higher than formation pressure, the pressure differential causes mud filtrate to invade the formation. Invasion stops when mudcake builds and prevents further flow of mud-filtrate into the formation. The recent increase in deep drilling operations around the world has popularized the use of OBM (Cheung et al. 2001) due to their ability to promote faster penetration, and ability to inhibit chemical alteration with shale sections (Andrew et al. 2001). Since the invading filtrate is partially to completely miscible with the native formation hydrocarbons, the OBM causes changes in fluid viscosity, fluid density, and GOR. Thus, it becomes imperative to accurately model their effect on the invasion process and, subsequently, on WFT measurements such as sand-face pressure and downhole GOR.

Due to the complexity of modeling miscible flow into the probe of a WFT, limited work has been performed to simulate formation-testing measurements in the presence of OBM. McCalmont et al. (2005) performed a sensitivity study to determine fluid pumpout volume for pre-job planning in gas condensates using an immiscible fluid-flow formulation. Alpak et al. (2006) used a first-contact miscible flow approach with a compositional equation-of-state (EOS) simulator to compare field examples of sampled fluid GOR to their simulated GOR. However, they did not include comparisons of field measurements of transient probe pressure against numerical simulations.

In this chapter, we simulate multi-component OBM and formation oil using a compositional EOS simulator and match our calculated pressure transients (at the sink and observation probes) and sampled GOR to the corresponding field measurements. The field data sets are particularly suitable for comparison to our simulations because all of the tests were acquired in the same lithology and in close vertical and lateral proximity to each other. The formation contains light oil of about 70% $C_1$-$C_4$ molar content; therefore, given that the OBM filtrate is assumed to be free of gas, GOR serves as a strong discriminator between mud filtrate and formation hydrocarbons.

Our compositional model consists of eight pseudo-components in order to accurately model the time evolution of miscible flow properties: five formation oil components and three oil-base mud filtrate components. Component properties are assigned based on laboratory analysis of screened and quality-checked PVT (pressure, volume, and temperature) samples (Dindoruk and Christman, 2004). Hydrocarbon phase compositions are tracked using the Peng-Robinson EOS (Peng and Robinson, 1976) with a Peneloux correction for the volume shift parameter. We use the Lohrenz-Bray-Clark

(LBC) correlation to compute fluid viscosity for the hydrocarbon phase (Lohrenz et al., 1964). Phase density is calculated with an EOS to account for variations of fluid density due to pressure and compositional changes during the process of fluid withdrawal.

The main technical contribution of this chapter is the development of a rigorous and reliable method to simulate compositional mixing of mud filtrate and native hydrocarbons and the corresponding effect on transient measurements of both pressure and GOR acquired under extreme field conditions. We show that the comparison of simulations against field measurements is a viable strategy to verify the internal consistency and reliability of the acquired measurements of flow rate, probe pressure, and GOR, otherwise affected by biasing acquisition problems. Further, we appraise the sensitivity of transient measurements of pressure and GOR to several petrophysical properties and provide guidelines to assess the relative influence of these properties on field measurements. Finally, we show that permeability, anisotropy, and radial length of invasion can be estimated from history matching of field measurements with prior information of relative permeability and capillary pressure.

In the sections to follow, we describe the simulation method and consider three field cases for comparison of WFT measurements against numerical predictions. Subsequently, we perform sensitivity analyses with our base-case model to identify the dominant governing parameters in the transient measurements, including formation permeability, permeability anisotropy, formation porosity, probe flow rate, pulsing, and radial length of mud-filtrate invasion.

## 4.2 METHOD

We use a commercial compositional EOS simulator[6] and model the probe in a three-dimensional (3D) cylindrical-coordinate system centered at the axis of the borehole.

---

[6] CMG-GEM, Trademark of Computer Modeling Group Limited

Our simulation framework is similar to the one described by Alpak et al. (2006). The process of mud-filtrate invasion is modeled assuming a known radial length of invasion axisymmetrically distributed about the axis of a vertical well. Probe measurements of sand-face pressure, observation probe pressure, and GOR are numerically simulated and compared to corresponding field measurements. All of the measurements are sensitive to formation permeability, permeability anisotropy, and radial length of mud-filtrate invasion as we show in a subsequent sensitivity analysis.

The 3D cylindrical grid captures the geometry of the flow into a WFT probe and simulates probe measurements at the center of the cylindrical grid. Grid refinement studies were performed to secure numerically accurate and field consistent simulations within a quadratic relative error of 0.01%. The relative error was computed with respect to a fine mesh where the probe opening was modeled with 64 gridblocks. **Table 4.1** describes the finite-difference grid configuration, consisting of 35 blocks in the radial ($r$) direction, 20 blocks in the azimuthal ($\theta$) direction, and 27 blocks in the vertical ($z$) direction. At the wellbore, the probe was modeled with three azimuthal and three vertical gridblocks, amounting to a total of nine gridblocks. **Figure 4.1** is a perspective view of the probe location with respect to the cylindrical grid. There are 3740 gridblocks in a radius of one foot around the probe to capture flow dynamics in the near-probe region. **Figure 4.2** is a side view of the WFT with respect to the finite-difference grid. The probe is aligned with the center of the vertical well.

Previous studies that simulated probe dynamics assumed a symmetric geometry in the azimuthal direction and modeled only half of the probe to economize computer time (Alpak et al. 2006, McCalmont et al. 2005). Here, we use a full 3D grid geometry and make no assumption of spatial symmetry. In order to decrease computer time, we use a single 180-degree azimuthal gridblock behind the probe. This selection is in agreement with our observations that the pressure decrease is higher in the region in front of the probe than in the region behind the probe.

The process of mud-filtrate invasion is modeled with a known radial length of invasion around the near-wellbore region. We assume that invasion is axial-symmetric and initialize the near-wellbore region with component concentrations of the oil-base mud. The simulated GOR response is very sensitive to radial length of invasion of the oil-base mud. Deeper mud-filtrate invasion leads to a slow buildup of GOR and shallow mud-filtrate invasion leads to a fast buildup of GOR during fluid sampling with a WFT. In the extreme case of zero radial length of mud-filtrate invasion, GOR remains constant and corresponds to in-situ fluids. The simulated transient pressure response is also sensitive to radial length of invasion. Although both oil-base mud filtrate and reservoir oil constitute the same phase, their viscosity and density contrasts affect pressure transients at early times when the near-probe region is contaminated with mud filtrate. Therefore, while comparing our simulation results to field data, the simulated radial length of mud-filtrate invasion was initialized on the basis of well-log data and then adjusted by history matching field observations of both GOR and pressure.

Our formulation enforces boundary and source flow-rate conditions on specific depth segments along the wellbore. At the wellbore, the WFT imposes a constant flow rate boundary condition during fluid production. The probe intake opening is modeled as a source or a well spread over nine gridblocks (three azimuthal and three vertical blocks) with a diameter of approximately one inch. The outer limits of the reservoir consist of impermeable zones with no-flow boundary conditions.

Imposed flow rates are determined from field measurements of pumpout volume and pumping rate. While comparing our simulation results to field cases, we assume that WFT flow rates and time schedules are accurately known. Under realistic sampling conditions, WFT flow rates are imposed by a bi-directional positive displacement pump, which typically exhibits rate fluctuations, especially during stroke reversals. Instead of attempting to capture localized high-frequency fluctuations, we time-averaged the fluid rate to remove such noise in the measurements. Time averaging of transient measurements decreases the noise effect and ensures that the total pumpout volume matches field measurements.

### 4.3 COMPARISONS OF SIMULATIONS TO FIELD MEASUREMENTS

In the following sub-sections, we introduce three examples comparing simulations to field measurements. All of the tests were performed in the same vertical well and were located within a depth interval of 30 feet. **Figure 4.3** shows the lithology and location of the formation tests. The formation consists of shale-laminated sandstone as indicated by the gamma-ray logs. There is a thin limestone bed of 1.8 feet where the neutron porosity decreases sharply and the density increases to 2.65 gm/cm$^3$. The data sets are useful for validating our simulation framework because all of the formation tests were performed in the same well. In addition, the tests were located close to each other thereby leading to negligible fluid compositional differences. The pressure gradient over the tested interval was found to be 0.25 psi/ft, which corresponds to the density of light oil. Since the $C_1$-$C_4$ content of the in-situ fluid in this case was about 70 mole %, GOR can be used to discriminate between mud filtrate and formation oil. If the formation fluid had negligible gas content, then the GOR measured with the optical fluid analyzer could not be used to discriminate between mud filtrate (assumed to have a GOR of zero) and formation fluid.

**Table 4.2** summarizes the petrophysical and fluid properties assumed in the simulation model for all cases of comparison to field measurements. Initial water saturation in the formation is 0.22. Since core data were not available for this well, we assumed a Brooks-Corey (Brooks and Corey, 1964) relationship to compute the saturation-dependent relative permeability and capillary pressure. According to this model, wetting phase relative permeability ($k_{rw}$) is given by

$$k_{rw} = k^{o}{}_{rw} S_n{}^{e_w}, \qquad \dots(4.1)$$

where $k^{o}_{rw}$ is wetting phase end-point relative permeability and $e_w$ is an empirical exponent for wetting phase. In **Eq. 4.1**, $S_n$ is the normalized wetting phase saturation, given by

$$S_n = \frac{S_w - S_{wr}}{1 - S_{wr} - S_{nwr}}, \qquad \dots(4.2)$$

where $S_w$ is saturation and $S_{wr}$ is irreducible saturation for the wetting phase, and $S_{nwr}$ is irreducible saturation for the non-wetting phase. The non-wetting phase relative permeability ($k_{nrw}$) is given by

$$k_{nwr} = k^{0}{}_{nwr} (1 - S_n)^{e_{nw}}, \qquad \dots(4.3)$$

where $k^{0}_{nwr}$ is non-wetting phase end-point relative permeability and $e_{nw}$ is an empirical exponent for non-wetting phase. Drainage capillary pressure is given by

$$P_c = P_c^0 \sqrt{\frac{\phi}{k}} (1 - S_n)^{e_p}, \qquad \dots(4.4)$$

where $P_c$ is capillary pressure, $P_c^0$ is the coefficient for capillary pressure, $e_p$ is the pore-size distribution exponent, $\phi$ is porosity, and $k$ is permeability in darcies. In our simulations, capillary pressure varies with formation permeability. **Table 4.3** describes the values of parameters included in **Eqs. 4.1-4.4** that were used to construct the formation models considered in this chapter.

Based on the PVT reports from laboratory analysis of samples, formation hydrocarbons consist of components in the range from $C_1$ to $C_{19+}$. We use actual field data to assign component concentrations to formation hydrocarbons and OBM. Formation hydrocarbons are lumped into five different components ($N_2C_1$, $CO_2C_3$, $C_4C_6$, $C_7C_{18}$, and $C_{19+}$). Their lumped pseudo-physical properties summarized in **Table 4.4**.

Such a reduction in the number of components is necessary to decrease the computer run time. OBM composition is lumped into three other components ($MC_{14}$, $MC_{16}$, and $MC_{18}$), as shown in **Table 4.5**. Therefore, our compositional simulations consist of eight different hydrocarbon pseudo-components. Before accepting the proposed fluid compositional breakdown, we performed a quality check against the measured PVT data and proved that the proposed eight-component fluid model properly accounted for density and viscosity changes (and other key parameters such as GOR and liberated gas volumes) due to variations of component concentrations and pressure.

The level of complexity in history matching progressively increases from Data Set No. 1 to Data Set No. 3. On average, we had to perform 30 iterations before we were able to secure a good match with field measurements. These iterations were performed manually by altering permeability, permeability anisotropy, and radial length of invasion. At the start of history matching, we filtered the flow rate in order to remove high-frequency noise. Subsequently, the smoothed flow rate was compared to the produced cumulative volume of fluid. If the two variables did not agree, then the flow rate was modified until an acceptable agreement was secured. Next, we proceeded to match the simulated formation pressures to the measured formation pressure. Subsequently, we changed the radial length of invasion to match the transient GOR measurements. In this step, we did not attempt to match the onset of GOR measurements, as there was a time lag because field and simulated measurements were not acquired at the same location. Instead, we matched the curvature and the end of the GOR curve. Matching the GOR before matching sand-face pressure is essential to removing the early-time behavior of the pressure plots that is attributed to changes of oil phase mobility due to invasion. Thereafter, we modified the formation permeability to secure a good match with sand-face transient pressure measurements. Lastly, the vertical permeability was modified to match the observation probe pressure.

We note that in this approach, the relative permeability and the formation porosity were kept constant. The assumed formation consisted of one infinite, homogeneous and anisotropic layer. Moreover, we neglected the presence of an invasion process in the formation while the WFT was withdrawing fluids. Finally, we assumed that the formation was at irreducible water saturation. We remark that history matching of field measurements in the presence of movable water could drastically modify the pressure response due to mobility and capillary pressure effects of the water phase.

### 4.3.1 Data Set No. 1

**Figures 4.4-4.8** summarize the comparison between simulated and field measurements for Field Data Set No. 1. Pumpout starts at 1036 sec in **Fig. 4.4** and continues to 1624 sec producing 0.1228 barrels of fluid. There was a sharp change in flow rate at 1396 sec where the rate increased from 15 reservoir barrels/day (RB/day) to 23 RB/day. [7]

Instead of attempting to match localized high-frequency fluctuations, we time-averaged the fluid rate to remove such noise in the measurements. The key to history matching is to preserve the cumulative volumes after the process of time smoothing. Figure 4 compares the smoothed input flow rate data used in the simulation model against field measurements. The corresponding probe pressures are shown in **Figs. 4.5-4.6**. At the end of fluid pumpout, sand-face pressure measured at the sampling probe in **Fig. 4.5**, rises to the formation pressure of 6845.8 psi. **Figures 4.5 and 4.6** indicate a good agreement between simulated and field results. Note that even though the imposed flow rate is constant between 1040 and 1375 sec, sand-face pressure increases with time. Such

---

[7] By reservoir barrels we mean fluid volume in barrels measured at formation temperature and pressure.

a behavior is attributed to the varying concentration of OBM contamination. In this particular case the OBM filtrate has a higher viscosity than that of formation oil. Therefore, the mobility of the sampled fluid increases with time due to the corresponding decrease of viscosity when the probe produces the formation oil.

In **Fig. 4.7**, the simulated GOR and the field GOR are separated by 22 sec at the start of fluid withdrawal. In practice, there is a time lag between the time when fluid enters the WFT tool and when the GOR measurement is acquired due to the distance of approximately 15 feet that exists between the sink probe and the optical fluid analyzer. In the simulations, GOR is determined at the sink probe itself, and therefore is measured slightly before the observed field GOR. We observe that if a time-shift of 22 sec is applied to the simulated GOR curve, it aligns very well with the field measurements. This small early-time discrepancy is common to all comparisons against field measurements but remains inconsequential to our fluid cleanup predictions given that it normally takes several hours to complete a sampling sequence.

For the studies described in this chapter, we consider a dimensionless fluid contamination function, C(t), (Austad et al. 2001) given by

$$C(t) = 1 - \frac{1}{\frac{\rho_m}{\rho_p}\left\{\frac{GOR_p}{GOR_t(t)} - 1\right\} + 1}, \qquad \ldots(4.5)$$

where *t* is time from the inception of fluid withdrawal (for t>0), $\rho_m$ is oil base mud-filtrate density, $\rho_p$ is formation oil or gas density, $GOR_p$ is the uncontaminated pure formation GOR, and $GOR_t(t)$ is the measured GOR which varies with time. In the absence of OBM-filtrate invasion, GOR and oil densities are equal to their corresponding in-situ fluid values, whereupon the fluid contamination function is equal to 0. In the presence of mud-filtrate invasion, the measured GOR at early times corresponds to that of mud filtrate that has negligible gas content and is therefore equal to 0. In this case, the denominator in the fraction approaches infinity and the fluid contamination function is equal to unity.

Ideally, the fluid contamination function decreases from 1 (at early times when the OBM concentration is the highest) to 0 (at infinite time when pure formation oil/gas is being produced). Under realistic sampling conditions, the contamination may stabilize at some value other than zero for a long period of time. This steady-state behavior and the overall nonlinear behavior with respect to time of the fluid cleanup process is due to flow dynamics around the near-probe region that depend on petrophysical and formation parameters as we show in subsequent sensitivity analyses. The dimensionless fluid contamination function is useful for comparing GOR measurements acquired in different formations in the presence of different values of fluid density and compositions.

**Figures 4.8, 4.13, and 4.19** show the fluid contamination function as defined by **Eq. 4.5** for the cases of field and simulated data. Field observations of percentage of contamination have been compared against actual laboratory measurements performed on the acquired samples. In general, the agreement is excellent, to within +/-1% contamination by weight in the live fluid. We also plot an analytical approximation to the time evolution of contamination. Various analytical expressions have been described in the literature (Alpak et al. 2006, Mullins et al. 2000, Hashem et al. 1999). Due to the non-linearity of the fluid contamination function with time and its dependence on different petrophysical, formation, and fluid properties, all of the analytical expressions simply serve as guidelines when adapted to the present use. Here, we use an analytical formulation similar to that advanced by Mullins et al. (2000), given by

$$C(t) \sim f(t) \equiv \frac{a}{t^{5/12}} - b, \qquad \ldots(4.6)$$

where t is time in seconds from the inception of fluid withdrawal. The exponent 5/12 was defined after examining over 70 optical fluid-analyzer logs (Mullins et al., 2000). Unlike the contamination function in **Eq. 4.5**, the analytical expression in **Eq. 4.6** is not bounded between 0 and 1. At the start of fluid withdrawal, the above expression tends to infinity. At late times, the same expression tends to -b. However, in real applications the contamination function is always bounded between 0 and 1. It is useful to compare the contamination function calculated from field data to an analytical model. In this chapter, rather than exploring different analytical expressions, we simply compare our simulations to predictions based on **Eq. 4.6**. We emphasize that the contamination functions (**Eqs. 4.5-4.6**) were not used to make sampling decisions in real time.

### 4.3.2 Data Set No. 2

In this data set, the flow rate was progressively increased from 9 RB/day to 19.4 RB/day. Fluid pumpout starts at 950 sec in **Fig. 4.9** and continues to 4622 sec producing 0.725 RB of fluid. **Figures 4.9-4.13** summarize the comparison between simulations and measurements for Field Data Set No. 2.

Probe transient pressures in **Figs. 4.10** and **4.11** vary with imposed probe flow rates. Formation pressure was 6849.3 psi. We were unable to match the sink probe pressure to field data after 2057 sec when the flow rate increased to 19.4 RB/day (which is a relatively high rate in practical applications of formation testing).

There were sharp fluctuations in the field sand-face pressure measurements that were inconsistent with the assumed flow rate in our simulations. In addition, pressure changes at the observation probe (**Fig. 4.11**) do not concur with sink-probe field measurements. The GOR in **Fig. 4.12** and the contamination function in **Fig. 4.13** do not indicate plugging effects. The discrepancy in sand-face pressure shown in **Fig. 4.10** was caused by particle plugging that, in turn, caused an excessive drop in flowing pressure. This behavior was recognized in real time, hence the flowing probe was switched off during the remainder of the fluid sampling sequence.

### 4.3.3 Data Set No. 3

In this data set, the fluid pumping schedule consisted of thirteen different flow rates, varying from 11.5 RB/day to 19.9 RB/day. **Figures 4.14-4.19** summarize the comparison between simulations and field measurements for Field Data Set No. 3.

Fluid pumpout starts at 702 sec and continues to 3944 sec, producing 0.52 RB of fluid. After 2500 sec, we observe several shut-in periods in the fluid sampling sequence during which the sand-face pressure was allowed to build up to the static formation pressure of 6852.4 psi. In this example, the time pulsing of the flow rate is due to fluid collection in the sample bottles. The measurement of flow rate is imprecise when sample bottles are being filled. At late times during such a process, the pump piston is slowed down and may even stop thereby decreasing the flow rate at the sand face to practically null values. As shown in **Fig. 4.14**, during history matching, we set the flow rates to zero when the sample bottles are being filled. Subsequently, in order to history match the rate measured at the sand face, we matched the cumulative fluid produced in **Fig. 4.15** rather than the flow rate. This correction step was introduced to match the pressure transient plots.

**Figures 4.16-4.17** indicate a good match between simulated and measured probe transient pressures. Sample collection can cause a discrepancy between the flow rate averaged over time and the cumulative volume of fluid produced. An approach to resolve this discrepancy in field measurements is to recompute the flow rate from the cumulative volume of fluid produced. **Figure 4.18** shows an early buildup of GOR compared to previous cases due to reduced radial length of mud-filtrate invasion, in this case equal to 0.26 inches. In our simulation model, we considered a homogeneous formation. However, heterogeneity in spatial petrophysical properties leads to a short radial length of invasion for Field Data Set No. 3.

### 4.3.4 Summary of History Matching of Field Measurements

**Table 4.6** summarizes the estimated formation permeability for all cases of comparison to field data. Horizontal permeability varies from 215 mD to 240 mD, and vertical permeability varies from 128 mD to 160 mD. These values compare very well to permeability estimates based on NMR, and core samples acquired in adjacent wells. Final (late time) GOR for field measurements and their corresponding simulations were slightly different for all cases and ranged from 2028 to 2161 SCF/STB.

**Table 4.7** summarizes the parameters $a$ and $b$ used to curve fit the analytical expression given by **Eq. 4.6**. In Data Set No. 3, with the shortest radial length of invasion of 0.26 inches, $a$ was 0.4 whereas in Data Sets No. 1 and 2, the value of $a$ was much higher. The parameter $b$ was adjusted to change the end-point of the curves.

## 4.4 SENSITIVITY ANALYSIS

We performed sensitivity analysis on the simulations arising from the study of Data Set No. 1 to investigate the effect of formation and fluid parameters on the time evolution of fluid cleanup and WFT measurements of sand-face pressure and GOR. Ideally, we would like to secure zero contamination in fluid samples to determine in-situ fluid composition. Laboratory PVT testing techniques combined with analytical fluid models can be used to mathematically “clean” or correct contaminated fluid samples to calculate in-situ fluid composition; however, excessively high fluid contamination precludes reliable corrections. The accuracy of numerical “decontamination” is a function of both fluid type and level of contamination. Therefore, it is critical to identify the factors that influence the time evolution of fluid contamination and, as a result, to determine formation properties and effective techniques that can potentially accelerate the decrease of fluid contamination with time.

For the sensitivity analysis, the assumed production time was increased to 10000 sec and we assumed a constant probe flow rate of 8 RB/day. Total fluid pumpout volume was 0.926 RB. **Table 4.8** displays the petrophysical, formation, and simulation properties for the base case. Five different sensitivity studies were considered for each governing parameter, namely formation permeability, permeability anisotropy, porosity, probe flow rate, and radial extent of invasion. Both initial water saturation and relative permeability were kept constant for the sensitivity analysis. However, capillary pressure was allowed to vary with formation permeability and porosity based on **Eq. 4.4**. For conciseness, in this section we do not include simulation results for observation-probe pressures and GOR.

### 4.4.1 Sensitivity to Permeability

We considered five different cases of permeability for the sensitivity analysis. The formation was assumed isotropic and the porosity was taken to be 0.275 for all cases. In addition, the radial length of mud-filtrate invasion was kept constant at 1.76 inches.

As expected, sand-face transient pressure in **Fig. 4.20** is very sensitive to formation permeability. However, fluid contamination curves in **Fig. 4.21** show negligible sensitivity to permeability for the same radial length of mud-filtrate invasion and rate of fluid flow. This behavior can be somewhat contradictory but is explained by the specific lack of sensitivity of the measurements to permeability when all the remaining petrophysical properties are kept constant. In practice, permeability is one of the key controlling formation properties in fluid sampling because it affects the radial length of mud-filtrate invasion, the rate of fluid cleanup possible for a given drawdown, and the rate of filtrate influx around the sampling point.

### 4.4.2 Sensitivity to Permeability Anisotropy

For this analysis, we considered five different cases of permeability anisotropy ranging from 0.05 to 1. Radial permeability for all cases was 250 mD and vertical permeability was modified to obtain different values of permeability anisotropy. **Figure 4.22** shows that sand-face drawdown pressure is sensitive to formation anisotropy. Fluid contamination curves exhibit more sensitivity to permeability anisotropy than to permeability. Fluid cleanup improves in **Fig. 4.23** as anisotropy increases due to the corresponding decrease of vertical flow.

Another instance of limited vertical flow is fluid sampling performed in the presence of a shale boundary. The operator can take advantage of the shale boundary by performing the formation test in close proximity to the shale zone. In our analysis, the density of mud filtrate is higher than the density of light oil and therefore mud filtrate will tend to slump toward the lower part of the formation. Thus, if a wireline formation test is performed with an impermeable shale layer above the tool, contamination will decrease faster than without the presence of that layer.

### 4.4.3 Sensitivity to Porosity

We considered five cases of formation porosity in the range of 0.05 to 0.4. Formation permeability was kept constant at 250 mD for all cases.

Sand-face transient pressure in **Fig. 4.24** shows very little sensitivity to formation porosity. Compared to pressure transient curves, fluid contamination curves exhibit enhanced sensitivity to porosity. **Figure 4.25** shows that fluid cleanup improves as porosity decreases. This behavior may appear counter-intuitive as we would expect fluid cleanup to be slower for the case of low porosity due to deeper invasion. In our analysis, we assumed that the radial length of mud-filtrate invasion was the same for all cases of porosity. In practice, the radial length of invasion will vary depending on formation porosity for the same volume of invasion as well as with the inter-dependency of permeability and porosity that is characteristic of clastic rocks. This behavior is further investigated in the following section.

### 4.4.4 Combined Sensitivity to Permeability and Porosity

We performed a sensitivity analysis by simultaneously varying both porosity and permeability. The two variables are assumed to be related in a sandstone formation by the expression (Dussan et al., 1994):

$$\phi = 0.11 * \log_{10}(k) + 0.011, \qquad \ldots(4.7)$$

where $\phi$ is porosity, and $k$ is permeability measured in millidarcies.

**Figures 4.26** and **4.27** display the sand-face transient pressure and fluid contamination function, respectively. Sand-face pressure is very sensitive to permeability. In the fluid contamination curves, we observe lower sensitivity to formation porosity when compared to the previous cases of sensitivity analysis. This behavior is due to the interdependence of permeability and porosity (except for extreme cases such as those related to fractures).

### 4.4.5 Sensitivity to Probe Flow Rate

We considered an additional sensitivity analysis by changing the probe sampling rate. Flow rates vary from 2 RB/day to 16 RB/day. Cleaner fluid samples can be obtained faster if the sampling rate is high. For the same cumulative volume of produced fluids, a higher sampling rate is more effective to control contamination than a longer test duration. Increasing the test duration enables gravitational flow (when the density contrast between mud filtrate and formation oil/gas is high) of mud filtrate in the partially cleaned near-wellbore region, whereas increasing the sampling rate causes the near-wellbore region to clean faster.

Sand-face transient pressure in **Fig. 4.28** is very sensitive to sampling rate. Increased rates lead to higher pressure differentials. In addition, while sampling at a high flow rate, sand-face pressure should be maintained above saturation pressure in order to obtain representative fluid samples. **Figure 4.29** indicates that fluid cleanup is highly dependent on the rate of fluid withdrawal. The cumulative volume of produced fluids is the product of flow rate of fluid withdrawal and the duration of the formation test. In order to produce the same cumulative volume of fluids, the duration of the formation test needs to be modified for different values of flow rate of fluid withdrawal.

### 4.4.6 Sensitivity to Radial Length of Invasion

We performed a sensitivity analysis for five different cases of radial length of mud-filtrate invasion in the range from 0.42 to 5.02 inches.

**Figure 4.30** shows that sand-face transient pressures during drawdown are sensitive to the radial length of invasion. Since both formation oil and oil-base mud filtrate constitute the same phase (i.e., liquid), there is minimal alteration of phase relative permeability with respect to changes of PVT and transport properties. For example, composition changes in the oils due to mixing with OBM can lead to significant variations of both phase viscosity and phase density. Such properties can vary significantly within the mixing zone (radial distance into the formation). The change of viscosity alters phase mobility with radial distance and affects the decrease of sandface pressure at early times. At late times, when the near-probe region is cleaned up from oil-base mud filtrate, sand-face pressure curves converge due to negligible variation of phase mobility from composition contrasts. Fluid cleanup is slower in **Fig. 4.31** as the radial length of invasion increases and fluid contamination remains very sensitive to mud filtrate invasion. Fluid contamination at the end of fluid withdrawal (10,000 seconds) is

12% for a radial length of invasion of 5.02 inches, whereas it is less than 1% for a radial length of invasion of 0.42 inch.

### 4.4.7 Sensitivity to Flow-Rate Pulsing

In principle, it is possible to design the time schedule of the rate of fluid withdrawal to improve the efficiency of fluid cleanup. We performed a sensitivity analysis to explore this possibility. Ten flowing and nine shut-in periods were selected such that the average flow rate in **Fig. 4.32** was 8 RB/day. The total pumpout volume shown in **Fig. 4.33** was the same for the two cases.

Sand-face transient pressure in **Fig. 4.34** is very sensitive to flow-rate pulsing. When the WFT stops withdrawing fluids, sand-face pressure quickly rises to formation pressure. At the onset of fluid sampling, there is a marked decrease of pressure in the pulsed case as the pumpout rate is approximately twice that of the case of constant rate. At early times, fluid cleanup in **Fig. 4.35** improves for the pulsed case, although toward the end of the test all the fluid contamination curves converge. This late-time phenomenon can be explained from the study of **Fig. 4.33**: at early times, cumulative fluid produced for the pulsed case increases sharply due to a higher flow rate. However, as time progresses, the total volume produced is the same for both cases. Therefore, the fluid contamination curve depends more on cumulative fluid produced than on pulsing rate.

## 4.5 CONCLUSIONS

The following concluding remarks stem from the comparisons of field measurements and numerical simulations considered in this chapter:

1. The comparison of numerical simulations to field measurements helped us to diagnose and quantify adverse field conditions such as noisy data, mud plugging

in the sink probe for Data Set No. 2, and sample collection that caused incorrect measurement of flow rate for Data Set No. 3. Some of these conditions would be difficult to detect and appraise without the use of numerical simulations. Comparisons of simulations and field measurements considered in this chapter indicate that numerical simulation is a good alternative to verify the internal consistency and reliability of transient measurements of flow rate, pressure, and GOR.

2. We observed a time lag in the buildup of the simulated GOR in all comparisons to field measurements of GOR. Separation in the GOR curves at early times is due to the time required to (a) break mudcake, (b) for fluid to move from the probe to the optical fluid analyzer that is located approximately 15 feet away, and (c) for the assessment of GOR with the optical fluid analyzer. While it was important to diagnose this fluid sampling condition, we found that it had negligible influence on our numerical simulation results.
3. As expected, sand-face pressure exhibited high sensitivity to formation permeability, whereas the fluid contamination function exhibited high sensitivity to the radial length of mud-filtrate invasion. Miscibility of mud filtrate with formation oil affects the early-time behavior of pressure transients because of the accompanying changes of fluid viscosity and GOR transients due to alteration of fluid composition. The use of multiple pseudo-components is essential to accurately simulate GOR measurements.
4. Uncertainty in the values used for relative permeability and fluid viscosity, as well as inaccurate assessment of movable-water saturation can drastically bias the estimates of permeability obtained from pressure transient measurements.

5. We considered the possibility of time pulsing fluid withdrawal rates to assess whether it was possible to obtain cleaner samples faster than when using a constant flow rate. Simulations showed that fluid cleanup behavior is dependent on the cumulative volume of fluids produced and is negligibly influenced by flow-rate pulsing.
6. The duration of formation tests should be increased drastically to secure clean fluid samples and to increase the cumulative volume of produced fluids for cases of mud-filtrate invasion deeper than 0.5 ft. The flow rate of fluid withdrawal can be increased to increase the cumulative volume of produced fluid. However, this latter acquisition strategy requires careful assessment to prevent high pressure differentials that could cause the sandface pressure to fall below the bubble point.

Table 4.1: Summary of geometrical and numerical simulation parameters assumed for all field cases considered in this chapter.

| Parameter | Units | Value |
|---|---|---|
| Wellbore radius ($r_w$) | ft | 0.45 |
| External radius ($r_e$) | ft | 300 |
| Reservoir thickness | ft | 41.75 |
| Number of nodes - radial axis | -- | 35 |
| Number of nodes - azimuthal axis | -- | 20 |
| Number of nodes - vertical axis | -- | 27 |
| Grid cell size - $r$ | ft | Variable |
| Grid cell size - $\theta$ | degrees | Variable |
| Grid cell size - $z$ | ft | Variable |

Table 4.2: Summary of the assumed petrophysical and fluid properties for all field cases considered in this chapter.

| Property | Units | Value |
|---|---|---|
| Initial water saturation | fraction | 0.22 |
| Water Compressibility | 1/psi | $3\text{x}10^{-6}$ |
| Formation porosity | fraction | 0.275 |
| Temperature | Fahrenheit | 140 |
| Formation compressibility | 1/psi | $10^{-9}$ |
| Reservoir oil density | g/cc | 0.60 |
| Reservoir oil viscosity | cp | 0.36 |
| Saturation pressure @140 $^{\text{o}}$F | psi | 1528 |
| Clean gas-oil ratio | SCF/STB | 2207 |

Table 4.3: Summary of relative permeability and capillary pressure parameters used in Brooks-Corey equations.

| Parameter | Value |
|---|---|
| Empirical exponent for wetting phase, $e_w$ | 2.2 |
| Empirical exponent for non-wetting phase, $e_{nw}$ | 3.0 |
| End-point for wetting phase, $k^0_{rw}$ | 0.8 |
| End-point for non-wetting phase, $k^0_{nwr}$ | 0.9 |
| Wetting phase irreducible saturation, $S_{wr}$ | 0.22 |
| Non-wetting phase irreducible saturation, $S_{nwr}$ | 0.1 |
| Empirical exponent for pore-size distribution, $e_p$ | 1.2 |
| Capillary pressure coefficient, $P_c^0$, $[psi.D^{1/2}]$ | 4 |

Table 4.4: Equation-of-state parameters and mole fractions of the pseudo-components used in this chapter to describe the behavior of in-situ fluid.

| Parameter | $N_2$ $C_1$ | $CO_2$ $C_3$ | $C_4$ $C_6$ | $C_7$ $C_{18}$ | $C_{19+}$ |
|---|---|---|---|---|---|
| Molar Concentration | 0.6183 | 0.0792 | 0.0875 | 0.1786 | 0.0362 |
| Critical Temperature (°F) | -125.7 | 125.9 | 359.8 | 656.2 | 1059.9 |
| Critical Pressure (psi) | 653.3 | 839.4 | 498.2 | 322.3 | 184.4 |
| Acentric Factor | 0.0105 | 0.1458 | 0.2302 | 0.4904 | 0.9192 |
| Molar Weight (lbs/lb-moles) | 16.6 | 36.23 | 67.73 | 132.79 | 303.21 |
| Volume Shift Parameter | -0.193 | -0.131 | -0.056 | 0.171 | 0.231 |

Table 4.5: Equation-of-state parameters and mole fractions of the pseudo-components used in the study to describe the behavior of oil-base mud.

| Parameter | $MC_{14}$ | $MC_{16}$ | $MC_{18}$ |
|---|---|---|---|
| Molar Concentration | 0.6489 | 0.2145 | 0.1364 |
| Critical Temperature ($^oF$) | 755.1 | 822.5 | 878.1 |
| Critical Pressure (psi) | 261.8 | 240.2 | 224.4 |
| Acentric Factor | 0.6257 | 0.7118 | 0.7842 |
| Molar Weight (lbs/lbmoles) | 190 | 222 | 251 |
| Volume Shift Parameter | 0.0792 | 0.0666 | 0.0439 |

Table 4.6: Summary of simulation results obtained from the comparison of field cases.

| Case | Formation Pressure (psi) | $k_h$ (mD) | $k_v$ (mD) | Final GOR (SCF/STB) |
|---|---|---|---|---|
| 1 | 6845.8 | 240 | 160 | 2028 |
| 2 | 6849.3 | 220 | 128 | 2125 |
| 3 | 6852.4 | 215 | 135 | 2161 |

Table 4.7: Summary of parameters used to define the analytical approximation of fluid contamination for the field cases considered in this chapter. Note that parameters *a* and *b* refer to the expression $f(t)=a/t^{5/12}-b$, where *t* is time in seconds measured from the start of fluid withdrawal.

| Case | *a* | *b* | Radial length of invasion (inches) |
|---|---|---|---|
| 1 | 2.3 | 0.15 | 1.76 |
| 2 | 3 | 0.1 | 1.58 |
| 3 | 0.4 | 0.01 | 0.26 |

Table 4.8: Summary of petrophysical, formation, and simulation parameters for the base-case formation model

| Parameter | Units | Value |
|---|---|---|
| Horizontal Permeability | mD | 250 |
| Vertical Permeability | mD | 250 |
| Porosity | - | 0.275 |
| Test Duration | sec | 10000 |
| Probe Flow rate | RB/day | 8 |
| Water Saturation | - | 0.22 |
| Radial length of invasion | inches | 1.76 |

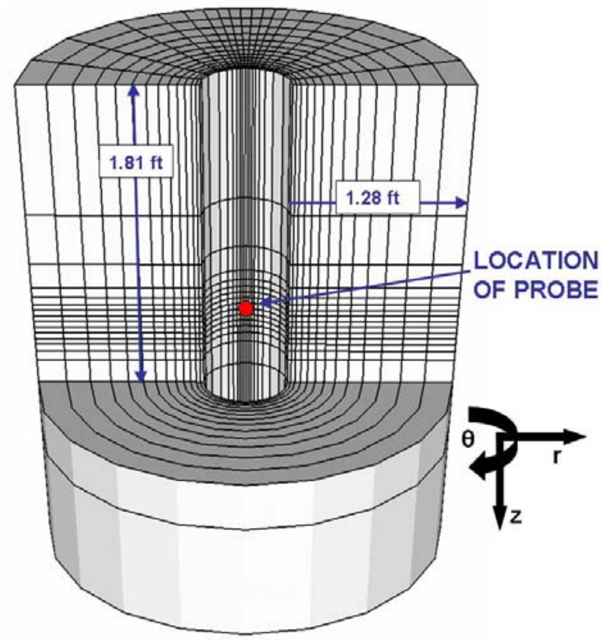

Figure 4.1: Three-dimensional view of the probe opening with respect to a cylindrical finite-difference grid. The probe opening is highlighted with a red dot. Note that the region around the probe opening is discretized in all directions (r,θ,z) to accurately simulate transient measurements of pressure, flow rate, and GOR.

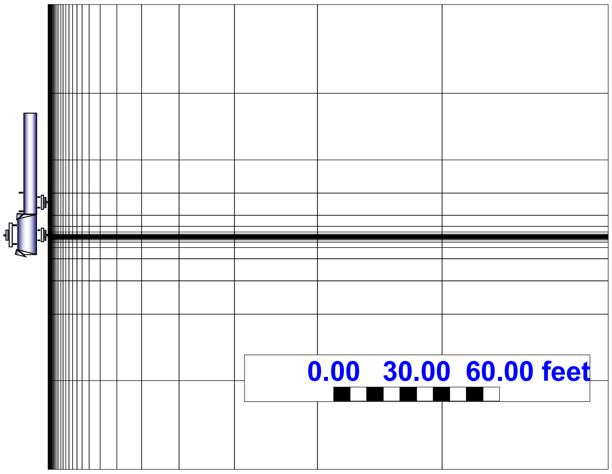

Figure 4.2: Side view of the WFT with respect to the cylindrical finite-difference grid. The probe opening is simulated at the center of the grid. Gridblock size increases logarithmically with radial distance away from the probe opening.

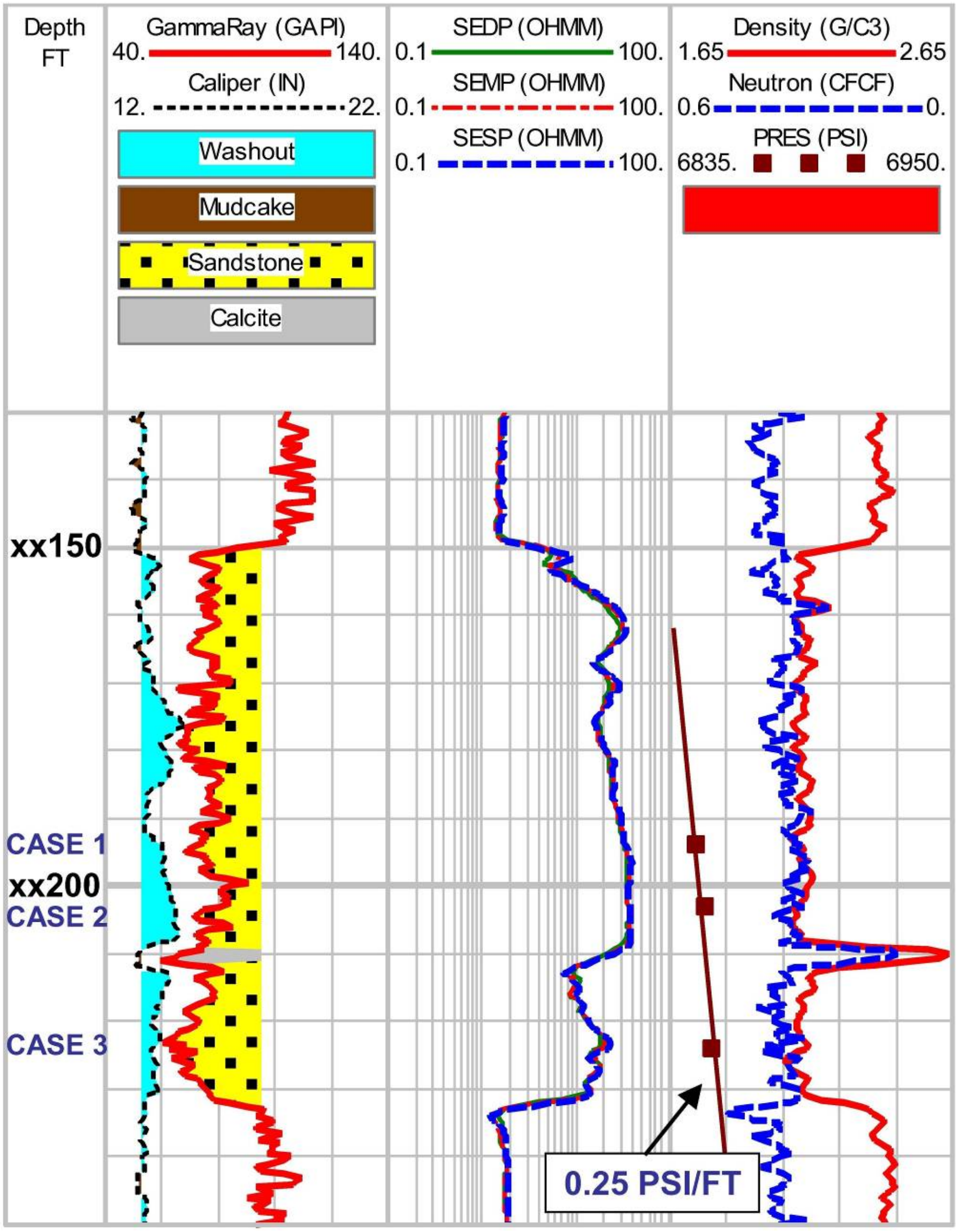

Figure 4.3: *Field data.* Track 1: gamma-ray and caliper logs. Track 2: array induction resistivity logs. Track 3: density and neutron porosity logs, and formation pressure (shown with squares). The formation consists of shale-laminated sandstones with an intervening limestone streak.

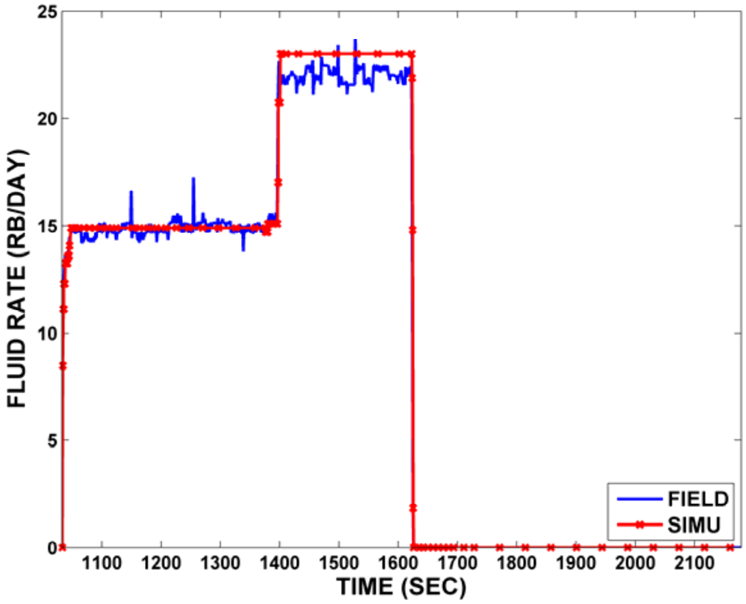

Figure 4.4: Time evolution of probe flow rate at the sink used in the comparisons of simulations to field measurements for Field Data Set No. 1.

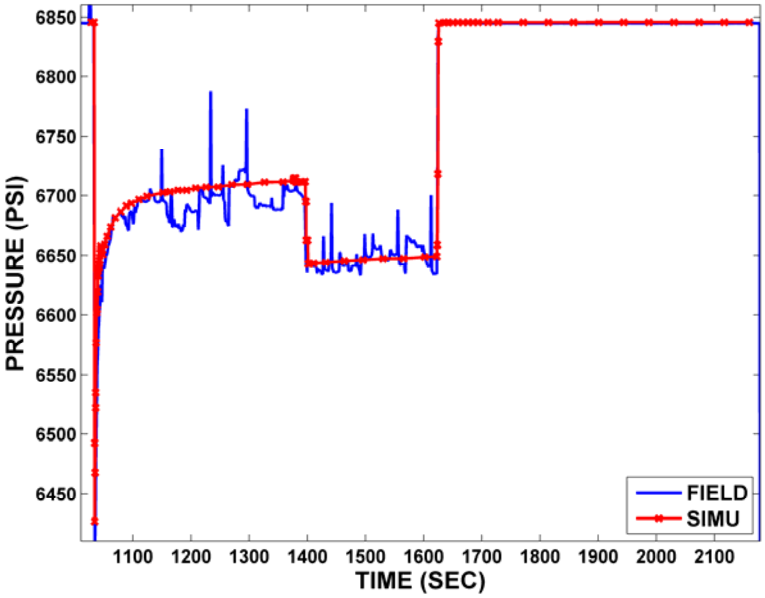

Figure 4.5: Simulated transient pressure response at the sink probe compared to Field Data Set No. 1.

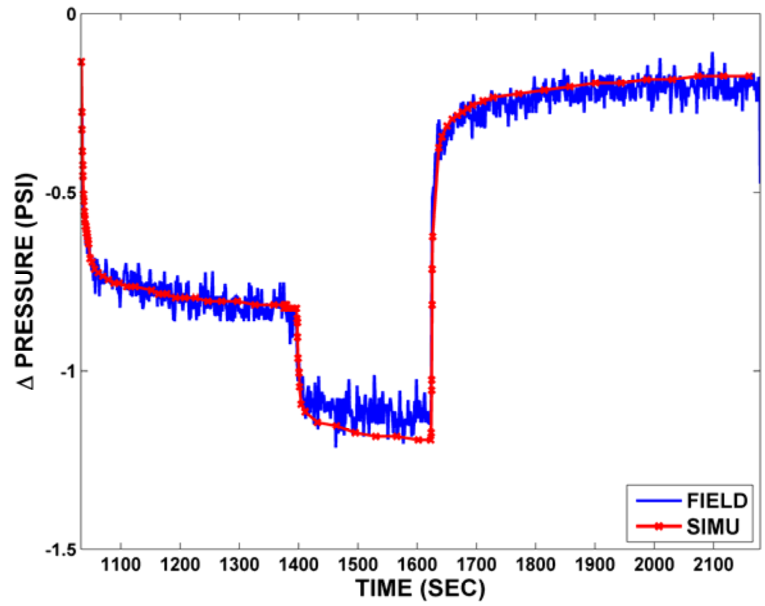

Figure 4.6: Simulated transient pressure response at the observation probe compared to Field Data Set No. 1.

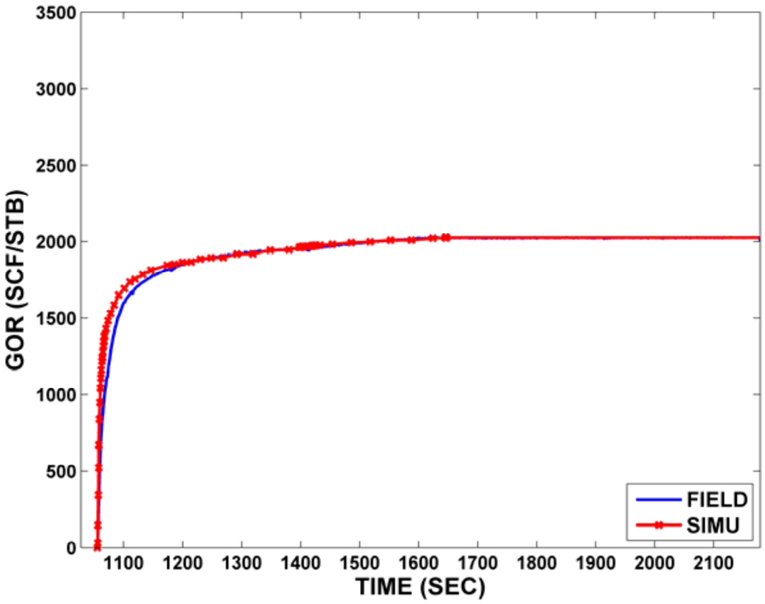

Figure 4.7: Time evolution of the simulated GOR response compared to Field Data Set No. 1.

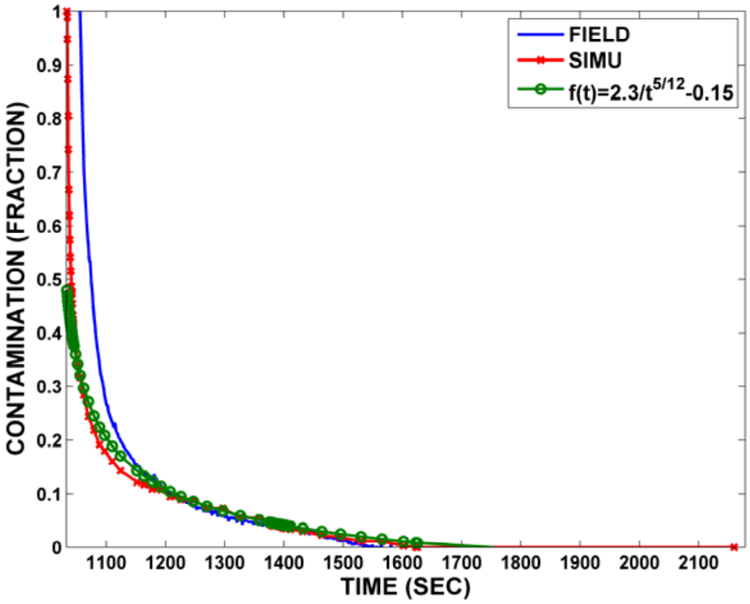

Figure 4.8: Fluid contamination functions for simulated GOR response, field GOR, and analytical approximation to Field Data Set No. 1.

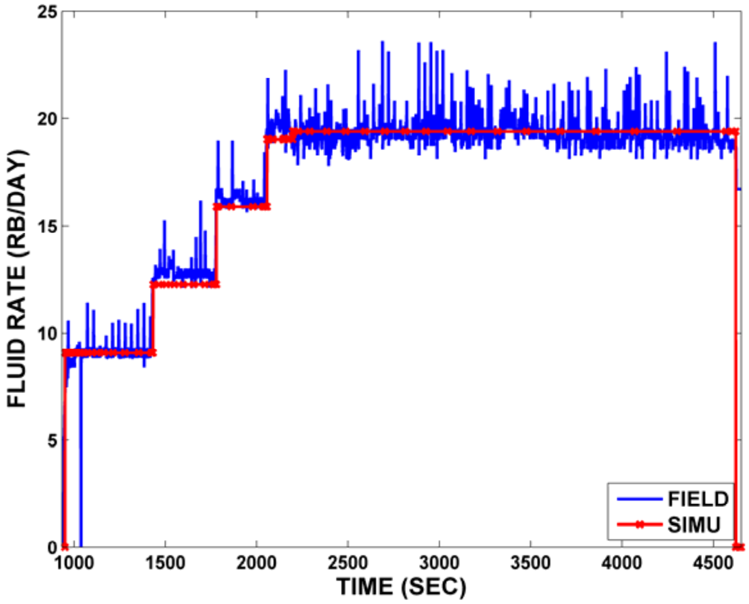

Figure 4.9: Time evolution of probe flow rate at the sink probe assumed in the comparison of simulations and field measurements for Field Data Set No. 2.

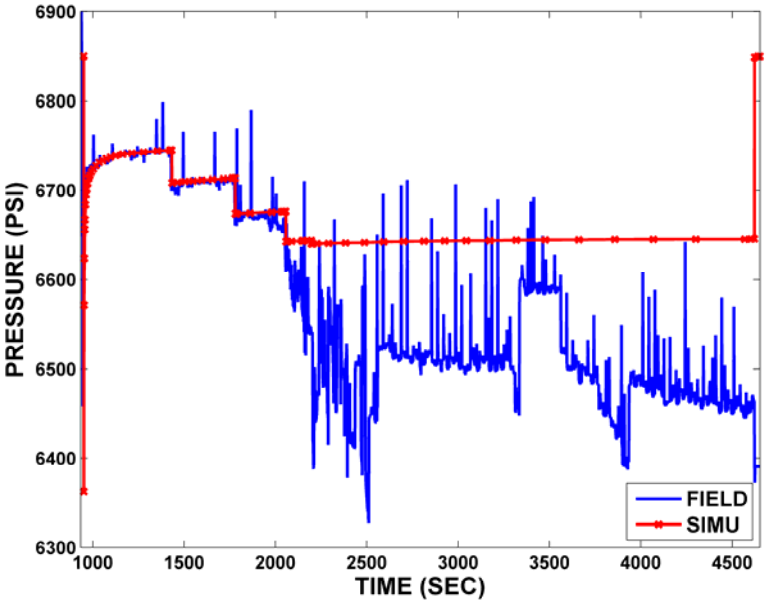

Figure 4.10: Simulated transient pressure response at the sink probe compared to Field Data Set No. 2.

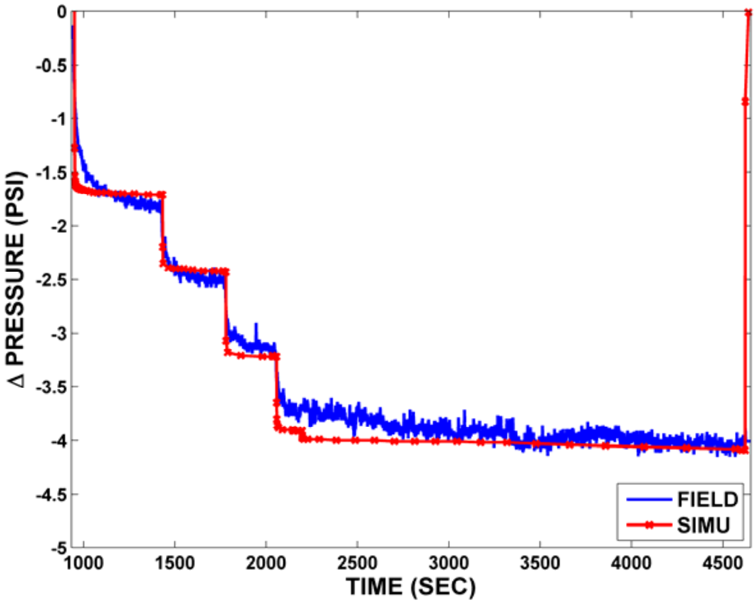

Figure 4.11: Simulated transient pressure response at the observation probe compared to Field Data Set No. 2.

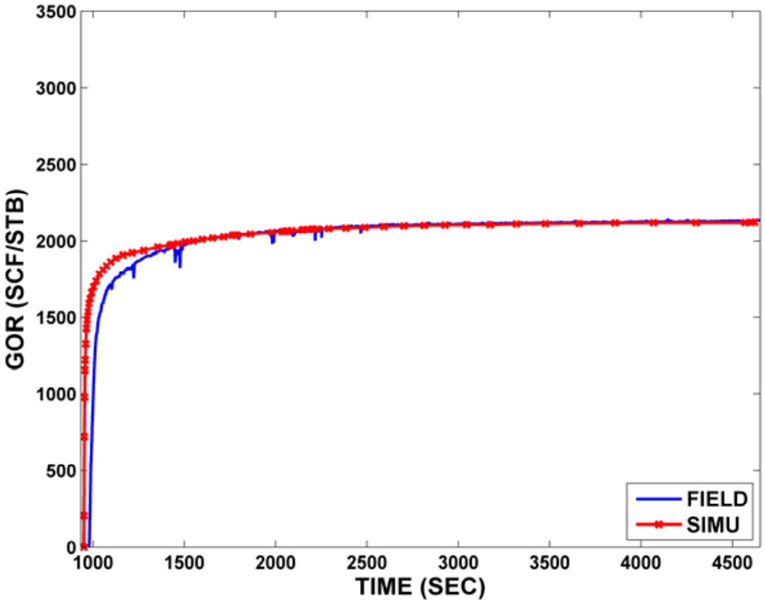

Figure 4.12: Time evolution of simulated GOR response compared to Field Data Set No. 2.

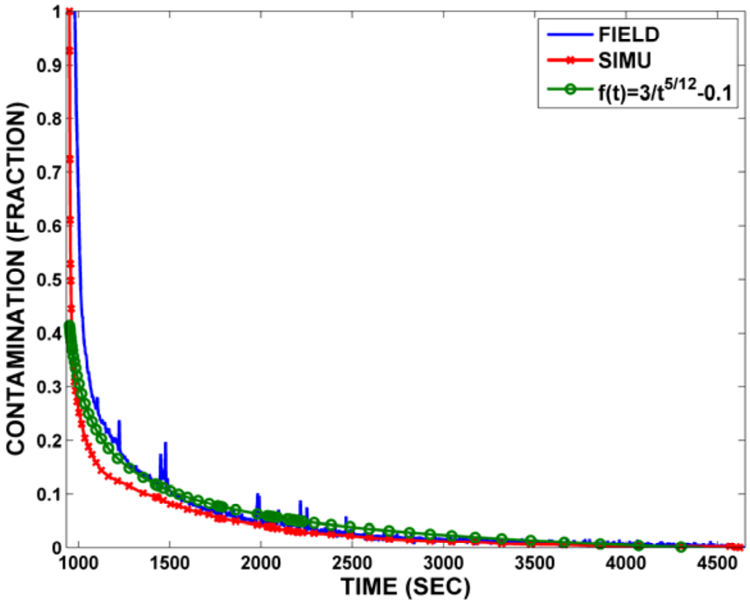

Figure 4.13: Fluid contamination functions for simulated GOR, field GOR, and analytical approximation of GOR for Field Data Set No. 2.

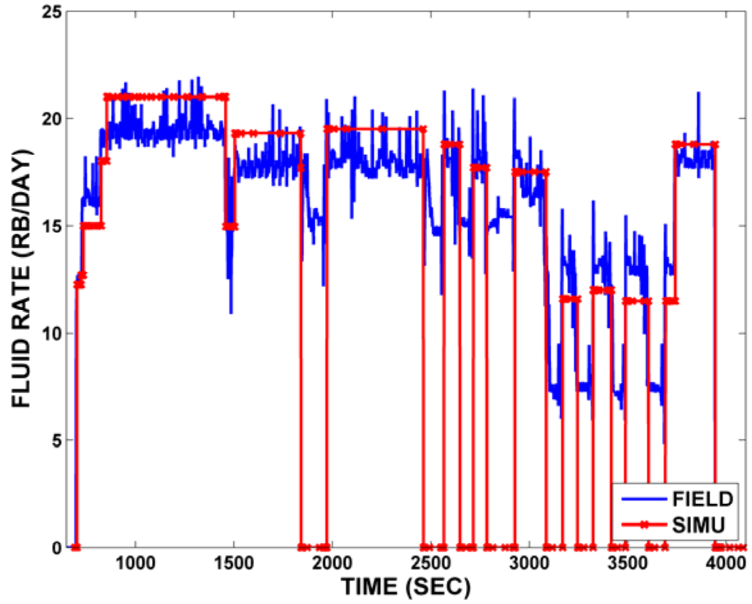

Figure 4.14: Time evolution of probe flow rate at the sink probe assumed for the comparison of simulations to field measurements for Field Data Set No. 3.

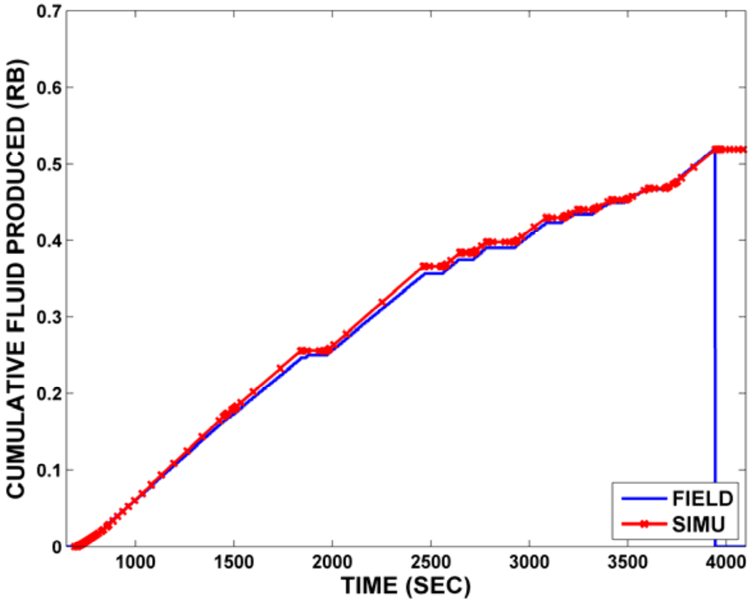

Figure 4.15: Comparison of the simulated and measured time evolution of cumulative fluid produced for Field Data Set No. 3.

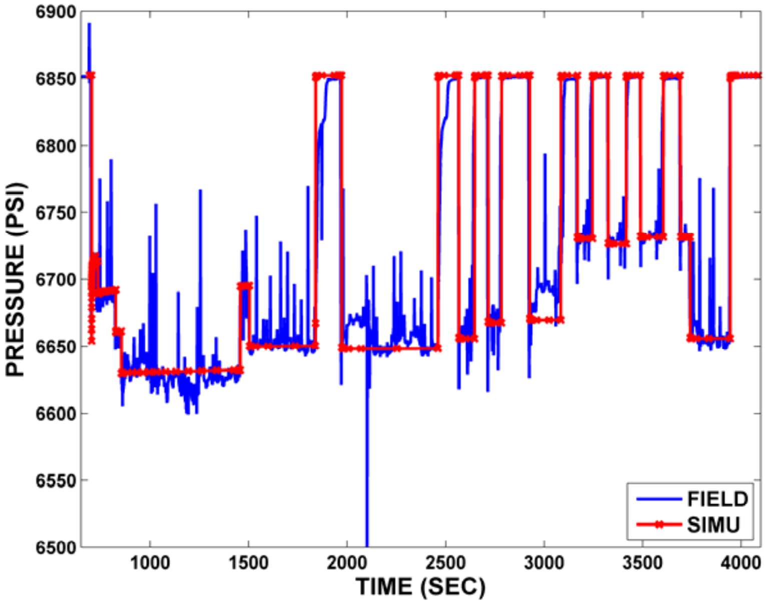

Figure 4.16: Simulated transient pressure response at the sink probe compared to Field Data Set No. 3.

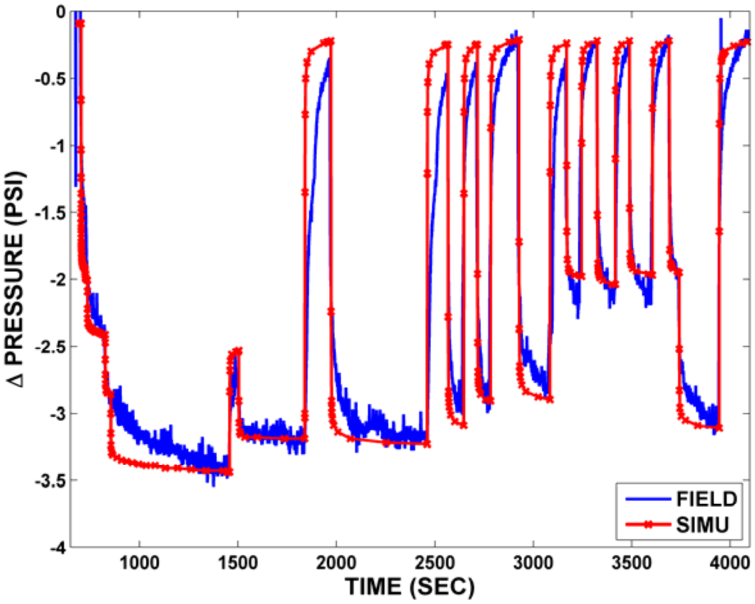

Figure 4.17: Simulated transient pressure response at the observation probe compared to Field Data Set No. 3.

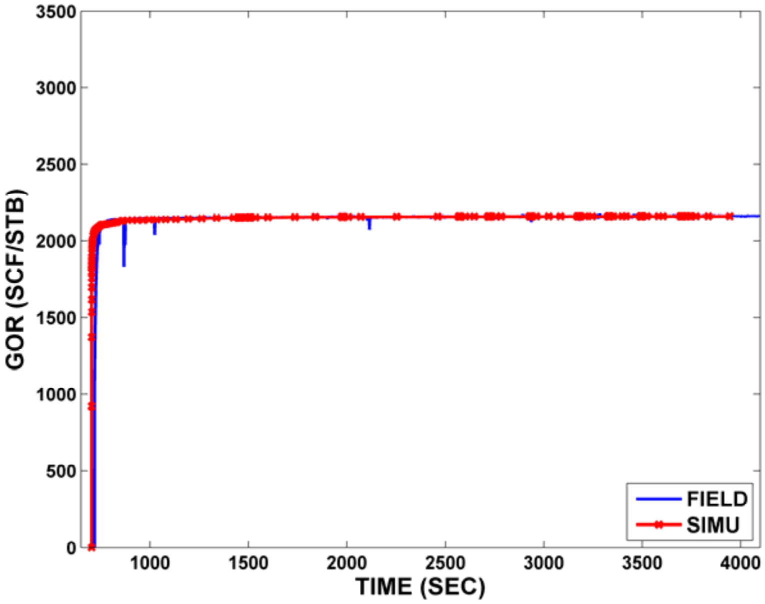

Figure 4.18: Time evolution of simulated GOR response compared to Field Data Set No. 3.

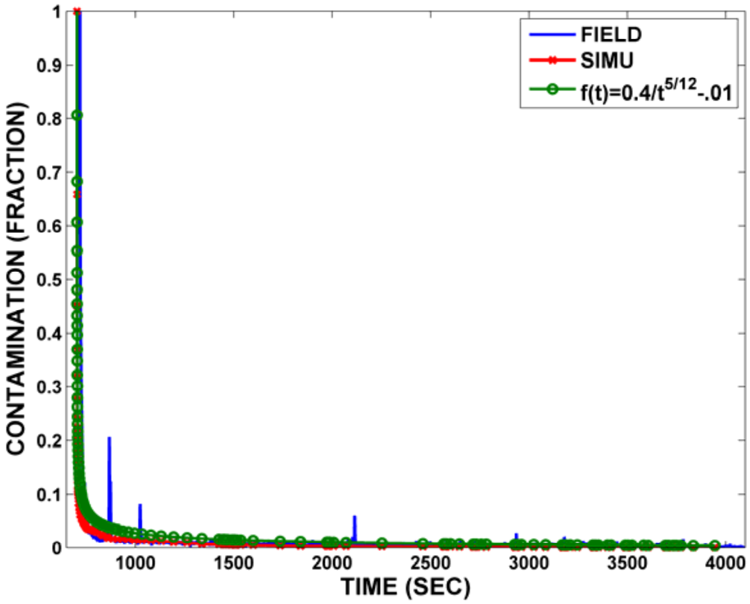

Figure 4.19: Fluid contamination functions for simulated GOR response, field GOR, and analytical approximation of GOR for Field Data Set No. 3.

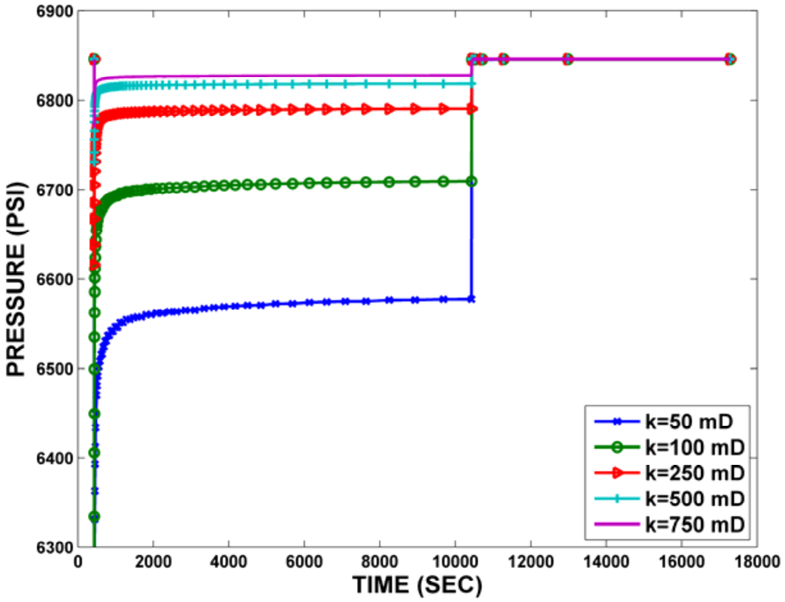

Figure 4.20: Simulated transient pressure response at the sink probe for different values of formation permeability.

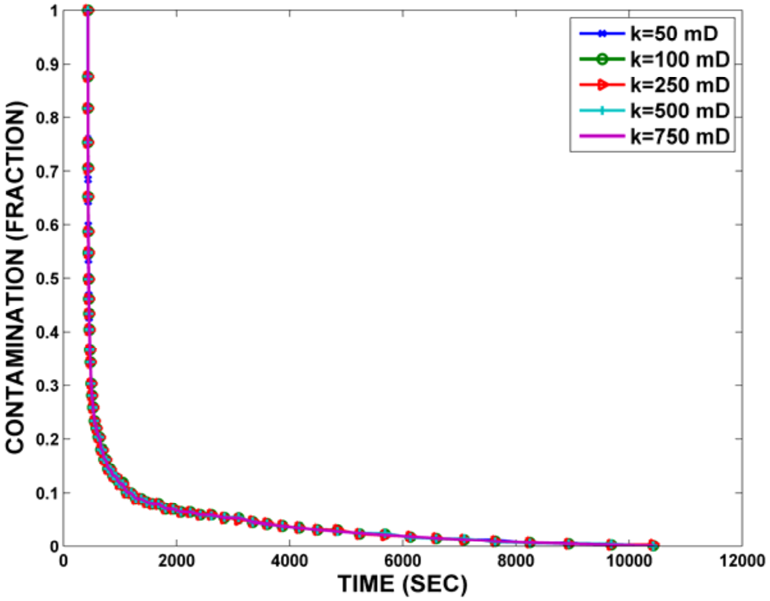

Figure 4.21: Time evolution of simulated fluid contamination for different values of formation permeability.

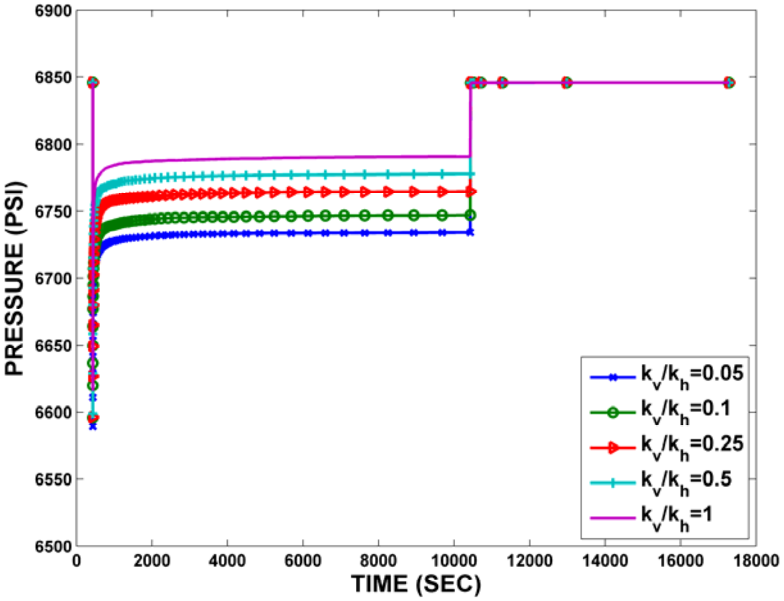

Figure 4.22: Simulated transient pressure response at the sink probe for different values of permeability anisotropy.

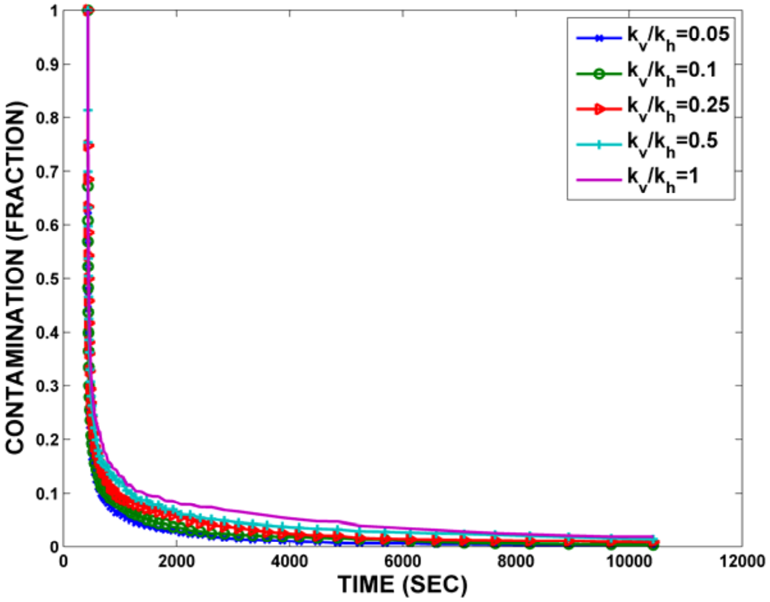

Figure 4.23: Time evolution of simulated fluid contamination for different values of permeability anisotropy.

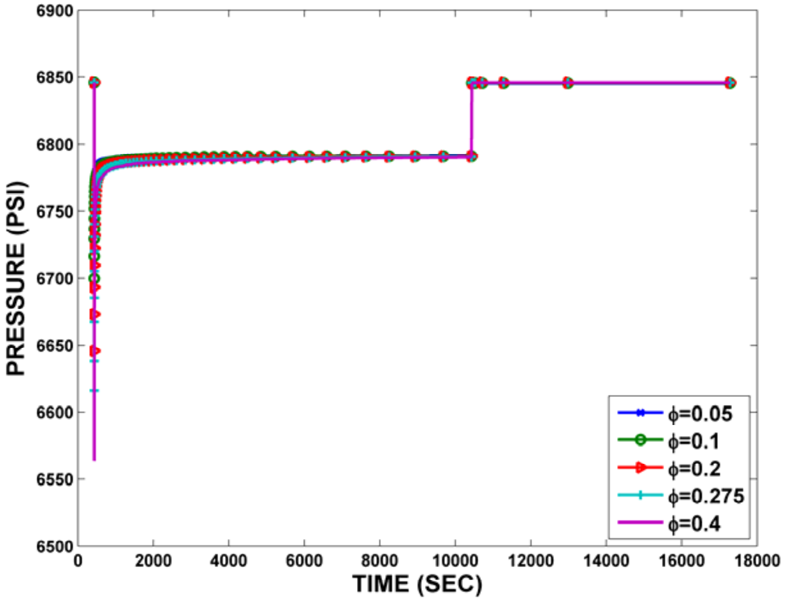

Figure 4.24: Simulated transient pressure response at the sink probe for different values of formation porosity.

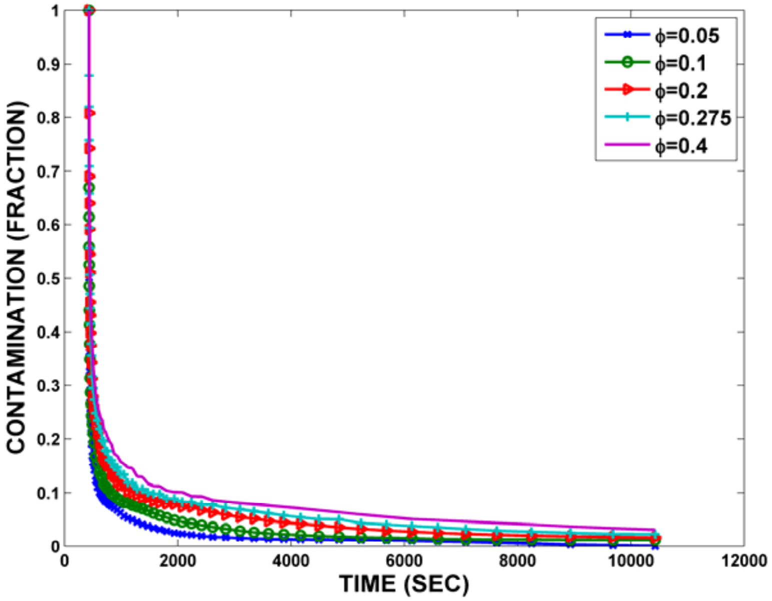

Figure 4.25: Time evolution of simulated fluid contamination for different values of formation porosity.

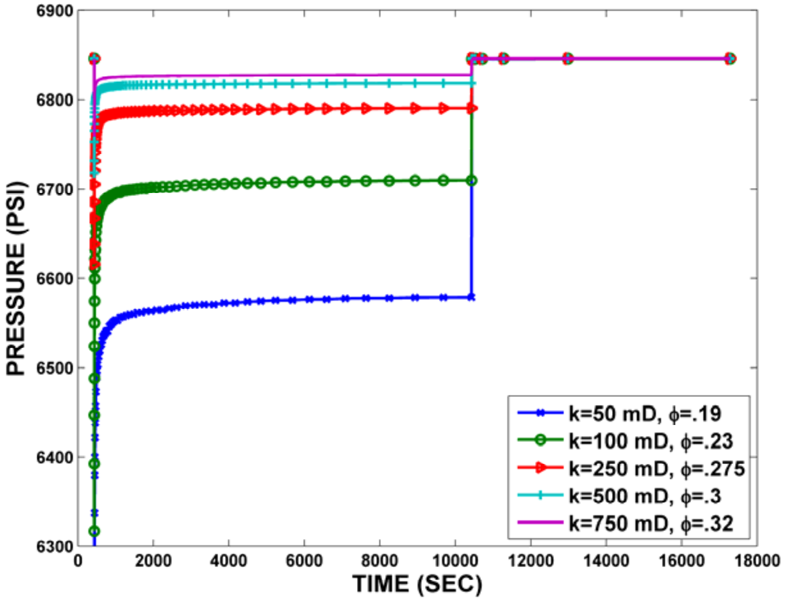

Figure 4.26: Simulated transient pressure response at the sink probe for different values of formation permeability and porosity.

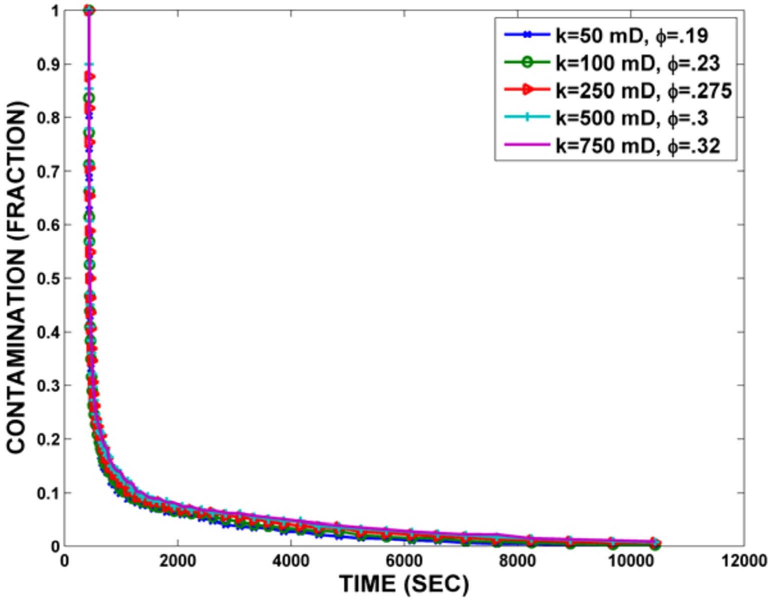

Figure 4.27: Time evolution of simulated fluid contamination for different values of formation permeability and porosity.

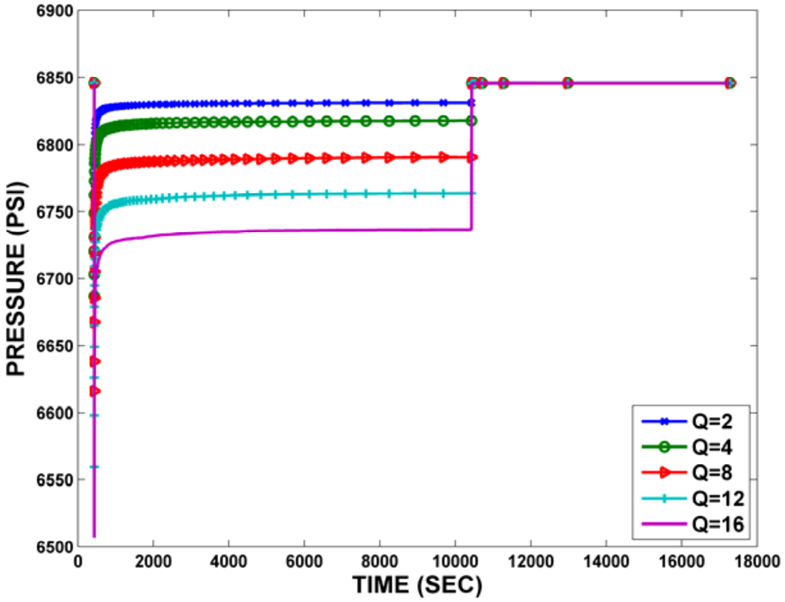

Figure 4.28: Simulated transient pressure response at the sink probe for different values of probe flow rates.

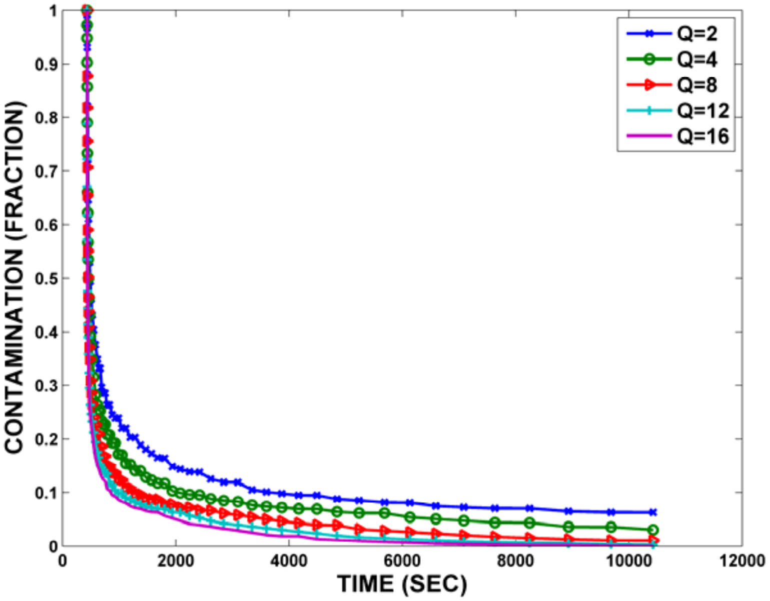

Figure 4.29: Time evolution of simulated fluid contamination for different values of probe flow rates.

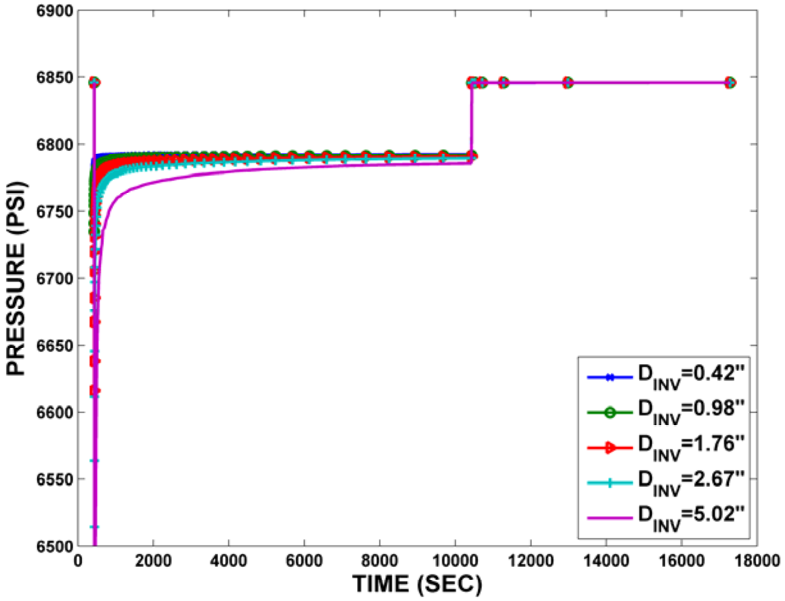

Figure 4.30: Simulated transient pressure response at the sink probe for different values of radial length of mud-filtrate invasion.

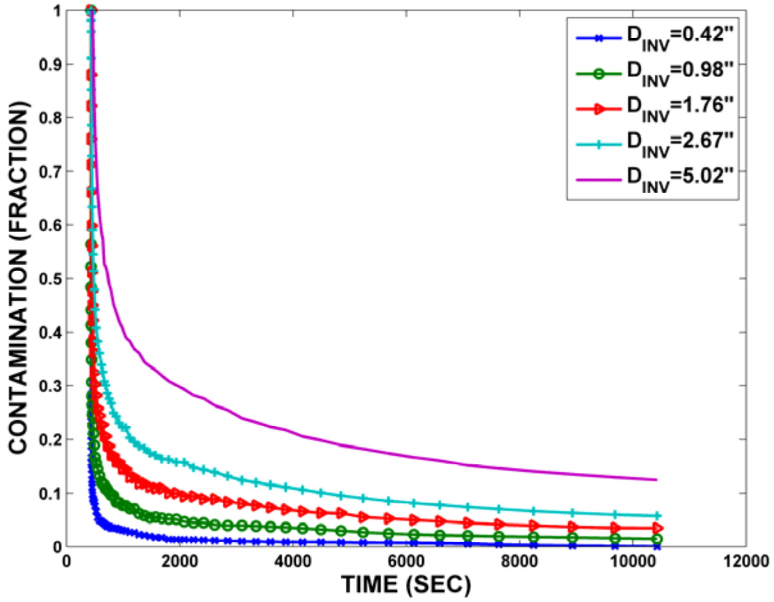

Figure 4.31: Time evolution of simulated fluid contamination for different values of radial length of mud-filtrate invasion.

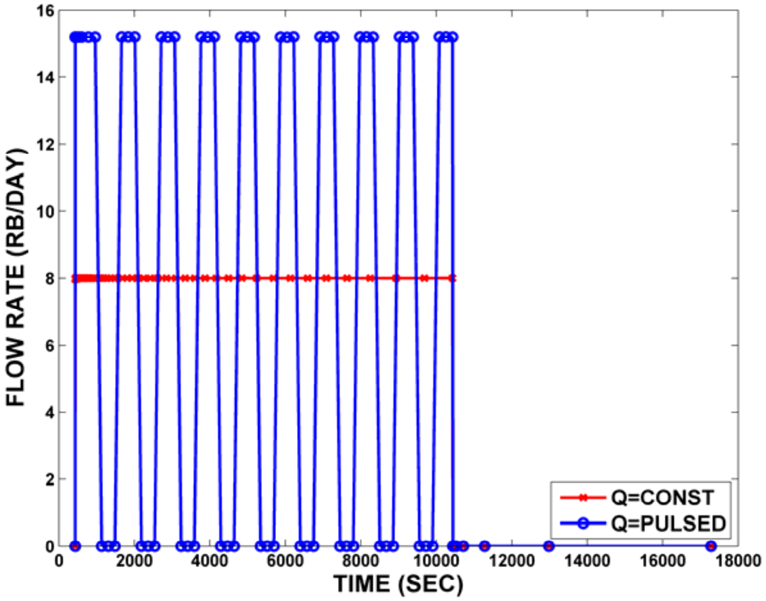

Figure 4.32: Time evolution of simulated flow rates for the cases of constant and pulsed rates of fluid withdrawal.

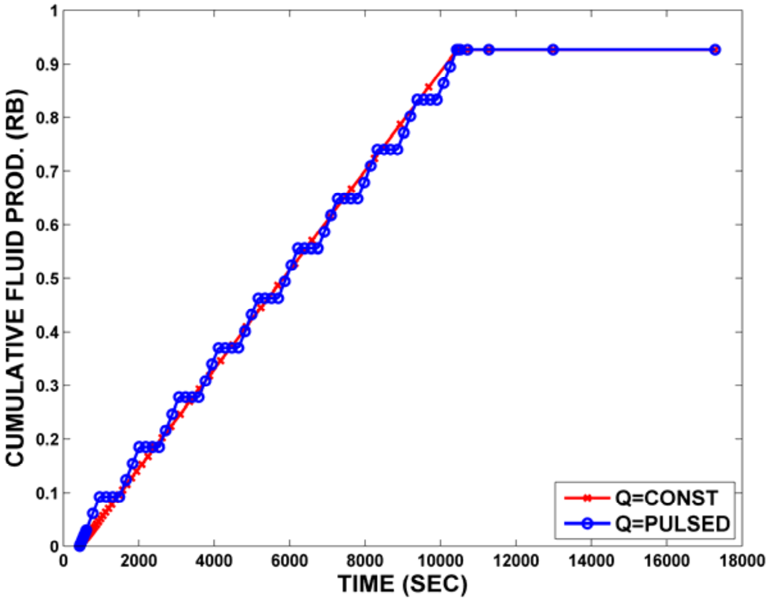

Figure 4.33: Time evolution of simulated cumulative fluid produced for the cases of constant and pulsed rates of fluid withdrawal.

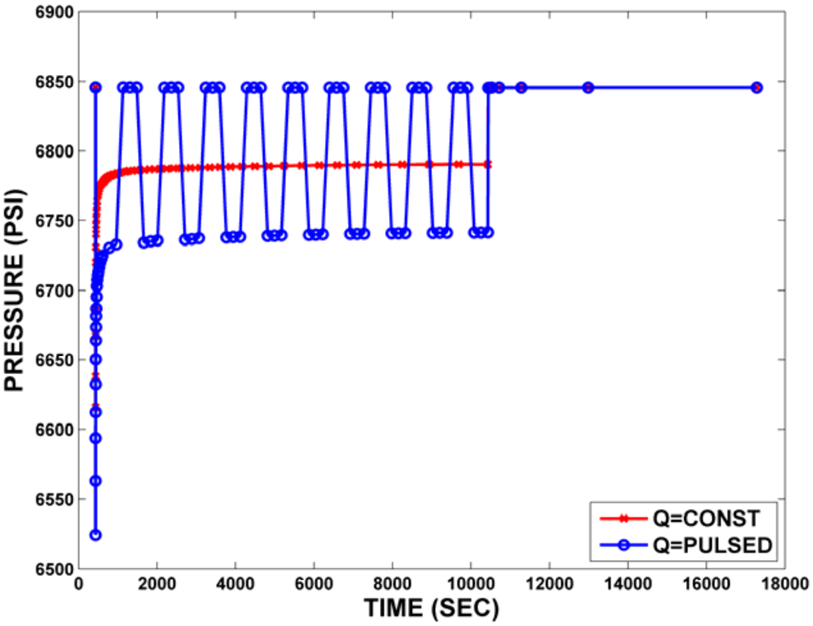

Figure 4.34: Simulated transient pressure response at the sink probe for the cases of constant and pulsed rates of fluid withdrawal.

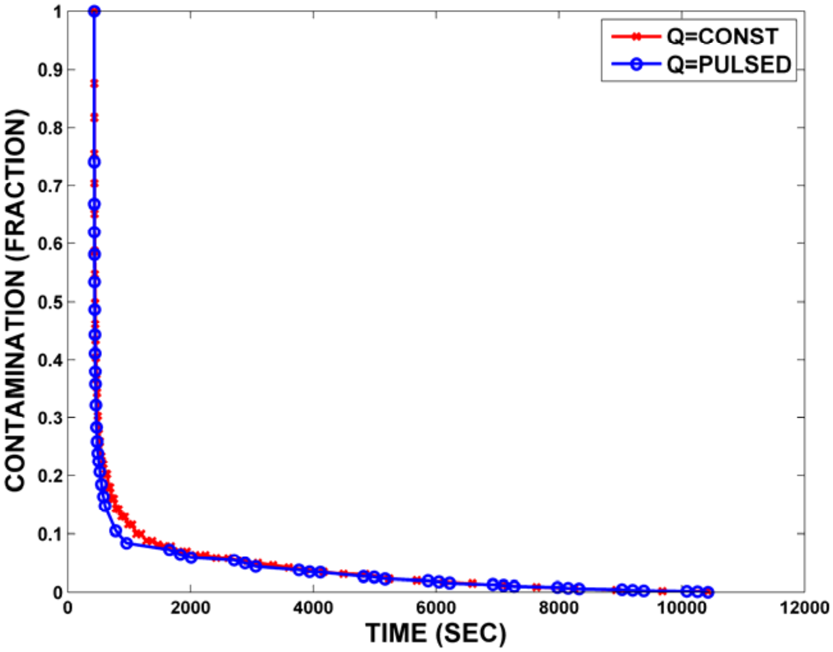

Figure 4.35: Time evolution of simulated fluid contamination for the cases of constant and pulsed rates of fluid withdrawal.

# Chapter 5: A Dual-Grid Automatic History Matching Technique with Applications to 3D Formation Testing in the presence of Oil-Base Muds

Probe-type formation testers are often used to estimate permeability and permeability anisotropy from pressure transient measurements. The interpretation of these measurements is not trivial in the presence of oil-base mud-filtrate invasion due to miscibility with formation oil and gas. Simple analytical expressions of spherical and linear single-phase flow may not give correct estimates of permeability in miscible or partially miscible flow regimes. A computationally demanding three-dimensional (3D) numerical model is required to provide accurate and reliable estimates of formation properties. Because pressure transients are nonlinearly dependent on the permeability of the formation, repeated 3D numerical simulations are necessary to match the measured pressure transients.

In this chapter, we describe the development and successful implementation of a new inversion method that efficiently estimates permeability and permeability anisotropy with a cascade sequence of least-squares minimizations. Measurements consist of pressure transients acquired at the sand face with a probe-type wireline formation tester (WFT). The new inversion method executes the forward 3D problem only in an outer loop. In the inner loop, we perform fast minimizations with an equivalent two-dimensional (2D) cylindrical grid. Transient measurements of pressure at the sand face simulated with the 2D cylindrical grid are correlated to the corresponding measurements simulated with the 3D grid. Once the 2D minimization is completed, we perform a 3D simulation of transient pressure to update the 2D-3D correlation parameter and a new 2D minimization is performed until convergence is reached. The process repeats itself until the simulated 3D pressure transients reproduce the field measurements within pre-stipulated error bounds.

We perform tests of the new inversion algorithm on synthetic and field data sets acquired in the presence of oil-base mud-filtrate invasion. Results successfully confirm that our coupled 2D/3D hybrid inversion approach enables significant savings in computer time and provides reliable and accurate estimates of permeability and anisotropy. In most cases, we are able to estimate permeability under 2% error within 20% of the computational time required by 3D minimization. Sensitivity analysis indicates that permeability estimates may be biased by noisy measurements and uncertainty in (a) flow rates, (b) relative permeability, (c) radial extent of invasion, (d) formation damage, and (e) location of bed boundaries.

## 5.1 INTRODUCTION

Formation testers are widely used to measure pressure and to estimate permeability from pressure transient measurements acquired with sink and observation probes. Often, WFT measurements remain influenced by the process of mud-filtrate invasion that takes place prior to measurement acquisition (Alpak et al., 2006). Mud-filtrate invasion makes it inadequate to use single-phase analytical solutions of pressure transient measurements to estimate permeability. Commercial pressure-transient interpretation methods take invasion into account by invoking a dynamic skin factor. Typically, these methods estimate permeability by neglecting early-time pressure data that are attributed to noisy measurements. However, previous studies on formation testing have shown that early-time pressure measurements can provide useful information about both radial extent of mud-filtrate invasion and relative permeability (Gok et al., 2006; Zeybek et al., 2004). Formation-testing measurements can also be integrated into reservoir models to diagnose and quantify spatial variations of permeability. Therefore, it is important to use a 3D numerical model to simulate measurements acquired with probe-type WFT in order to obtain reliable estimates of formation permeability, radial extent of invasion, relative permeability, location of layers, and for integration with an underlying geological model. However, such an exercise entails executing a computationally intensive 3D numerical simulation of the forward model to invert for permeability. A hybrid inversion technique can be useful to decrease computer times without compromising the accuracy and reliability of the permeability estimates.

Torres-Verdín et al. (2000) successfully implemented a dual-grid cascade sequence of minimizations to invert cross- and single-well direct-current (dc) resistivity measurements into 2D spatial distributions of electrical conductivity. Using a forward model as an approximation to the model used to acquire the measurements, they were able to solve the inversion problem with significant savings in computer time. They also advanced a proof of convergence for the hybrid minimization method. In this chapter, we use a similar inversion method to estimate permeability and permeability anisotropy from transient pressure measurements acquired with a probe-type WFT. The method neglects azimuthal variations of permeability but does take into account the 3D spatial distribution of pressure within the formation. This assumption is not restrictive in field applications of WFT considering that, in general, azimuthal permeability is the same as radial permeability. Our dual grid consists of (a) 3D grid that models the probe geometry, and (b) a 2D axi-symmetric grid. For the same assumed flow rates of fluid withdrawal, the simulated 2D and 3D pressure transients are different in the corresponding grids because of the difference of surface area of probe opening in the two cases. To circumvent this problem, we correlate the transient pressure measurements simulated separately with the 2D and 3D grids. Upon obtaining the correlation parameter between the two sets of simulations, we only use the 2D grid for minimization.

Due to the complexity of miscible flow in the formation, limited work has been advanced to simulate formation-tester measurements in the presence of oil-base muds (OBM). McCalmont et al. (2005) performed sensitivity analyses to determine pumpout volume for gas condensates using an immiscible flow formulation. Alpak et al. (2006) used a miscible flow approach with a compositional equation-of-state (EOS) simulator and compared field measurements of gas/oil ratio (GOR) to their simulated GOR estimates. However, their work lacked comparisons of field measurements of probe pressure against numerical simulations. Angeles et al. (2005) described applications of a least-squares inversion technique that was used to estimate permeability from transient pressure measurements acquired with a packer-type WFT. Wu et al. (2002) used a commercial compositional simulator with a binary component formulation to estimate permeability using a neural network approach.

In this chapter, we simulate displacement of multi-component OBM and formation oil in porous media with CMG-GEM. The unknown inversion parameters are formation permeability and permeability anisotropy. Our compositional model consists of eight pseudo-components: five formation oil components and three oil-base mud-filtrate components, included to accurately model the time-space evolution of miscible flow. Hydrocarbon phase compositions are tracked using the Peng-Robinson EOS. Phase density is calculated from the EOS to account for variations of fluid density due to changes of pressure and fluid composition. Similarly, fluid viscosity is calculated from the Lohrenz-Bray-Clark correlation to account for time-space variations of fluid composition. We model static mud-filtrate invasion assuming piston-like fluid-front displacement in the formation. In this approach, the GOR is sensitive to fluid composition but exhibits negligible sensitivity to formation permeability. Therefore, we only use transient pressure measurements to estimate permeability and permeability anisotropy.

The following section describes our technique for modeling mud-filtrate invasion in the near-wellbore region with a commercial compositional simulator. Subsequently, we discuss the new inversion method that uses a dual-grid hybrid technique to estimate permeability and permeability anisotropy from transient pressure measurements. Thereafter, we describe specific test cases that include noisy pressure measurements, uncertainty in flow rates, uncertainty in relative permeability, mud-filtrate invasion, and layered formations. Lastly, we describe the field case of a rock formation saturated with light-oil that was drilled with OBM. In all cases, our hybrid inversion technique yields reliable estimates of permeability and permeability anisotropy while remaining computationally efficient.

## 5.2 NUMERICAL SIMULATION OF MUD-FILTRATE INVASION AND PROBE-TYPE FORMATION TESTER MEASUREMENTS

We use CMG-GEM and model the probe in a 3D cylindrical-coordinate system centered with the vertical axis of the borehole. Our simulation framework is similar to the one described by Alpak et al. (2006). The process of mud-filtrate invasion is modeled with a known radial length of invasion axi-symmetrically distributed about the axis of a vertical well. Probe measurements of sand-face pressure and observation probe pressure are numerically simulated and inverted with corresponding simulated and field measurements. Pressure measurements are sensitive to formation permeability, permeability anisotropy, and radial length of mud-filtrate invasion as we show in a subsequent sensitivity analysis.

The simulation framework is discussed in detail in Chapter 4. **Table 4.1** describes the finite-difference grid, consisting of 35 blocks in the radial (r) direction, 20 blocks in the azimuthal (θ) direction, and 27 blocks in the vertical (z) direction. At the wellbore, the probe was modeled with three azimuthal and three vertical gridblocks, amounting to nine gridblocks. **Figure 4.1** is a perspective view of the probe location with respect to the cylindrical grid. There are 3740 gridblocks included within a radius of one foot around the probe to accurately capture flow dynamics in the near-probe region. The corresponding 2D grid has only one gridblock in the azimuthal direction. **Figure 5.1** is a side view of the WFT. It consists of three probes to measure pressure - one sink probe and two observation probes. In the simulations, the sink probe is aligned with the center of the vertical well. **Table 4.2** gives a summary of the petrophysical parameters used for the simulation model. The formation fluid composition and mud-filtrate composition were described in **Tables 4.4** and **4.5**, respectively.

### 5.2.1 Base Case Model

**Table 5.1** summarizes the petrophysical, formation, and numerical simulation properties for the base case simulation model. We assume a homogeneous, single-layer anisotropic formation as our base case model.

**Figure 5.2** shows the assumed saturation-dependent Brooks-Corey (Brooks and Corey, 1964) relative permeability and drainage capillary pressure curves. The irreducible water saturation is 0.22, whereas the simulated production time is 3600 sec and buildup time is 504 sec. Rate of fluid pumpout is 12 RB/day for the first 1800 sec of production and 18 RB/day for the subsequent 1800 sec. Total fluid pumpout volume is 0.625 barrels.

## 5.3 NONLINEAR INVERSION ALGORITHM

For inversion, we implement the general nonlinear least-squares minimization method described by Madsen et al. (2004). The following sub-sections describe our inversion algorithm as implemented to interpret formation-tester measurements. We describe the cost function that is composed of transient pressure measurements at the sand face and at the observation probes. Subsequently, we discuss the Levenberg-Marquardt (Levenberg, 1944; Marquardt, 1963) algorithm that is used to estimate permeability and permeability anisotropy from transient pressure measurements. In the next sub-section, we introduce a hybrid grid technique that uses 2D simulations to approximate 3D probe measurements. Then, Cramer-Rao (Habashy and Abubakar, 2004) bounds are introduced to quantify confidence bounds in the estimated values of permeability and permeability anisotropy from noisy measurements. Lastly, we describe some features specific to the CMG-GEM simulator that significantly improve the efficiency of the hybrid minimization method.

### 5.3.1 Cost Function

Given a vector residual function $\mathbf{e}:\mathbb{R}^n \to \mathbb{R}^m$ with $m \geq n$, the quadratic cost function $(C(\mathbf{x}))$ is defined as

$$C(\mathbf{x}) = \frac{1}{2}\sum_{i=1}^{i=m}(e_i(\mathbf{x}))^2 = \frac{1}{2}\mathbf{e}(\mathbf{x})^{\mathrm{T}}\mathbf{e}(\mathbf{x}), \qquad \ldots(5.1)$$

where $m$ is the length of the data vector and $n$ is the length of the model vector. There are $m$ time samples of pressure measurements and $n$ unknown parameters in **Eq. 5.1**. The factor ½ in the above equation is introduced for convenience and has no effect on convergence. In formation testing applications, the model vector (**x**) typically describes the permeability tensor, which includes radial and vertical permeability. The dimensionless residual vector is the relative pressure difference between the simulated and the observed measurements, defined as

$$\mathbf{e}(\mathbf{x}) = \begin{bmatrix} e_1(\mathbf{x}) \\ \vdots \\ e_i(\mathbf{x}) \\ \vdots \\ e_m(\mathbf{x}) \end{bmatrix} = \begin{bmatrix} p_{sim_1}(\mathbf{x}) / p_{obs_1}(\mathbf{x}) - 1 \\ \vdots \\ p_{sim_i}(\mathbf{x}) / p_{obs_i}(\mathbf{x}) - 1 \\ \vdots \\ p_{sim_m}(\mathbf{x}) / p_{obs_m}(\mathbf{x}) - 1 \end{bmatrix}, \qquad \ldots(5.2)$$

where subscript *sim* identifies the numerically simulated and *obs* identifies the observed transients, pressure measurements ($p$), respectively. Since we use 3 transient pressure probe measurements (sink probe and two observation probes), the data residual vector is concatenated with the three pressure vectors. In **Eq. 5.1**, the cost function is composed of the relative pressure difference and therefore its units are dimensionless. The inversion algorithm estimates permeability and permeability anisotropy, denoted by the vector **x**, by simultaneously honoring the three available pressure measurements of sink and two observation probes. We introduce a Jacobian matrix that contains, as entries, the first-order partial derivatives of the residual vector as

$$\left(\mathbf{J}(\mathbf{x})\right)_{ij} = \frac{\partial e_i}{\partial x_j}(\mathbf{x}), \qquad \ldots(5.3)$$

where $\mathbf{J} \in \mathbb{R}^{m \times n}$ is the Jacobian matrix. The gradient of the cost function is given by

$$\frac{\partial C}{\partial x_j}(\mathbf{x}) = \sum_{i=1}^{m} e_i(\mathbf{x}) \frac{\partial e_i}{\partial x_j}. \qquad \ldots(5.4)$$

Thus, in vector notation, **Eq. 5.4** can be written as

$$C'(\mathbf{x}) = \mathbf{J}(\mathbf{x})^{\mathrm{T}} \mathbf{e}(\mathbf{x}), \qquad \ldots(5.5)$$

where superscript $^{\mathrm{T}}$ refers to the transpose of the matrix. Similarly, the Hessian of the cost function is given by

$$C''(\mathbf{x}) = \mathbf{J}(\mathbf{x})^{\mathrm{T}} \mathbf{J}(\mathbf{x}) + \sum_{i=1}^{m} e_i(x) e_i''(\mathbf{x}). \qquad \ldots(5.6)$$

We assume that the quadratic cost function $(C(\mathbf{x}))$ is differentiable and smooth such that the Taylor series expansion gives

$$C(\mathbf{x}+\mathbf{h}) = C(\mathbf{x}) + \mathbf{h}^{\mathrm{T}}\mathbf{J}(\mathbf{x})^{\mathrm{T}}\mathbf{e}(\mathbf{x}) + \frac{1}{2}\mathbf{h}^{\mathrm{T}}\mathbf{H}(\mathbf{x})\mathbf{h} + O(\|\mathbf{h}\|^3), \qquad \ldots(5.7)$$

where $\mathbf{H}$ is the Hessian matrix and **h** is a small perturbation on the model vector (**x**).

In our implementation, we observed that the pressure output from CMG-GEM has only two decimal figures of precision. This numerical precision is inadequate for inversion, especially in high-porosity high-permeability formations when the pressure differential during drawdown and buildup is small. Extensive simulation exercises indicate that CMG-GEM allows six-decimal precision for pressure differential output and hence becomes better suitable for inversion. Therefore, instead of using the pressure output, we used the pressure differential from time zero. The residual based on pressure differential at the *i*th time step is given by

$$e_i(\mathbf{x}) = \Delta p_{sim_i}(\mathbf{x}) / \Delta p_{obs_i}(\mathbf{x}) - 1, \qquad \ldots(5.8)$$

where $\Delta p_i = p_i - p_o$ is the pressure difference between the *i*th time step and the *0*th time step. Moreover, the data residual vector includes pressure measurements acquired with both drawdown and the buildup periods. If the pressure differential is zero, the error function in **Eq. 5.8** will tend to infinity. However, cases of zero pressure differential arise when the sand face pressure rises to the formation pressure (either before the sampling operation or at late times of buildup after sampling). In such cases, pressure is insensitive to variations of permeability. Therefore, we neglect pressure measurements acquired at those time steps when the pressure differential is less than 0.05 psi. Our observation is that by performing this modification, we achieve better convergence and are successfully prevent the residual function from approaching infinity.

### 5.3.2 Levenberg-Marquardt Minimization

We use the Levenberg-Marquardt method for nonlinear minimization. This algorithm is a variation of the Gauss-Newton method with a damping parameter. Our minimization algorithm is based on the formulation given by Madsen et al. (2004) as

$$(\mathbf{J}(\mathbf{x})^{\mathrm{T}}\mathbf{J}(\mathbf{x})+\mu\mathbf{I})\mathbf{h}=-\mathbf{J}(\mathbf{x})^{\mathrm{T}}\mathbf{e}(\mathbf{x}), \qquad \ldots(5.9)$$

and damping or Lagrange parameter $\mu \geq 0$. In the above equation, **I** designates the identity matrix. For large values of $\mu$, one has

$$\mathbf{h} \simeq -\frac{\mathbf{J}(\mathbf{x})^{\mathrm{T}}\mathbf{e}(\mathbf{x})}{\mu}, \qquad \ldots(5.10)$$

and is equivalent to a short step in the steepest-descent direction. For small values of $\mu$, **Eq. 5.9** is equivalent to the Gauss-Newton method and provides quadratic convergence near the minima. At the outset, the initial $\mu$ relates to the size of the elements in the Jacobian matrix as

$$\mu_o = \tau \cdot \max_i\{\mathbf{J}(\mathbf{x_0})^{\mathrm{T}}\mathbf{J}(\mathbf{x_0})\}, \qquad \ldots(5.11)$$

where $\tau$ is a parameter that influences the convergence behavior in early iterations. Based on sensitivity analysis, we used a value of $\tau$ equal to 0.125 in all the inversion exercises reported in this chapter. During subsequent iterations, $\mu$ varies depending on the norm of the Jacobian matrix. In order to decrease the computer time necessary to calculate the Jacobian matrix, we use Broyden's (1965) secant updates, given by

$$\mathbf{J}_{k+1}(\mathbf{x}_{k+1}) = \mathbf{J}_k(\mathbf{x}_k) + \frac{\{\mathbf{e}(\mathbf{x}_{k+1})-\mathbf{e}(\mathbf{x}_k)-\mathbf{J}(\mathbf{x}_k)\mathbf{h}\}}{\mathbf{h}^{\mathrm{T}}\mathbf{h}}\cdot\mathbf{h}, \qquad \ldots(5.12)$$

where the subscript *k* identifies the iteration number. At the start of the minimization, we calculate the Jacobian matrix numerically by perturbing the model vector (**x**) by 0.5 mD. Subsequently, we only use Broyden's updates to approximate the Jacobian matrix. Our observation is that Broyden's updates are much cheaper computationally than calculating the Jacobian matrix at each iteration. In addition, the number of iterations required to reach the minimum with Broyden's updates is similar to the number of iterations required to reach the minimum using Jacobian matrix calculations.

There are instances in practical applications where the minimization algorithm converges to local minima and is unable to find a suitable direction that decreases the cost function for subsequent iterations. If this condition occurs for over 4 subsequent iterations, then we recalculate the Jacobian matrix numerically.

### 5.3.3 Hybrid Inversion Technique

We provide a systematic description of our hybrid inversion technique in this section. Underlying the algorithm is the assumption that we neglect azimuthal variations of permeability and porosity. Torres-Verdín et al. (2000) give a proof of convergence of the hybrid minimization technique.

We assume that the pressure differential during drawdown and buildup between the 2D and 3D simulation is proportional in certain range of permeability for the same imposed flow rates of fluid withdrawal. Thus, we can use a correlation vector to determine the pressure differential between the 2D and 3D simulations. Due to different geometry of the probe opening and presence of mud-filtrate invasion that causes transient variations of pressure differential, pressure differentials simulated with the two simulation grids will never be exactly proportional. Therefore, we have to recalculate the correlation vector between the 2D and 3D simulations at the end of successive minimizations. Our sensitivity analysis shows that we are able to closely approach the minima by calculating the correlation vector just three times between the 2D and 3D grids. Since the computer time required for function evaluations with the 2D grid is much shorter than the corresponding time with the 3D grid, significant savings in computer time are achieved with the hybrid minimization method. **Figure 5.3** is a flowchart that describes the minimization procedure. The following is a summary of steps that explain our hybrid minimization method:

(1) Perform 3D and 2D simulations of transient pressure and compute the relation between pressure differentials as

$$\mathbf{f_{rel}}(\mathbf{x}) = \frac{\Delta\mathbf{p_{3D}}(\mathbf{x})}{\Delta\mathbf{p_{2D}}(\mathbf{x})}, \qquad \text{…(5.13)}$$

where $\mathbf{f_{rel}}$ is the transformation or correlation vector of the pressure differential between corresponding 2D and 3D simulations.

(2) The pseudo-pressure differential from the 2D simulation is calculated with the transformation

$$\Delta\mathbf{p}^{*}\mathbf{_{2D}}(\mathbf{x}) = \mathbf{f_{rel}}(\mathbf{x}) \cdot \Delta\mathbf{p_{2D}}(\mathbf{x}). \qquad \text{…(5.14)}$$

(3) The residual vector between the pseudo-pressure differential and the measured pressure differential is calculated as

$$\mathbf{e}^{*}\mathbf{_{2D}}(\mathbf{x}) = \begin{bmatrix} \Delta p^{*}{}_{2Dsim_1}(\mathbf{x}) / \Delta p_{obs_1}(\mathbf{x}) - 1 \\ \vdots \\ \Delta p^{*}{}_{2Dsim_i}(\mathbf{x}) / \Delta p_{obs_i}(\mathbf{x}) - 1 \\ \vdots \\ \Delta p^{*}{}_{2Dsim_m}(\mathbf{x}) / \Delta p_{obs_m}(\mathbf{x}) - 1 \end{bmatrix}. \qquad \text{…(5.15)}$$

(4) Minimization is performed with the new data residual vector based only on 2D simulations. The corresponding cost function for minimization is defined as

$$C(\mathbf{x}) = \frac{1}{2}\mathbf{e}^{*}\mathbf{_{2D}}(\mathbf{x})^{\mathrm{T}}\mathbf{e}^{*}\mathbf{_{2D}}(\mathbf{x}). \qquad \text{…(5.16)}$$

Note that this step does not involve 3D simulations. Two-dimensional simulations are performed until the norm of the error is below a certain pre-defined value or if 12 iterations of the Levenberg-Marquardt minimization are reached. We refer to this 2D minimization as the "**inner loop**" minimization.

(5) A 3D simulation is performed and a new relation between the 2D and 3D simulations is computed based on **Eq. 5.10**. If the error norm is below a certain threshold, the inversion stops. If not, then we go back to step 2 ("**outer loop**"). The hybrid minimization ends when we reach three outer loops (the specific choice of three loops of hybrid minimization was made based on extensive sensitivity analysis).

(6) By this step, the permeability vector (**x**) has improved due to the repeated iterations of the hybrid minimization. We are very close to the minimum, but not exactly at it given that the 2D minimization is an approximation. Therefore, in order to complete the inversion, we need to proceed with a Levenberg-Marquardt minimization of the 3D simulation. The cost function is based on the pressure differential calculated with the 3D code as

$$C(\mathbf{x}) = \frac{1}{2}\mathbf{e}_{\mathbf{3D}}(\mathbf{x})^{\mathrm{T}}\mathbf{e}_{\mathbf{3D}}(\mathbf{x}) . \qquad \ldots(5.17)$$

### 5.3.4 Stopping Criteria for Minimization

There are three stopping criteria that are built in the Levenberg-Marquardt algorithm: (a) number of iterations, (b) quadratic norm of the cost function, and (c) infinity norm of the cost function. In our implementation, the maximum number of iterations is 12, the minimum quadratic norm and the infinity norm of the cost function are $10^{-5}$, and the stopping criteria are the same for the hybrid and for the 3D minimization. We performed sensitivity analyses to determine suitable stopping criteria. The stopping criteria were helpful in terminating the minimization when the cost function was very close to the minima. In cases of noisy measurements, the cost function will not approach zero and will keep oscillating around a certain local minimum. In such cases, sensitivity analyses of the stopping criteria are helpful to determine at what point to terminate the minimization.

### 5.3.5 Cramer-Rao Uncertainty Bounds

We use the Cramer-Rao method to quantify uncertainty (non-uniqueness) in our estimates of permeability and permeability anisotropy (Angeles et al., 2005; Habashy and Abubakar, 2004). In this method, a perturbation is performed at the end of convergence in order to calculate the Jacobian matrix and to estimate the model covariance matrix ($\Sigma$), given by

$$\bar{\Sigma} = \sigma^2 \left[ \mathbf{J}(\bar{\mathbf{x}})^{\mathrm{T}} \mathbf{J}(\bar{\mathbf{x}}) + \frac{\sigma^2}{\mu} \mathbf{I} \right]^{-1} , \qquad \ldots(5.18)$$

where $\sigma$ is the standard deviation of the Gaussian noise used to contaminate the pressure data, $\mu$ is the Lagrange or damping parameter, $\bar{\mathbf{x}}$ is the vector of inverted model parameters, and $\bar{\Sigma}$ is defined as the estimator's covariance matrix. The square root of the diagonal terms of the covariance matrix provides the uncertainty of the estimated model parameters. Uncertainty bounds are calculated only for noisy measurements with non-zero standard deviation for the assumed Gaussian noise.

### 5.3.6 Optimizing CMG-GEM for Inversion

We constructed two CMG-GEM simulation files: (a) 3D grid described in the previous section, and (b) 2D axial-symmetric grid. Since the 2D grid uses 20 times fewer gridblocks in the simulation, we observe an improvement of CPU simulation time of approximately 20 times with respect to 3D simulations.

CMG-GEM is an adaptive-implicit simulator that can take large time steps if the variation of fluid properties is below a certain tolerance. In our simulations, we initially executed the simulator to determine the time steps that are considered essential by the simulator. In general, time steps are small at the start of a simulation due to rapid time-space variations of multi-phase flow in the near-wellbore region. The time step increases at late times in the simulation when the flow regime is mainly single phase with negligible compositional variations. In addition, the time step decreases when there is a variation of the assumed flow rate. In a subsequent section of sensitivity analysis, we first executed CMG-GEM to determine the time steps essential for the simulation. Thereafter, we only compared pressure data at those critical time steps. This procedure enabled lower CPU times because the simulator needs to output pressure data at only critical time steps and thus improved the efficiency of the inversion by decreasing the size of the Jacobian matrix without compromising information at critical time steps. Not only does this decrease the size of the Jacobian matrix but also requires fewer derivatives, thereby additionally decreasing CPU times.

Lastly, as discussed by Collins et al. (1992), CMG-GEM allows for stability control of the simulation with the numerical options included in the input file. In order to obtain accurate solutions, we observed that the simulation should be performed with the "AIM STAB 3" option. This means that the adaptive-implicit (AIM) simulation has a stability switching option of level 3 under which all gridblocks are checked to determine whether a gridblock should be run either explicitly or implicitly after each Newtonian iteration within a time step. Another option for the numerical section is "AIM STAB 2" which means that only selected gridblocks are checked (determined internally by the simulator) for convergence once per time step. The CPU run time can be increased by over 10% if level-2 option is used instead of level 3. In our simulations, we realized that it is essential to use the level-3 option to accurately model probe measurements. However, for the 2D grid, we realized that since the 2D simulation is an approximation, we can use the level 2 option to decrease the CPU time. Based on a similar observation, while investigating mud-filtrate invasion we realized that we only needed to model invasion in the 3D code. By not modeling invasion at all with the 2D simulations, we achieved further savings in CPU time. If we perform three outer loops of our hybrid minimization, the run time to compute 36 function evaluations (12 inner iterations x 3 loops) with the 2D model is approximately equivalent to one function evaluation for the 3D model. For the purposes of this chapter, one function evaluation is equivalent to a single forward modeling calculation.

## 5.4 SENSITIVITY ANALYSIS OF PROBE-TYPE FORMATION-TESTER MEASUREMENTS

We performed sensitivity analyses on our Base Case Model. Sensitivity analyses are essential to appraise the performance of our hybrid inversion technique vis-à-vis 3D minimization. In addition, sensitivity analyses are important to diagnose noisy pressure and flow-rate measurements, presence of mud-filtrate invasion, as well as possible bed-boundary, relative permeability, and formation damage effects on the estimates of permeability and permeability anisotropy. In the following subsections, we discuss our noise-free, no-invasion Base Case Model and compare inversion performance against 3D simulations. Thereafter, we introduce more realistic cases of mud-filtrate invasion and cases of noisy pressure measurements. Results show that, in most cases, our dual-grid hybrid inversion algorithm approaches the minima within 2% error using only 20% of the computational time of a corresponding 3D inversion.

### 5.4.1 Homogeneous and Anisotropic Formation - Base Case Model

As discussed in the previous section, we considered a single- layer anisotropic model (no invasion at irreducible water saturation) to appraise our inversion technique. We emphasize that our Base-Case Model corresponds to single-phase flow of formation oil as the formation water is at irreducible saturation and there is no mud-filtrate invasion. **Figure 5.4** shows the simulated pressure measurements at the start of each inner 2D loop. The pressure differential improves toward the minima from loop 1 to loop 3. Similarly, the cost function decreases from loop 1 to loop 3. The quadratic norm of the minima was

$10^{-5}$ for all cases as described earlier in the stopping criteria sub-section. We start the minimization with 3D simulations at the end of the 3rd inner loop. Note that there are only 30 time samples of pressure measurements in the plots. CMG-GEM identified these critical time intervals during the simulation. **Table 5.2** shows the estimates of permeability and the corresponding CPU time required for minimization. All of the simulations were performed on an Intel Pentium[8] D Dual Processor, 3.2 GHz PC with 3.2 Gigabytes of RAM. By optimizing the 2D simulations, we were able to achieve a function evaluation time of only 12 sec. At the end of the 3rd loop, our estimates of permeability obtained with the 2D code were within 0.5% of the assumed formation permeability. The CPU time for the inner loop includes the time for function evaluation necessary to correlate 3D and 2D simulations. For the Base-Case Model, the CPU time necessary for each function evaluation of the 3D simulation was approximately equal to 242 sec. The number of iterations in **Fig. 5.4** is less than the number of function evaluations in **Table 5.2** as there are three additional function evaluations required to calculate the entries of the Jacobian matrix.

We performed another inversion from an initial guess of horizontal and vertical permeability of 100 mD using only the 3D grid model. Results showed that the CPU time for 3D simulation was 3113 sec and the estimates of permeability were similar to the ones obtained with our hybrid inversion technique at a much lower CPU time. This comparison shows that our inversion technique is reliable and efficient to estimate formation permeability. In addition, our results could be improved if we included additional loops for 2D minimization and by circumventing the 3D minimization. The total number of function evaluations associated with the hybrid inversion is much higher than the number of function evaluations associated with the 3D inversion. However,

---

[8] Trademark of Intel Inc.

savings in CPU time are achieved because the 2D simulation is much faster than the corresponding 3D simulation. The comparison against 3D simulations is performed only for our Base Case Model. We note that CPU times increase drastically for 3D probe simulations when more time intervals of pressure output are selected and when mud-filtrate invasion is considered in the simulations. Therefore, the hybrid inversion technique becomes more efficient when the complexity of field conditions increases.

### 5.4.2 Effect of 5% Noise in Pressure Transient Measurements

We added 5% zero-mean Gaussian noise to the simulated pressure measurements of the sink probe. The noise amplitude was based on the standard deviation of the measurement. In field applications, it is observed that noise is generally higher at the sink probe than at the observation probe. Based on this observation, we added only 2.5% noise to both observation probes. **Figure 5.5** compares noisy and noise-free pressure differentials at the sink probe.

**Figure 5.6** displays the convergence behavior of the inversion. The cost function asymptotes toward a constant value at the end of each minimization loop. Horizontal permeability in **Table 5.2** is varied by 1.2% and vertical permeability is varied by 7.2%. Although we considered less noise in the observation probes, estimates of vertical permeability are more affected by noise than the estimates of horizontal permeability. This behavior is due to the fact that measurements acquired with both observation probes are significantly affected by noise.

### 5.4.3 Uncertainty in Probe Sampling Flow Rates

In practical applications of formation testing, there are instances in which the measured sampling flow rate is inaccurate. This is likely to occur when sample bottles are filled. We perform the corresponding uncertainty assessment by perturbing sampling rates by ±10%. In the first case, rates increase by 10%, whereas in the second case the rates decrease by 10%. Remaining parameters were the same as those of the Base Case Model. **Table 5.2** shows that the estimates of horizontal permeability can vary by over 10% due to 10% uncertainty in flow rate. However, estimates of vertical permeability vary by only 5% due to 10% uncertainty in flow rate. This behavior is due to the flow regime that is mainly radial during fluid withdrawal because the degree of anisotropy is quite high. If the vertical permeability were higher than the horizontal permeability, this would lead to increased vertical cross-flow during fluid withdrawal thereby causing greater uncertainty in vertical permeability estimates. **Figure 5.7** shows the converge behavior for the case of perturbation of the flow rate by -10%.

### 5.4.4 Uncertainty in Oil Relative Permeability

We perturbed the oil-phase relative permeability to assess the corresponding effect on permeability estimates. The end-point of the oil-phase relative permeability (shown in **Fig. 5.2**) was perturbed by 11%. **Figure 5.8** shows that the end-point for the base case is 0.9 whereas the end-point of the perturbed case is 0.8. Water-phase relative permeability and capillary pressure were not modified for this sensitivity exercise.

**Figure 5.9** displays the corresponding convergence behavior of the inversion. The variation of oil relative permeability leads to a decrease in the oil relative mobility. Because pressure transient measurements depend on the product of relative permeability times absolute permeability, decreasing the mobility leads to an increase of the estimated permeability for the same pressure differential. Therefore, both radial and vertical permeability estimates increase by 11% to offset the decrease of relative permeability. This sensitivity analysis shows that uncertainty in relative permeability can affect the estimates of absolute permeability obtained from WFT measurements. In our sensitivity analysis, we assumed that the formation oil viscosity was known a priori. However, uncertainty in oil viscosity will lead to a similar effect on permeability estimates.

### 5.4.5 Sensitivity to Radial Length of OBM-Filtrate Invasion

We performed a sensitivity analysis on the process of OBM-filtrate invasion by assuming that the near-wellbore region was fully invaded with mud-filtrate to a radial length of 0.42 ft. Invasion is only modeled in the 3D simulations as the 2D simulations assume single-phase flow. Properties of mud-filtrate were previously described in **Table 4.5**. Since both formation oil and oil-base mud filtrate constitute the same phase (i.e., liquid), there is minimal alteration of oil-phase relative permeability. However, early-time oil viscosity, density, and GOR are very sensitive to mud-filtrate invasion. Such properties can vary significantly within the mixing zone (short radial distance into the formation). **Figure 5.10** shows that pressure differential is higher in the presence of mud-filtrate invasion. The change of viscosity modifies the phase mobility with radial distance and, in turn, this affects early-time pressure differentials. At late times, when the near-probe region is cleaned from oil-base mud filtrate, sand-face pressure curves converge because of negligible variation of phase mobility due to low compositional contrasts. We note that time intervals of pressure measurements increased to 122 in panels (a), (b), and (c) as the flow regime becomes more dynamic in the presence of invasion thereby causing the simulator to take smaller time steps.

**Figure 5.11** compares the GOR of our Base Case Model for the present sensitivity analysis. The curvature of the GOR plot is very sensitive to the radial length of invasion and can be used to determine sample quality from WFT measurements. We note that, even after one hour of fluid pumpout, the GOR for the invasion case increases to 2057 SCF/STB whereas the Base Case exhibits a constant GOR equal to 2193 SCF/STB.

Therefore, even a small fraction of mud-filtrate components present in the fluid stream at late times can substantially impact the GOR measurements and hence the sample quality.

**Table 5.2** shows that CPU time for the 3D simulation increases drastically when mud-filtrate invasion is taken into consideration. Each function evaluation of the 3D simulation takes approximately 740 sec. The 3D minimization after inner 2D loops takes 10891 sec of CPU time and decreases the permeability uncertainty by 1.3% vis-à-vis the hybrid minimization. In this instance, we could have achieved further savings of CPU time by stopping the inversion at the end of the 3rd loop or by adding a 4th loop of 2D minimization to prevent the use of a 3D minimization. Even without considering invasion in the 2D simulation, we were able to achieve inversion results within 1.3% of the corresponding results obtained with 3D inversion. This behavior indicates that our inversion technique can be easily extended to single-phase analytical solutions or commercial pressure transient software as an alternative to using the 2D simulation grid.

### 5.4.6 Uncertainty in the Radial Length of OBM-filtrate Invasion

We now consider the hypothetical case in which the inversion is performed without including transient GOR measurements (or, equivalently, by neglecting mud-filtrate invasion effects). To that end, we make use of pressure transient measurements previously simulated for the case of a radial length of invasion of 0.42 ft. **Table 5.2** shows that unaccounted mud-filtrate invasion effects in the near-wellbore region cause significant errors in the permeability estimates. Both horizontal and vertical permeability estimates decrease due to the high-pressure differential. We observe that cost function is excessively large, even after the third minimization loop despite the fact that there is no Gaussian noise present in the measurements.

### 5.4.7 Formation Damage due to Invasion

There are instances in which the near-wellbore permeability decreases locally due to dynamic drilling conditions that cause solid particles to invade the formation along with mud-filtrate. To appraise such a deleterious condition on the inversion of pressure transient measurements, we performed a sensitivity analysis in which we assumed a horizontal permeability of 100 mD at 0.42 feet radially away from the wellbore and 200 mD elsewhere. Vertical permeability was assumed equal to 0.335 times the value of horizontal permeability. Inversion results show that it is difficult to obtain reliable estimates of permeability radially away into the formation in the presence of unaccounted invasion and formation damage. In this case, both the 3D minimization and the hybrid minimization were unable to approach the minimum of the cost function.

### 5.4.8 OBM-Filtrate Invasion in both 2D and 3D simulations

In the previous case of sensitivity on the process of OBM-filtrate invasion, we modeled invasion only in the 3D simulations and the 2D simulations assumed single-phase flow. In this section, we model mud-filtrate invasion in both the 2D and 3D simulations by assuming that the near-wellbore region was fully invaded with mud-filtrate to a radial length of 0.42 ft. **Table 5.3** shows that CPU time for the 2D simulations increase by over 10% in the presence of mud-filtrate invasion. In addition, the minimization achieved with the 2D simulations is inferior to the minimization achieved in the previous case when we did not consider invasion in the 2D simulations. Although, in this example we are honoring the physics by modeling invasion in the 2D simulations, the pressure measurements between the two grids do not correlate well with each other. In the presence of invasion, the probe pressures change with time due to cleanup of the filtrate. The probe pressures are dependent on the formation permeability and increase the non-uniqueness in our transformation vector. Hybrid minimization works better if we do not consider any invasion in the 2D simulations.

### 5.4.9 High Permeability Formation

We consider invasion in a high permeability formation of 500 mD. The formation is assumed isotropic and the radial length of mud-filtrate invasion is 0.42 ft. We did not consider any invasion in the 2D simulations. **Table 5.3** shows that the performance of the hybrid minimization suffers in the presence of invasion for the high permeability formation. The pressure differential in the 2D simulation is much less than the pressure differential in the 3D simulation. We are limited by the commercial simulator as it only outputs 6 decimal places of precision that is used to calculate our cost function and the Jacobian matrix. The results show that it is difficult to obtain good estimates of anisotropy for a high permeability formation using hybrid minimization.

### 5.4.10 Layered and Anisotropic Formation

We assume a three-layer formation model with non-uniform layer thickness of 17 ft, 4 ft, and 21.75 ft from top to bottom of the formation. Observation probes are located at the center of the top two layers. Radial permeability of the layers are 200 mD, 150 mD, and 75 mD from top to bottom, respectively. Anisotropy ratio is assumed 0.335 and porosity is 0.18 for all the layers. Relative permeability and capillary pressure curves were assumed the same for all layers (shown in **Fig. 5.2**). **Figure 5.12** displays the convergence behavior of the multi-layered case. **Table 5.4** describes the values of permeability estimated from inversion. Results from this exercise indicate that our hybrid inversion technique is reliable to estimate the permeability values included in a multi-layer system.

### 5.4.11 Effect of 5% Noise in Pressure Measurements

Similar to the case of adding noise for the Base Case Model, we added 5% Gaussian noise to the sink-probe pressure measurements and 2.5% noise to the observation-probe pressure measurements simulated for the multi-layer formation. **Table 5.4** indicates that the estimated layer permeabilities are marginally affected by presence of noise in the transient pressure measurements.

### 5.4.12 Incorrect Assumption of a Single Layer

In order to quantify the uncertainty in layer permeability, we considered a single-layer formation model for the inversion. Measurements were simulated from the previous case of 5% noise in a three-layer formation model. **Figure 5.13** displays the convergence behavior for this sensitivity case. We note that the cost function is quite high even at the end of the minimization. **Table 5.4** shows that incorrect assumptions about the number of permeability layers drastically affect the estimated values of permeability and anisotropy. The cost function at the end of the minimization is higher than for the previous case of 5% noise. Permeability and anisotropy estimates are quite different from those of the assumed formation. The anisotropy ratio decreases to 0.21 even though the assumed formation had a ratio of 0.335. Therefore, this exercise shows that it is important to include layer boundaries in the vicinity of pressure measurements to secure reliable estimates of permeability and anisotropy.

### 5.4.13 Presence of an Impermeable Bed Boundary

The objective of this exercise is to quantify the effect of unaccounted impermeable beds in the pinversion of pressure transient measurements. To that end, an impermeable bed boundary was included 10 ft below the sink probe. The impermeable zone was modeled with a permeability of 0.01 mD and a porosity of 0.01 units.

Measurements consist of pressure transients simulated for the previously described case of three anisotropic layers. Anisotropy ratio is assumed 0.335 and porosity is 0.18 for all the layers. Pressure differential during drawdown and buildup varies in the presence of a bed boundary with respect to the pressure differential simulated without including the boundary. In addition, as shown in **Fig. 5.14**, the convergence behavior of the inversion is affected by the presence of the bed boundary. This exercise indicates that unaccounted impermeable beds can drastically bias permeability estimates obtained with models that include no such boundaries.

### 5.5 INVERSION EXAMPLE WITH FIELD DATA

**Figure 4.3** shows the lithology and location of the formation test for the example of inversion with field measurements. We only considered field measurements associated with the "Case 1" identified in the same figure. Porosity is approximately 0.28 around this region. The formation consists of shale-laminated sandstone as indicated by the gamma-ray logs. There is a thin limestone bed of 1.8 ft where the neutron porosity decreases sharply and the density increases to 2.65 gm/cm$^3$. The pressure gradient is 0.25 psi/ft, representing a formation with light oil. Formation oil exhibits the same composition as described in **Table 4.4**. Since the $C_1$-$C_4$ content of the in-situ fluid was about 70 mole %, GOR can be used to discriminate between mud filtrate and formation oil. After analyzing the resistivity and density logs, we assumed a single-layer anisotropic formation. Pressure differential measurements were not available at observation probe 2. Therefore, for this example, we only considered measurements acquired with both the sink probe and observation probe 1.

In general, flow rates measured in the field are not constant, and exhibit noise with local fluctuations. There is no need to capture these localized high frequency fluctuations (i.e. noise). Instead, we time averaged the fluid rate to remove noise from the measurements. **Figure 5.15** compares the time-smoothed input flow-rate data in the simulation model against the corresponding field measurements. As can be concluded from this figure, the key to inversion is to preserve the cumulative volumes after the process of time-smoothing. Fluid pumpout starts at 1036 sec in **Fig. 5.15** and continues to 1624 sec producing 0.1228 barrels of fluid. There was a sharp change in flow rate at 1396 sec where the rate increased from 15 barrels/day to 22.4 barrels/day.

Before starting our inversion technique, we determined the radial length of invasion given that the early time behavior in the pressure transient measurements is very sensitive to presence of mud-filtrate. The left-hand panel of **Fig. 5.16** shows the simulated GOR and the field GOR. The simulated GOR was calculated by considering a homogeneous isotropic formation of permeability equal to 100 mD with a radial length of invasion of 1.76 inches. While modeling static invasion for a given radial length of invasion in the formation, we observed that transient GOR measurements do not exhibit much variation with time unless there is at least an order of magnitude difference of permeability. The left-hand panel in the **Fig. 19** also shows that the simulated GOR and field GOR are separated by 22 sec at the onset of fluid withdrawal. This difference is due to the time taken to break the mudcake and for the fluid to move through the WFT. There is an additional time lag in the interpretation of GOR due to the distance of approximately 15 ft that exists between the sink probe and the optical fluid analyzer. In the simulations, GOR is measured at the sink probe itself and, therefore, is initiated slightly before the observed field GOR. The right-hand panel of **Fig. 18** shows that if a time-shift of 22 sec is applied to the simulated GOR curve, it aligns very well with the field measurements. The time lag in the GOR initiation can be regarded a tool storage effect.

**Figure 5.17** displays the pressure differentials measured at the observation and sink probes together with the approximations to the same measurements that were used for inversion. We note that not all the available time samples of pressure were included in the inversion. Field measurements consist of pressure transients sampled at 1 sec intervals. However, executing the simulator to output results every second will make the simulations extremely slow. In addition, pressure measurements exhibit locally abnormal fluctuations and noise due to dynamic field conditions that may not be possible to replicate in the simulations. Therefore, we only attempted to match pressure measurements within critical time intervals and minimized the noise present in those intervals. The simulator automatically chose these critical time intervals as described in a previous section. We note that the inversion of field measurements was not performed in automatic fashion. Quality checks were necessary prior to performing the inversion, including the assessment of the radial length of mud-filtrate invasion and optimal pressure sampling rates.

**Figures 5.18** and **5.19** show the convergence behavior of the hybrid minimization applied to field measurements. In the 3D simulations, we assumed a radial length of invasion of 1.76 inches; however, in the 2D simulations, we did not include an invaded zone. Plots of pressure transients indicate a good agreement between simulated and field measurements. Note that even though the imposed flow rate is constant between 1040 and 1375 sec, the sand-face pressure increases with time. This behavior is attributed to OBM contamination. Specifically, OBM has a higher viscosity than formation oil, and therefore the mobility of the oil phase increases with time due to the corresponding decrease of fluid viscosity when the probe produces clean formation oil. **Table 5.5** summarizes the inversion results obtained with field measurements. The minimization starts with an initial permeability value of 100 mD. We observe a 1.1% improvement in the permeability estimate at the end of the 3rd loop and the last 3D minimization loop. However, CPU times show that the hybrid minimization takes 25% of the CPU time of the last 3D minimization. We performed another inversion with an initial value of horizontal and vertical permeability equal to 100 mD using only the 3D grid model. Results form this latter exercise indicate that the CPU time for 3D simulations was 15798 sec and the estimates of permeability were within 0.07% of those obtained with the hybrid inversion technique with only 15% of CPU time. This comparison confirms that the hybrid inversion technique is reliable and efficient to estimate both permeability and anisotropy.

## 5.6 CONCLUSIONS

The following conclusions stem from the work described in this chapter:

1. Inversion exercises performed on synthetic and field measurements showed that the hybrid minimization method yielded reliable estimates of permeability and anisotropy and was more efficient than the corresponding inversion implemented with 3D simulations. In our 2D grid, we did not model invasion and were still able to obtain reliable permeability estimates, within 2% of target values in most cases and with 20% CPU time of the time required for the inversion with 3D simulations.
2. We performed sensitivity analyses of our inversion technique and observed that estimates of permeability and anisotropy were dependent on specific assumptions made about fluid mobility, i.e. relative permeability and viscosity. Flow rates of fluid withdrawal can drastically affect permeability estimates. Therefore, it is essential to remove noise from field measurements prior to performing inversion to secure reliable and accurate estimates of permeability.

3. Because filtrate viscosity is higher than light-oil viscosity, mud-filtrate invasion can influence the early-time behavior of pressure transients. In such instances, GOR can provide useful information to determine the radial length of invasion.
4. In the case of near-wellbore formation damage due to invasion, it is difficult to obtain reliable permeability estimates. This behavior shows that radially-varying permeability estimates and formation heterogeneity are difficult to diagnose and quantify from pressure transient measurements acquired with a probe-type WFT.
5. The performance of the hybrid inversion technique degrades if we model OBM-filtrate invasion in the 2D simulations. Modeling mud-filtrate invasion increases the computational time of 2D simulations, while pressure measurements do not correlate well with the 3D simulation due to transient variations. In high permeability formations, the pressure drop in 2D simulations is relatively low and the minimization converges to a local minima. We are limited by 6 decimal places of precision when using the commercial simulator and this affects the numerical perturbation required to calculate both the Jacobian matrix and the cost function.
6. Underlying the hybrid inversion method is the assumption that we neglect azimuthal permeability variations. Our algorithm is not reliable if radial permeability is different from azimuthal permeability.
7. We evaluated the hybrid inversion method on field measurements and observed that the estimated values of permeability were within 0.07% of those obtained with the corresponding 3D inversion but within 15% of the CPU time. However, quality checks are necessary to reduce deleterious noise from pressure measurements prior to performing the inversion as well as to determine the associated flow rate of fluid withdrawal and radial length of invasion. We found

that early-time pressure measurements could provide useful information to quantify fluid and formation properties.

Table 5.1: Summary of petrophysical, formation, and simulation parameters for the base-case formation model.

| Parameter | Units | Value |
|---|---|---|
| Horizontal Permeability | mD | 200 |
| Vertical Permeability | mD | 67 |
| Porosity | - | 0.18 |
| Test Duration | sec | 4320 |
| Probe Flow rate | RB/day | 12-18 |
| Irreducible Water Saturation | - | 0.22 |
| Radial length of invasion | inches | 0 |

Table 5.2: Summary of sensitivity analyses performed for the single-layer formation model. Permeability units are in mD and CPU time is in sec. CPU time for 2D loops include the time required for one 3D function evaluation.

| **Sensitivity Parameter** | **Loop 1** | **Loop 2** | **Loop 3** | **3D minimization** |
|---|---|---|---|---|
| **Base Case Model** | $k_H$=250.7 | $k_H$=190.5 | $k_H$=201.1 | $k_H$=200 |
| | $k_V$=60.12 | $k_V$=65.79 | $k_V$=66.84 | $k_V$=67 |
| Cost function | 0.12445 | 0.01083 | $1.02 \times 10^{-4}$ | $6.8 \times 10^{-6}$ |
| Funt. Evals. | 14 | 9 | 7 | 5 |
| CPU time | 445 | 380 | 355 | 1443 |
| **Base Case Model** | - | - | - | $k_H$=200 |
| **(3D ONLY)** | | | | $k_V$=67 |
| Cost function | - | - | - | $8.1 \times 10^{-7}$ |
| Funt. Evals. | - | - | - | 12 |
| CPU time | - | - | - | 3113 |
| | $k_H$=256.3 | $k_H$=184.3 | $k_H$=199.0 | $k_H$=197.6 |
| **Base Case Model** | ±1.35 | ±0.27 | ±0.03 | ±0.001 |
| **(5% Noise)** | $k_V$=56.97 | $k_V$=63.12 | $k_V$=64.28 | $k_V$=62.14 |
| | ±1.17 | ±0.025 | ±0.03 | ±0.001 |
| Cost function | 3.31329 | 3.19986 | 3.20719 | 3.20592 |
| Funt. Evals. | 13 | 13 | 6 | 5 |
| CPU time | 427 | 426 | 339 | 1436 |
| **Flow rate +10%** | $k_H$=283.3 | $k_H$=209.8 | $k_H$=223.6 | $k_H$=221.7 |
| | $k_V$=63.00 | $k_V$=68.8 | $k_V$=70.05 | $k_V$=70.41 |
| Cost function | 0.13967 | 0.01463 | 0.00418 | 0.00419 |
| Funt. Evals. | 14 | 17 | 8 | 8 |
| CPU time | 459 | 479 | 366 | 2167 |
| **Flow rate** | $k_H$=217.9 | $k_H$=171.6 | $k_H$=179.8 | $k_H$=178.6 |
| **-10%** | $k_V$=58.18 | $k_V$=62.07 | $k_V$=62.93 | $k_V$=63.5 |
| Cost function | 0.11531 | 0.01505 | 0.00511 | 0.00465 |
| Funt. Evals. | 14 | 10 | 7 | 5 |
| CPU time | 441 | 412 | 355 | 1452 |
| **Relative Permeability** | $k_H$=293.2 | $k_H$=214.8 | $k_H$=226.4 | $k_H$=225.2 |
| | $k_V$=66.04 | $k_V$=74.19 | $k_V$=75.37 | $k_V$=75.47 |
| Cost function | 0.13239 | 0.00978 | $1.3 \times 10^{-4}$ | $9.4 \times 10^{-6}$ |
| Funt. Evals. | 14 | 9 | 7 | 5 |
| CPU time | 439 | 376 | 352 | 1447 |
| **OBM-filtrate Invasion** | $k_H$=272.2 | $k_H$=188.9 | $k_H$=202.6 | $k_H$=200.0 |
| | $k_V$=75.67 | $k_V$=65.01 | $k_V$=67.18 | $k_V$=67.01 |
| Cost function | 1.30456 | 0.05141 | 0.00254 | $7.9 \times 10^{-6}$ |
| Funt. Evals. | 13 | 13 | 13 | 14 |
| CPU time | 1127 | 1202 | 1111 | 10891 |
| **Invasion Uncertainty** | $k_H$=231.5 | $k_H$=166.6 | $k_H$=173.8 | $k_H$=172.8 |
| | $k_V$=34.62 | $k_V$=35.74 | $k_V$=36.04 | $k_V$=39.84 |
| Cost function | 12.7397 | 13.8576 | 13.4828 | 13.4801 |
| Funt. Evals. | 13 | 15 | 15 | 14 |
| CPU time | 930 | 987 | 990 | 8349 |
| **Formation Damage** | $k_1$=110.9 | $k_1$=110.9 | $k_1$=110.9 | $k_1$=110.9 |
| | $k_2$=166.4 | $k_2$=166.4 | $k_2$=166.4 | $k_2$=166.4 |
| Cost function | 2.08271 | 1.67854 | 1.67854 | 1.67854 |
| Funt. Evals. | 13 | 15 | 15 | 15 |
| CPU time | 1102 | 1331 | 1332 | 14307 |

Table 5.3: Summary of sensitivity analyses performed for the single-layer formation model. Permeability units are in mD and CPU time is in sec. CPU time for 2D loops include the time required for one 3D function evaluation.

| Sensitivity Parameter | Loop 1 | Loop 2 | Loop 3 | 3D minimization |
|---|---|---|---|---|
| **OBM-filtrate Invasion in 2D** | $k_H$=295.5 | $k_H$=176.6 | $k_H$=205.4 | $k_H$=200 |
|  | $k_V$=48.7 | $k_V$=61.07 | $k_V$=64.86 | $k_V$=66.7 |
| Cost function | 2.48489 | 0.82015 | 0.02071 | 0.00663 |
| Funt. Evals. | 13 | 13 | 13 | 14 |
| CPU time | 1211 | 1309 | 1198 | 10760 |
| **High Permeability** | $k_H$=547.7 | $k_H$=531.7 | $k_H$=518.3 | $k_H$=484.2 |
|  | $k_V$=261.6 | $k_V$=271.2 | $k_V$=284.6 | $k_V$=463.1 |
| Cost function | 5.67898 | 1.71181 | 1.50472 | 0.81955 |
| Funt. Evals. | 13 | 13 | 15 | 14 |
| CPU time | 1131 | 1333 | 1362 | 14549 |

Table 5.4: Summary of sensitivity analyses performed for the three-layer formation model. The initial guess of permeability was 100 mD for all cases. Permeability units are in mD and CPU time is in sec.

| Sensitivity Parameter | Loop 1 | Loop 2 | Loop 3 | 3D minimization |
|---|---|---|---|---|
| **Noise free** | $k_1$=211.2 | $k_1$=196.8 | $k_1$=200.3 | $k_1$=200.3 |
|  | $k_2$=157.6 | $k_2$=149.9 | $k_2$=149.7 | $k_2$=149.9 |
|  | $k_3$=65.59 | $k_3$=77.98 | $k_3$=75.25 | $k_3$=75.0 |
| Cost function | 0.03284 | 0.00451 | $1.2\text{x}10^{-4}$ | $3.9\text{x}10^{-6}$ |
| Funt. Evals. | 14 | 9 | 8 | 5 |
| CPU time | 472 | 399 | 384 | 1508 |
| **5% Pressure Noise** | $k_1$=205.7 | $k_1$=197.5 | $k_1$=197.8 | $k_1$=196.2 |
|  | ±1.83 | ±0.33 | ±0.04 | ±0.003 |
|  | $k_2$=148.3 | $k_2$=143.3 | $k_2$=143.8 | $k_2$=144.7 |
|  | ±1.82 | ±0.29 | ±0.04 | ±0.003 |
|  | $k_3$=66.26 | $k_3$=76.76 | $k_3$=74.07 | $k_3$=74.0 |
|  | ±1.77 | ±0.28 | ±0.04 | ±0.003 |
| Cost function | 3.23426 | 3.18783 | 3.19376 | 3.19241 |
| Funt. Evals. | 14 | 10 | 7 | 8 |
| CPU time | 440 | 389 | 351 | 2151 |
| **Assumption of Single Layer** | $k_H$=130.8 | $k_H$=102.0 | $k_H$=105.4 | $k_H$=103.7 |
|  | ±1.22 | ±1.18 | ±0.72 | ±0.15 |
|  | $k_V$=19.67 | $k_V$=19.65 | $k_V$=19.75 | $k_V$=22.32 |
|  | ±1.41 | ±1.23 | ±0.83 | ±0.16 |
| Cost function | 3.40353 | 3.82748 | 3.73181 | 3.71214 |
| Funt. Evals. | 13 | 13 | 7 | 8 |
| CPU time | 430 | 431 | 354 | 2157 |
| **Impermeable Bed Boundaries** | $k_1$=245.0 | $k_1$=215.2 | $k_1$=224.1 | $k_1$=225.3 |
|  | $k_2$=144.2 | $k_2$=139.1 | $k_2$=138.4 | $k_2$=143.2 |
|  | $k_3$=70.12 | $k_3$=80.98 | $k_3$=78.83 | $k_3$=76.63 |
| Cost function | 0.38471 | 0.14009 | 0.21739 | 0.19801 |
| Funt. Evals. | 14 | 14 | 9 | 7 |
| CPU time | 446 | 456 | 381 | 1932 |

Table 5.5: Summary of inversion results obtained with field data acquired in the presence of mud-filtrate invasion for a radial length of invasion equal to 1.76 inches. The initial guess of permeability was 100 mD. Permeability units are in mD and CPU time is in sec. CPU time for a 2D minimization loop includes the time required for one 3D function evaluation. For the case of "3D ONLY" minimization, the starting values of permeability and permeability anisotropy were 100 mD.

| **Parameter** | **Loop 1** | **Loop 2** | **Loop 3** | **3D minimization** |
|---|---|---|---|---|
| **Hybrid Minimization** | $k_H$=278.9<br>$k_V$=154.0 | $k_H$=235.2<br>$k_V$=148.2 | $k_H$=240.7<br>$k_V$=153.0 | $k_H$=240.8<br>$k_V$=154.8 |
| Cost function | 0.16996 | 0.01761 | 0.00741 | 0.00684 |
| Function Evaluations | 13 | 7 | 5 | 16 |
| CPU time | 900 | 762 | 695 | 9477 |
| **3D ONLY Minimization** | - | - | - | $k_H$=240.8<br>$k_V$=153.1 |
| Cost function | - | - | - | 0.00706 |
| Function Evaluations | - | - | - | 27 |
| CPU time | - | - | - | 15798 |

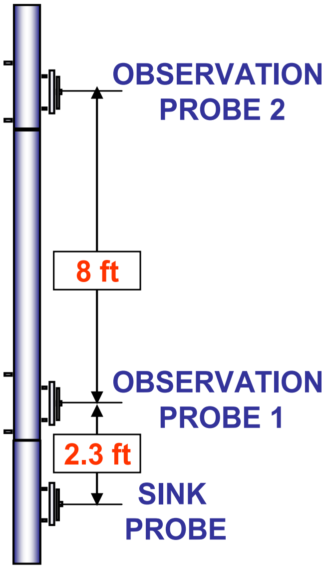

Figure 5.1: Configuration of the probe-type wireline formation tester consisting of two vertical observation probes and one sink probe. The sink probe is located at the center of the numerical grid for all the simulations described in the chapter.

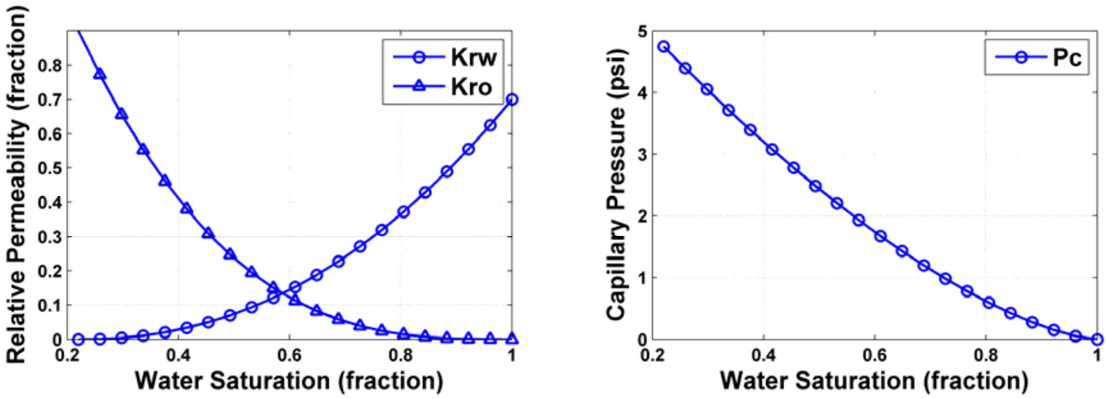

Figure 5.2: Water-oil relative permeability and capillary pressure curves assumed in the numerical simulation of formation-tester measurements described in this chapter.

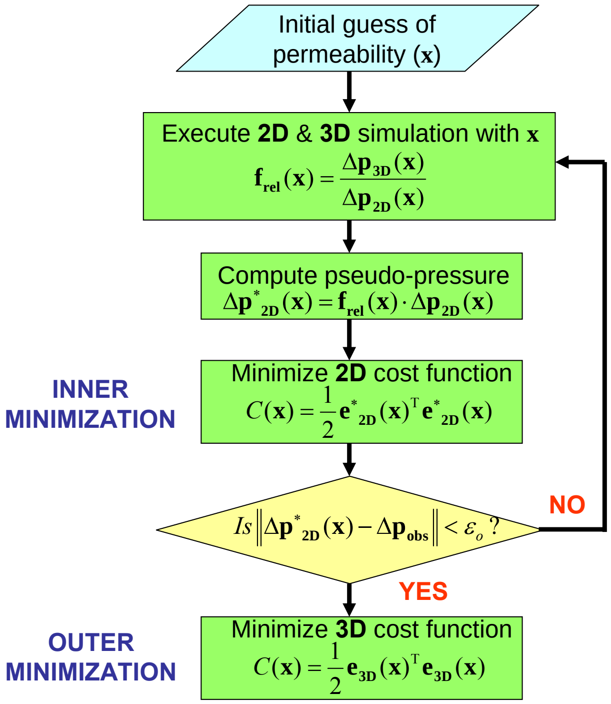

Figure 5.3: Flowchart of the dual-grid hybrid minimization algorithm used in this chapter to estimate permeability and permeability anisotropy from transient pressure measurements. The inner minimization proceeds for a maximum of three loops.

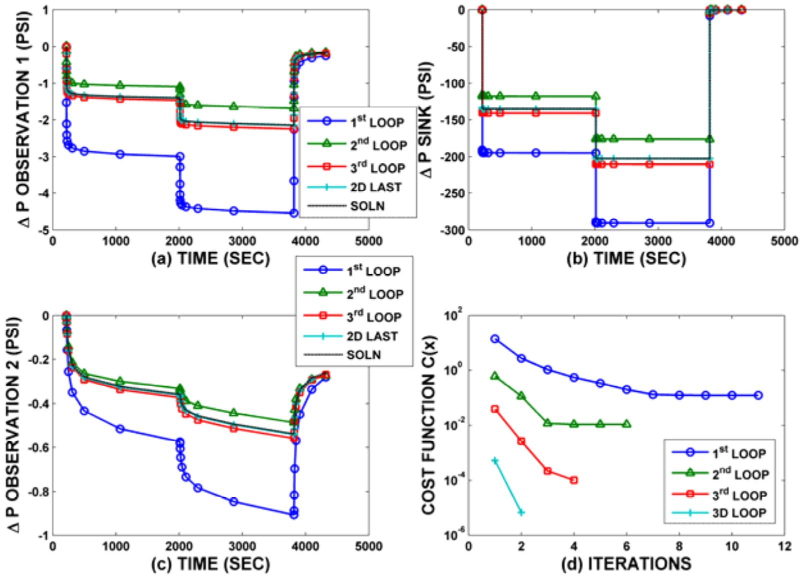

Figure 5.4: Convergence of the hybrid inversion technique for the Base Case Model. Panels (a), (b), and (c) show the pressure at observation probe 1, sink probe, and observation probe 2, respectively, as functions of time. Panel (d) shows the cost function as a function of iteration number.

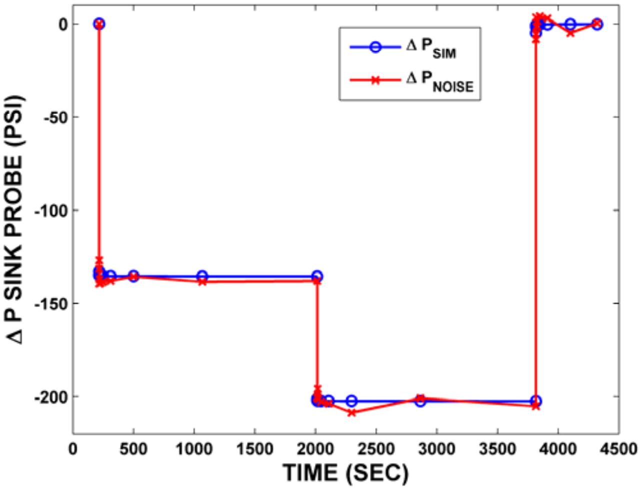

Figure 5.5: Comparison of simulated pressure transients at the sink probe contaminated with 5% additive zero-mean Gaussian noise. By contrast, 2.5% noise was added to the simulated observation probe measurements.

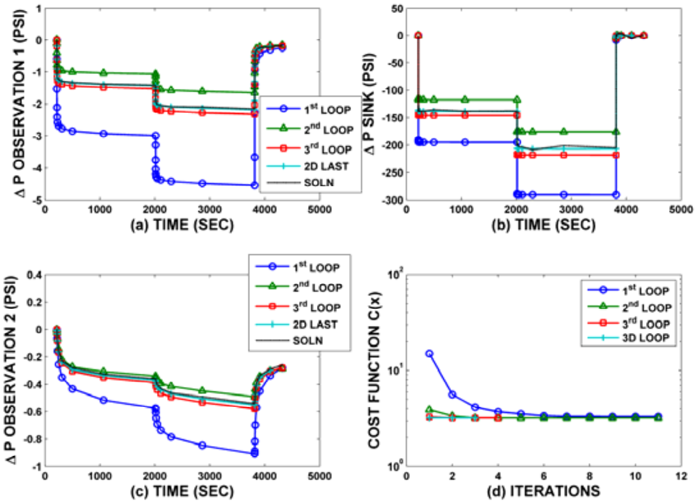

Figure 5.6: Convergence of the hybrid inversion technique for the 5% noise case. The cost function asymptotes toward the same value at the end of all minimizations. Panels (a), (b), and (c) show the pressure at observation probe 1, sink probe, and observation probe 2, respectively, as functions of time. Panel (d) shows the cost function as a function of iteration number.

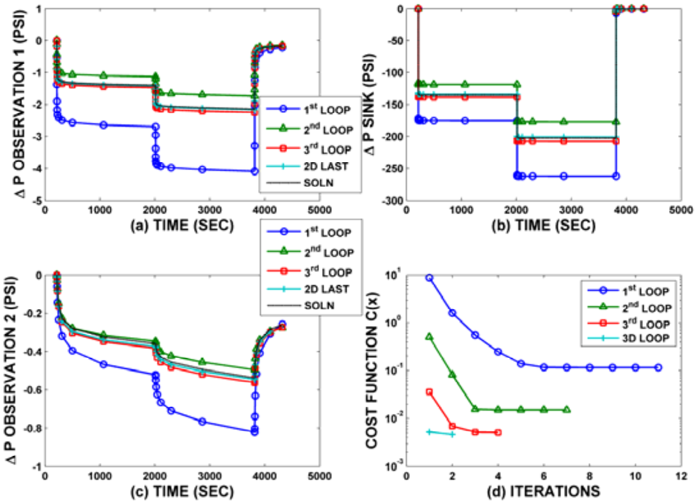

Figure 5.7: Convergence of the hybrid inversion technique for the case of perturbation of the flow rate by -10%. Panels (a), (b), and (c) show the pressure at observation probe 1, sink probe, and observation probe 2, respectively, as functions of time. Panel (d) shows the cost function as a function of iteration number.

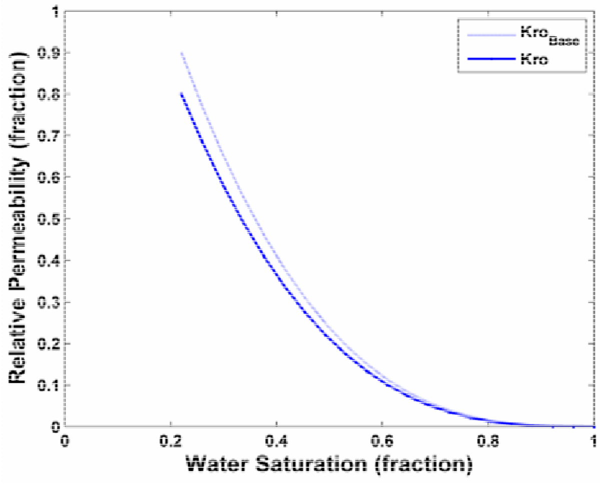

Figure 5.8: Perturbation of the oil-phase relative permeability by 11%. The assumed oil relative permeability end-point was decreased from 0.9 to 0.8.

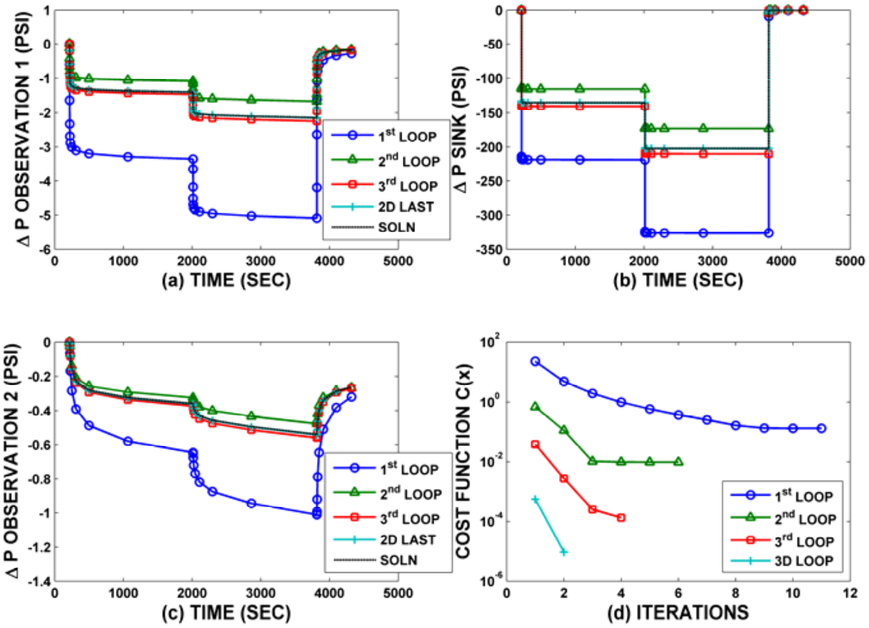

Figure 5.9: Convergence of the hybrid inversion technique for the case of perturbed relative permeability. Panels (a), (b), and (c) show the pressure at observation probe 1, sink probe, and observation probe 2, respectively, as functions of time. Panel (d) shows the cost function as a function of iteration number.

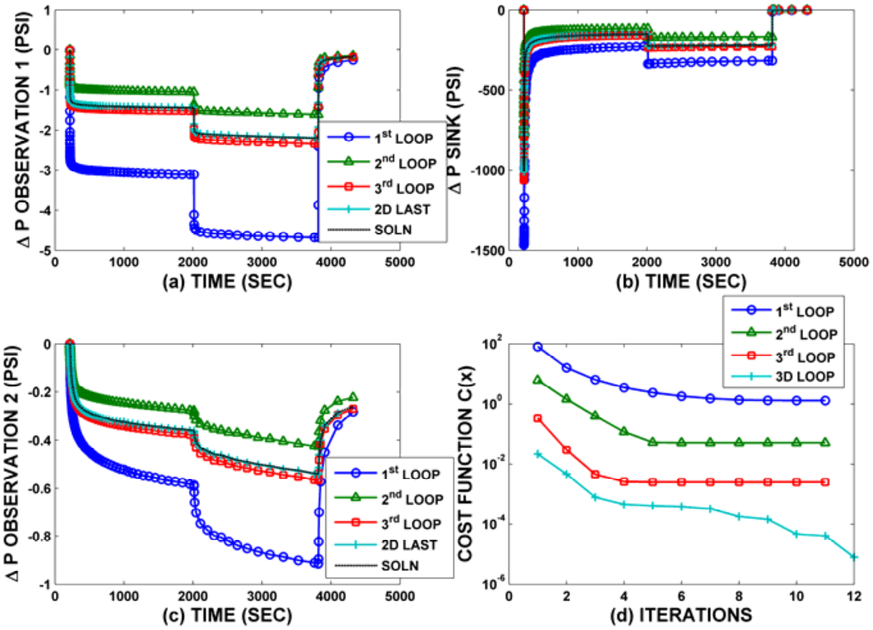

Figure 5.10: Convergence of the hybrid inversion technique with presence of mud-filtrate invasion. Note that the pressure differential in the sink probe at early times is much higher than for the Base Case Model. Panels (a), (b), and (c) show the pressure at observation probe 1, sink probe, and observation probe 2, respectively, as functions of time. Panel (d) shows the cost function as a function of iteration number.

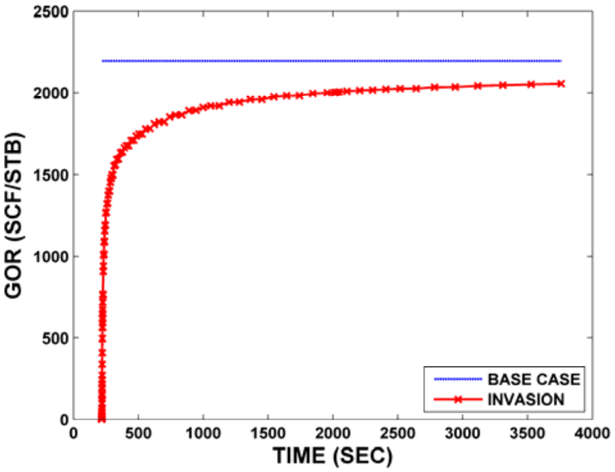

Figure 5.11: Comparison of GOR for the Base Case Model and the case with 0.42 ft radial length of mud-filtrate invasion. The GOR for the Base Case is constant at 2193 SCF/STB because of the absence of invasion.

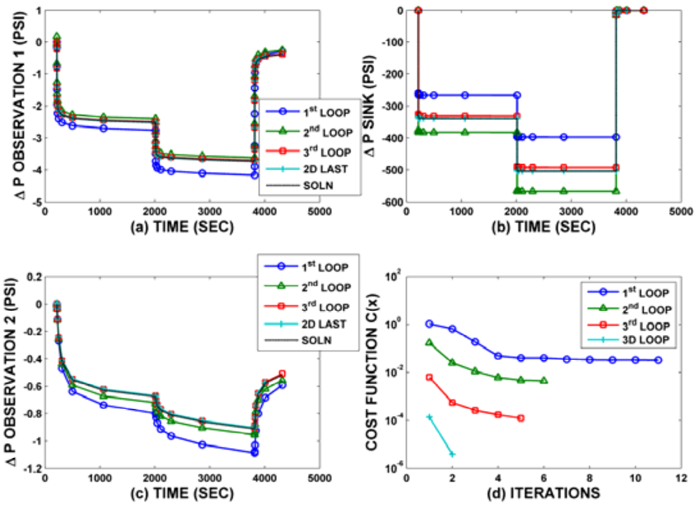

Figure 5.12: Convergence for the three-layer formation model. Pressure differential at the sink probe is relatively high due to the reduced horizontal permeability of 75 mD. Panels (a), (b), and (c) show the pressure at observation probe 1, sink probe, and observation probe 2, respectively, as functions of time.

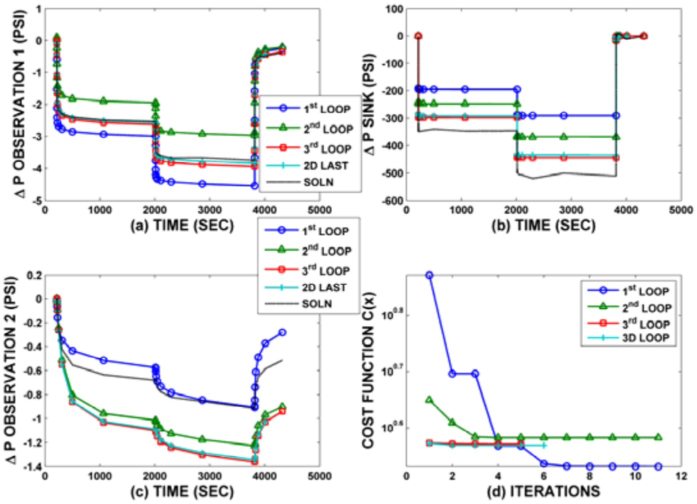

Figure 5.13: Convergence of the hybrid inversion technique for the case of incorrect single-layer assumption for the three-layer formation model and noisy measurements. Panels (a), (b), and (c) show the pressure at observation probe 1, sink probe, and observation probe 2, respectively, as functions of time. Panel (d) shows the cost function as a function of iteration number.

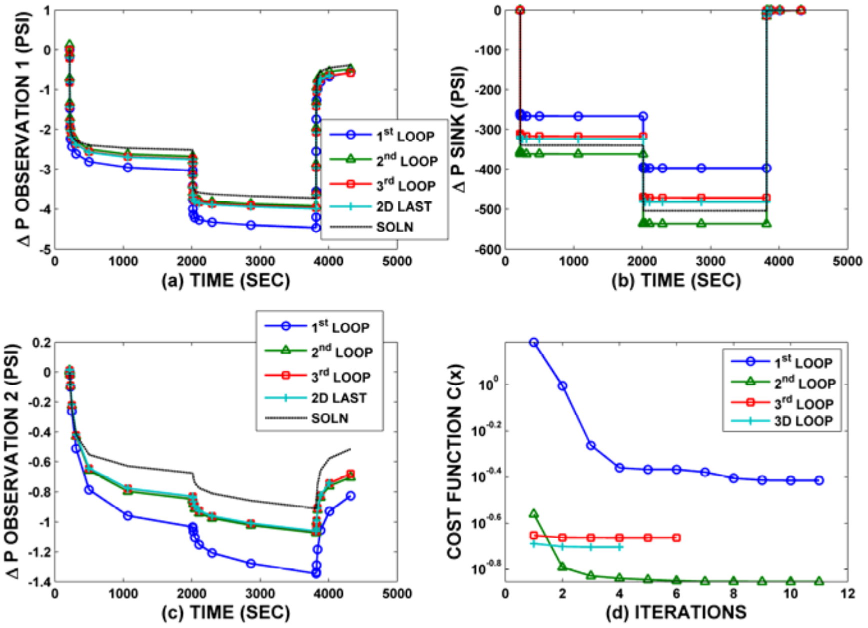

Figure 5.14: Convergence of the hybrid inversion technique for the three-layer formation model with impermeable bed boundaries located 10 ft below the sink probe. Panels (a), (b), and (c) show the pressure at observation probe 1, sink probe, and observation probe 2, respectively, as functions of time. Panel (d) shows the cost function as a function of iteration number.

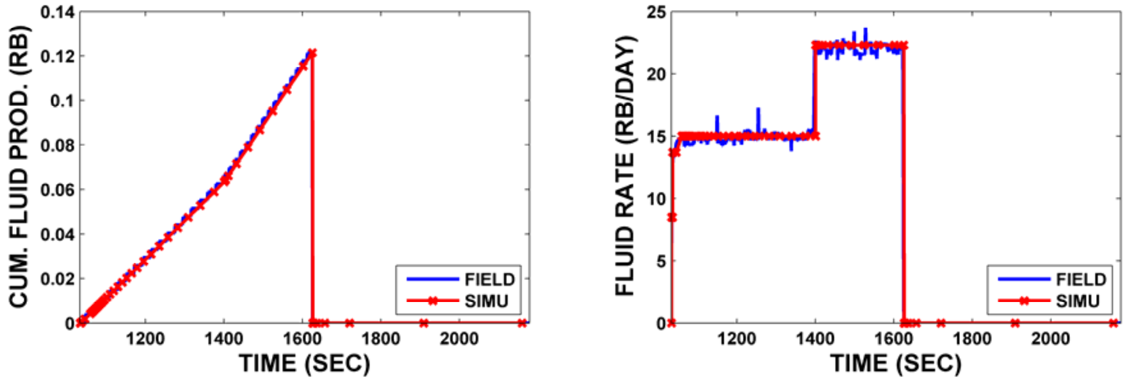

Figure 5.15: Time evolution of simulated probe flow rate (left-hand panel) and cumulative fluid produced at the sink probe (right-hand panel) compared to field data.

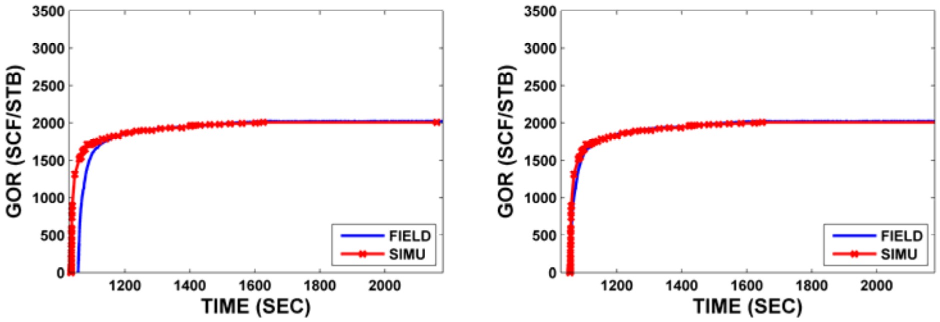

Figure 5.16: Time evolution of simulated GOR and measured GOR. Simulated GOR was calculated assuming a radial length of invasion of 1.76 inches. The right-hand panel shows that GOR curves align very well with each when a time-shift of 22 sec is applied to the simulated GOR curve on the left-hand panel.

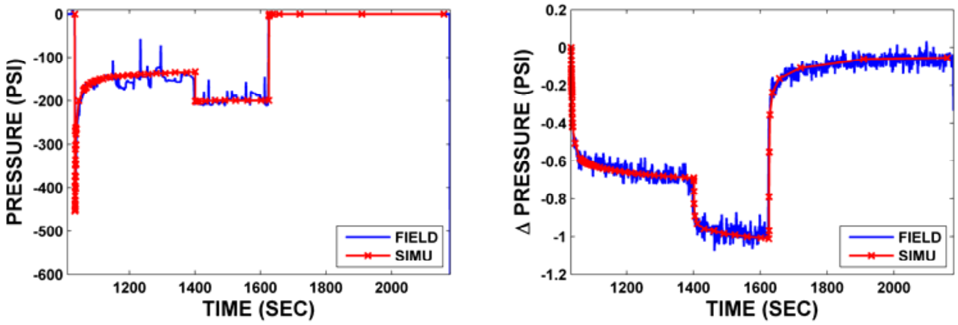

Figure 5.17: Time evolution of transient pressure differentials at the sink probe (left-hand panel) and at the observation probe (right-hand panel). In the two panels, the red curve identifies the approximation to the pressure differential that was used for inversion.

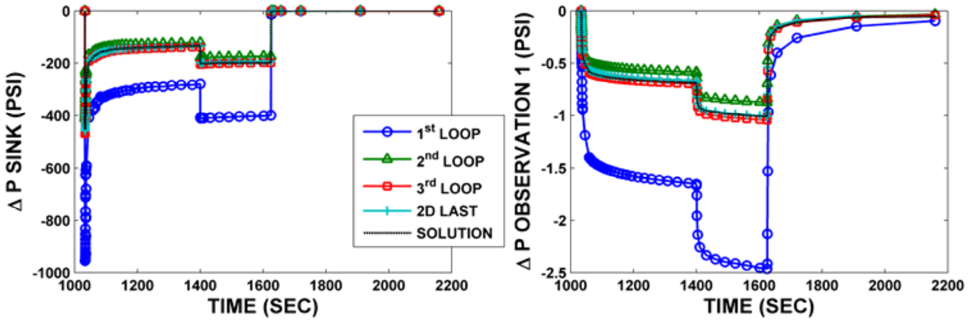

Figure 5.18: Pressure differential at the sink probe (left-hand panel) and at the observation probe (right-hand panel) after a given loop of hybrid inversion.

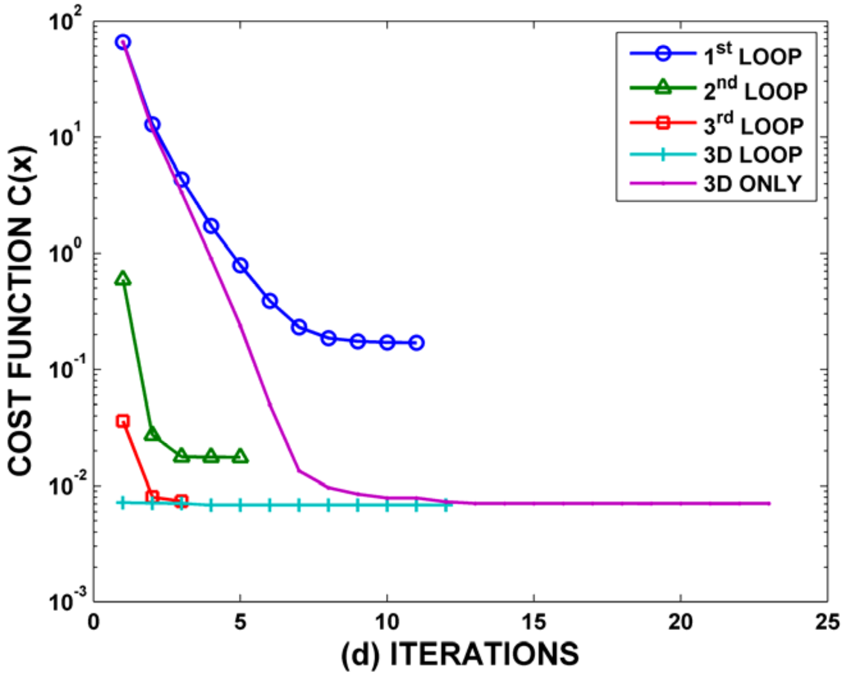

Figure 5.19: Convergence behavior of the cost functions for the hybrid inversion of field data. In the figure, the last loop of the 3D minimization performed at the end of the hybrid minimization is identified as “3D LOOP”. The minimization performed using only the 3D grid with a starting value of permeability of 100 mD is identified as “3D ONLY”.

# Chapter 6: Comparison of Wireline Formation-Tester Sampling with Focused and Conventional Probes in the presence of Oil-Base Mud-Filtrate Invasion

Acquisition of fluid samples is challenging in the presence of oil-base mud (OBM) filtrate invasion due to its partial or full miscibility with reservoir hydrocarbons. In the course of fluid sampling, varying concentrations of OBM will lead to variations of fluid properties such as viscosity, density, and gas-oil ratio (GOR). Contamination of OBM filtrate in the sampled fluid can drastically affect sample quality and lead to non-representative fluid properties. Fluid pumpout time can be extended to reduce filtrate contamination, although at the expense of increasing overall rig cost. A focused probe can be useful in reducing OBM contamination by diverting flow into different channels without compromising fluid pumpout time. However, it is important to properly quantify the relative performance of focused and conventional probes for a wide range of field conditions.

The objective of this chapter is to appraise the performance of different probes under the same simulated field conditions and for a comprehensive set of petrophysical and fluid properties. We simulate the process of fluid sampling with a focused probe in a vertical well and compare its performance to that of a one-inch diameter conventional probe in the presence of mud-filtrate invasion. A commercial adaptive-implicit compositional reservoir simulator is used to model both invasion and filtrate-cleanup processes. Comparison between fluid sampling with focused and conventional probes identifies cases in which focused fluid sampling leads to improved sample quality in a shorter period of time.

Results indicate that sample quality generally improves when the flow is split between the guard and sample probes, but the specific amount of improvement depends on probe geometry, fluid composition, and formation properties. In addition, because the focused probe withdraws fluids through a larger cross-sectional area, the pressure drop caused by the focused probe is smaller than the pressure drop associated with a conventional probe. Permeability anisotropy, presence of a shale boundary, and lack of mud-filtrate invasion can help to improve sample quality. In addition, fluid cleanup can be accelerated by altering both the probe design and the flow-rate ratio between the sample and guard fluid streams thereby leading to increased pressure differential between the sample and guard areas. Performance of the focused probe improves with increasing fluid-front dispersion because focusing enhances the “coning” of the mud-filtrate invasion front.

Lastly, we perform inversion jointly from transient measurements of GOR and probe pressures to estimate formation permeability, anisotropy, and rate of mud-filtrate invasion. It is shown that, in general, focused fluid sampling provides enhanced degrees of freedom in the pressure and GOR transient measurements to improve both accuracy and reliability of the estimated formation properties.

## 6.1 INTRODUCTION

Formation testers are widely used for downhole fluid analysis (Dong et al., 2007) to measure in real time fluid properties such as color, viscosity, density, chemical composition, pH, optical refractive index, and GOR (volumetric gas-to-liquid ratio of crude oil measured at standard conditions of 1 atm and 60 °F). Wireline formation-tester (WFT) measurements remain influenced by the process of mud-filtrate invasion that takes place prior to measurement acquisition (Malik et al., 2007). Consequently, early-time sampling can give non-representative fluid samples due to excessive OBM contamination. On the other hand, extended duration of the test to render clean fluid samples can escalate rig costs and lead to greater chances of the tool being differentially stuck to the borehole wall. Optimizing the time required to obtain clean fluid samples can be challenging due to a variety of circumstances, including the drilling environment, formation properties, and radial extent of mud-filtrate invasion. Alternatively, focused probe-type formation testers can be used to secure clean fluid samples faster than with a conventional probe. Because there is a rubber sealing between the guard and sample regions of a focused probe, OBM- contaminated fluid tends to flow toward the guard region whereas native formation fluids tend to preferentially flow toward the sample probe. Ideally, the guard flow line withdraws OBM filtrate whereas the sample flow line withdraws clean formation fluids. In theory, the physical design of the focused-sampling probe should help to acquire cleaner fluid samples faster especially in the presence of deep OBM-filtrate invasion. If an appropriate pressure differential is maintained, diversion of the fluid stream to different channels can lead to faster cleanup thereby reducing fluid sampling time. However, it is critical to compare the performance of the probes under a variety of petrophysical, fluid, and field conditions to quantify the time improvement in fluid cleanup. Numerical modeling provides a general, efficient, and consistent method to compare the performance of different fluid probes under the same sampling conditions. Moreover, the outcome of such studies can help to optimize fluid sampling operations.

Hrametz et al. (2001) patented the original work on focused fluid sampling. They introduced different geometrical configurations of probes to isolate pressure regions from the borehole fluid. Schlumberger designed the Quicksilver[9] probe to achieve higher-purity fluid sampling in shorter times than with a conventional probe (Weinheber and Vasques, 2006). Akkurt et al. (2006) described several field cases of fluid sampling acquired in light-oil formations drilled with OBM and water-base muds (WBM). Results

---

[9] Trademark of Schlumberger

showed that focusing provided better fluid-sample quality. Due to the higher purity of samples acquired with the Quicksilver probe, Akkurt et al. (2006) indicated that many of the samples they collected had levels of contamination that were “too small to measure.” Kumar et al. (2006) compared the performance of the focused probe against that of a conventional formation tester in high-viscosity oil formations where obtaining representative fluid samples was challenging. They concluded that the focused probe enabled the acquisition of low-contamination fluid samples in typically half the time required by conventional fluid sampling. O’Keefe et al. (2006) described applications of the focused probe in wells drilled in the Norwegian continental shelf for four case studies: (a) oil zone drilled with WBM, (b) water zone drilled with WBM, (c) water zone drilled with WBM, and (d) gas-condensate zone drilled with OBM. They also compared the performance of the focused probe to that of a conventional probe in cases (a), (b), and (c) and concluded that focusing led to faster fluid cleanup. In case (d), they observed 2% contamination in the sample flow line even after 10,200 sec of fluid sampling. In addition, they indicated that contamination was higher in case (d) as the environmental conditions were less conducive to WFT sampling. Alpak et al. (2006) modeled a conventional probe with a compositional equation-of-state (EOS) simulator to compare field examples of sampled-fluid GOR to their simulated GOR. We note that GOR is one of the standard metrics to evaluate fluid sample quality (Mullins et al., 2001). Sherwood (2005) documented the first numerical simulation results that modeled the focused probe to assess optimal probe design for withdrawing uncontaminated fluid samples. In order to derive analytical expressions for fluid cleanup, Sherwood (2005) assumed that mud filtrate and formation fluid were identical and neglected gravity segregation effects in the near-probe flow region. These assumptions were useful in designing optimal probe geometries that could provide lower levels of fluid contamination.

In this chapter, we numerically simulate the process of fluid withdrawal with focused and conventional probes and compare their performance to determine the petrophysical, fluid, and field conditions under which usage of a focused probe can lead to improved fluid cleanup. Fluid properties are modeled in the form of multiple components using a compositional EOS simulator (CMG-GEM[10]). Our compositional model consists of eight pseudo-components: five formation oil components and three oil-base mud-filtrate components, to model accurately the time-space evolution of miscible flow for both invasion and fluid withdrawal. Hydrocarbon-phase compositions are tracked in time using the Peng-Robinson EOS (Peng and Robinson, 1976). Fluid phase density is calculated from the EOS to account for variations of fluid density due to time-space variations of pressure and composition. Moreover, fluid viscosity is calculated with the Lohrenz-Bray-Clark (Lohrenz et al., 1964) correlation to account for time-space variations of fluid composition.

The following section describes our technique for simulating mud-filtrate invasion and formation-tester measurements in the near-wellbore region with a commercial finite-difference compositional simulator. Subsequently, we introduce a base-case light-oil formation model without invasion. Thereafter, we perform sensitivity analyses in the presence of OBM-filtrate invasion to quantify the relative effects of various petrophysical and geometrical variables on the performance of fluid sampling with the focused probe, including permeability, porosity, anisotropy, presence of a shale boundary, rate of mud-filtrate invasion, plugging in the guard region, and presence of movable connate water. We modify the probe design and the ratio of flow rate between the sample and guard fluid streams to appraise improvements in the time evolution of fluid-sample quality. In all of the simulation cases considered in this chapter, GOR is

---

[10] Trademark of Computer Modeling Group Limited

used to evaluate fluid sample quality. Lastly, we perform inversion jointly from transient measurements of GOR and probe pressures to estimate formation permeability, anisotropy, and rate of mud-filtrate invasion. In the first loop of inversion, we estimate the rate of mud-filtrate invasion from GOR measurements. In the second loop of inversion, we estimate permeability and anisotropy from probe pressure measurements. The two-loop minimization approach yields reliable estimates of petrophysical properties. Furthermore, it is observed that measurements acquired with the focused fluid probe provide additional degrees of freedom compared to those of a conventional probe, thus potentially enabling more accurate and reliable estimation of formation properties.

## 6.2 METHOD

The simulation framework employed in this work is similar to the one introduced in chapter 4. **Table 6.1** describes the finite-difference simulation grid, consisting of 29 blocks in the radial ($r$) direction, 33 blocks in the azimuthal ($\theta$) direction, and 40 blocks in the vertical ($z$) direction. At the wellbore, the focused-probe opening is modeled with sixty gridblocks such that the guard opening area is 2.5 times larger than the sample opening area. The sample-probe opening is modeled as a source or a well spread over twenty-four gridblocks with a diameter of approximately one inch. There is a separation of 0.16 inches between the guard region and the sample region where no-flow boundary conditions are enforced in order to model the presence of rubber sealing. We model the conventional probe with the same area as that of the sample line included in the focused probe. **Figure 6.1** is a perspective view of the probe location with respect to the cylindrical grid. There are 9240 gridblocks in a radius of one foot around the probe to properly capture flow dynamics in the near-probe region. Gridblock sizes increase logarithmically in the radial direction starting with 0.165 inches at the wellbore. We use a three-dimensional (3D) grid geometry and make no restricting assumptions regarding spatial symmetry. Moreover, as shown in **Fig. 6.1**, we use a 180-degree azimuthal gridblock behind the probe in order to decrease the CPU time required by the computations.

The process of mud-filtrate invasion is modeled with a volume-averaged flow-rate of mud-filtrate invasion across the borehole wall for 36 hours prior to simulating formation-tester measurements. We assume that invasion is axial-symmetric and that the injected fluid stream includes the component concentrations of oil-base mud filtrate. The outer limits of the reservoir consist of impermeable zones with no- flow boundary conditions. The simulated time evolution of GOR after the onset of fluid withdrawal is very sensitive to the radial length of invasion of oil-base mud. Deep mud-filtrate invasion leads to a slow buildup of GOR whereas shallow mud-filtrate invasion leads to a fast buildup of GOR during fluid sampling with a WFT. In the absence of invasion, GOR remains constant and is equal to the GOR of in-situ fluids.

Subsequently, fluid production is modeled at the probe opening within a time interval of 3 hours. Our model assumes that the volume of mud filtrate invading the formation during sampling is negligible compared to the volume of fluids that have previously entered the formation. Therefore, invasion and fluid-withdrawal processes do not occur simultaneously.

The fluid composition assumed in this chapter is also similar to the one described in chapter 4. **Figure 6.2** shows the Brooks-Corey (Brooks and Corey, 1964) saturation-dependent relative permeability and capillary pressure curves. Initial and irreducible water saturation in the formation is 0.22, whereas irreducible oil saturation is equal to 0.1.

### 6.3 BASE CASE MODEL IN THE ABSENCE OF INVASION

**Table 6.2** summarizes the petrophysical, formation, and numerical simulation properties for the base-case simulation model. The Base Case Model consists of a homogeneous, single-layer isotropic formation. In the focused probe, flow rates at the fluid and guard lines are 2 RB/day[11] and 6 RB/day, respectively, while the corresponding flow rate at the conventional probe is 8 RB/day. The complete duration of the formation test is 3 hours. Therefore, the cumulative fluid produced by both focused and conventional probes is the same and equal to 1 reservoir barrel. We neglect the process of mud-filtrate invasion for the Base Case Model, whereupon the WFT produces fluids from an uncontaminated formation. This exercise is performed with the sole objective of calibrating our simulation model.

**Figure 6.3** and **Table 6.3** show that GOR describes the virgin formation composition for both guard and sample lines of the focused probe. The guard line in the focused probe (**Fig. 6.3**) is identified with the label "guard" whereas the sample line in the focused probe is identified with the label "sample." The one-inch diameter conventional probe, identified with the label "conventional," exhibits the same GOR. This behavior indicates that in either an uncontaminated formation or an underbalanced drilling environment, there is no difference between the performances of focused or conventional probes when used for fluid sampling. Data points yielded by the simulations are non-uniform in time because the fully-implicit compositional simulator can automatically take longer time steps in the absence of mud-filtrate invasion without compromising the numerical accuracy.

### 6.4 BASE CASE MODEL IN THE PRESENCE OF INVASION

This case is different from the Base Case Model as we incorporate the process of OBM-filtrate invasion for a time interval of 36 hours. To that end, we assume a volume-averaged flow rate of invasion that is imposed at the wellbore. Fluid composition of the invaded fluid stream is the same as the composition of mud filtrate shown in **Table 6.1**.

---

[11] One RB/day is equal to 1.8 cc/sec

**Figure 6.4** displays the time-space variations of the $MC_{14}$ fluid component of OBM filtrate that was modeled with an invasion rate of 0.345 $ft^3$/day/ft. The dominant component in the OBM is $MC_{14}$ and hence this component is used to assess radial extent of invasion in the formation. We observe that at 1.5 days after the onset of invasion, the radial length of invasion of that component is approximately 1 ft. This value is consistent with previously documented studies on the subject of mud-filtrate invasion (Wu et al., 2002; Malik et al., 2007).

The left-hand panel in **Fig. 6.5** shows the transient pressure simulated at the sink probe for the duration of the formation test. Initial formation pressure is 6800 psi. We emphasize that, even though the imposed flow rate is constant for the test duration, sandface pressure increases with time. Mud filtrate has a higher viscosity than formation oil thereby leading to a higher drop of formation pressure. As the near-probe region is cleaned up during fluid sampling, OBM-filtrate concentration decreases with time while native fluid concentration increases. Thus, variations of oil viscosity in the sampled fluid affect the transient probe measurements. There is a small pressure difference between the sample and guard flow lines of the focused probe. Moreover, the pressure drop is much higher for the case of the conventional probe because it withdraws fluids from a smaller cross-sectional area. If the formation pressure is close to the bubble point pressure, sampling is more challenging with a conventional probe because the pressure drop will be higher for the same flow rate of fluid withdrawal, whereupon gas will be liberated from the mixture.

Presence of OBM filtrate even in low concentrations influences the GOR of the sampled fluid. Therefore, GOR serves as a good discriminator for fluid-sample quality. The right-hand panel in **Fig. 6.5** displays the transient GOR over the duration of 3 hours of fluid sampling after 36 hours of mud-filtrate invasion. **Table 6.3** describes the GOR at all of the flow lines at the end of 3 hours of fluid sampling. The GOR at the sample line is 2032 SCF/STB whereas the GOR at the conventional probe line is 1851 SCF/STB. Focusing provides an improvement of 181 SCF/STB or 8.2% for the same duration of fluid withdrawal. The time required by the sample line in the focused probe to obtain a GOR of 1851 SCF/STB is 1.16 hours. Thus, using a focused probe for sampling in this case leads to a 58% savings in time compared to the time required when using a conventional probe. The time savings is defined as the reduction in sampling time when using a focused probe such that the measured GOR at the end of fluid sampling is the same with the two probes. The GOR simulated for the probes is in good agreement with the relation

$$GOR_{reg} \approx \frac{GOR_{guard} * Q_{guard} + GOR_{sample} * Q_{sample}}{Q_{guard} + Q_{sample}}, \qquad \ldots(6.1)$$

where the subscripts *reg, guard,* and *sample* identify the GOR for the conventional probe flow line, the guard probe flow line, and the sample probe flow line, respectively, and $Q$ designates the corresponding flow rate of fluid withdrawal (measured in RB/day) at the sample and guard flow lines. **Equation 6.1** indicates that if the sandface pressure is maintained above the dew-point pressure for the duration of fluid sampling, the sample quality produced by the conventional probe will be identical to that of the focused probe when operating in commingled mode. **Equation 6.1** assumes that the flow rate associated with the conventional probe is equal to that of the focused probe.

**Figures 6.6** and **6.7** describe the simulated spatial distribution of the $MC_{14}$ fluid component of OBM in the near-probe region after 5 minutes of fluid sampling. The focused probe withdraws fluids through a larger area (**Fig. 6.6**) compared to the conventional probe. Consequently, mud-filtrate concentration decreases faster in the near-probe region, and the sample line produces relatively cleaner fluid compared to the conventional probe (**Fig. 6.7**). The figures are not symmetric in the vertical direction due to gravity segregation. Streamlines in the near-probe region divert the contaminated fluid to the guard region whereas formation-fluid streamlines converge toward the sample region. Clearly, the guard region establishes a higher intake velocity than the sample region and hence the former provides a preferential path for contaminated fluid. Fluid flow is split into two paths whereby the central sample region is largely isolated from the outer guard region. As emphasized by Kumar et al. (2006), focusing creates a conical fluid-concentration front with mud filtrate moving along the wellbore toward the guard region, whereas formation fluids flow directly into the sample region. This example shows that a focused probe provides better sample quality and contributes to decreasing the cleanup time in the presence of mud-filtrate invasion. However, we note that even after 3 hours of sampling, the GOR increases to 2032 SCF/STB but still remains lower than the pure, native fluid GOR. This behavior is primarily due to the presence of a mixing layer at the interface between the sample and guard areas as well as to the presence of a blind zone on the opposite side of the wellbore. In the next section, we perform perturbations on our Base Case Model (in the presence of invasion) to further quantify the impact of both formation properties and probe design on fluid-sample quality.

## 6.5 SENSITIVITY ANALYSIS IN THE PRESENCE OF MUD-FILTRATE INVASION

We perform a sensitivity analysis of our Base Case Model in the presence of OBM-filtrate invasion. It is important to compare the performance of the focused and conventional probes in different field conditions and to assess the corresponding impact on fluid-sample quality. This sensitivity analysis shows that both probe design and formation properties such as porosity, permeability anisotropy, heterogeneity, shale boundary, and movable water may all substantially affect fluid-sample quality. We also consider possible improvements in the design of focused probes by altering the flow rates in the sample and guard lines, by flow rate pulsing, and by modeling a new focused probe that withdraws fluids through three rather than two fluid channels. In all of the sensitivity cases, GOR is used to quantify sample quality. **Table 6.3** summarizes the GOR simulated in the fluid stream at the end of the fluid sampling operation.

### 6.5.1 Case No. 1: Sensitivity to anisotropy

We consider an anisotropic rock formation by decreasing the vertical permeability to 25 mD. Thus, the anisotropy ratio is 1:10. Remaining simulation parameters are the same as those of the Base Case Model in the presence of invasion. **Figure 6.8** compares the GOR simulated at the focused and conventional probes. The simulated GOR toward the end of sampling is much higher than that of the Base Case in the presence of invasion at all of the simulated probes. **Figure 6.9** shows the simulated spatial distribution of the $MC_{14}$ fluid component of OBM in the near-probe region after 5 minutes of sampling for the anisotropic formation. The diameter of the cone-shaped region has increased in size compared to that of the Base Case Model in the presence of invasion. Thus, we conclude that anisotropy helps to improve sample quality by limiting vertical flow, thereby providing a natural focusing mechanism.

### 6.5.2 Case No. 2: Sensitivity to porosity

We decrease the formation porosity to 0.05. Although porosity and permeability are in general interdependent, in order to quantify the impact of porosity, we did not modify formation permeability. **Figure 6.10** compares the simulated GOR at the probes. The GOR at all of the probes is much lower than shown in **Fig. 6.5** due to the decrease of porosity. **Figure 6.11** shows the simulated spatial distribution of the $MC_{14}$ fluid component of OBM in the near-probe region after 5 minutes of fluid sampling in the low-porosity formation. For a given volume of invasion, decreasing the value of porosity leads to increased dispersion of the fluid-concentration front together with deeper invasion in the formation. Therefore, decreasing porosity leads to poorer fluid-sample quality. We observe that focused fluid sampling provides an improvement in GOR of 9.1% in the presence of a dispersed fluid-concentration front. By contrast, focused fluid sampling is less effective in a high-porosity, high-permeability formation where the fluid-concentration, invasion front exhibits a piston-like shape.

### 6.5.3 Case No. 3: Sensitivity to presence of an impermeable shale boundary

We consider an impermeable shale boundary at the top of the formation where we simulate the formation test. The shale boundary is located 1 foot above the assumed location of the formation tester. We include the shale boundary in the model by assuming a low permeability of 0.1 mD and neglecting invasion in the shale region. **Figure 6.12** indicates that presence of a shale boundary contributes to improving fluid cleanup as the GOR increases to 2081 SCF/STB at the sample line. However, additional simulation exercises indicate that the improvement in fluid cleanup time is negligible when the shale boundary is located 3 feet above the assumed location of the formation tester. In our analysis, the density of mud filtrate is higher than the density of light oil and therefore mud filtrate tends to slump toward the lower part of the formation. This simulation exercise clearly indicates that if the WFT is performed with an impermeable shale layer in close proximity to the tool, fluid contamination will decrease faster than without the presence of that layer.

### 6.5.4 Case No. 4: Sensitivity to flow-rate ratio between guard and sample flow lines

We altered the ratio of flow rate between the guard and sample lines of the focused probe. Changing the flow rate leads to a variation in the pressure differential.

Fluid cleanup can be accelerated if the pressure differential between the guard and sample lines increases. We consider two cases of flow-rate ratios: (a) 4 RB/day[12] in the sample line and 4 RB/day in the guard line (flow-rate ratio of 1:1), and (b) 0.8 RB/day in the sample line and 7.2 RB/day in the guard line (flow-rate ratio of 1:9). The conventional probe flow rate is 8 RB/day, whereupon the cumulative volume of fluid produced is the same for all cases.

The left-hand panel in **Fig. 6.13** shows the simulation results obtained for case (a). Note that, due to the increase in the volume of fluid produced by the sample probe, fluid-sample quality decreases. This behavior may appear counter-intuitive as increasing the flow rate should lead to an improvement in fluid-sample quality. However, the geometry of the focused probe is such that the guard flow line produces mud filtrate. Therefore, decreasing the guard flow rate from 6 RB/day to 4 RB/day leads to poor sample quality. The right-hand panel in **Fig. 6.13** displays the results obtained for case (b). Increasing the guard-line flow rate from 6 RB/day to 7.2 RB/day leads to better fluid-sample quality. By increasing the flow rate in the guard region, we enforce a higher pressure differential and hence cause preferential flow of mud filtrate into the guard region. By contrast, the sample region produces cleaner fluids albeit at a slower flow rate of 0.8 RB/day. This exercise shows that an increase of flow-rate ratio will lead to better fluid sample quality. However, there may be design limitations on the maximum flow rate that the pump can deliver at the guard region. Relatively low flow rates at the sample region will also increase the time necessary to fill large-volume fluid-sample chambers. In ideal conditions, the flow rate could be dynamically adjusted to optimize fluid sampling through a feedback control mechanism in response to differential values of GOR and pressure between the two probes.

---

[12] One RB/day is equal to 1.8 cc/sec

### 6.5.5 Case No. 5: Sensitivity to formation-tester production rates

We assess the effect of gravitational flow on fluid-sample quality by changing the fluid-production rates of the formation tester. To that end, we increase the flow rates by a factor of two and decrease the production time by a factor of two such that the cumulative volume of fluid produced is the same in the two cases. **Figure 6.14** indicates that for practical durations of formation testing there is negligible influence of gravity on the behavior of fluid cleanup.

### 6.5.6 Case No. 6: Sensitivity to pulsing of flow rates

For a conventional probe, sample quality is largely affected by the cumulative volume of produced fluid and is negligibly influenced by flow-rate pulsing (Malik et al., 2007). However, we performed sensitivity analysis on the focused-probe performance to assess whether pulsing between the guard and sample lines could improve fluid sample quality. The left-hand panel in **Fig. 6.15** shows that flow rates are pulsed in a step-wise manner. Initially, all of the fluid is produced through the sample line in order to decrease mud-filtrate contamination from the near-probe region. We gradually decrease the flow rate in the sample line and increase the flow rate in the guard line. During this transition, the total flow rate is the same as that of a conventional probe and is equal to 8 RB/day. The right-hand panel of **Fig. 6.15** indicates that sample quality improves due to pulsing of the rates between the guard and sample flow lines. **Table 6.3** shows that the sampled GOR of 2048 SCF/STB is higher than the sample GOR associated with the Base Case in the presence of invasion (2032 SCF/STB). However, the sampled GOR is lower than in the sensitivity case with a flow-rate ratio of 1:9. For the cases in which there is a limitation on the maximum flow rate delivered by the pump, pulsing of the flow rates becomes a practical alternative to improve fluid-sample quality.

### 6.5.7 Case No. 7: Sensitivity to commingled flow

We studied commingled flow to quantify the effect of combining the fluid sampled at both the sample and guard lines on the measured GOR. **Figure 6.16** indicates that there is no improvement in fluid cleanup time over that of a conventional probe if the flow is commingled. The advantage of focused fluid sampling arises because of the splitting of flow into different fluid channels. Therefore, it is important either to use two downhole fluid analyzers or to measure the GOR from the sample line separately.

### 6.5.8 Case No. 8: Sensitivity to flow in three fluid-collection channels

We modeled the design of an alternative probe that could withdraw fluids through three fluid channels as opposed to the two channels included in the commercial focused probe. The assumed third fluid channel comprises the region between the guard and the sample probe, with a flow rate equal to 0.8 RB/day in the sample line, 1.6 RB/day in the middle flow line, and 5.6 RB/day in the outer guard flow line. **Figure 6.17** indicates that using three fluid channels leads to improved sample quality; the value of GOR is 2071 SCF/STB at the end of sampling. However, withdrawing fluid through three channels imposes a design limitation, as it requires an additional fluid-flow line and a pump to withdraw fluids. In addition, due to the absence of insulation between the guard and sample lines, fluid streamlines can be altered and, consequently, mud filtrate may flow toward the sample line.

### 6.5.9 Case No. 9: Sensitivity to partial plugging in the guard flow line

In all of the previous cases, we assumed ideal field performance of the fluid probes. However, in field applications there are instances when plugging of the probes may occur. This problem can be critical for the focused probe as it withdraws fluids through several small openings that could be blocked by particles and fines. In this sensitivity analysis, we model a partially-blocked focused probe by allowing fluid flow only into the lower half of the guard region; the upper half does not withdraw fluids. However, the flow rate from the lower region is the same as that of the Base Case in the presence of invasion (6 RB/day).

**Figure 6.18** shows the simulated transient GOR measurements. In this case, the sample region is in hydraulic communication with mud filtrate entering the upper region as the partially plugged guard region does not provide insulation. Thus, the sample GOR is lower than the guard GOR and fluid sample quality is poorer in the sample line. If the flow from the sample line is used to fill sample bottles, then the quality of the samples will be inferior to that of samples acquired with a conventional probe. This exercise indicates that the performance of the focused probe can vary with realistic field conditions in which mudcake could cause some degree of plugging in the guard region.

### 6.5.10 Case No. 10: Sensitivity to the rate of mud-filtrate invasion

We decreased the flow rate of mud-filtrate invasion by a factor of two, to 0.1725 $ft^3$/day/ft, in order to assess the corresponding effect on overbalance pressure. All of the remaining simulation parameters were kept the same as those of the Base Case Model. Radial length of invasion decreases to 0.6 ft with the corresponding decrease of invasion rate. Accordingly, **Figure 6.19** shows that the simulated GOR in all of the probes is much higher than for the Base Case in the presence of invasion. By decreasing the rate of mud-filtrate invasion, the volume of mud filtrate invading the formation decreases and this expedites the acquisition of clean fluid samples. Overbalance pressure controls the rate of mud-filtrate invasion; low overbalance pressure leads to relatively shallow invasion.

### 6.5.11 Case No. 11: Sensitivity to formation fluids

In this case, we modify the native formation fluid to heavy oil (GOR 93 SCF/STB) in order to quantify the effect of fluid cleanup in the near-wellbore region. Heavy oil has a viscosity of 8.8 cp and a density of 0.85 g/cc. **Figure 6.20** shows that the simulated GOR in all the probes is much lower than for the Base Case in the presence of invasion. An increase in the viscosity of formation oil leads to increased dispersion of the fluid concentration front. Focused fluid sampling provides an improvement of cleanup time of 11.4% and is advantageous over conventional fluid sampling in the presence of a dispersed fluid concentration front wherein fluid coning becomes dominant. The mobility contrast between formation fluid and mud filtrate plays an important role in fluid-sample quality. Increasing the viscosity contrast may help to provide better fluid-sample quality. However, we warn that in the case of gas formations invaded with OBM filtrate, the increased viscosity contrast may lead to sudden non-Darcy flow during gas breakthrough.

### 6.5.12 Case No. 12: Sensitivity to movable water

In field applications, there are instances when a formation test is performed within a capillary transition zone with movable water. We consider a movable-water zone with initial saturation equal to 0.5. The objective of this case of study is to quantify the influence of mobile water in the time evolution of GOR during fluid withdrawal. **Figure 6.21** indicates that the simulated GOR in all the probes is much lower than that of the Base Case in the presence of invasion. Fluid-sample quality deteriorates in the presence of mobile water due to the interplay of relative permeability, capillary pressure, and mud filtrate in a capillary transition zone. **Figure 6.22** shows the simulated spatial distribution of the $MC_{14}$ fluid component of OBM in the near-probe region after 5 minutes of fluid sampling. The diameter of the cone-shaped region is much smaller than that of the Base Case Model in the presence of invasion. However, we observe that when fluid flow is split into two paths, fluid coning is effective in the presence of a dispersed saturation front thereby improving the GOR by 10.1% at the end of the sampling operation.

## 6.6 INVERSION OF MUD-FILTRATE INVASION RATE AND PERMEABILITY FROM TRANSIENT MEASUREMENTS OF PRESSURE AND GOR

Compared to conventional fluid-probe sampling, focused fluid sampling provides enhanced degrees of freedom in pressure and GOR transient measurements because it withdraws fluids through two fluid channels instead of one. Therefore, when used to estimate underlying petrophysical properties, the additional information provided by focused fluid-sampling probes should improve both the reliability and accuracy of the estimated properties.

We implement a general nonlinear least-squares inversion method (Madsen et al., 2004) for the estimation of permeability, anisotropy, and rate of mud-filtrate invasion from both focused and conventional fluid-sampling probes using a two-loop minimization approach. The quadratic cost function used for the estimation (inversion) quantifies the misfit between measured and simulated transient pressure and GOR. We apply nonlinear inversion to estimate petrophysical properties associated with our Base Case Model by minimizing the cost function.

### 6.6.1 Cost Function

The quadratic cost function used for inversion quantifies the relative difference between simulated and measured pressure and GOR differences, and is defined as

$$C(\mathbf{x}) = \frac{1}{2}\sum_{i=1}^{m}(e_i(\mathbf{x}))^2, \qquad \ldots(6.2)$$

where $m$ is the number of measurements and $e_i(\mathbf{x})$ is the dimensionless data residual that measures the relative difference between the numerically simulated and observed measurements. There is no regularization parameter in the cost function. Permeability, anisotropy, and flow rate of mud-filtrate invasion are all included in vector **x**, and given in arithmetic rather than logarithmic values. Additional technical details about the inversion algorithm can be found in chapter 5.

### 6.6.2 Two-loop Minimization

The minimization algorithm estimates permeability, anisotropy, and flow rate of mud-filtrate invasion by simultaneously honoring both transient pressure and GOR measurements at the probes. Pressure measurements are simulated at the sink and observation probes that are offset 2.6 ft and 8 ft above the sink probe to estimate permeability and anisotropy. In addition, we use the transient GOR measurements acquired at the sample and guard lines of the focused probe to estimate flow rate of mud-filtrate invasion.

**Figure 6.23** is a flowchart of the inversion procedure. While performing the inversion, we observed that simultaneously estimating all transient measurements increases non-uniqueness and leads to poor convergence. To circumvent this problem, we implemented the inversion with two nested loops: in the first loop, we estimate only the rate of mud-filtrate invasion from transient GOR measurements; in the second loop, we estimate permeability and anisotropy from transient pressure measurements. Joint inversion is essential to improve the reliability of the estimation as pressure and GOR transients are interdependent on both rate of mud-filtrate invasion and permeability. Therefore, the inverted rate of mud-filtrate invasion from the first loop is input to the second loop to improve the estimation of permeability and anisotropy. Subsequently, the inverted permeability and anisotropy from the second loop are input to the first loop to improve the estimation of rate of mud-filtrate invasion. The inversion stops when the misfit between simulations and measurements is below a certain threshold; otherwise, we repeat the two-loop minimization until achieving the required data misfit.

Experience with this inversion procedure indicates that final estimates can be obtained with at most two iterations between inner and outer loops. An underlying assumption for inversion is that fluid sampling measurements are available to yield PVT properties of both mud filtrate and in-situ fluid components. In addition, we assume *a-priori* knowledge of porosity, relative permeability, capillary pressure, and initial water saturation.

**Table 6.1** describes the finite-difference grid implemented for inversion. By contrast, the simulation grid used to generate the synthetic measurements is much finer, consisting of 36 blocks in the radial ($r$) direction, 41 blocks in the azimuthal ($\theta$) direction, and 70 blocks in the vertical ($z$) direction. Thus, the spatial resolution of the simulation grid is approximately three times the spatial resolution of the inversion grid. Increased spatial resolution of the simulation grid is necessary to offset potential favorable biases in the calculation of data misfit (hence overly optimistic inversion results).

### 6.6.3 Application of Inversion

We applied the inversion algorithm to our Base Case Model in the presence of invasion. **Table 6.4** summarizes the estimated properties with both noise-free and noisy synthetic measurements. The starting guess for permeability was 150 mD for both horizontal and vertical permeability, whereas the starting guess for rate of mud-filtrate invasion was 0.023 ft$^3$/day/ft. Results show improved estimation of flow-rate of invasion with the focused probe as it withdraws fluids through two fluid channels and therefore augments the redundancy of input data available for inversion.

One limitation of the compositional simulator used for inversion is that it provides only six significant decimal figures of accuracy. Because the focused probe withdraws fluids through a larger cross-sectional area compared to that of a conventional probe, the pressure differential caused by the focused probe is lower than that caused by the conventional probe. Consequently, the lower pressure differential simulated at the focused probe could increase non-uniqueness of the estimations under finite numerical accuracy. Experience shows, however, that the additional information provided by the two flow lines offsets the limitations of numerical accuracy.

**Figure 6.24** shows the sample-line GOR (left-hand panel) and the pressure drop for the sample probe (right-hand panel) at the start and end of the two-loop minimization performed with the focused probe. Both GOR and pressure transients converge toward the final noise-free minima with consecutive minimization loops. **Figure 6.25(a)** indicates that the corresponding cost function decreases as the number of iterations increases for all successive minimization loops. Convergence from GOR is faster in the second minimization loop than in the first loop because of improved estimation of the rate of mud-filtrate invasion, permeability, and anisotropy. **Figure 6.25(b)** displays the evolution of the cost function with iteration number when the inversion is performed with measurements acquired with a conventional probe.

Comparison of the panels shown in **Fig. 6.25** indicates an order of magnitude difference in the cost function for the second GOR minimization loop with the two probes. Measurements acquired with the guard and sample lines included in the focused probe improve both accuracy and reliability of the estimated formation properties by providing additional degrees of freedom to the estimation. Because the early-time pressure response is dependent on mud-filtrate invasion, inaccurate estimation of invasion affects the reliability of permeability obtained from pressure measurements (first inner loop).

## 6.7 DISCUSSION

In general, a focused probe will reduce OBM contamination in fluid samples by splitting flow streamlines into different fluid channels without compromising pumpout time. In addition, the focused probe enables efficient downhole fluid analysis by achieving lower contamination levels more rapidly. Comparison of simulated spatial distributions of mud filtrate for both focused and conventional probes (**Figs. 6.6, 6.7, 6.9, 6.11,** and **6.22**) helped us to analyze the corresponding variations of fluid streamlines in the near-probe region. We conclude that focused fluid sampling is clearly advantageous over conventional sampling in the presence of dispersed fluid concentration and saturation fronts and whenever fluid coning is dominant (**Figs. 6.11** and **6.22**). By contrast, in the presence of a piston-like displacement front, focused sampling provides marginal time savings over conventional fluid sampling. Sharp fluid concentration fronts can arise in high-permeability formations or in the presence of high mobility contrasts, such as those associated with low-viscosity, gas-bearing formations or with the presence of vertically bounding sealing features.

In all of the simulations, formation fluids were flowing above the saturation pressure in a single hydrocarbon phase. If the sandface pressure falls below the saturation pressure, fluids will preferentially flow in two hydrocarbon phases and will alter the flow streamlines, with heavier components in the oil-rich phase and lighter components in the gas-rich phase. Fluid-component streamlines will have different velocities in each phase that will be governed by relative mobility of the two hydrocarbon phases. Therefore, GOR of the two flowing phases will be non-representative of virgin fluid GOR. Simulations in the presence of movable water also indicated that focused sampling was less effective when the movable phases were flowing at different velocities.

The mud-filtrate invasion process described in this chapter is based on the assumption of a radial formation model penetrated by a vertical well. Field examples show that eccentric invasion profiles are common in deviated and horizontal wells, but the scope of our work was limited to understanding the invasion process in a vertical well. All the simulations with the focused probe indicated improved fluid cleanup compared to a conventional probe. The actual performance of the focused probe will vary even more significantly under field conditions due to spatial heterogeneities, blocking at one of the probes, or malfunctioning of one of the pumps

Simulations described in this chapter considered a constant flow rate in both guard and sample flow lines of the focused probe. Ideally, the flow rates should be adjusted automatically in response to differential values of GOR and pressure between the two probes to optimize fluid sampling. Such a dynamic feedback loop could lead to improved fluid-cleanup time under a wide range of formation and fluid conditions. Currently, measurement acquisition is only achievable manually by monitoring the fluid-analyzer and pressure-gauge responses and by adjusting the pump outputs during the progress of sampling stations.

## 6.8 CONCLUSIONS

The following concluding remarks stem from the comparisons of simulations performed with focused and conventional probes considered in this chapter:

1. The quality of hydrocarbon samples acquired in the presence of mud-filtrate invasion improves when using a focused-probe geometry and when GOR is measured separately on fluids flowing through the sample and guard areas. On average, our numerical simulations indicated 58% time savings when using a focused probe. When the focused and conventional probes withdrew fluids during the same period of time, focused fluid sampling provided an average improvement in sample quality of 8.2%. The efficiency of fluid cleanup depends on both probe geometry and formation properties that can alter flow streamlines, including porosity and presence of movable water. It was found that focusing becomes more effective in the presence of dispersed invasion fronts. Sharp

invasion fronts due to high mobility contrasts between mud filtrate and formation hydrocarbons decreased the utility of focused fluid sampling.

2. Anisotropy, impermeable shale boundaries, and thin beds provide a natural focusing mechanism for formation fluids. Thus, in such cases the advantage of using a focused probe over a conventional probe will be reduced, and a conventional probe becomes the most economical alternative to fluid sampling.
3. Optimizing the flow-rate ratio between the sample and guard probes can help to expedite fluid-sample quality by causing preferential flow of mud filtrate into the guard region. However, design restrictions may limit the maximum flow rate that can be used to withdraw fluids by the guard pump.
4. Pulsing of the flow rates between the guard and sample regions can help to improve sample quality by gradually increasing the flow rate at the guard line. Withdrawing fluids through three channels as opposed to the two channels used in the focused probe may also help to improve sample quality because the cleaner fluid preferentially flows through the sample line. Sample quality may decrease with a focused probe if mud plugging occurs in the smaller openings of the guard region.
5. Inversion exercises performed on synthetic measurements indicated that the two-loop minimization method yields reliable estimates of permeability, anisotropy, and rate of mud-filtrate invasion. Results show improved estimation of invasion with the focused probe as it withdraws fluids from two channels, thereby increasing the redundancy of input data available for the estimation.

Table 6.1: Summary of geometrical and numerical simulation parameters assumed for all cases considered in this chapter.

| Parameter | Units | Value |
|---|---|---|
| Wellbore radius ($r_w$) | ft | 0.354 |
| External radius ($r_e$) | ft | 300 |
| Reservoir thickness | ft | 43.4 |
| Number of nodes - radial axis | -- | 29 |
| Number of nodes - azimuthal axis | -- | 33 |
| Number of nodes - vertical axis | -- | 40 |
| Grid cell size - r | ft | Variable |
| Grid cell size - θ | degrees | Variable |
| Grid cell size - z | ft | Variable |

Table 6.2: Summary of the assumed petrophysical and fluid properties for all simulation cases considered in this chapter.

| Property | Units | Value |
|---|---|---|
| Initial water saturation | Fraction | 0.22 |
| Water compressibility | 1/psi | $3\text{x}10^{-6}$ |
| Porosity | Fraction | 0.275 |
| Horizontal permeability | mD | 250 |
| Vertical permeability | mD | 250 |
| Mud-filtrate invasion duration | Hours | 36 |
| Mud-filtrate viscosity | cp | 1.8 |
| Mud-filtrate density | g/cc | 0.8 |
| Formation-test duration | Hours | 3 |
| Conventional-probe flow rate | RB/Day | 8 |
| Focused-probe flow rate | RB/Day | 6 |
| Sample-probe flow rate | RB/Day | 2 |
| Invasion flow rate | $\text{ft}^3$/day/ft | 0.345 |
| Temperature | °F | 140 |
| Formation pressure | psi | 6800 |
| Formation compressibility | 1/psi | $10^{-8}$ |
| Light-oil density | g/cc | 0.60 |
| Light-oil viscosity | cp | 0.36 |
| Light-oil gas-oil ratio | SCF/STB | 2200 |
| Heavy-oil density | g/cc | 0.85 |
| Heavy-oil viscosity | cp | 8.8 |
| Heavy-oil gas-oil ratio | SCF/STB | 93 |

Table 6.3: Summary of final GOR values in SCF/STB obtained at the end of fluid sampling for all the simulation cases considered in the chapter. Fluid sampling time was three hours for all the cases of study.

| Sensitivity Case | Guard GOR | Sample GOR | Conventional GOR | Time Savings | Increase in GOR |
|---|---|---|---|---|---|
| Base Case, No Invasion | 2200 | 2200 | 2200 | 0 % | 0 % |
| Base Case, Invasion | 1794 | 2032 | 1851 | 58 % | 8.2 % |
| Anisotropic Formation | 1987 | 2161 | 2027 | 78 % | 6.1 % |
| Low Porosity | 1522 | 1787 | 1586 | 36 % | 9.1 % |
| Shale Boundary | 1904 | 2081 | 1946 | 52 % | 6.1 % |
| Flow-Rate Ratio (1:1) | 1741 | 1968 | 1851 | 44 % | 5.3 % |
| Flow-Rate Ratio (1:9) | 1827 | 2077 | 1851 | 66 % | 10.2 % |
| Production Rate | 1794 | 2032 | 1851 | 57 % | 8.2 % |
| Pulsing of Rates | 1806 | 2048 | 1851 | 40 % | 8.9 % |
| Commingled Flow | 1851 | 1851 | 1851 | 0 % | 0 % |
| 3-Channel Flow | 1792 | 2071 | 1851 | 66 % | 10.1 % |
| Plugging in Guard | 1876 | 1775 | 1851 | 0 % | -3.5 % |
| Invasion Rate | 1983 | 2133 | 2019 | 72 % | 5.2 % |
| Heavy Oil | 70.5 | 84.6 | 74.1 | 49 % | 11.4 % |
| Movable Water | 1606 | 1901 | 1678 | 44 % | 10.1 % |

Table 6.4: Summary of inversion results for mud-filtrate invasion and permeability. The rate of mud-filtrate invasion is given in ft3/day/ft and permeability is given in mD.

| Case | Inversion Loop | $k_h$ | $k_v$ | Invasion Rate |
|---|---|---|---|---|
| Focused Probe (no noise) | GOR Loop 1 | | | 0.325 |
| | Pressure Loop 1 | 245.5 | 201.4 | |
| | GOR Loop 2 | | | 0.344 |
| | Pressure Loop 2 | 249.4 | 201.6 | |
| Conventional Probe (no noise) | GOR Loop 1 | | | 0.323 |
| | Pressure Loop 1 | 251.6 | 228.1 | |
| | GOR Loop 2 | | | 0.335 |
| | Pressure Loop 2 | 248.1 | 225.7 | |
| Focused Probe (5% noise) | GOR Loop 1 | | | 0.323±0.005 |
| | Pressure Loop 1 | 242.2±1.32 | 208.5±1.32 | |
| | GOR Loop 2 | | | 0.337±0.021 |
| | Pressure Loop 2 | 246.2±1.53 | 194.8±1.55 | |
| Conventional Probe (5% noise) | GOR Loop 1 | | | 0.321±0.002 |
| | Pressure Loop 1 | 247.4±0.57 | 161.4±0.56 | |
| | GOR Loop 2 | | | 0.361±0.024 |
| | Pressure Loop 2 | 255.7±1.7 | 192.3±1.5 | |

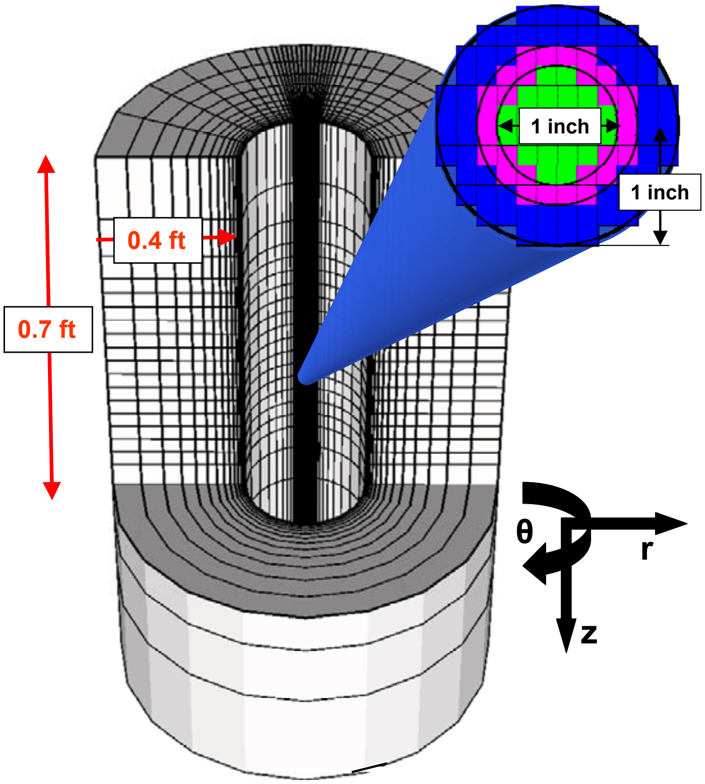

Figure 6.1: Three-dimensional view of the probe opening with respect to a cylindrical finite-difference grid. Note that the region around the probe opening is discretized in all directions (r,θ,z) to simulate transient measurements of pressure, flow rate, and GOR. The 1-inch diameter, green inner region identifies the sample line of the focused probe, and the outer blue region describes the guard line of the focused probe, while the region between the guard and sample lines corresponds to the rubber sealing. In the simulations, the conventional probe is modeled with the same area as that of the sample line of the focused probe.

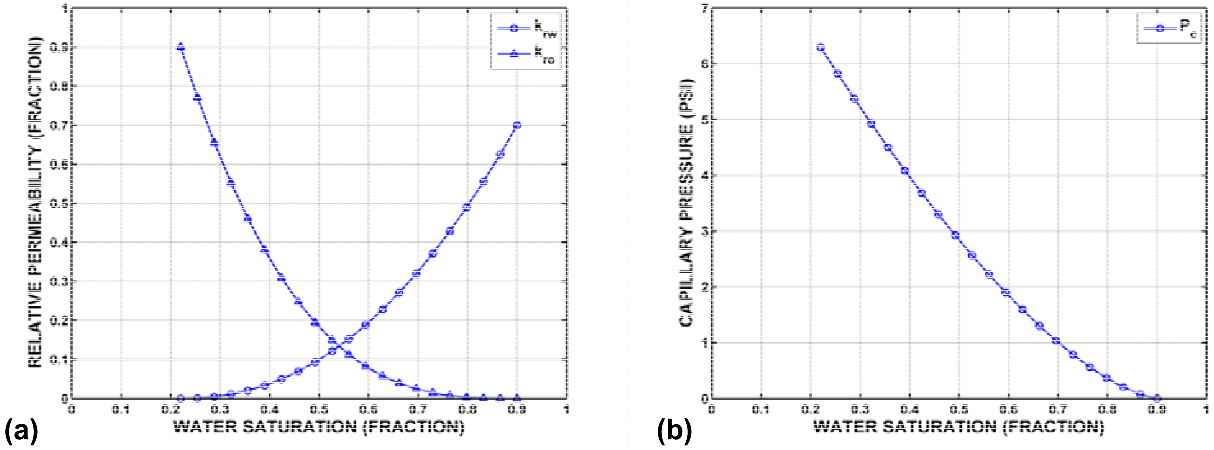

Figure 6.2: Water-oil relative permeability (left-hand panel) and capillary pressure (right-hand panel) curves assumed in the simulations of mud-filtrate invasion and fluid pumpout. Panel (a) describes relative permeability curves as a function of water saturation for water ("krw") and oil ("kro") phases, respectively. Irreducible water and oil saturations are 0.22 and 0.1, respectively.

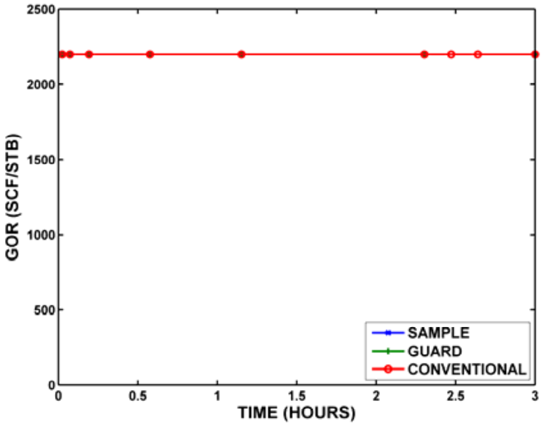

Figure 6.3: Comparison of transient GOR measurements simulated with focused and conventional probes for the Base Case Model without presence of mud-filtrate invasion. Labels "guard," "sample," and "conventional" identify GOR simulated at the guard probe flow line, the sample probe flow line, and the conventional probe flow line, respectively.

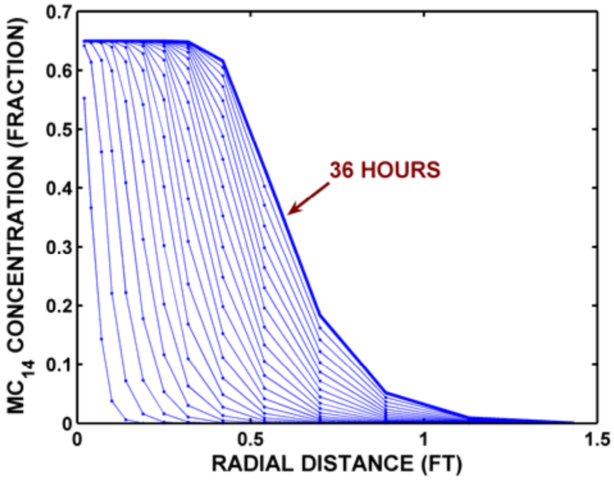

Figure 6.4: Simulated time-space variation of the MC$_{14}$ fluid component of OBM during the process of mud-filtrate invasion for the Base Case Model. Twenty-four curves are shown at time increments of 1.5 hours after the onset of invasion.

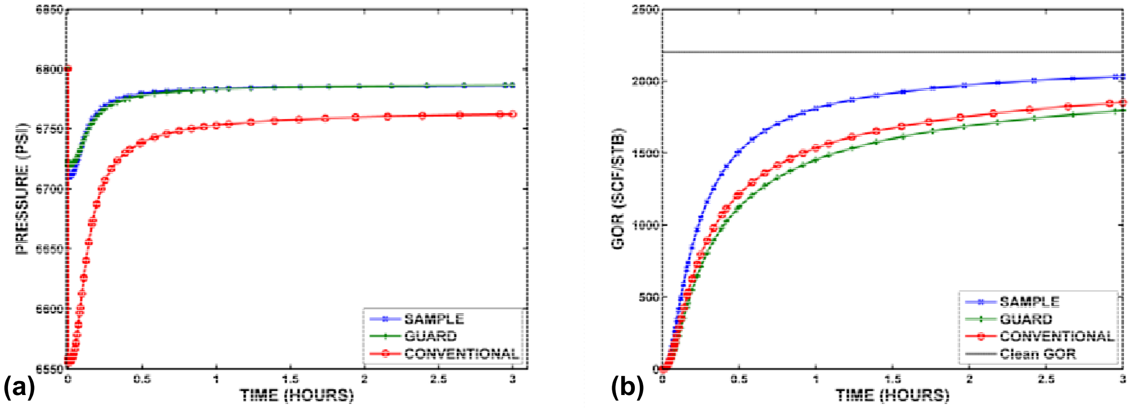

Figure 6.5: Panel (a) compares transient probe-pressure measurements simulated with focused and conventional probes for the Base Case Model in the presence of mud-filtrate invasion. Pressure drop is higher with the conventional probe as the latter withdraws fluids from a smaller cross-sectional area. Formation pressure is 6800 psi at time 0 hours, before the onset of fluid withdrawal. Panel (b) compares transient GOR measurements simulated with focused and conventional probes for the Base Case Model in the presence of mud-filtrate invasion. Labels “guard,” “sample,” and “conventional” identify GOR simulated at the guard probe flow line, the sample probe flow line, and the conventional probe flow line, respectively.

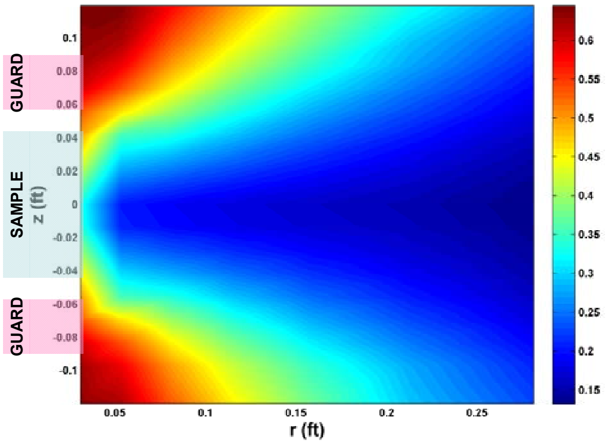

Figure 6.6: Spatial distribution (radial and vertical directions) of $MC_{14}$ fluid component concentration in the near-probe region after 5 minutes of fluid sampling with the focused probe for the Base Case Model in the presence of invasion. The sample- and guard-line openings extend from -0.0417 ft to +0.0417 ft and -0.0833 ft to +0.0833 ft, respectively, in the vertical direction.

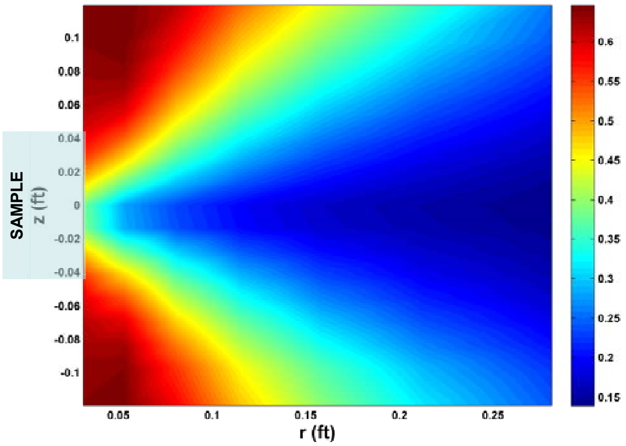

Figure 6.7: Spatial distribution (radial and vertical directions) of $MC_{14}$ fluid component concentration in the near-probe region after 5 minutes of fluid sampling with the conventional probe for the Base Case Model with invasion. The probe opening extends from -0.0417 ft to +0.0417 ft in the vertical direction.

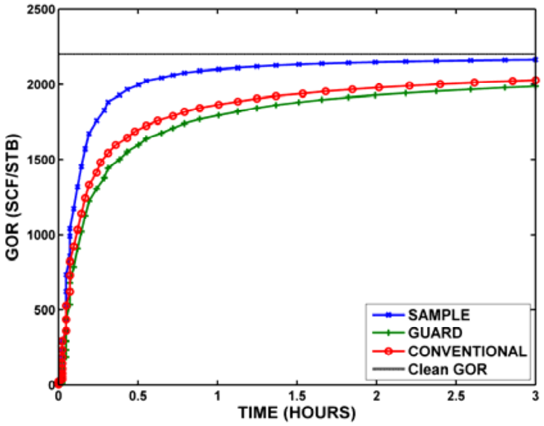

Figure 6.8: Comparison of transient GOR measurements simulated with focused and conventional probes for Case No. 1. Labels “guard,” “sample,” and “conventional” identify GOR simulated at the guard probe flow line, the sample probe flow line, and the conventional probe flow line, respectively.

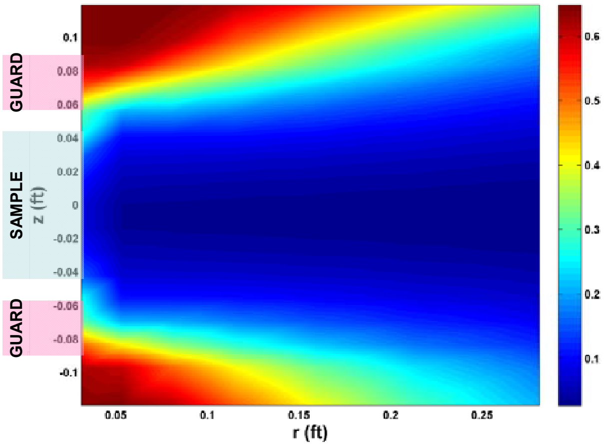

Figure 6.9: Spatial distribution (radial and vertical directions) of $MC_{14}$ fluid component concentration in the near-probe region after 5 minutes of fluid sampling with the focused probe for Case No. 1. The sample- and guard-line openings extend from -0.0417 ft to +0.0417 ft and -0.0833 ft to +0.0833 ft, respectively, in the vertical direction.

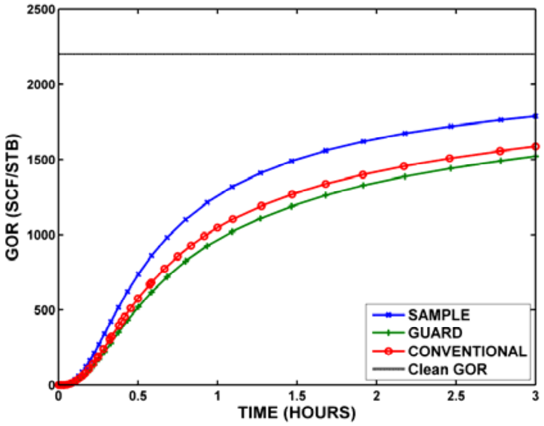

Figure 6.10: Comparison of transient GOR measurements simulated with focused and conventional probes for Case No. 2. Labels "guard," "sample," and "conventional" identify GOR simulated at the guard probe flow line, the sample probe flow line, and the conventional probe flow line, respectively.

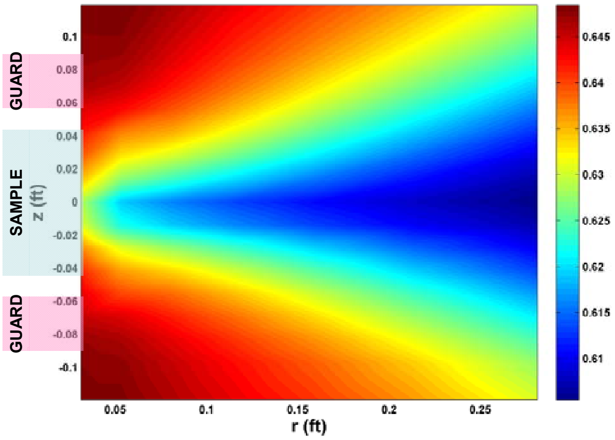

Figure 6.11: Spatial distribution (radial and vertical directions) of $MC_{14}$ fluid component concentration in the near-probe region after 5 minutes of fluid sampling with the focused probe for Case No. 2. The sample- and guard-line openings extend from -0.0417 ft to +0.0417 ft and -0.0833 ft to +0.0833 ft, respectively, in the vertical direction.

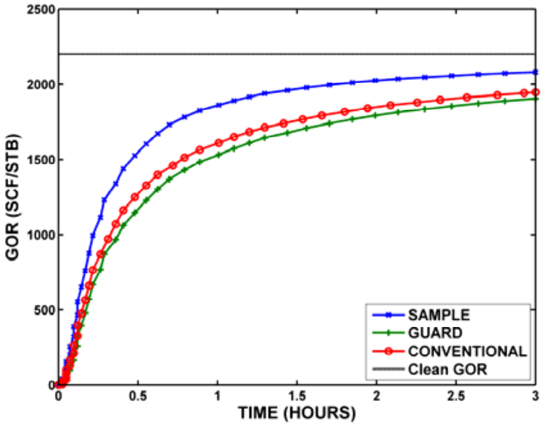

Figure 6.12: Comparison of transient GOR measurements simulated with focused and conventional probes for Case No. 3. Labels “guard,” “sample,” and “conventional” identify GOR simulated at the guard probe flow line, the sample probe flow line, and the conventional probe flow line, respectively.

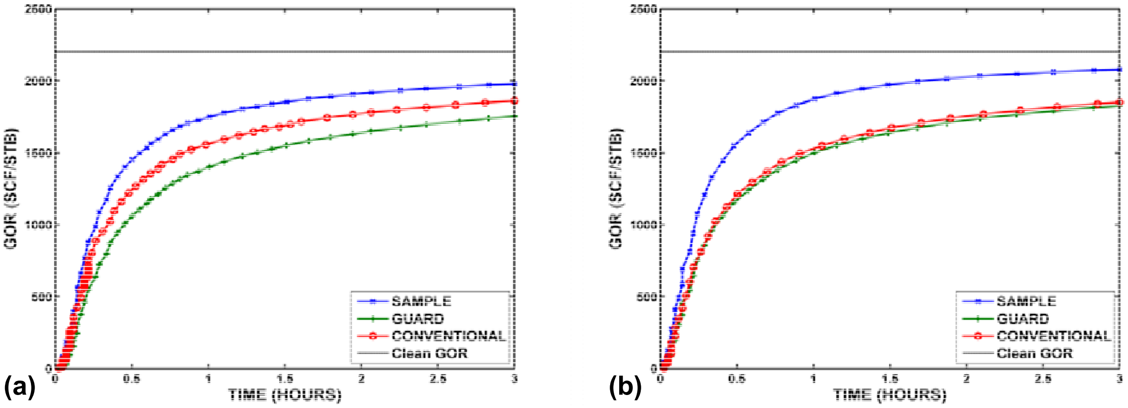

Figure 6.13: Comparison of transient GOR measurements simulated with focused and conventional probes for Case No. 4. Panel (a) compares simulations for the case of flow-rate ratio of 1:1 through the focused probe. Panel (b) compares simulations for the case of flow-rate ratio of 1:9 through the focused probe. Labels “guard,” “sample,” and “conventional” identify GOR simulated at the guard probe flow line, the sample probe flow line, and the conventional probe flow line, respectively.

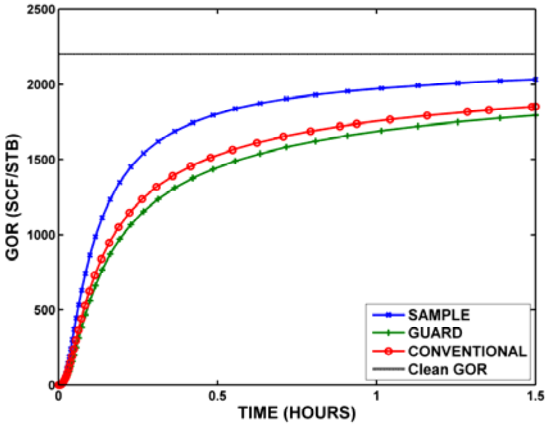

Figure 6.14: Comparison of transient GOR measurements simulated with focused and conventional probes for Case No. 5. Labels "guard," "sample," and "conventional" identify GOR simulated at the guard probe flow line, the sample probe flow line, and the conventional probe flow line, respectively.

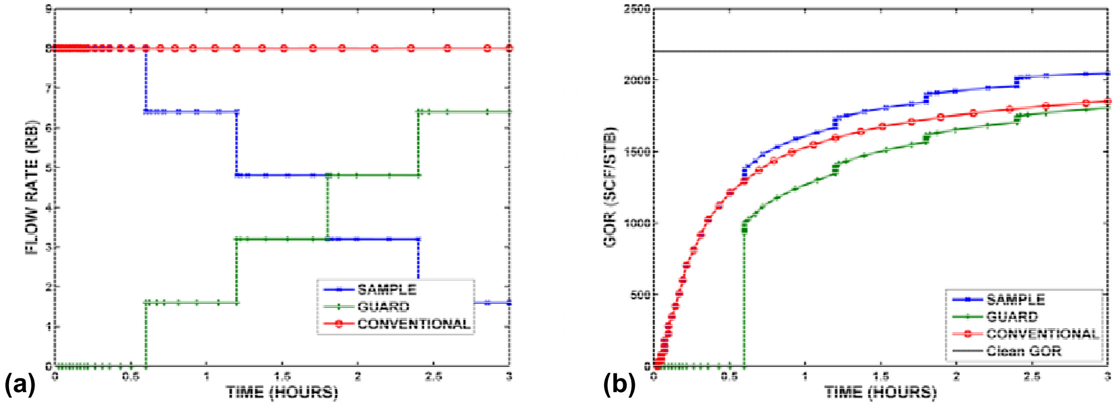

Figure 6.15: Panel (a) shows variations of flow rate (units of reservoir barrels) through the focused probe. Five constant pulses of varying intervals were considered for analysis. Panel (b) compares transient GOR measurements simulated with focused and conventional probes for Case No. 6. The guard-line GOR is equal to zero until 0.6 hours because fluids have not entered the line prior to that time. Labels "guard," "sample," and "conventional" identify GOR simulated at the guard probe flow line, the sample probe flow line, and the conventional probe flow line, respectively.

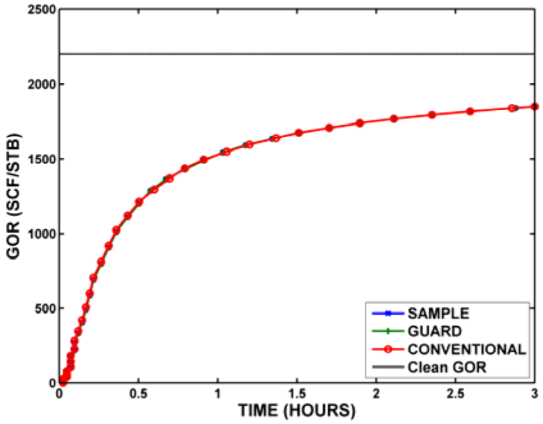

Figure 6.16: Comparison of transient GOR measurements simulated with focused and conventional probes for Case No. 7. Labels “guard,” “sample,” and “conventional” identify GOR simulated at the guard probe flow line, the sample probe flow line, and the conventional probe flow line, respectively.

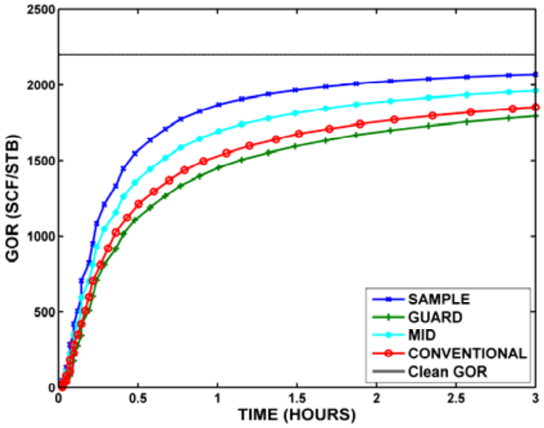

Figure 6.17: Comparison of transient GOR measurements simulated with focused and conventional probes for Case No. 8. For the case of the focused probe, labels “guard” and “sample” identify GOR simulated at the guard and sample lines, respectively. Labels “mid” and “conventional” identify GOR simulated at the intermediate- and conventional-probe flow lines, respectively.

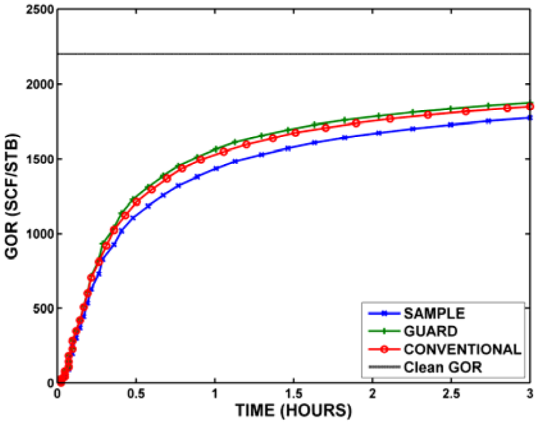

Figure 6.18: Comparison of transient GOR measurements simulated with focused and conventional probes for Case No. 9. Labels "guard," "sample," and "conventional" identify GOR simulated at the guard probe flow line, the sample probe flow line, and the conventional probe flow line, respectively.

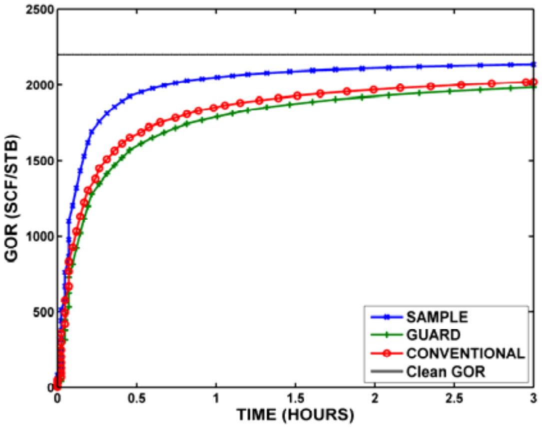

Figure 6.19: Comparison of transient GOR measurements simulated with focused and conventional probes for Case No. 10. Labels "guard," "sample," and "conventional" identify GOR simulated at the guard probe flow line, the sample probe flow line, and the conventional probe flow line, respectively.

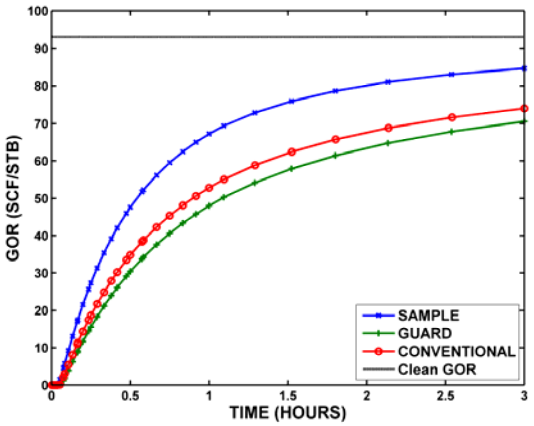

Figure 6.20: Comparison of transient GOR measurements simulated with focused and conventional probes for Case No. 11. Labels “guard,” “sample,” and “conventional” identify GOR simulated at the guard probe flow line, the sample probe flow line, and the conventional probe flow line, respectively.

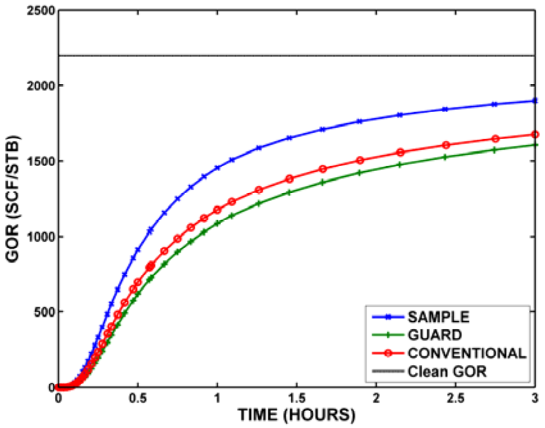

Figure 6.21: Comparison of transient GOR measurements simulated with focused and conventional probes for Case No. 12. Labels “guard,” “sample,” and “conventional” identify GOR simulated at the guard probe flow line, the sample probe flow line, and the conventional probe flow line, respectively.

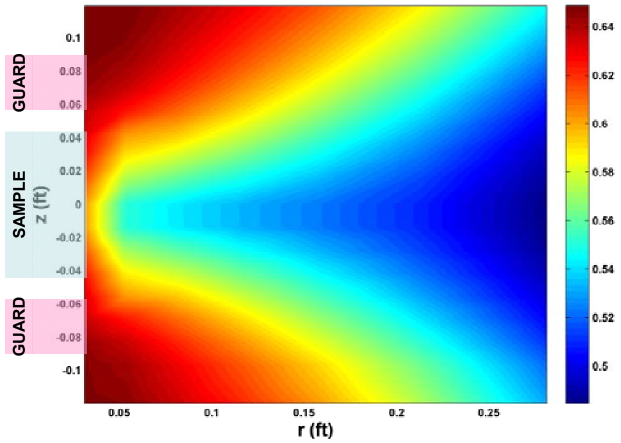

Figure 6.22: Spatial distribution (radial and vertical directions) of $MC_{14}$ fluid component concentration in the near-probe region after 5 minutes of fluid sampling with the focused probe for Case No. 12. The sample- and guard-line openings extend from -0.0417 ft to +0.0417 ft and -0.0833 ft to +0.0833 ft, respectively, in the vertical direction.

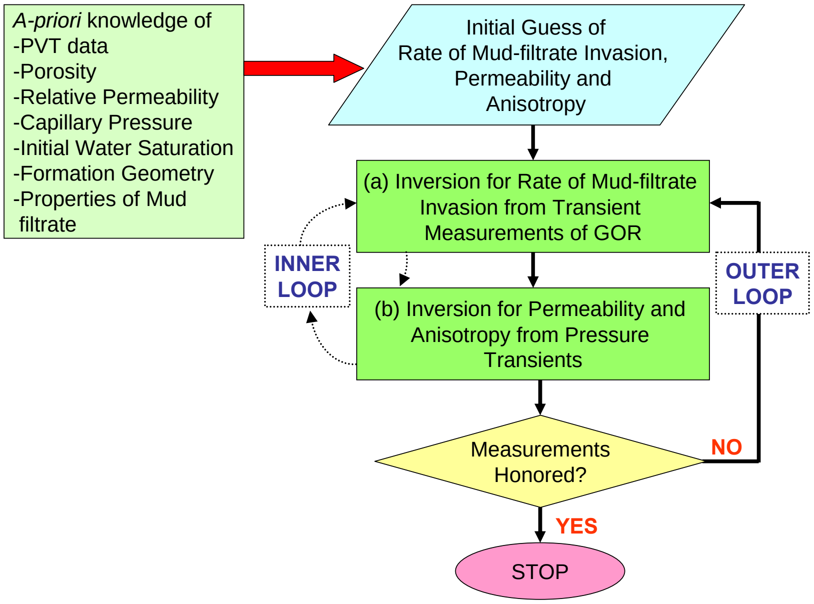

Figure 6.23: Flowchart of the two-loop minimization algorithm used in this chapter to jointly estimate (a) rate of mud-filtrate invasion from GOR, and (b) permeability and anisotropy from transient measurements of pressure. The inner loop proceeds for a maximum of two iterations.

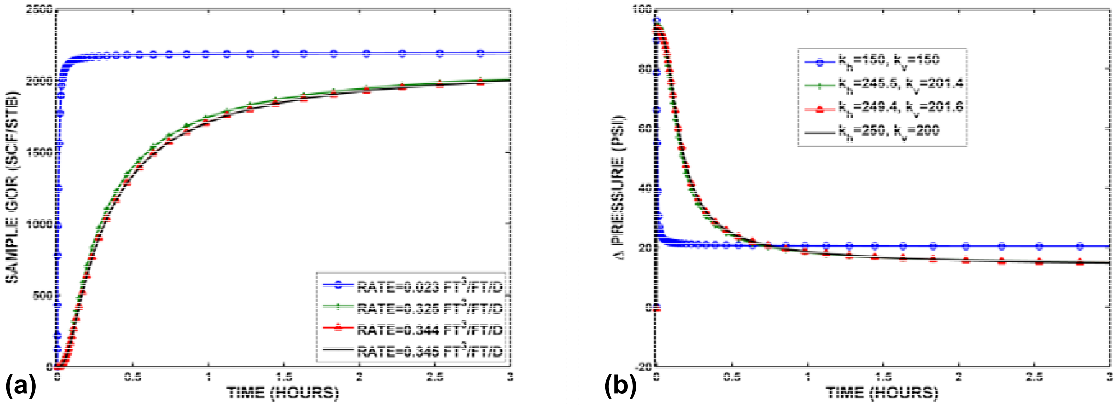

Figure 6.24: Convergence of the (noise-free) two-loop minimization algorithm applied to synthetic measurements acquired with the focused probe. Panel (a) shows the sample GOR as a function of time for different inversion loops of invasion rate. The starting guess for inversion was 0.023 ft$^3$/ft/day and the final noise-free minimum was 0.345 ft$^3$/ft/day. Panel (b) shows the sink probe pressure differential as a function of time for different inversion loops of permeability and anisotropy. The starting guess for inversion was 150 mD for both horizontal and vertical permeability. Final noise-free minima were 250 mD for horizontal permeability and 200 mD for vertical permeability.

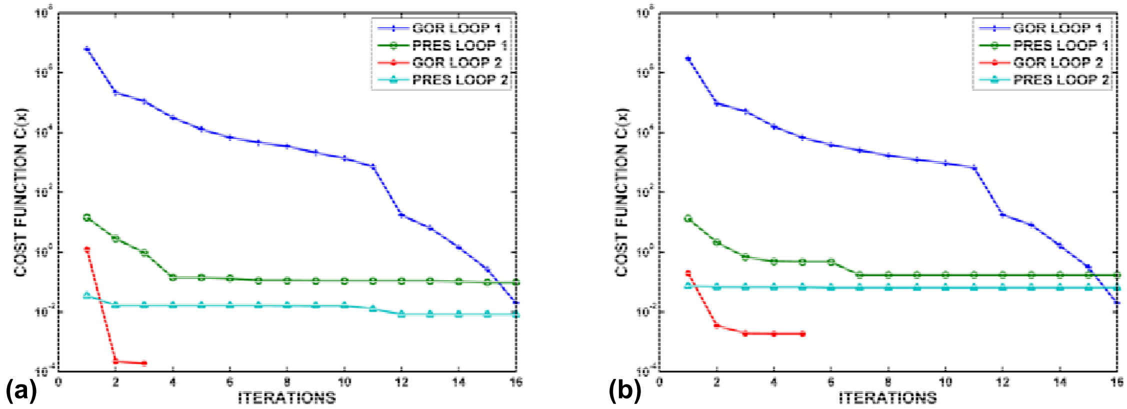

Figure 6.25: Cost function as a function of iteration number for different inversion loops. Panel (a) shows the convergence of the (noise-free) two-loop minimization algorithm applied to synthetic measurements acquired with the focused probe. Panel (b) shows the convergence of the (noise-free) two-loop inversion algorithm applied to synthetic measurements acquired with the conventional probe.

# Chapter 7: Estimation of Parametric Models of Capillary Pressure and Relative Permeability from Focused Formation-Tester Measurements

Quantification of the process of water-base mud (WBM)-filtrate invasion is necessary to assess the corresponding impact on petrophysical estimates derived from measurements acquired with a formation tester. The process of WBM-filtrate invasion is governed by petrophysical properties such as relative permeability of oil and water phases, capillary pressure, initial connate-water saturation, porosity, permeability, and anisotropy. Similarly, fractional flow during fluid sampling is affected by petrophysical and fluid properties; extended pumpout times are often needed to reduce filtrate contamination to acceptable levels. Focused probes are a new commercial alternative to reduce WBM contamination faster by diverting flow into different fluid channels. The objective of this chapter is to evaluate the possibility of estimation saturation-dependent relative-permeability and capillary-pressure functions jointly from transient measurements of pressure and fractional flow acquired with a focused probe.

Early-time fractional flow is typically ignored in the estimation of petrophysical properties from fluid-sampling measurements. However, fractional-flow measurements can provide valuable information to estimate relative permeability and capillary pressure. Previous studies have explored the possibility of using both fluid-sampling measurements acquired with dual-packer formation testers and borehole resistivity measurements to estimate saturation-dependent petrophysical properties. In this chapter, we introduce an inversion method to estimate Brooks-Corey parametric functions of capillary pressure and relative permeability using exclusively transient measurements acquired with probe-type formation testers. Both focused and conventional probes are considered for the analysis of measurements simulated for three synthetic rock formations that comprise a realistic range of petrophysical properties. Inversion is performed jointly from transient measurements of fractional flow and probe pressures to estimate formation permeability, relative permeability, irreducible phase saturations, and capillary pressure. We emphasize that estimating Brooks-Corey saturation-dependent parameters can yield non-unique results because of paucity of data. However, we show that, in general, focused fluid sampling entails enhanced degrees of freedom in the pressure and fractional flow transient measurements to improve both accuracy and reliability of the estimated formation properties.

Simulations of WBM-filtrate invasion indicate that fractional flow is governed by the mobility of formation fluids, which in turn is affected by absolute permeability, relative permeability, and fluid viscosity. We show that fast decay of fractional flow for high-porosity, high-permeability rocks decreases the sensitivity of measurements to appraising saturation-dependent petrophysical properties in a gas zone with shallow invasion. Results also show that permeability and relative permeability are interdependent on pressure drop, whereupon their joint estimation is technically challenging. In general, we observe that focused fluid sampling improves the assessment of relative mobility and irreducible water saturation compared to conventional fluid sampling.

## 7.1 INTRODUCTION

While drilling porous and permeable rocks, overbalance pressure dominates the process of mud-filtrate invasion. In turn, mud-filtrate invasion influences wireline formation-tester (WFT) measurements. Formation testers are widely used for downhole fluid analysis (Dong et al., 2007) to measure fluid properties in real time, such as pressure, color, viscosity, density, chemical composition, pH, optical refractive index, and GOR (volumetric gas-to-liquid ratio of crude oil measured at standard conditions of 1 atm and 60 $^{\circ}$F). Early-time fluid sampling can give non-representative fluid samples due to WBM contamination. It is essential for fluid samples to exhibit less than 5% contamination to be representative of in-situ pressure, volume and temperature (PVT) properties.

Previous studies have suggested that resistivity and transient measurements of fractional flow be used jointly to estimate saturation-dependent petrophysical properties of the invaded rock formation (Semmelbeck et al., 1995; Ramakrishnan and Wilkinson, 1997; Zeybek et al., 2004; Alpak et al., 2004). To that effect, Ramakrishnan and Wilkinson (1997) introduced a radial one-dimensional (1D) fluid transport model based on the method of characteristics. The model assumed WBM with convective displacement of oil, water, and salt. They analyzed three different fractional flow curves and concluded that formation oil producibility and water cut could be estimated from resistivity logs. Semmelbeck et al. (1995) described a similar approach that used the signature of invasion on resistivity logs in tight-gas sands to estimate permeability. Zeybek et al. (2004) combined formation-tester pressure and water-cut measurements with openhole-array resistivity logs to estimate relative permeability of oil and water. They used a dual-packer configuration of the Modular Formation Dynamics Tester (MDT[13]) and estimated relative permeability with a history-matching algorithm. Alpak et al. (2004) implemented an automated global minimization method to estimate multi-phase petrophysical properties jointly from wireline formation tester and induction resistivity measurements; inversion products were permeability, anisotropy, relative permeability for oil and water phases, and capillary pressure curves. However, an undesirable feature of Alpak et al.'s (2004) algorithm was the necessary adjustment of data and regularization weights to obtain reliable inversion results especially in the presence of noisy synthetic measurements. They emphasized that both multi-pulse flow

---

[13] Trademark of Schlumberger

rate schedules and long-time sampling intervals were essential for decreasing the non-uniqueness of the estimation. Chen et al. (2005) introduced a technique for in-situ estimation of relative permeability curves from well-test measurements using a Levenberg-Marquardt (Marquardt, 1963) inversion algorithm. They used both fractional flow and pressure transient measurements for minimization and concluded that changes of sandface mobility were highly sensitive to relative-permeability parameters.

Recently, Schlumberger introduced the Quicksilver[14] focused-sampling probe. It includes two fluid channels with the intent of achieving higher-purity fluid samples in a shorter period of time than with a conventional probe (Weinheber and Vasques, 2006). Because there is a rubber sealing between the guard and sample regions of the focused probe, WBM-contaminated fluid tends to flow toward the guard region whereas native formation fluids tend to preferentially flow toward the sample probe. If an appropriate pressure differential is maintained, diversion of the fluid stream to different fluid channels can lead to faster cleanup thereby reducing fluid-sampling time.

The central hypothesis of this chapter is that the additional fluid channel in the focused probe should increase the redundancy of input data available for estimation of saturation-dependent petrophysical properties with formation-tester measurements. To test this hypothesis, in chapter 6 we considered the estimation of mud-filtrate invasion rate, permeability, and anisotropy jointly from transient measurements of gas-oil ratio (GOR) and probe pressure acquired with both focused and conventional probe-type formation testers. They showed that focused fluid sampling entailed enhanced degrees of freedom for the estimation of unknown properties compared to conventional probe fluid sampling, thereby reducing the non-uniqueness of the inversion and hence improving the reliability and accuracy of the estimation. However, the estimation method proposed in

---

[14] Trademark of Schlumberger

chapter 6 assumed *a-priori* information about saturation-dependent functions from independent sources of information.

In this chapter, we simulate measurements acquired with both focused and conventional probes and compare their performance for a wide range of petrophysical and fluid properties to determine the operating conditions under which usage of a focused probe leads to improved fluid cleanup. Moreover, we develop a method to estimate Brooks-Corey relative permeability and capillary pressure parametric functions jointly from transient measurements of fractional flow and probe pressures. To that end, fluid properties are modeled in the form of components using a compositional equation-of-state (EOS) simulator (CMG-GEM[15]). Hydrocarbon viscosity is calculated with the Lohrenz-Bray-Clark (Lohrenz et al., 1964) correlation and hydrocarbon density is calculated from the EOS to account for time-space variations of pressure.

The following section describes the method adopted in this chapter to simulate the processes of mud-filtrate invasion and formation-tester measurements in the near-wellbore region with a commercial adaptive-implicit finite-difference compositional simulator. Subsequently, we analyze the WBM-filtrate invasion process for three synthetic rock formations that span a realistic range of petrophysical properties. Interpretation of the invasion process in both gas- and oil-bearing formations leads to improved understanding of fractional flow curves. Comparison of fluid sampling processes with both conventional and focused probes identifies field conditions where focusing provides faster fluid cleanup. Lastly, we estimate permeability, relative permeability for oil and water, capillary pressure and irreducible phase saturations jointly from transient measurements of fractional flow and probe pressures. In the first loop of the method, we estimate Brooks-Corey's (Brooks and Corey, 1964) saturation-dependent

---

[15] Trademark of Computer Modeling Group Limited

parameters from fractional flow measurements. In the second loop, we estimate only absolute permeability from probe pressure measurements. The two-loop minimization method yields reliable estimates of petrophysical properties from noise-free synthetic measurements. Furthermore, it is confirmed that measurements acquired with the focused fluid probe provide additional degrees of freedom than equivalent measurements acquired with a conventional probe thereby leading to more accurate and reliable estimates of petrophysical properties.

## 7.2 METHOD

The simulation framework is similar to the one introduced in chapter 6. **Table 6.1** describes the finite-difference simulation grid, consisting of 29 blocks in the radial ($r$) direction, 33 blocks in the azimuthal ($\theta$) direction, and 40 blocks in the vertical ($z$) direction. At the wellbore, the focused-probe opening is modeled with sixty gridblocks such that the guard opening area is 2.5 times the area of the fluid-sample conduit. The sample-probe opening is modeled as a source or a well spread over twenty-four gridblocks with a diameter of approximately one inch. There is a separation of 0.16 inches between the guard region and the sample region where no-flow boundary conditions are enforced in order to account for the presence of rubber sealing. **Figure 6.1** is a perspective view of the probe location with respect to the cylindrical grid. There are 9240 gridblocks in a radius of one foot around the probe to properly capture flow dynamics in the near-probe region. Gridblock sizes increase logarithmically in the radial direction starting with 0.165 inches at the wellbore. We use a three-dimensional (3D) grid geometry and make no restricting assumptions regarding spatial symmetry. Moreover, to economize computer time, as shown in **Fig. 6.1**, we use a 180-degree azimuthal gridblock behind the probe.

### 7.2.1 Mud-Filtrate Invasion

The process of mud-filtrate invasion is modeled with a volume-averaged flow-rate of mud-filtrate invasion across the borehole wall prior to simulating formation-tester measurements. We assume that invasion is axial-symmetric with respect to the axis of a vertical wellbore, and that the injected fluid stream consists of WBM filtrate. Mud-filtrate invasion is modeled for 36 hours with a constant volume-averaged invasion rate. We emphasize that the simulated time evolution of fractional flow after the onset of fluid withdrawal is very sensitive to the radial length of invasion of WBM: deep mud-filtrate invasion leads to a slow buildup of fractional flow whereas shallow mud-filtrate invasion leads to a fast buildup of fractional flow during fluid sampling with a WFT.

### 7.2.2 Fluid Withdrawal with a Formation tester

Our numerical formulation enforces boundary and source flow-rate conditions on specific depth segments along the wellbore: At the wellbore, the WFT imposes a constant flow rate boundary condition during fluid production. The outer limits of the reservoir consist of impermeable zones with no-flow boundary conditions. Fluid production from the probe opening is simulated for a time interval of 3 hours. Our model assumes that the volume of mud filtrate invading the formation during sampling is negligible compared to the volume of fluids that have previously entered the formation. Therefore, invasion and fluid-withdrawal processes do not occur simultaneously.

### 7.2.3 Formation Fluid Composition

The fluid composition assumed in this chapter is different from the one described in chapter 6 where numerical simulations included eight different hydrocarbon pseudo-components that were essential to model transient measurements of GOR in miscible flow with oil-base mud filtrate. Here, rather than considering multiple pseudo-components in the hydrocarbon phase, we lump all hydrocarbon components in one pseudo-component. Because WBM filtrate is immiscible with formation hydrocarbons, lumping of components into one pseudo-component provides faster computational time without compromising the physics of immiscible flow. **Table 7.1** summarizes the pseudo-physical properties of formation hydrocarbons lumped into one component. Two formation-fluid compositions are considered for analysis, identified as “Oil Zone” and “Gas Zone,” respectively. Dead-oil and dry-gas viscosities are assumed equal to 0.44 cp and 0.03 cp, respectively. We quantify the effect of mobility contrast by comparing simulations of the processes of WBM-filtrate invasion and fluid withdrawal for different petrophysical properties of hydrocarbon-bearing formations.

### 7.2.4 Parametric Relative-Permeability and Capillary-Pressure Functions

In this study, we consider three synthetic rock types that span a realistic range of petrophysical properties. The processes of mud-filtrate invasion and fluid withdrawal depend on the choice of rock type. **Figure 7.1** shows the modified Brooks-Corey (Brooks and Corey, 1964) saturation-dependent relative permeability and **Fig. 7.2** displays the capillary pressure curves for our three synthetic rock types. Rock No. 1 represents a low-porosity, low-permeability (poor-quality) tight rock, whereas Rock No. 3 describes a high-porosity, high-permeability (good-quality) rock. Finally, Rock No. 2 represents a medium-quality rock. Initial and irreducible water saturation in the formation vary with rock type, whereas irreducible oil saturation is assumed constant and equal to 0.2. Because the formation of interest is assumed previously unexplored, initial connate-water saturation is equal to irreducible water saturation. The saturation-dependent functions can be expressed as

$$k_{rw}(S_w) = k_{rw}^{o}\left(\frac{S_w - S_{wr}}{1 - S_{wr} - S_{or}}\right)^{(3+2/\ell)}, \qquad \ldots(7.1)$$

$$k_{ro}(S_w) = k_{ro}^o \left( \frac{1 - S_w - S_{or}}{1 - S_{wr} - S_{or}} \right)^{(1+2/\ell)} , \qquad \ldots(7.2)$$

and

$$P_c(S_w) = P_{ce}^o \left( \frac{S_w - S_{wr}}{1 - S_{wr} - S_{or}} \right)^{-1/\ell} , \qquad \ldots(7.3)$$

where $S_w$ is water saturation, $k^o{}_{rw}$ and $k^o{}_{ro}$ are end-point relative permeability for water and oil, respectively, $S_{wr}$ and $S_{or}$ are irreducible saturations for water and oil, respectively, $\ell$ is pore-size distribution index, $P_c$ is capillary pressure difference between water and oil, and $P^o{}_{ce}$ is capillary entry pressure. Relative permeability curves for the three rock types are modified by altering the irreducible water saturation and exponents included in Brooks-Corey equations. **Table 7.2** describes the Brooks-Corey parameters used to compute the relative permeability and capillary pressure curves for the three synthetic rock types.

### 7.3 WBM-FILTRATE INVASION IN AN OIL ZONE

We simulate the process of WBM-filtrate invasion within a time interval of 36 hours. To that end, we assume a volume-averaged flow rate of invasion that is imposed at the wellbore. **Figure 7.3** displays the time-space variation of the water saturation that is simulated with an invasion rate of 0.576 ft$^3$/day/ft for the three synthetic rock types. We observe that the radial length of invasion varies from 1 to 3 feet depending on rock type. Invasion is deepest for Rock No. 1 (**Fig. 7.3a**) and shallowest for Rock No. 3 (**Fig. 7.3c**). In addition, the water saturation front is dispersed for Rock No. 1 whereas the front is sharper for Rock No. 3 (best quality). Rock No. 1 has a higher capillary pressure contrast between oil and water, thereby resulting in a dispersed fluid-saturation front. The radial extent of invasion is consistent with previous studies on the subject of mud-filtrate invasion (Wu et al., 2002; Malik et al., 2007).

**Table 7.3** summarizes the petrophysical and formation properties for all simulation cases considered in this chapter. We assume a homogeneous, single-layer isotropic formation. **Table 7.1** describes the formation fluid in the Oil Zone, which exhibits a gas-oil ratio (GOR) of 0 SCF/STB. For the focused probe, the flow rates at the fluid-sample and guard lines are 2 RB/day[16] and 6 RB/day, respectively, while the corresponding rate at the conventional-probe flow line is 8 RB/day. The duration of the formation test is 3 hours. Therefore, the cumulative fluid produced by both focused and conventional probes is the same and equal to one reservoir barrel.

**Figure 7.4** shows the transient fractional flow simulated during fluid withdrawal with both focused and conventional probes for all three rock types. In that figure, the guard and sample lines in the focused probe are identified with the labels “guard” and “sample,” respectively, while the one-inch diameter conventional probe is identified with the label “conventional.” **Figure 7.4a** indicates that the fractional flow for Rock No. 1 is much higher than that of Rock No. 3 (**Fig. 7.4c**). Both permeability and saturation-front dispersion control the velocity of flow for different rock types if the formation fluid under consideration is the same. Even though the volume of mud-filtrate invasion is the same for both rock types, the increased dispersion of the fluid-saturation front in Rock No. 1 (poor quality) leads to a slower time evolution of fractional flow.

**Table 7.4** summarizes the values of fractional flow simulated in the fluid stream at the end of fluid sampling for all three rock types. Time savings is defined as the reduction in fluid sampling time when using a focused probe such that the measured fractional flow at the end of fluid sampling is the same with the two probes. Using the focused probe leads to a time savings of approximately 28% with respect to that of a conventional probe in the Oil Zone for all synthetic rock types. Time savings decrease

---

[16] One RB/day is equal to 1.8 cc/sec

progressively from Rock No. 1 (poor quality) to Rock No. 3 (best quality). Thus, focused sampling becomes advantageous when the invasion front is dispersed. In high-porosity, high-permeability formations, the advantage of fluid sampling with a focused probe decreases due to the sharpness of the invasion front together with faster breakthrough of native formation fluids. Irrespective of probe geometry, sample quality improves in the presence of a piston-like invasion front resulting from marginal influence of capillary forces.

**Table 7.4** also indicates that the simulated fractional flow at the probes is in good agreement with the relation

$$fw_{reg} \approx \frac{fw_{guard} * Q_{guard} + fw_{sample} * Q_{sample}}{Q_{guard} + Q_{sample}}, \qquad \ldots(7.4)$$

where the subscripts *reg, guard,* and *sample* identify the fractional flow at the conventional probe flow line, the guard flow line, and the sample flow line, respectively, and *Q* designates the corresponding flow rate of fluid withdrawal (measured in RB/day) in the sample and guard flow lines. **Equation 7.4** assumes that the flow rates associated with conventional and focused probes are equal and therefore the sample quality associated with the conventional probe is identical to that of the focused probe when operating in commingled or hydraulically-connected mode.

**Figures 7.5, 7.6,** and **7.7** describe the simulated spatial distributions of water saturation in the near-probe region after 5 minutes of fluid sampling for Rock Nos. 1, 2, and 3, respectively. The focused probe withdraws fluids through a larger conduit area (**Fig. 7.5b**) compared to the conventional probe and, therefore, water saturation decreases faster in the near-probe region. In addition, the sample line of the focused probe produces relatively cleaner fluid than the flow line of the conventional probe (**Fig. 7.5a**) after 1.5 hours of fluid sampling. Fluid focusing results in a conical fluid-saturation front with mud filtrate moving along the wellbore toward the guard region, whereas formation fluids flow directly into the sample region. We remark that coning is less effective when the fluid-saturation front is sharp, as in the case for Rock No. 3 (**Fig. 7.7**). This simulation exercise confirms that a focused probe provides improved sample quality compared to a conventional probe and helps to decrease the cleanup time in the presence of mud-filtrate invasion.

### 7.4 WBM-FILTRATE INVASION IN A GAS ZONE

In this section, we simulate the processes of mud-filtrate invasion and fluid withdrawal in a gas-bearing formation. **Table 7.1** shows that gas has a lower viscosity (0.03 cp) than oil and therefore the mobility contrast between mud filtrate and formation fluids is much higher than in the Oil Zone. The adverse mobility ratio entails piston-like fluid displacement. In addition, the density contrast between gas (0.24 g/cc) and water (1 g/cc) leads to gravity segregation of the invading fluid. **Figure 7.8** indicates that the invasion front in the gas-bearing formation is much sharper than the invasion front in the oil-bearing formation for all rock types. At the same time, the radial distribution of water saturation indicates that movable gas is completely displaced from the near-wellbore region by mud filtrate.

**Figure 7.9** displays the transient fractional flow simulated during fluid withdrawal with focused and conventional probes for the three rock types. Comparison of **Figs. 7.4** and **7.9** indicates that fractional flow decreases faster in the gas- than in the oil-bearing formation. Improved fluid cleanup is attributed to both the higher mobility of gas and sharper invasion front. The increased mobility of gas leads to a faster breakthrough of formation fluids, whereas the piston-like fluid-saturation front enables the WFT to withdraw cleaner fluids faster. Comparison of fractional flow simulated at the focused and conventional probes in **Fig. 7.9** indicates that there is negligible improvement from focused fluid sampling in a gas-bearing zone. In this situation, the focused probe could be operated in commingled mode by hydraulically connecting the guard and sample flow lines and using only one pump to withdraw fluids. In so doing, the focused probe would function as a conventional probe although with a larger cross-sectional area at the sandface.

### 7.5 INVERSION OF RELATIVE PERMEABILITY, CAPILLARY PRESSURE, IRREDUCIBLE PHASE SATURATIONS, AND PERMEABILITY JOINTLY FROM TRANSIENT MEASUREMENTS OF PRESSURE AND FRACTIONAL FLOW

As emphasized in previous studies (Alpak et al., 2004; Zeybek et al., 2004), inversion of saturation-dependent relative permeability and capillary pressure parametric models from fractional flow can be non-unique. In this section of the chapter, we invoke the fact that, compared to conventional fluid-probe sampling, focused fluid sampling provides enhanced degrees of freedom in pressure and fractional flow transient measurements because it withdraws fluids through two fluid channels instead of one. Thus, we hypothesize that the redundancy of information contained in the measurements should improve both accuracy and reliability of the estimated petrophysical properties. By testing the inversion method for all three rock types, we are able to quantify the effect of a realistic range of petrophysical properties on both pressure and fractional flow transient measurements acquired with conventional and focused probes.

We implement a general nonlinear least-squares inversion method (Madsen et al*.,* 2004) to estimate permeability, relative permeability, irreducible phase saturations, and capillary pressure for both focused and conventional fluid-sampling probes using a two-loop minimization method. Inversion is approached by expressing the saturation-dependent functions via the Brooks-Corey parametric model. The quadratic cost function used for the estimation (inversion) quantifies the misfit between measured and simulated transient pressure and fractional flow. We apply the inversion method to numerically simulated, noise-free measurements for the three synthetic rock types in the presence of

WBM-filtrate invasion. Inversion exercises do not consider the effect of deleterious noise in the measurements.

### 7.5.1 Cost Function

The quadratic cost function used for inversion quantifies the relative difference between numerically simulated and measured pressure difference and fractional flow difference, and is defined as

$$C(\mathbf{x}) = \frac{1}{2}\sum_{i=1}^{m}[e_i(\mathbf{x})]^2, \qquad \ldots(7.5)$$

where $m$ is the number of measurements. In **Equation 7.5**, the dimensionless data residuals, $e_i(\mathbf{x})$, quantify the relative difference between the simulated and observed measurements, namely,

$$e_i(\mathbf{x}) = \left[\eta_{sim_i}(\mathbf{x})/\eta_{obs_i}(\mathbf{x}) - 1\ \right], \qquad \ldots(7.6)$$

where subscript *sim* identifies the numerically simulated transients and *obs* identifies the observed transients. The variable $\eta$ designates the measurements and can be either pressure drop measured at the probes or fractional flow interpreted with downhole fluid analyzers. There is no regularization parameter in the cost function. We calculate the Jacobian matrix necessary for nonlinear iterative minimization via finite differences by numerically perturbing the model vector **x**. Additional technical details about the inversion algorithm can be found in chapter 5. The vector of model parameters for inversion is given by

$$\mathbf{x} = \left[k,\ k^o{}_{rw},\ k^o{}_{ro},\ S_{wr},\ S_{or},\ P^o{}_{ce},\ \ell\right]^{\mathrm{T}},$$

where the embedded Brooks-Corey parameters are given by **Eqs. 7.1-7.3**. Permeability, relative permeability, capillary pressure, and irreducible phase saturations included in the vector **x** are given in arithmetic rather than in logarithmic values. For simplicity but without loss of generality, in this chapter we focus our attention exclusively to isotropic permeability models.

### 7.5.2 Rock Formation Model

We limit our analysis to a single-layer hydrocarbon-bearing isotropic rock formation as described in **Tables 7.1-7.3**. The inversion algorithm is applied to numerically simulated measurements for all three rock types. We assume the availability of laboratory measurement of PVT properties such as viscosity, compressibility, reservoir temperature, and density (**Table 7.1** and **7.3**) for both formation oil and mud filtrate. Initial connate-water saturation is assumed to be equal to irreducible water saturation. This assumption is not restrictive in an unexplored and un-invaded formation. Therefore, the inversion algorithm yields initial connate-water saturation from the inversion of transient measurements of fractional flow. We assume *a-priori* knowledge of (a) mud-filtrate invasion rate from formation and mud properties and (b) porosity from nuclear logs.

To further enhance the sensitivity of the measurements to perturbations of unknown petrophysical properties, we modified the constant flow rate to include a multi-pulse flow rate schedule (Alpak et al., 2004). **Figure 7.10** shows that test duration is extended to 5 hours to sample late-time transient fractional flow measurements. The flow rate ratio between sample and guard flow lines of the focused probe is fixed at 0.25, whereas the flow rate of the conventional probe is equal to the total rate at the focused probe. **Table 6.1** describes the finite-difference grid used for inversion. By contrast, the simulation grid used to generate the synthetic measurements is much finer, consisting of 36 blocks in the radial ($r$) direction, 41 blocks in the azimuthal ($\theta$) direction, and 70 blocks in the vertical ($z$) direction. Thus, the spatial resolution of the simulation grid is approximately three times that of the inversion grid. Increased spatial resolution of the simulation grid is necessary to offset potential favorable biases in the calculation of data misfit.

### 7.5.3 Two-loop Minimization

In order to estimate permeability, we simulate pressure measurement at the sink and observation probes that are offset 2.6 ft and 8 ft above the sink probe. In addition, we use transient fractional flow measurements simulated at the sample and guard lines of the focused probe to estimate the Brooks-Corey relative permeability and capillary pressure curves. **Figure 7.11** is a flowchart of the inversion procedure.

While implementing the inversion, we observed that simultaneously estimating all transient measurements increases non-uniqueness and leads to poor convergence. In addition, relative permeability and capillary pressure parameters are sensitive to both fractional flow and flowing probe pressure. **Figure 7.12** compares the impact of the initial guess and final Brooks-Corey parameters on sandface pressure (left-hand panel) and fractional flow (right-hand panel) for Rock No. 2 (medium quality). Sandface pressure at the sample and guard probes is very sensitive to relative-permeability and capillary-pressure parameters. Although flow rates are constant in the multi-pulse schedule, sandface pressure indicates sensitivity to the fractional flow due to variations in mobility of the produced fluid phases. Following these observations, we implemented the inversion with two nested loops: in the first loop, we estimate only the Brooks-Corey parameters (**Eqs. 7.1-7.3**) from fractional flow and flowing-probe pressure measurements; in the second loop, we estimate permeability from pressure measurements acquired at all pressure probes. Joint inversion is essential to improve the reliability of the estimation as pressure and fractional flow transients are interdependent on both Brooks-Corey parameters and permeability. Therefore, the inverted Brooks-Corey parameters from the first loop are input to the second loop to improve the estimation of permeability. Subsequently, the inverted permeability from the second loop is input to the first loop to improve the estimation of Brooks-Corey parameters. Inverting the Brooks-Corey parameters prior to inverting permeability is essential because early-time pressure measurements are very sensitive to mud-filtrate invasion. The inversion comes to an end when the misfit between simulations and measurements is below a certain threshold, otherwise, we repeat the two-loop minimization process until securing a low data misfit. Experience with this inversion procedure indicates that final estimates can be achieved with at most two iterations between inner and outer loops.

### 7.5.4 Application of Inversion

We applied the inversion algorithm to measurements simulated for all three rock-types in an Oil Zone. **Table 7.5** summarizes the estimated properties for all synthetic rock types along with the starting guess for saturation-dependent parameters. The starting guess for permeability is 100 mD in all cases. **Figure 7.13(a)** shows the cost function as a function of iteration number when the inversion is performed with measurements simulated at the conventional probe for Rock No. 2 (medium quality), whereas **Fig. 7.13(b)** displays the corresponding cost function when the inversion is performed with measurements simulated at the focused probe. The two cost functions consistently decrease with iteration number for all successive loops of inversion. Comparison of the panels included in **Fig. 7.13** indicates that the cost function is lower toward the end of inversion for the case of focused-probe fluid sampling than for the case of conventional-probe fluid sampling. **Figure 7.14** displays the initial, final, and inverted relative permeability and capillary pressure curves obtained with the focused probe for Rock No. 2. We observe a good agreement between actual parameters and inverted results. Measurements acquired with the guard and sample lines included in the focused probe improve the accuracy and reliability of the estimated formation properties by providing additional degrees of freedom to the estimation.

**Table 7.5** indicates increased non-uniqueness of the estimated properties from measurements simulated for both Rock No. 1 (poor quality) and Rock No. 3 (best quality). Both increased dispersion of the saturation front for Rock No. 1 and sharper decay of fractional flow for Rock No. 3 affect the inversion results. Thus, specific petrophysical properties of the formation play an important role in controlling the non-uniqueness of the inversion. Improved estimation of irreducible water saturation is confirmed for all rock types from measurements acquired with the focused probe as it withdraws fluids through two fluid channels and therefore increases the redundancy of input data available for inversion. Estimation of capillary entry pressure is slightly inferior for Rock No. 1 with both focused- and conventional-probe measurements because of increased dispersion of the fluid-saturation front.

Absolute permeability estimates obtained from focused-probe measurements are inferior to estimates obtained from conventional-probe measurements for Rock Nos. 1 and 3. The conventional probe functions with a higher-pressure drop as it withdraws fluids through a smaller cross-sectional area than that of the focused probe.

We note that the CMG-GEM simulator provides only six decimal figures of precision in the simulations of both fractional flow and pressure. High precision is essential to accurately calculating the entries of the Jacobian matrix by numerical differences. Therefore, measurements simulated for the focused probe yield poorer estimated values of permeability for Rock Nos. 1 and 3 than measurements simulated for the conventional probe. Because the focused probe has twice the number of measurements available for inversion (from sample and guard flow lines), the additional information should de-emphasize limitations of numerical precision. If we compare the product of absolute permeability times relative permeability for oil and water phases, yielded by the inversion of measurements simulated for focused and conventional probes, we observe that focused-sampling results are closer to the phase relative permeability for all three rock-types. Thus, focusing enables the improved estimation of mobility of the flowing phases for all cases. We emphasize that both permeability and relative permeability are interdependent on pressure drop and hence estimating them independently from formation tester measurements can be difficult.

### 7.5.4 Assessment of uncertainty in *a-priori* information

In all of the previous inversion exercises, we assumed accurate knowledge of *a-priori* information. However, uncertainty in rate of mud-filtrate invasion, porosity, and other assumed petrophysical and fluid properties can bias the estimation results. Therefore, we perform an uncertainty analysis by perturbing the assumed rate of mud-filtrate invasion and porosity by 10% for Rock No. 2. Decreasing the rate of mud-filtrate invasion by 10% leads to shallower invasion. By contrast, decreasing the porosity by 10% leads to deeper invasion in the formation for the same volume of invading fluids. Table 6 clearly shows that uncertainty in *a-priori* information can severely bias the estimation of petrophysical properties. We observe that uncertainty in the rate of mud-filtrate invasion largely affects the capillary entry pressure whereas uncertainty in the porosity largely affects end-point relative permeability for oil. A perturbation of 10% in *a-priori* information leads to 10-13% variation in estimation of absolute permeability. However, in both sensitivity cases, we remark that focused-sampling inversion results are closer to the petrophysical properties of Rock No. 2 than conventional-sampling inversion results.

## 7.7 DISCUSSION

The process of mud-filtrate invasion is complex as it involves both solid and solute transport along with two-phase flow, wettability changes, capillary-pressure hysteresis, fines migration, chemical adsorptions, stress-induced changes in the near-wellbore region, dynamic borehole environment, and gravity segregation (Gok et al., 2006). One of the main difficulties in interpreting formation-tester measurements is to quantify the effect of both invasion and fluid withdrawal processes in a high-pressure, high-temperature downhole environment. In our simulation model, we assumed that porosity and permeability impairment from solute invasion and precipitation are negligible, and considered invasion as a two-phase immiscible flow process. Therefore, rock properties were assumed to be independent of the WBM-filtrate invasion process.

**Figure 7.15** compares the simulations of invasion and fluid cleanup processes for all three rock-types in both oil and gas zones. Dispersion of the fluid-saturation front due to capillary pressure and mobility contrast between mud filtrate and formation fluid affects the fluid withdrawal process. Focusing is more advantageous over conventional probe sampling when the invasion front is dispersed. Either a piston-like displacement front in the absence of capillary forces, a high mobility contrast, or lack of heterogeneity in the formation can all lead to improvements in fluid cleanup time.

Inversion performed on simulated probe measurements showed that estimating Brooks-Corey parameters from fractional flow could be non-unique. Results can be improved if initial and irreducible water saturation are calculated from ancillary information, such as resistivity logs, for instance. If a salinity contrast exists between connate water and mud-filtrate, transient measurements of salinity or pH can provide additional degrees of freedom to the inversion. In addition, core measurements can be useful in providing bounds for inversion, thereby decreasing the interdependence of absolute permeability and relative permeability on pressure drop. Therefore, combining resistivity logs, formation-tester measurements, and core data acquired in the vicinity of the formation test will lead to improved assessment of petrophysical properties.

In our simulation model, we assumed a single-layer homogeneous and isotropic formation and considered *a-priori* knowledge of porosity, rate of mud-filtrate invasion, properties of mud filtrate, and PVT data of formation fluids. Presence of noise in the measurements and uncertainty in both *a-priori* information and flow rates imposed by the WFT can bias the estimation results, as investigated previously in chapter 5. Non-uniqueness of the inversion will increase in the presence of shale laminations because measurements acquired with a probe-type WFT are less sensitive to spatially varying formation properties than measurements acquired with a packer-type WFT (Angeles et al., 2007). In such instances, estimating multi-layer formation and petrophysical properties from WFT measurements can be challenging.

### 7.8 CONCLUSIONS

The following concluding remarks stem from the simulations and inversion exercises performed in this chapter:

1. Fluid-sample quality improves in the presence of WBM-filtrate invasion when using a focused-probe geometry and two flow lines to measure fractional flow separately. The specific time of cleanup depends on the invasion front, petrophysical properties of the formation, and mobility of the formation fluids. Sharp invasion fronts in a gas-bearing formation decrease the efficiency of focused fluid sampling due to faster breakthrough of native hydrocarbons. We observe that in an oil-bearing formation, focused sampling provides a time savings of 28% over conventional fluid sampling. However, in a gas-bearing

formation, focused sampling provides only marginal time savings over conventional fluid sampling.

2. Dispersion of the fluid-saturation front decreases the efficiency of fluid displacement and requires extended pumpout to withdraw clean fluids. Focusing provides faster fluid cleanup compared to a conventional probe in the presence of a dispersed fluid saturation front because it channels fluids through two flow lines. By the same token, cleanup is faster in good-quality than in poor-quality rock formations.
3. Inversion exercises indicate that fractional flow and pressure transients offer valuable information to determine saturation-dependent properties. Simulations show that focused sampling provides additional degrees of freedom compared to conventional sampling to estimate relative permeability and capillary pressure curves. In addition, we observed that estimates of relative mobility and irreducible water saturation improved with focused sampling for all three synthetic rock formations.
4. Faster decay of the fractional flow for Rock No. 3 (good quality) confirms the difficulty of estimating relative permeability, and indicates the lack of measurement sensitivity for appraising saturation-dependent petrophysical properties in a gas zone with shallow invasion. Inversion results show that permeability and relative permeability are interdependent on pressure drop; therefore, estimating them independently from formation tester measurements is challenging.
5. Both variance of petrophysical properties and interdependence of permeability and relative permeability on pressure drop can increase the non-uniqueness of inversion results. In such instances, coupling formation tester measurements with

resistivity logs, nuclear logs, and core-data can help to reduce non-uniqueness in the estimation of formation properties. Multi-pulse flow rate schedules can also increase the sensitivity of fractional flow to petrophysical properties.

Table 7.1: Equation-of-state parameters and mole fractions of fluid components assumed in this chapter to describe the behavior of in-situ fluid.

| Parameter | Gas Zone | Oil Zone |
|---|---|---|
| Molar Concentration | 1.0 | 1.0 |
| Critical Temperature ($^o$F) | -125.7 | 359.8 |
| Critical Pressure (psi) | 653.3 | 498.2 |
| Acentric Factor | 0.0105 | 0.2302 |
| Molar Weight (lbs/lb-mols) | 16.6 | 67.73 |
| Volume Shift Parameter | -0.193 | -0.056 |
| Fluid Density (g/cc) | 0.24 | 0.69 |
| Fluid Viscosity (cp) | 0.03 | 0.44 |

Table 7.2: Summary of petrophysical properties for the three synthetic rock types considered in this chapter. The Brooks-Corey parametric parameters are explained in Equations 7.1-7.3.

| Case | $S_{wr}$ | $S_{or}$ | $k^0_{rw}$ | $k^0_{ro}$ | $\ell$ | $P^0_{ce}$ (psi) | $k$ (mD) | $\phi$ |
|---|---|---|---|---|---|---|---|---|
| Rock No. 1 | 0.35 | 0.2 | 0.2 | 0.8 | 2.0 | 2.0 | 50 | 0.12 |
| Rock No. 2 | 0.3 | 0.2 | 0.2 | 0.8 | 2.0 | 1.0 | 150 | 0.18 |
| Rock No. 3 | 0.22 | 0.2 | 0.2 | 0.8 | 2.1 | 0.75 | 250 | 0.32 |

Table 7.3: Summary of the assumed petrophysical and fluid properties for all simulation cases considered in this chapter.

| Property | Units | Value |
|---|---|---|
| Mud-filtrate invasion duration | Hours | 36 |
| Formation-test duration | Hours | 3 |
| Conventional-probe flow rate | RB/Day | 8 |
| Focused-probe flow rate | RB/Day | 6 |
| Sample-probe flow rate | RB/Day | 2 |
| Invasion flow rate | ft3/day/ft | 0.576 |
| Temperature | °F | 140 |
| Formation pressure | psi | 6800 |
| Formation compressibility | 1/psi | $10^{-8}$ |
| Water compressibility | 1/psi | $3\text{x}10^{-6}$ |
| Water density | g/cc | 1.0 |
| Water viscosity | cp | 1.0 |

Table 7.4: Summary of final fractional flow values in percentage obtained at the end of fluid sampling for all the simulation cases considered in the chapter. Fluid sampling time is three hours for all the study cases.

| Sensitivity Case | Guard Line Fractional Flow | Sample Line Fractional Flow | Conventional Probe Fractional Flow | Time Savings |
|---|---|---|---|---|
| Rock No. 1, Oil Zone | 10.95 % | 6.46 % | 9.82 % | 28.5 % |
| Rock No. 2, Oil Zone | 8.09 % | 4.81 % | 7.27 % | 28.1 % |
| Rock No. 3, Oil Zone | 5.93 % | 3.39 % | 5.28 % | 27.1 % |
| Rock No. 1, Gas Zone | 2.32 % | 2.03 % | 2.24 % | 9.8 % |
| Rock No. 2, Gas Zone | 1.63 % | 1.50 % | 1.6 % | 5.3 % |
| Rock No. 3, Gas Zone | 1.15 % | 1.06 % | 1.13 % | 5.2 % |

Table 7.5: Summary of inversion results for saturation-dependent Brooks-Corey parameters and absolute permeability. Permeability is given in mD and capillary entry pressure is given in psi. Initial and irreducible water saturations are assumed identical. Table 3 describes the petrophysical properties of the three rock types considered for inversion.

| Case | Inversion Loop | $S_{wr}$ | $S_{or}$ | $k^o_{rw}$ | $k^o_{ro}$ | $\ell$ | $P^o_{ce}$ | $k$ |
|---|---|---|---|---|---|---|---|---|
| Initial Guess | | 0.1 | 0.1 | 0.5 | 0.5 | 2.5 | 1.5 | 100 |
| Focused Probe (Rock No. 1) | Fractional Flow Loop 1 | 0.33 | 0.207 | 0.104 | 0.549 | 2.417 | 1.376 | |
| | Pressure Loop 1 | | | | | | | 80.4 |
| | Fractional Flow Loop 2 | 0.335 | 0.193 | 0.125 | 0.508 | 1.973 | 1.778 | |
| | Pressure Loop 2 | | | | | | | 80.5 |
| Conventional Probe (Rock No. 1) | Fractional Flow Loop 1 | 0.325 | 0.205 | 0.101 | 0.534 | 2.439 | 1.375 | |
| | Pressure Loop 1 | | | | | | | 76.7 |
| | Fractional Flow Loop 2 | 0.302 | 0.172 | 0.127 | 0.501 | 2.051 | 1.591 | |
| | Pressure Loop 2 | | | | | | | 76.3 |
| Focused Probe (Rock No. 2) | Fractional Flow Loop 1 | 0.299 | 0.199 | 0.206 | 0.827 | 2.006 | 1.448 | |
| | Pressure Loop 1 | | | | | | | 148.3 |
| | Fractional Flow Loop 2 | 0.302 | 0.201 | 0.201 | 0.794 | 2.038 | 1.042 | |
| | Pressure Loop 2 | | | | | | | 148.4 |
| Conventional Probe (Rock No. 2) | Fractional Flow Loop 1 | 0.290 | 0.202 | 0.192 | 0.850 | 2.180 | 1.454 | |
| | Pressure Loop 1 | | | | | | | 138.4 |
| | Fractional Flow Loop 2 | 0.307 | 0.204 | 0.215 | 0.860 | 2.006 | 1.035 | |
| | Pressure Loop 2 | | | | | | | 139.6 |
| Focused Probe (Rock No. 3) | Fractional Flow Loop 1 | 0.214 | 0.207 | 0.130 | 0.586 | 2.364 | 1.406 | |
| | Pressure Loop 1 | | | | | | | 323.1 |
| | Fractional Flow Loop 2 | 0.222 | 0.202 | 0.153 | 0.618 | 2.110 | 0.755 | |
| | Pressure Loop 2 | | | | | | | 323.1 |
| Conventional Probe (Rock No. 3) | Fractional Flow Loop 1 | 0.212 | 0.207 | 0.136 | 0.611 | 2.338 | 1.329 | |
| | Pressure Loop 1 | | | | | | | 310.4 |
| | Fractional Flow Loop 2 | 0.221 | 0.201 | 0.159 | 0.636 | 2.142 | 0.768 | |
| | Pressure Loop 2 | | | | | | | 309.9 |
| Focused Probe (Rock No. 2) -10% uncertainty in rate of mud-filtrate invasion | Fractional Flow Loop 1 | 0.319 | 0.211 | 0.176 | 0.673 | 2.369 | 1.452 | |
| | Pressure Loop 1 | | | | | | | 155.9 |
| | Fractional Flow Loop 2 | 0.331 | 0.216 | 0.192 | 0.738 | 2.082 | 0.825 | |
| | Pressure Loop 2 | | | | | | | 160.8 |
| Conventional Probe (Rock No. 2) -10% uncertainty in rate of mud-filtrate invasion | Fractional Flow Loop 1 | 0.308 | 0.204 | 0.170 | 0.634 | 2.343 | 1.456 | |
| | Pressure Loop 1 | | | | | | | 163.8 |
| | Fractional Flow Loop 2 | 0.342 | 0.223 | 0.182 | 0.693 | 2.094 | 0.866 | |
| | Pressure Loop 2 | | | | | | | 170.6 |
| Focused Probe (Rock No. 2) -10% uncertainty in porosity | Fractional Flow Loop 1 | 0.276 | 0.204 | 0.172 | 0.886 | 2.261 | 1.535 | |
| | Pressure Loop 1 | | | | | | | 135.7 |
| | Fractional Flow Loop 2 | 0.291 | 0.196 | 0.220 | 0.894 | 1.991 | 1.049 | |
| | Pressure Loop 2 | | | | | | | 136.4 |
| Conventional Probe (Rock No. 2) -10% uncertainty in porosity | Fractional Flow Loop 1 | 0.275 | 0.206 | 0.172 | 0.896 | 2.295 | 1.528 | |
| | Pressure Loop 1 | | | | | | | 129.1 |
| | Fractional Flow Loop 2 | 0.296 | 0.198 | 0.231 | 0.935 | 1.982 | 1.075 | |
| | Pressure Loop 2 | | | | | | | 131.6 |

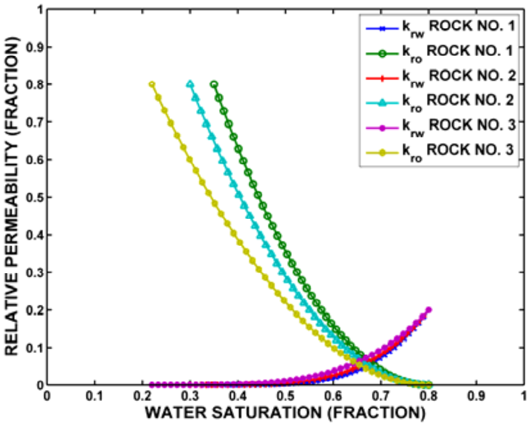

Figure 7.1: Water-oil relative permeability curves assumed in the simulations of mud-filtrate invasion and fluid pumpout for three different synthetic rock types. The figure describes relative permeability curves as a function of water saturation for water (“krw”) and oil (“kro”) phases, respectively. Irreducible oil saturation is 0.2 for all three synthetic rock types.

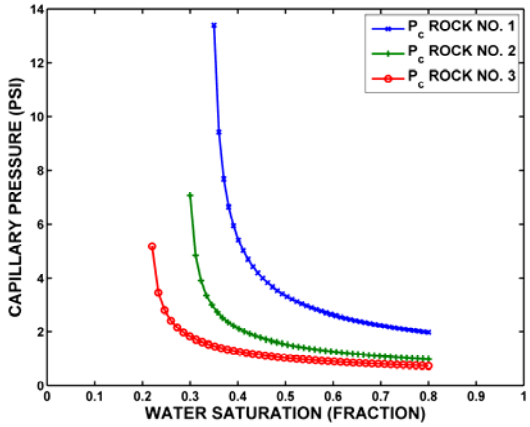

Figure 7.2: Water-oil capillary pressure curves assumed in the simulations of mud-filtrate invasion and fluid pumpout for three different synthetic rock types. Irreducible oil saturation is 0.2 for all three synthetic rock types.

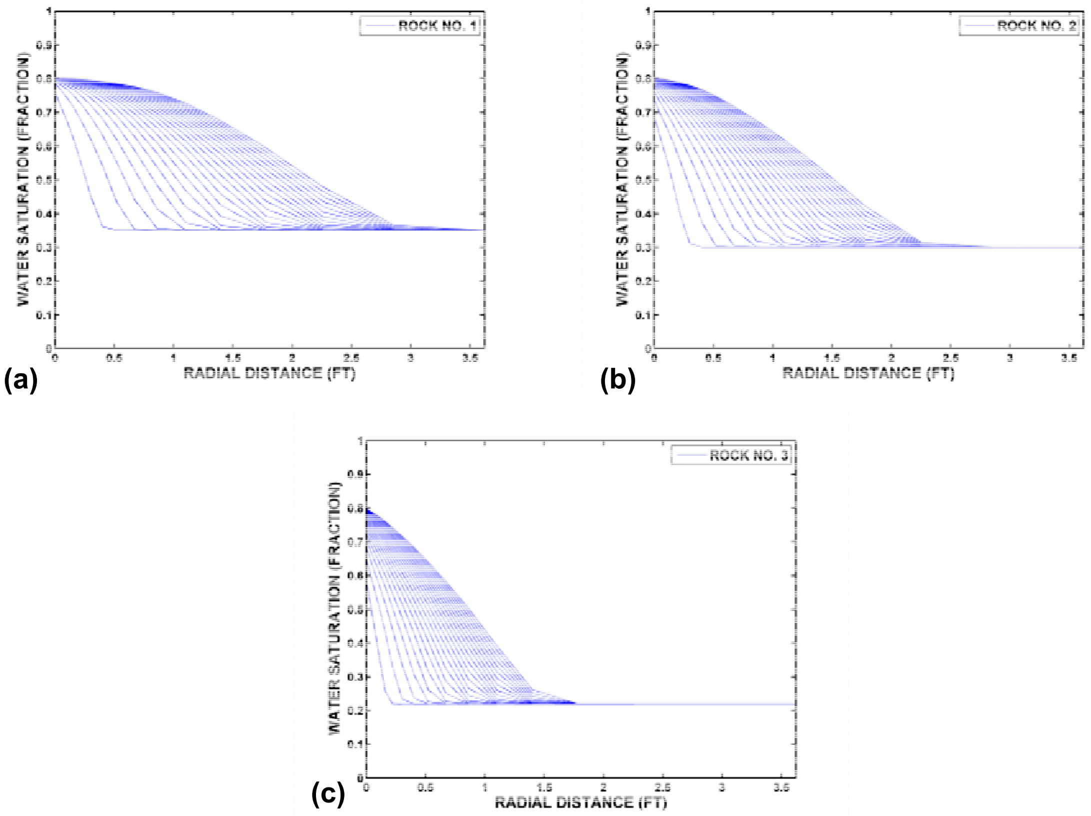

Figure 7.3: Simulated time-space variations of water saturation in an oil zone during the process of mud-filtrate invasion for the three synthetic rock types. Twenty-four curves are shown at time increments of 1.5 hours after the onset of invasion.

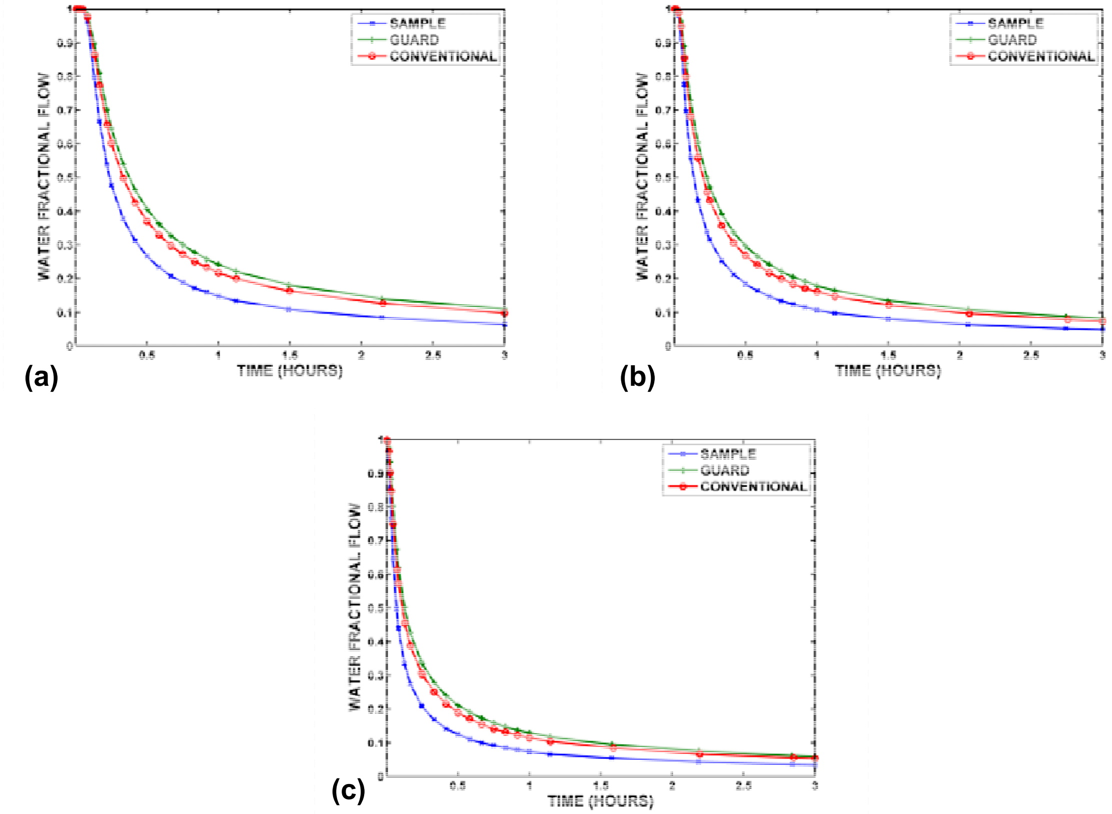

Figure 7.4: Comparison of transient, water fractional flow measurements in an oil zone simulated with focused and conventional probes for the three synthetic rock types. Labels “guard,” “sample,” and “conventional” identify fractional flow of water simulated at the guard-probe flow line, the sample-probe flow line, and the conventional-probe flow line, respectively.

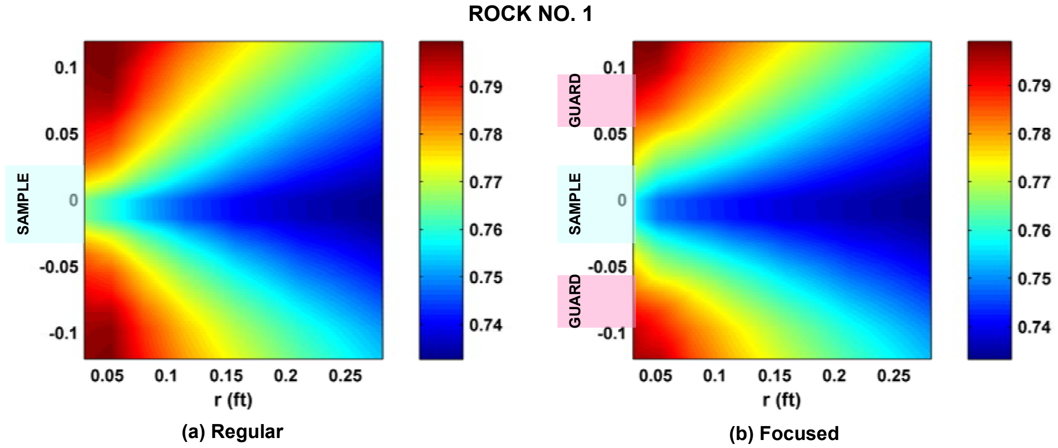

(a) Regular

(b) Focused

Figure 7.5: Spatial distribution (radial and vertical directions) of water saturation in an oil zone in the near-probe region after 5 minutes of fluid sampling with conventional (left-hand panel) and focused (right-hand panel) probes for Rock No. 1 in the presence of invasion. For the focused probe, sample- and guard-line openings extend from -0.0417 ft to +0.0417 ft and -0.0833 ft to +0.0833 ft, respectively, in the vertical direction. The conventional probe is modeled with the same area as that of the sample line of the focused probe.

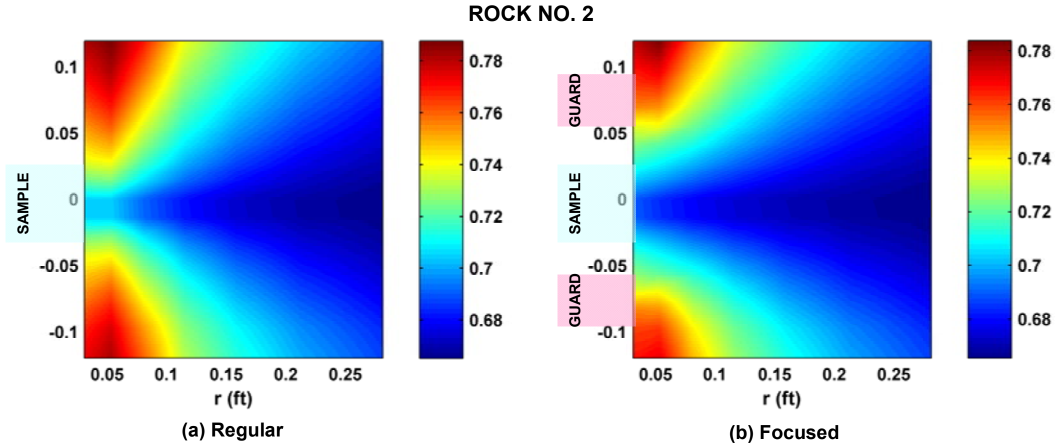

(a) Regular

(b) Focused

Figure 7.6: Spatial distribution (radial and vertical directions) of water saturation in an oil zone in the near-probe region after 5 minutes of fluid sampling with conventional (left-hand panel) and focused (right-hand panel) probes for Rock No. 2 in the presence of invasion. For the focused probe, sample- and guard-line openings extend from -0.0417 ft to +0.0417 ft and -0.0833 ft to +0.0833 ft, respectively, in the vertical direction. The conventional probe is modeled with the same area as that of the sample line of the focused probe.

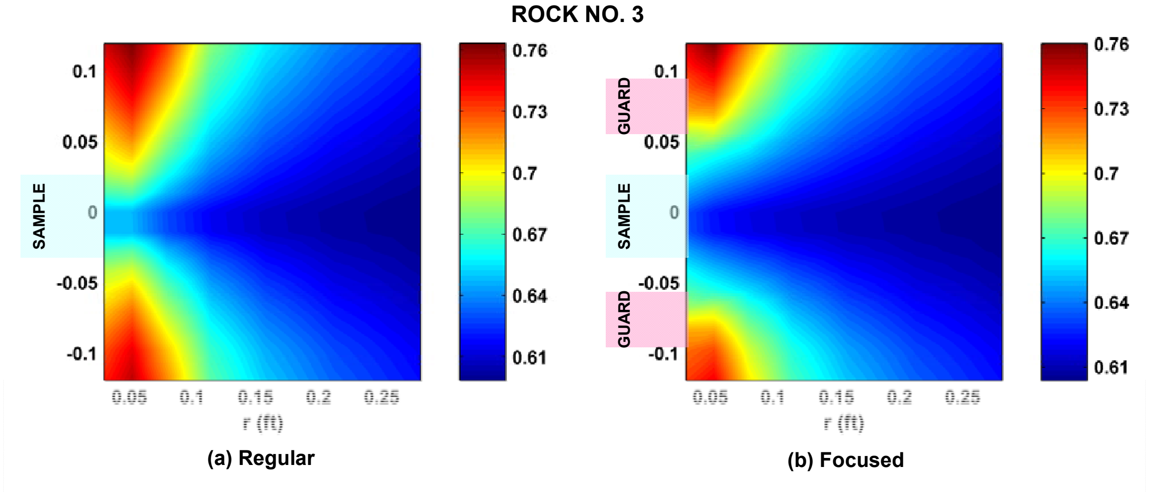

(a) Regular

(b) Focused

Figure 7.7: Spatial distribution (radial and vertical directions) of water saturation in an oil zone in the near-probe region after 5 minutes of fluid sampling with conventional (left-hand panel) and focused (right-hand panel) probes for Rock No. 3 in the presence of invasion. For the focused probe, sample- and guard-line openings extend from -0.0417 ft to +0.0417 ft and -0.0833 ft to +0.0833 ft, respectively, in the vertical direction. The conventional probe is modeled with the same area as that of the sample line of the focused probe.

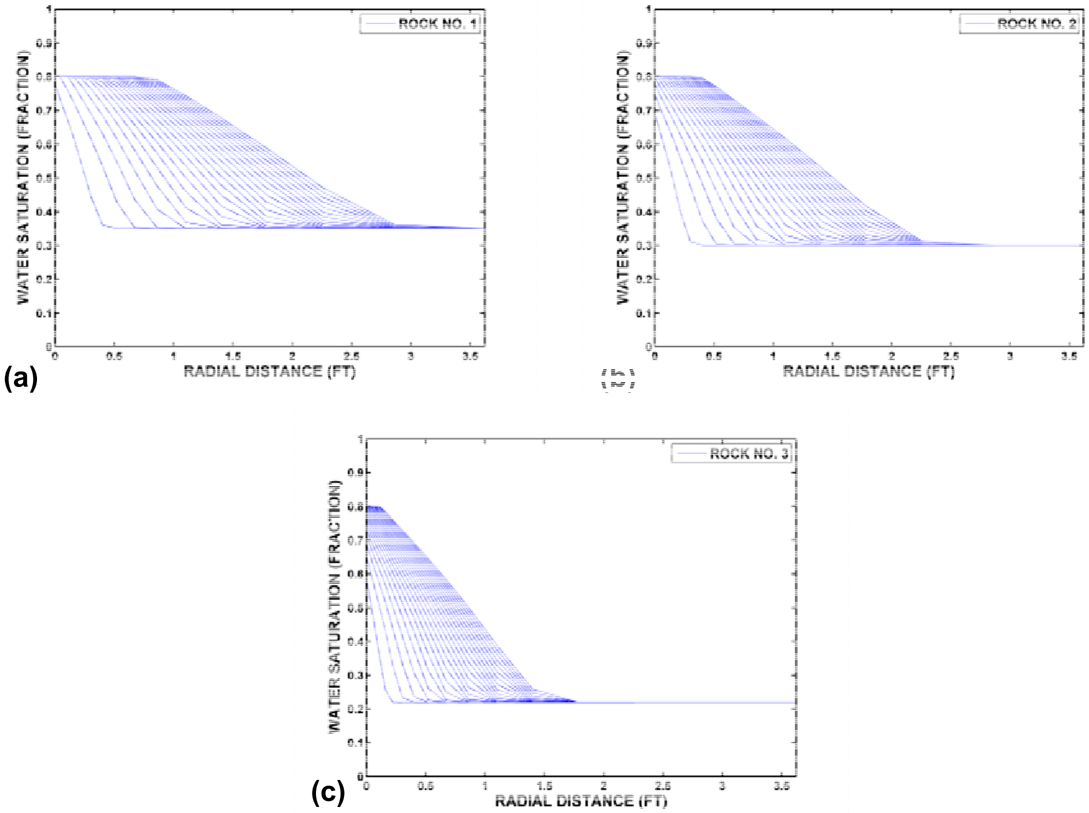

Figure 7.8: Simulated time-space variations of water saturation in a gas zone during the process of mud-filtrate invasion for the three synthetic rock types. Twenty-four curves are shown at time increments of 1.5 hours after the onset of invasion.

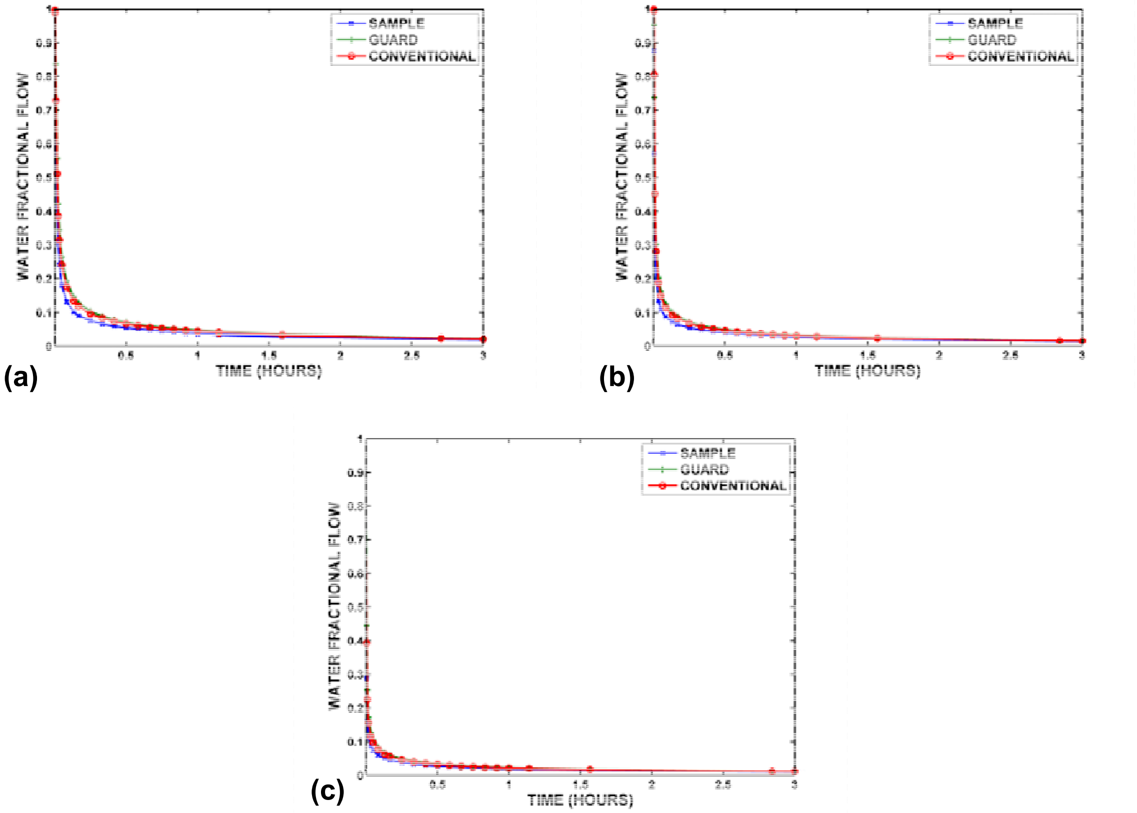

Figure 7.9: Comparison of transient, water fractional flow measurements in a gas zone simulated with focused and conventional probes for the three synthetic rock types. Labels “guard,” “sample,” and “conventional” identify fractional flow of water at the guard probe flow line, the sample probe flow line, and the conventional probe flow line, respectively.

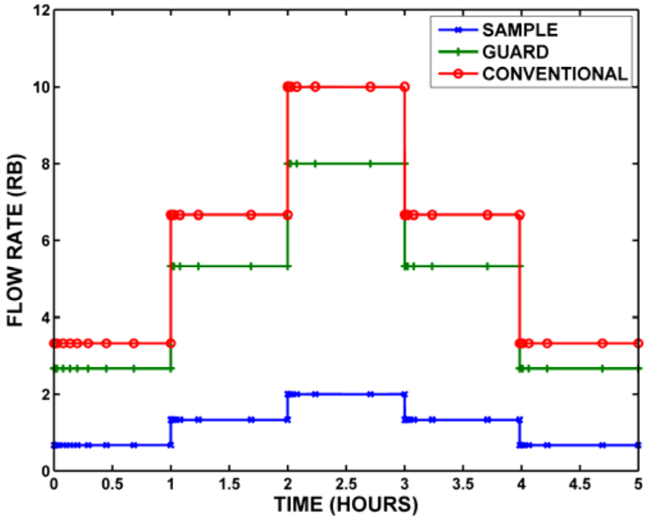

Figure 7.10: Multi-pulse flow-rate schedule used for the estimation of Brooks-Corey relative permeability and capillary pressure parameters. A constant flow rate ratio of 1:4 is enforced at the sample and guard lines of the focused probe. Labels "guard," "sample," and "conventional" identify fractional flow of water at the guard probe flow line, the sample probe flow line, and the conventional probe flow line, respectively.

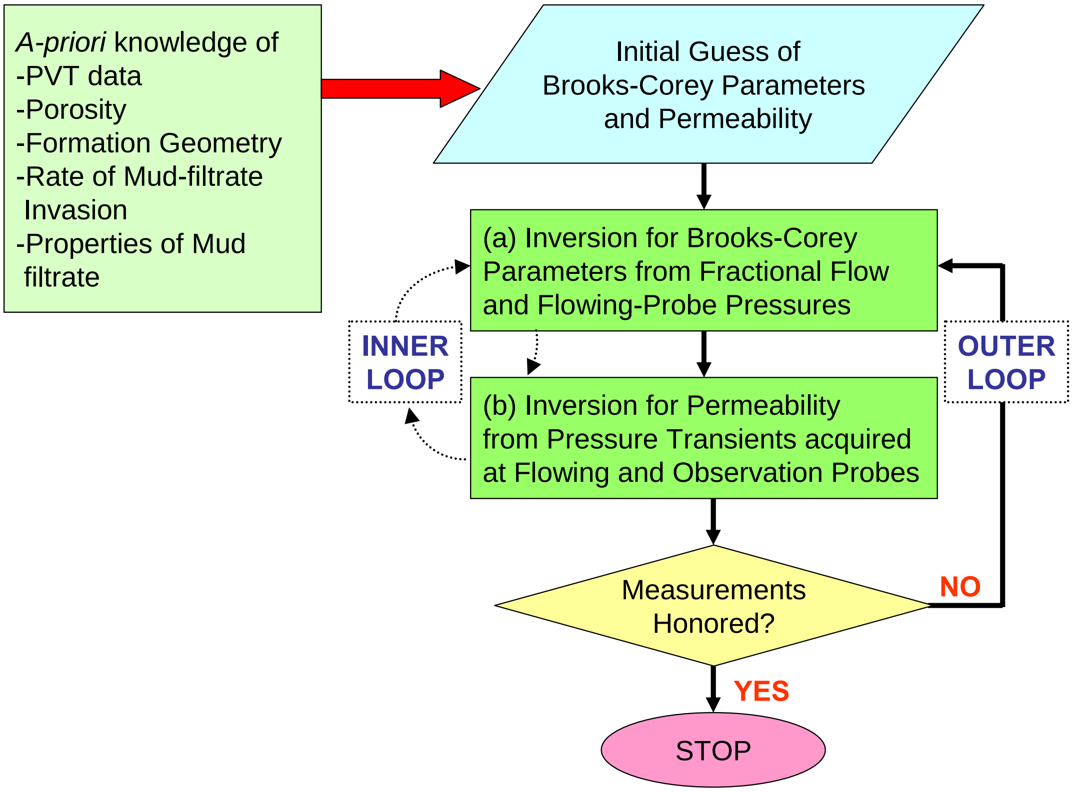

Figure 7.11: Flowchart of the two-loop minimization algorithm used in this chapter to jointly estimate (a) Brooks-Corey parameters from transient measurements of fractional flow and flowing-probe pressure, and (b) permeability from transient measurements of pressure acquired at sink and observation probes. The inner loop proceeds for a maximum of two iterations.

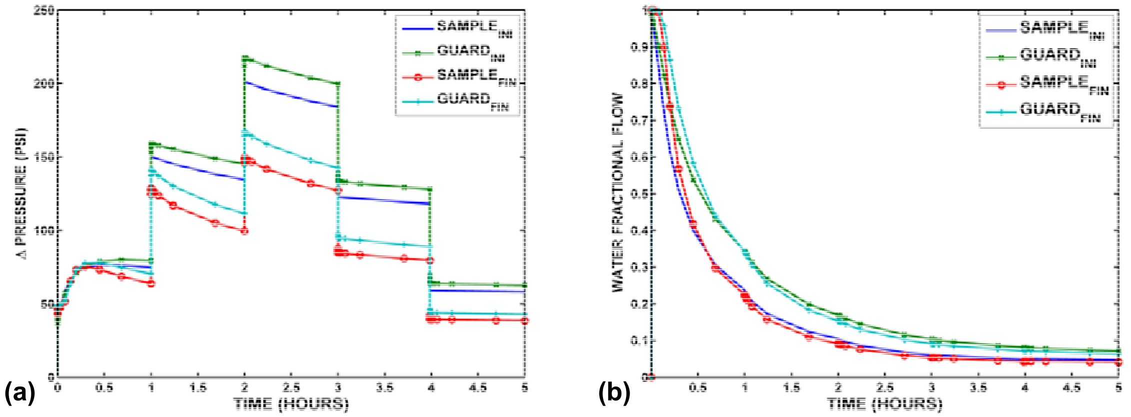

Figure 7.12: Panel (a) shows the impact of the initial guess and final estimates for Brooks-Corey parameters on the sandface pressure simulated at the focused fluid probe for Rock No. 2. Panel (b) shows the corresponding impact on the fractional flow of water.

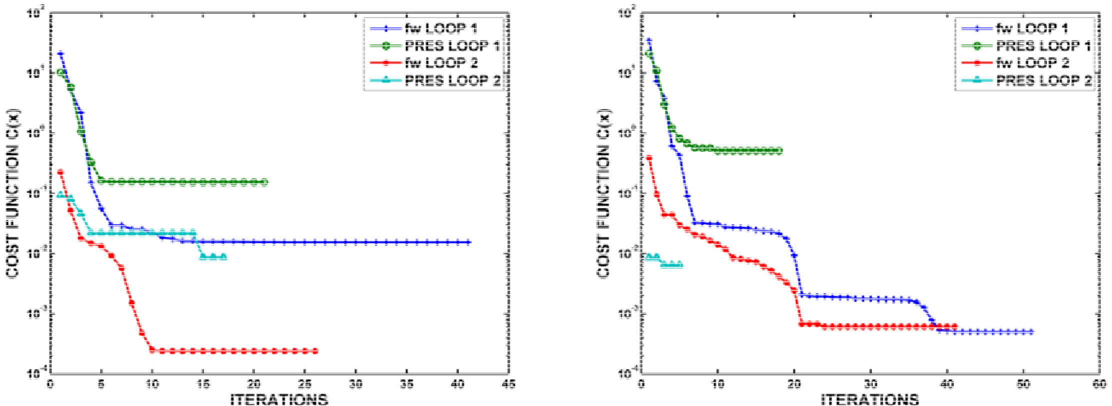

(a) Conventional

ROCK NO. 2

(b) Focused

Figure 7.13: Cost function as a function of iteration number for different inversion loops. Panel (a) shows the convergence of the (noise-free) two-loop minimization technique applied to synthetic measurements acquired with the conventional probe. Panel (b) shows the convergence of the (noise-free) two-loop minimization technique applied to synthetic measurements acquired with the focused probe.

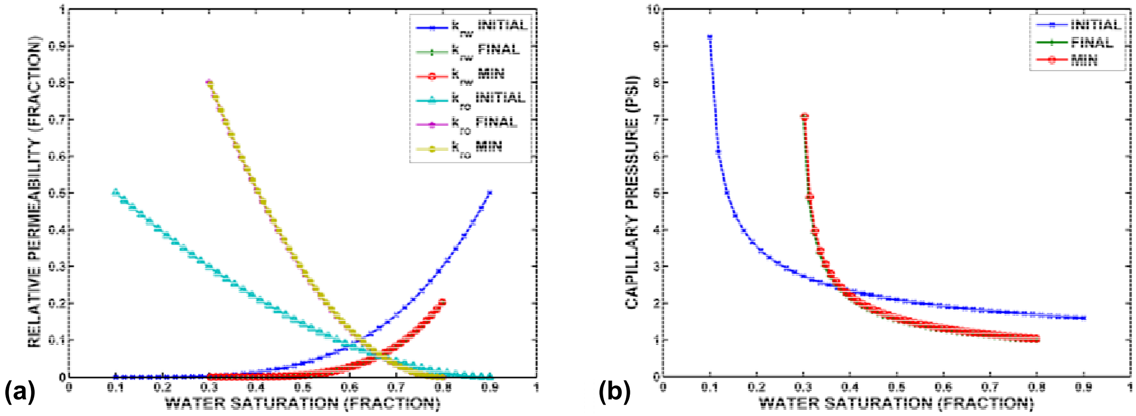

Figure 7.14: Initial and estimated two-phase relative permeability and capillary pressure curves for Rock No. 2.

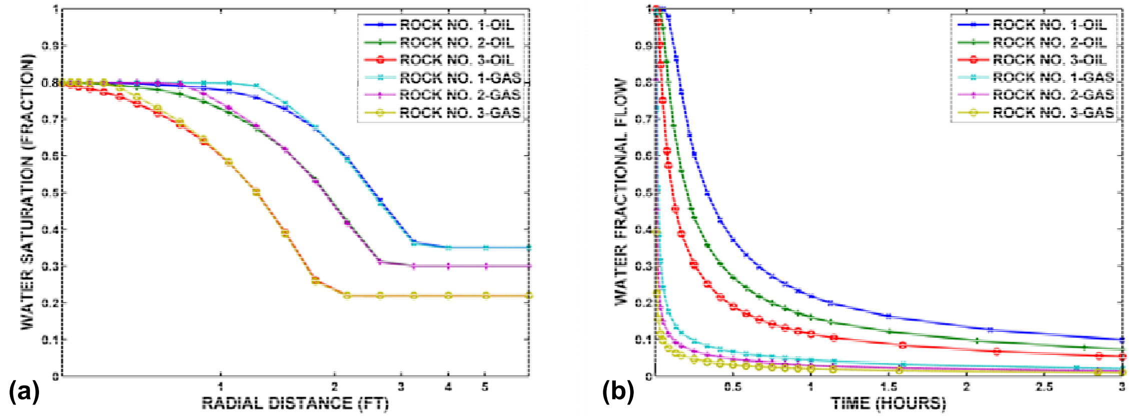

Figure 7.15: Panel (a) shows the invasion front (water saturation) after 1.5 days for the three synthetic rock-types in oil and gas zones. Panel (b) shows the corresponding impact of the invasion front on fractional flow measurements acquired at the conventional probe.

# Chapter 8: Conclusions and Recommendations

This chapter summarizes the general conclusions of the dissertation and provides recommendations for future research. The objective of this dissertation was three-fold: (1) to quantify the effect of OBM-filtrate invasion on WFT measurements, (2) to estimate in-situ petrophysical properties concomitantly from transient measurements of pressure, flow rate and GOR acquired with formation testers, and (3) to quantify petrophysical, geometrical, and fluid properties that can minimize the time of withdrawal of uncontaminated fluid samples.

We used a multi-component compositional formulation to model accurately the process of mud-filtrate invasion and WFT measurements. Analysis of transient measurements of pressure and fractional flow clearly showed that early-time measurements could be used to reliably estimate petrophysical properties and to diagnose adverse field-operating conditions. Our study also compared the performance of focused and conventional probe-type WFT measurements and assessed factors that enhanced fluid-sample quality and improved the estimation of petrophysical properties.

## 8.1 CONCLUSIONS

The following sections describe the conclusions stemming from the various research projects considered in the dissertation. Each subsection summarizes the most important conclusions for a given research sub-project.

### 8.1.1 Axially Symmetric Compositional Simulation of Formation Tester Measurements

1. Simulation of packer-type formation-tester measurements indicate that the time required to acquire clean fluid samples of formation oil is governed by the

petrophysical and fluid properties of the tested formation, by the radial length of invasion of OBM, and by the flow rates imposed during fluid pumpout. In addition, for reservoirs that are not at irreducible water saturation, the dynamic behavior of fractional flow of water is largely conditioned by both relative permeability and capillary pressure. The pressure differential is very sensitive to both formation permeability and relative mobility of fluids in the near-packer region.

2. Reliable assessment of petrophysical properties from pressure-transient measurements acquired during fluid pumpout requires quantitative understanding of the interplay between oil density, oil viscosity, component concentrations, phase mobility, and fractional flow of water on the space-time evolution of fluid component concentrations in the near-wellbore region.
3. Numerical simulations indicate that transient measurements of oil density and oil viscosity can be used to determine sample quality as both quantities are sensitive to component molar concentrations. The early-time behavior of pressure transients is largely governed by the mobility of mud filtrate.

### 8.1.2 Effects of Petrophysical Properties on Array-Induction Measurements acquired in the presence of Oil-Base Mud-Filtrate Invasion

1. Numerical simulations of EM measurements indicate that resistivity measurements are highly sensitive to porosity and permeability, rock wettability, and rate of mud-filtrate invasion. Alteration of rock wettability in the near-wellbore region increases the mobility of the water phase and influences array-induction measurements. Our simulation results also showed that time-varying radial distribution of fluid properties will lead to corresponding time variations of array-induction measurements. Therefore, to properly quantify the influence of

the process of oil-base mud-filtrate invasion on borehole resistivity measurements, it is important to quantify the mud loss in the invaded formation as well as the duration of the invasion process.

2. Simulation results indicate that it is possible to secure a good match with field measurements by simultaneously modifying both critical water saturation and rate of mud-filtrate invasion. However, uncertainty on the value of critical water saturation rendered our history matching algorithm difficult to adapt for automatic inversion.
3. We found that the variability of apparent resistivity curves with various radial lengths of investigation was controlled by the rock's relative permeability and capillary pressure. The separation of these curves is relatively large when the rock is preferentially oil wet, whereas the separation is negligible when the rock is preferentially water wet.
4. We showed that array-induction resistivity measurements can be highly affected by deep invasion (1.5 ft to 2 ft) in zones with movable water. The greater the differences between irreducible and initial water saturation, the smoother the radial distribution of water saturation, hence the larger the variability of apparent resistivity curves with different radial lengths of investigation.

### 8.1.3 History Matching and Sensitivity Analysis of Probe-Type Formation-Tester Measurements acquired in the presence of Oil-Base Mud-Filtrate Invasion

1. The comparison of numerical simulations to field measurements helped us to diagnose and quantify adverse field conditions such as noisy data, mud plugging in the sink probe, and sample collection that caused incorrect measurement of flow rate. Some of these conditions would be difficult to detect and appraise without the use of numerical simulations. Comparisons of simulations and field

measurements indicated that numerical simulation is a good alternative to verify the internal consistency and reliability of transient measurements of flow rate, pressure, and GOR.

2. As expected, sand-face pressure exhibited high sensitivity to formation permeability, whereas the fluid contamination function exhibited high sensitivity to the radial length of mud-filtrate invasion. Miscibility of mud filtrate with formation oil affects the early-time behavior of pressure transients because of the accompanying changes of fluid viscosity and GOR transients due to alteration of fluid composition.
3. Uncertainty in the values used for relative permeability and fluid viscosity, as well as inaccurate assessment of movable-water saturation can drastically bias the estimates of permeability obtained from pressure transient measurements.
4. We considered the possibility of time pulsing fluid withdrawal rates to assess whether it was possible to obtain cleaner samples faster than when using a constant flow rate. Simulations showed that fluid cleanup behavior is dependent on the cumulative volume of fluids produced and is negligibly influenced by flow-rate pulsing.
5. The duration of formation tests should be increased drastically to secure clean fluid samples and to increase the cumulative volume of produced fluids for cases of mud-filtrate invasion deeper than 0.5 ft. The flow rate of fluid withdrawal can be increased to increase the cumulative volume of produced fluid. However, this latter acquisition strategy requires careful assessment to prevent high pressure differentials that could cause the sandface pressure to fall below the bubble point.

### 8.1.4 A Dual-Grid Automatic History Matching Technique with Applications to 3D Formation Testing in the presence of Oil-Base Muds

8. Inversion exercises performed on synthetic and field measurements showed that the hybrid minimization method yielded reliable estimates of permeability and anisotropy and was more efficient than the corresponding inversion implemented with 3D simulations. In our 2D grid, we did not model invasion and were still able to obtain reliable permeability estimates, within 2% of target values in most cases and with 20% CPU time of the time required for the inversion with 3D simulations.
9. We performed sensitivity analyses of our inversion technique and observed that estimates of permeability and anisotropy were dependent on specific assumptions made about fluid mobility, i.e. relative permeability and viscosity. Flow rates of fluid withdrawal can drastically affect permeability estimates. Therefore, it is essential to remove noise from field measurements prior to performing inversion to secure reliable and accurate estimates of permeability.
10. Because filtrate viscosity is higher than light-oil viscosity, mud-filtrate invasion can influence the early-time behavior of pressure transients. In such instances, GOR can provide useful information to determine the radial length of invasion.
11. In the case of near-wellbore formation damage due to invasion, it is difficult to obtain reliable permeability estimates. This behavior shows that radially-varying permeability estimates and formation heterogeneity are difficult to diagnose and quantify from pressure transient measurements acquired with a probe-type WFT.
12. The performance of the hybrid inversion technique degrades if we model OBM-filtrate invasion in the 2D simulations. Modeling mud-filtrate invasion increases the computational time of 2D simulations, while pressure measurements do not

correlate well with the 3D simulation due to transient variations. In high permeability formations, the pressure drop in 2D simulations is relatively low and the minimization converges to a local minima. We are limited by 6 decimal places of precision when using the commercial simulator and this affects the numerical perturbation required to calculate both the Jacobian matrix and the cost function.

13. Underlying the hybrid inversion method is the assumption that we neglect azimuthal permeability variations. Our algorithm is not reliable if radial permeability is different from azimuthal permeability.
14. We evaluated the hybrid inversion method on field measurements and observed that the estimated values of permeability were within 0.07% of those obtained with the corresponding 3D inversion but within 15% of the CPU time. However, quality checks are necessary to reduce deleterious noise from pressure measurements prior to performing the inversion as well as to determine the associated flow rate of fluid withdrawal and radial length of invasion. We found that early-time pressure measurements could provide useful information to quantify fluid and formation properties.

### 8.1.5 Comparison of Wireline Formation-Tester Sampling with Focused and Conventional Probes in the presence of Oil-Base Mud-Filtrate Invasion

1. Fluid-sample quality improves in the presence of mud-filtrate invasion when using a focused-probe geometry and two flow lines to measure GOR separately. On average, numerical simulations indicate a 58% time savings when using a focused probe. If the focused and conventional probes withdraw fluids for the same time period, focused fluid sampling provides an improvement in GOR by 8.2%. The efficiency of fluid cleanup depends on both probe geometry and formation properties that can alter flow streamlines, including porosity and

presence of movable water. It was found that focusing becomes more effective in the presence of dispersed invasion fronts. Sharp invasion fronts or high mobility contrasts between mud filtrate and formation hydrocarbons decrease the efficiency of focused fluid sampling.

2. Anisotropy, shale boundaries, and thin beds provide a natural focusing mechanism for formation fluids. Thus, the advantage of using a focused probe over a conventional probe may be redundant under the latter field conditions as a conventional probe becomes the most economical alternative to fluid sampling.
3. Increasing the flow-rate ratio between the sample and guard probes can help to expedite fluid-sample quality by causing preferential flow of mud filtrate into the guard region. However, design restrictions may limit the maximum flow rate that can be used to withdraw fluids by the guard pump.
4. Pulsing of the flow rates between the guard and sample regions can help to improve sample quality by gradually increasing the flow rate at the guard line. Withdrawing fluids through three channels as opposed to the two channels used in the focused probe can also help to improve sample quality as the cleaner fluid preferentially flows through the sample line. Sample quality may decrease with a focused probe if mud plugging occurs in the smaller openings of the guard region.
5. Inversion exercises performed on synthetic measurements showed that the two-loop minimization method yields reliable estimates of permeability, anisotropy, and rate of mud-filtrate invasion. Results show improved estimation of invasion with the focused probe as it withdraws fluids from two channels, thereby increasing the redundancy of input data available for the estimation.

### 8.1.6 Estimation of Parametric Models of Capillary Pressure and Relative Permeability from Focused Formation-Tester Measurements

1. Fluid-sample quality improves in the presence of WBM-filtrate invasion when using a focused-probe geometry and two flow lines to measure fractional flow separately. The specific amount of cleanup depends on the invasion front, petrophysical properties of the formation, and mobility of the formation fluids. Sharp invasion fronts in a gas-bearing formation decrease the efficiency of focused fluid sampling due to faster breakthrough of native hydrocarbons. We observe that in an oil-bearing formation, focused sampling provides a time savings of 28% over conventional fluid sampling. However, in a gas-bearing formation, focused sampling provides only marginal time savings over conventional fluid sampling.
2. Dispersion of the fluid saturation front decreases sweep efficiency and requires extended pumpout to withdraw clean fluids. Focusing provides better fluid cleanup compared to a conventional probe in the presence of a dispersed fluid saturation front by channeling fluids in two flow lines. Cleanup is faster in good-quality rock formations as opposed to poor-quality rock formations.
3. Inversion exercises indicate that fractional flow and pressure transients can offer valuable information to determine saturation-dependent properties. Simulations show that focused sampling provides additional degrees of freedom compared to conventional sampling to estimate relative permeability and capillary pressure curves. In addition, we observed that estimates of relative mobility and irreducible water saturation are improved with focused sampling for all three rock formations.

4. Faster decay of the fractional flow for Rock No. 3 (good quality) demonstrates the difficulty of estimating relative permeability, and indicates the lack of measurement sensitivity for appraising saturation-dependent petrophysical properties in a gas zone with shallow invasion. Inversion results show that permeability and relative permeability are interdependent on pressure drop, therefore estimating them independently from WFT measurements is challenging.
5. Both variance of petrophysical properties and interdependence of permeability and relative permeability on pressure drop can increase the non-uniqueness of the inversion results. In such instances, coupling WFT measurements with resistivity logs, neutron logs, and core-data can help to reduce non-uniqueness in the estimation of formation properties. A multi-pulse flow rate schedule can also increase the sensitivity of the fractional flow to petrophysical properties.

## 8.2 RECOMMENDATIONS FOR FUTURE RESEARCH

The following list itemizes some suggested avenues for future research on topics related to the projects considered in this dissertation:

1. The mud-filtrate invasion process proposed in this dissertation is based on the assumption of a radial formation model penetrated by a vertical well. Forward modeling does not involve eccentric invasion flow in deviated or horizontal wells. Because many field examples involve eccentric invasion in deviated wells, the scope of our work is limited to understanding the invasion process in a vertical well. Further research is recommended to understand the invasion and fluid pumpout processes in horizontal and deviated wells.
2. In modeling WFT measurements, we assumed that only mud filtrate invaded the formation. However, most oil-based mud systems are emulsions with water as a constituting component. Formation-tester measurements can be affected by the

presence of water if the latter drops out of the oil phase. Resistivity modeling showed that array-induction measurements are sensitive to alterations of rock wettability due to invasion. However, the interplay of invasion and rock wettability is difficult to quantify with the simulation examples considered in this dissertation. Further experimental and field work is recommended to improve the understanding of the invasion process in the near-wellbore region in the presence of oil-base mud systems.

3. The simulation of mud-filtrate invasion assumes that formation properties such as porosity, relative permeability, and permeability remain constant during that process. In field cases, mud filtration and drilling may cause formation damage in the form of external solidification. As a result, near-wellbore formation properties could be altered. In addition, formation testers could formation damage in the near-wellbore region in unconsolidated formations. In this dissertation, the invasion process was modeled with a radial length of invasion in the formation and with a volume-averaged invasion rate. However, experimental results indicate that invasion begins with a high-flow rate due to the overbalance pressure in the wellbore, and the invasion rate gradually decreases with time as the pressure in the well equilibrates with the reservoir pressure due to the formation of mudcake. An oil-base mud invasion model is recommended that takes into account emulsified mud systems, overbalance pressure, formation damage, and formation of mud cake when performing the simulations of invasion.
4. The inversion and history matching algorithms developed in this dissertation should be applied to more field data sets in order to quantify and further evaluate the practical limitations of noisy and imperfect WFT measurements. Simulation exercises with the focused probe showed its practical advantages over

conventional probe. However, the performance of the focused probe may vary significantly under a variety of field conditions as the smaller guard line openings could be blocked by fines, sand, and mud particles. It is suggested that history matching be performed with field data sets acquired with focused probe measurements to appraise their validity and reliability as well as to diagnose adverse data-acquisition conditions.

5. Simulations described in this dissertation considered a constant flow rate in both guard and sample flow lines of the focused probe. Ideally, the flow rates could be automatically adjusted in response to differential values of GOR and pressure between the two probes to optimize fluid sampling. Such a dynamic feedback loop could lead to improved fluid-cleanup time under a wide range of formation and fluid conditions.
6. It was shown that estimating Brooks-Corey parameters from fractional flow measurements can yield non-unique results. Non-uniqueness could be reduced if initial and irreducible water saturation are known a-priori from resistivity logs. If a salinity contrast exists between connate water and mud-filtrate, transient measurements of salinity or pH could provide additional degrees of freedom for the estimation. In addition, core measurements could be useful in providing bounds for inversion variables, hence decreasing the interdependence of absolute permeability and relative permeability on pressure differentials. Thus, combining resistivity logs, WFT measurements, and core data acquired in the vicinity of the formation test, with WFT measurements will lead to improved assessment of petrophysical properties.
7. Simulation of WFT measurements in the presence of compositional flow can be computationally expensive. Estimation of petrophysical properties adds another

level of complexity due to repeated numerical simulations. Enhanced computational efficiency could be achieved with multi-level parallelization of fluid modeling and by implementing parallel inversion algorithms.

# Glossary

$a$ : Archie's tortuosity coefficient, []

$B$ : Equivalent conductance of conterions, [$\mathrm{cm}^2/(\Omega.\mathrm{meq})$]

$c_f$ : Formation compressibility, [1/psi]

$C(t)$ : Contamination function, []

$C(\mathbf{x})$ : Quadratic cost function, []

$\mathbf{e}(\mathbf{x})$ : Data residual vector, []

$\mathbf{e}_{\mathbf{2D}}(\mathbf{x})$ : 2D pressure residual, []

$\mathbf{e}_{\mathbf{3D}}(\mathbf{x})$ : 3D pressure residual, []

$e_{nw}$ : Empirical exponent for non-wetting phase relative permeability, []

$e_w$ : Empirical exponent for wetting phase relative permeability, []

$\mathbf{f}_{\mathbf{rel}}(\mathbf{x})$ : Transformation vector, []

fw : Fractional flow of water, []

$fw_{guard}$ : Guard-line fractional flow of water at the focused probe, []

$fw_{reg}$ : Conventional-probe fractional flow of water, []

$fw_{sample}$ : Sample-line fractional flow at the focused probe, []

$GOR_{guard}$ : Guard-line GOR at the focused probe, [SCF/STB]

$GOR_p$ : Uncontaminated pure formation GOR, [SCF/STB]

$GOR_{reg}$ : Conventional-probe GOR, [SCF/STB]

$GOR_{sample}$ : Sample-line GOR at the focused probe, [SCF/STB]

$GOR_t$ : Measured GOR, [SCF/STB]

$\mathrm{GUARD}_{\mathrm{INI}}$ : Initial measurements acquired at the guard line of the focused probe, []

$\mathrm{GUARD}_{\mathrm{FIN}}$ : Final measurements acquired at the guard line of the focused probe, []

$\mathbf{I}$ : Identity matrix, []

$i$ : $i^{\mathrm{th}}$ phase

$\mathbf{H}(\mathbf{x})$ : Hessian matrix, []

$\mathbf{h}$ : Small perturbation on the model vector, []

$\mathbf{J}(\mathbf{x})$ : Jacobian matrix, []

$j$ : $j^{\mathrm{th}}$ component

$k$ : Absolute permeability, [mD]

$k_h$ : Horizontal permeability, [mD]

$k_v$ : Vertical permeability, [mD]

$k_h /k_v$ : Permeability anisotropy ratio, [ ]

$k_{ro}^{o}$ : End-point relative permeability to oil phase, []

$k_{ro}$ : Relative permeability to oil phase, []

$k_{rw}$ : Wetting phase relative permeability, []

$k^{0}_{rw}$ : Wetting phase end-point relative permeability, []

$k_{rnw}$ : Non-wetting phase relative permeability, []

$k^{0}_{rnw}$ : Non-wetting phase end-point relative permeability, []

$\ell$ : Pore-size distribution index, []

$m^*$ : Clay-corrected Archie’s cementation exponent, []

$M_i$ : Molecular weight of component $i$, [lbs/lb-mole]

$\mathrm{N_i}$ : Number of moles of component $i$

$n^*$ : Clay-corrected Archie’s saturation exponent, []

$n_c$ : Number of components, []

$\mathrm{n}_p$ : Number of phases, []

$P$ : Pressure, [psi]

$P_c$ : Capillary pressure, [psi]

$P^0{}_c$ : Coefficient for capillary pressure, [psi.Darcy$^{1/2}$]

$P^o_{ce}$ : Capillary entry pressure, [psi]

$\mathrm{p_{obs}}$ : Observed pressure, [psi]

$\mathrm{p_{sim}}$ : Numerically simulated pressure, [psi]

$Q$ : Fluid flow rate [ft$^3$/day]

$Q_{guard}$ : Guard-line flow rate at the focused probe [RB/day]

$Q_{sample}$ : Sample-line flow rate at the focused probe [RB/day]

$Q_v$ : Volumetric concentration of sodium exchange cations, [meq/ml]

$q_i$ : Component molar injection rate [lb-moles/day]

$\mathrm{q_{mf}}$ : Flow rate of oil-base mud-filtrate, [ft$^3$/ft/day]

R10 : 10 inches radial length of investigation apparent resistivity, [Ω.m]

R20 : 20 inches radial length of investigation apparent resistivity, [Ω.m]

R30 : 30 inches radial length of investigation apparent resistivity, [Ω.m]

R60 : 60 inches radial length of investigation apparent resistivity, [Ω.m]

R90 : 90 inches radial length of investigation apparent resistivity, [Ω.m]

$R_t$ : True formation resistivity, [Ω.m]

$R_w$ : Connate water resisitivity, [Ω.m]

$r$ : Radial distance from the wellbore, [ft]

$\mathrm{r}_e$ : External radius, [ft]

$\mathrm{r}_w$ : Wellbore radius, [ft]

$S$ : Phase saturation, [fraction]

$\mathrm{SAMPLE}_{\mathrm{INI}}$ : Initial measurements acquired at the sample line of the focused probe, []

$\mathrm{SAMPLE}_{\mathrm{FIN}}$ : Final measurements acquired at the sample line of the focused probe, []

$S_o$ : Oil phase saturation, [ ]

$S_{or}$ : Irreducible oil saturation, []

$S_w$ : Water saturation, [ ]

$S_{wr}$ : Residual water saturation, []

$t$ : Time, [day]

$T$ : Temperature, [$^{o}$F]

$u_j$ : Darcy velocity of phase $j$

$V_b$ : Bulk volume, [ft$^3$]

$V_p$ : Pore volume, [ft$^3$]

$V_t$ : Total fluid volume [ft$^3$]

$\overline{V}_{ti}$ : Partial derivative of total fluid volume with respect to component $i$, [ft$^3$/lb-moles]

$\mathbf{x}$ : Minimization variable, []

$x_{fo}$ : Formation oil concentration, []

$x_{ij}$ : Mole fraction of component $i$ in phase $j$, [fraction]

$x_{OBM}$ : Oil-based mud concentration, []

$Z$ : Vertical distance, [ft]

$Z_j$ : Compressibility factor of phase $j$, []

## Greek Symbols

:

$\phi$ : Effective porosity, [fraction]

$\eta_{obs}$ : Observed measurement, []

$\eta_{sim}$ : Numerically simulated measurement, []

$\mu_{fo}$ : Formation oil viscosity, [cp]

$\mu_i$ : Viscosity of component $i$, [cp]

$\mu_j$ : Viscosity of phase $j$, [cp]

$\mu_o$ : Oil viscosity, [cp]

$\mu_{OBM}$ : Oil-based mud viscosity, [cp]

$\lambda_o$ : Oil-phase mobility, [1/cp]

$\rho_j$ : Density of phase $j$, [lbf/ft$^3$]

$\rho_{oi}$ : Oil density at the end of invasion, [lbf/ft$^3$]

$\rho_{of}$ : Formation oil density, [lbf/ft$^3$]

$\xi$ : Molar Density [moles/ft$^3$]

$\Phi$ : Potential [psi]

$\sigma$ : Standard deviation of gaussian noise, []

$\Sigma$ : Model covariance matrix, []

## Acronyms

*1D* : One-dimensional

*2D* : Two-dimensional

*3D* : Three-dimensional

*AIM* : Adaptive-implicit

*AIT* : Array induction tool

*ASP* : Alkaline/surfactant/polymer

*CMG* : Computer modelling group limited

*CPU* : Central processing unit

*EM* : Electro magnetic

*EOS* : Equation of state

*GEM* : Generalized equation-of-state model compositional reservoir simulator

*GOR* : Gas-oil ratio

*IMPEC* : Implicit-pressure explicit-concentration

*LBC* : Lohrenz-Bray-Clark

*OBM* : Oil-base mud

*MDT* : Modular formation dynamics tester

*PVT* : Pressure, volume, and temperature

*RB* : Reservoir barrel

*SBM* : Synthetic-base mud

*SCF* : Standard cubic feet

*STB* : Stock tank barrel

*WBM* : Water-base mud

*WFT* : Wireline formation tester

# References

Akkurt, R., Bowcock, M., Davies, J., Campo, C.D., Hill, B., Joshi, S., Kundu, D., Kumar, S., O'Keffe, M., Samir, M., Tarvin, J., Weinheber, P., Williams, S., and Zeybek, M.: "Focusing on downhole fluid sampling and analysis," *Oilfield Review*, Winter 2006.

Alpak, F.O., Dussan V., E.B., Habashy, T.M., and Torres-Verdín, C.: "Numerical simulation of mud filtrate invasion in horizontal wells and sensitivity analysis of array induction tools," *Petrophysics*, v. 44, no. 6, pp. 396-411, 2003.

Alpak, F.O., Torres-Verdín, C., Habashy, T.M., and Sepehrnoori, K.: "Simultaneous estimation of in-situ multi-phase petrophysical properties of rock formations from wireline formation tester and induction logging measurements," paper SPE 90960, presented at the SPE Annual Technical Conference & Exhibition, Houston, September 26-29, 2004.

Alpak, F.O., Elshahawi, H., Hashem, M., and Mullins, O.C.: "Compositional modeling of oil-base mud-filtrate cleanup during wireline formation tester sampling," paper SPE 100393, presented at the SPE Annual Technical Conference and Exhibition, San Antonio, Texas, September 24-27, 2006.

Andrew, R.J., Beck, G., Castelijns, K., Chen, A., Cribbs, M.E., Fadnes, F.H., Irvine-Fortescue, J., Williams, S., Hashem, M., Jamaluddin, A., Kurkjian, A., Sass, B., Mullins, O.C., Rylander, E., and Van Dusen, A.: "Quantifying fluid contamination using color of crude and condensate," *Oilfield Review*, pp. 24-43, Autumn 2001.

Angeles, R., Lee, H.J., Alpak, F.O., Torres-Verdín, C., and Sheng, J.: "Efficient and accurate estimation of permeability and permeability anisotropy from straddle-packer formation tester measurements using the physics of two-phase immiscible flow and invasion," paper SPE 95897, presented at the SPE Annual Technical Conference and Exhibition, Dallas, Texas, October 9-12, 2005.

Angeles, R., Torres-Verdín, C., Yuan, C., and Lee, H.J.: "Spatial sensitivity functions of two-phase formation-tester measurements acquired in vertical wells," *Petrophysics*, v. 48, no. 5, pp. 362-379, October 2007.

Archie, G.E.: "The electrical resistivity log as an aid in determining some reservoir characteristics," *Petroleum Transactions*, *AIME*, v. 146, pp. 54-62, 1942.

Austad, T. and Isom, T. P.: "Compositional and pvt properties of reservoir fluids contaminated by drilling fluid filtrate," *Journal of Petroleum Science and Engineering*, v. 30, pp. 213-244, 2001.

Ayan, C., Hafez, H., Hurst, S., Kuchuk, F., O'Callaghan, A., Peffer, J., Pop, J., and Zeybek, M.: "Characterizing permeability with formation testers," *Oilfield Review*, pp. 2-23, Autumn 2001.

Bourgoyne Jr., A.T., Millheim, K.K., Chenevert, M.E., and Young Jr., F.S.: "*Applied Drilling Engineering*," SPE Textbook Series, v. 2, Richardson, TX, 1986.

Brooks, R.H. and Corey, A.T.: "Hydraulic properties of porous media," *Hydrology Paper 3*, Colorado State University, Fort Collins, Colorado, 1964.

Broyden, C.G.: "A class of methods for solving nonlinear simultaneous equations," *Maths Comp.*, v. 19, pp. 577–593, 1965.

Chang, Y.: "Development and application of an equation of state compositional simulator," Ph.D. Dissertation, The University of Texas at Austin, Austin, Texas, 1990.

Chang, Y. B., Pope, G. A., and Sepehrnoori, K.: "A higher-order finite difference compositional simulator," *Journal of Petroleum Science and Engineering*, v. 5, no. 1, pp. 35-50, November 1990.

Chen, S., Li, G., Peres, A., and Reynolds, A.C.: "A well test for in-situ determination of relative permeability curves," paper SPE 96414, presented at the SPE Annual Technical Conference & Exhibition, Dallas, October 9-12, 2005.

Cheung, P., Hayman, A., Laronga, R., Cook, G., Goetz, P., Marshall, M., Hansen, S., Lamb, M., Li, B., Larsen, M., Orgren, M., and Redden, J.: "A clear picture in oil-base muds," *Oilfield Review*, 13, No. 4, pp. 2-27, Winter 2001.

Chew, W.C., Barone, S., Anderson, B., and Hennessy, C.: "Diffraction of axisymmetric waves in a borehole by bed boundary discontinuities," Geophysics, v. 49, no. 10, pp. 1586-1595, 1984.

Chin, W. C. and Proett, M. A.: "Formation tester immiscible and miscible flow modeling for job planning applications," presented at the SPWLA 46th Annual Logging Symposium, New Orleans, Louisiana, June 26-29, 2005.

Collins, D.A., Nghiem, L.X., Li, Y.K., and Grabenstetter, J.E.: "An efficient approach to adaptive-implicit compositional simulation with an equation of state," *SPERE*, v. 4, no. 6, pp. 259-264, May, 1992.

Corey, A.T.: "*Mechanics of Immiscible Fluids in Porous Media*," Water Resources Publications, Highland Ranch, Colorado, 1994.

Dewan, J.T. and Chenevert, M.E.: "A model for filtration of water-base mud during drilling: determination of mudcake parameters," *Petrophysics*, v. 42, no. 3, May-June, pp. 237-250, 2001.

Dindoruk, B. and Christman, P.G.: "PVT properties and viscosity correlations for gulf of mexico oils," *SPE Res. Eng. & Evaluation,* v. 9, no. 6, pp. 427-437.

Donaldson, E.C. and Siddiqui, T.K.: "Relationship between the Archie saturation exponent and wettability," *SPE Formation Evaluation*, v. 4, no. 3, pp. 359-362, 1989.

Dong, C., Elshahawi, H., Mullins, O.C., Venkataramanan, L., Hows, M., McKinney, D., Flannery, M., and Hashem, M.: "Improved interpretation of reservoir architecture and fluid contacts through the integration of downhole fluid analysis with geochemical and mud gas analyses," paper SPE 109683, presented at the Asia Pacific Oil and Gas Conference and Exhibition, Jakarta, Indonesia, October 30-November 1, 2007.

Dubost, F.X., Zheng, S.Y., and Corbett, P.W.M.: "Analysis and numerical modeling of wireline pressure tests in thin-bedded turbidites," *Journal of Petroleum Science and Engineering*, v. 45, no. 3-4, 2004.

Dussan V., E.B., Anderson, B.I., and Auzerais, F.M.: "Estimating vertical permeability from resistivity logs," paper UU, Transactions of 35th SPWLA Annual Logging Symposium.

Gok, I.M., Onur, M., Hegeman, P.S., and Kuchuk, F.J.: "Effect of an invaded zone on pressure-transient data from multiprobe and packer-probe wireline formation testers," *SPEREE*, v. 9, no. 1, pp. 39-49, February, 2006.

Goode, P.A. and Thambynayagam, R.K.M.: "Influence of an invaded zone on a multiprobe formation tester," *SPE Formation Evaluation*, v. 11, no. 1, pp. 31-40, 1996.

Habashy, T.M. and Abubakar, A.: "A general framework for constraint minimization for the inversion of electromagnetic measurements," *Progress in Electromagnetic Research*, v. 46, pp. 265-312, 2004.

Hashem, M.N., Thomas, E.C., McNeil, R.I., and Mullins O.: "Determination of producible hydrocarbon type and oil quality in wells drilled with synthetic oil-base muds," *SPE Reservoir Evaluation & Engineering*, v. 2, no. 2, April 1999.

Hrametz, A.A., Gardner, C.C., Waid, M.C., and Proett, M.A.: "Focused formation fluid sampling probe," *U.S. Patent no. 6301959 B1*, October 2001.

Koval, E.J.: "A method for predicting the performance of unstable miscible displacement in heterogeneous media," *SPE Journal*, v. 3, no. 2, pp. 145-154, 1963.

Kuchuk, F.J. and Onur, M.: "Estimating permeability distribution from 3D interval pressure transient tests," *Journal of Petroleum Science and Engineering*, v. 39, no. 1-2, pp. 5-27, 2003.

Kumar, S., Wheaton, S., Kundu, D., and Joshi, S.: "Wireline sampling technology enables fluid sampling without contamination," *Journal of Petroleum Technology*, September 2006.

Lavigne, J., Barber, T., and Bratton, T.: "Strange invasion profiles: what multiarray induction logs can tell us about how oil-based mud affects the invasion process and wellbore stability," paper B presented at the 38th Annual Logging Symposium: Society of Professional Well Log Analysts, Houston, TX, June 15-18, 1997.

Levenberg, K.: "A method for the solution of certain problems in least squares," *Quart. Appl. Math.*, v. 2, pp. 164–168, 1944.

Li, Y. and Johns, R. T.: "Rapid flash calculations for compositional modeling," *SPE Reservoir Engineering & Evaluation*, v. 9, no. 5, pp. 521-529, October 2006.

Lohrenz, J., Bray, B. G., and Clark, C. R.: "Calculating viscosity of reservoir fluids from their compositions," *Journal of Petroleum Technology*, SPE 915, pp. 1171-1176, October 1964.

Madsen, K., Nielsen, H.B., and Tingleff, O.: "Methods for Non-Linear Least Squares Problems," *2nd Edition IMM*, DTU 2004.

Malik, M., Torres-Verdín, C., and Sepehrnoori, K.: "Axially symmetric compositional simulation of formation tester measurements," *Journal of Petroleum Science and Engineering*, v. 59, no. 3-4, pp. 333-349, 2007.

Marquardt, D.: "An algorithm for least squares estimation on nonlinear parameters," *SIAM J. Appl. Math.*, v. 11, pp. 431–441, 1963.

McCalmont, S., Onu, C., Wu, J., Kiome, P., Sheng, J.J., Adegbola, F., Rajasingham, R., and Lee, J.: "Predicting pump-out volume and time based on sensitivity analysis for an efficient sampling pperation: prejob modeling through a near-wellbore simulator," paper SPE 95885, presented at SPE Annual Technical Conference & Exhibition, Dallas, Texas, October 9-12, 2005.

Mullins, O.C., Schroer, J., and Beck, G.F.: "Real-time quantification of OBM filtrate contamination during openhole wireline sampling by optical spectroscopy," presented at the 41st SPWLA Annual Logging Symposium, Dallas, Texas, June 4-7, 2000.

Mullins, O.C., Beck, G., Cribbs, M.Y., Terabayshi, T., and Kegasawa, K.: "Downhole determination of gor on single phase fluids by optical spectroscopy," paper M, presented at the 42nd SPWLA Annual Logging Symposium, Houston, Texas, 2001.

O'Keefe, M., Eriksen, K.O., Williams, S., Stensland, D., Vasques, R.: "Focused sampling of reservoir fluids achieves undetectable levels of contamination," paper SPE 101084, presented at the SPE Asia Pacific Oil & Gas Conference and Exhibition, Adelaide, Australia, September 11-13, 2006.

Peng, D. Y. and Robinson, J. D.: "A new two-constant equation of state," *Industrial and Engineering Chemistry Fundamentals*, v. 15, no. 59, 1976.

Proett, M.A., Chin, W.C., Wu, J., Manohar, M., and Belanger D.: "Sample quality prediction with integrated oil and water-based mud invasion modeling," paper SPE 77964, presented at the SPE Asia Pacific Oil and Gas Conference and Exhibition, Melbourne, Australia, October 8-10, 2002.

Ramakrishnan, T.S. and Wilkinson, D.J.: "Formation producibility and fractional flow curves from radial resistivity variation caused by drilling fluid invasion," *Physics of Fluids*, v. 9, no. 4, pp. 833-844, 1997.

Salazar, J.M., Torres-Verdín, C., Alpak, F.O., Habashy, T.M., and Klein, J.D.: "Estimation of permeability from borehole array induction measurements: application to the petrophysical appraisal of tight-gas sands," *Petrophysics*, v. 47, no. 6, pp. 527-544, 2006.

Semmelbeck, M.E., Dewan, J.T., and Holditch, S.A.: "Invasion-based method for estimating permeability from logs," paper SPE 30581, presented at the SPE Annual Technical Conference & Exhibition, Dallas, October 22-25, 1995.

Sherwood, J.D.: "Optimal probes for withdrawal of uncontaminated fluid samples," *Physics of Fluids*, v. 17, no. 083102, pp. 1-10, 2005.

Todd, M. R. and Longstaff, W. J.: "The development, testing, and application of a numerical simulator for predicting miscible flood performance," *Journal of Petroleum Technology*, v. 253, pp. 874-882, July 1972.

Torres-Verdín, C., Druskin, V.L., Fang, S., Knizhnerman, L.A., and Malinverno, A.: "A dual-grid inversion technique with applications to the interpretation of dc resistivity data," *Geophysics*, v. 65, no. 6, pp. 1733-1745, 2000.

Van Der Vorst, H. A.: "Bi-CGStab: a fast and smoothly converging variant of Bi-CG for the solution of nonsymmetric linear systems", *SIAM Journal Scientific and Statistic Computing*, v. 13, no. 2, pp. 631-644, 1992.

Waxman, M.H. and Smits, L.J.M. "Electrical conductivities in oil-bearing shaly sands," *Transactions* AIME, v. 243, Part II, pp. 107-122, 1968.

Wu, J., Torres-Verdín, C., Proett, M., Sepehrnoori, K., and Belanger, D.: "Inversion of multi-phase petrophysical properties using pumpout sampling data acquired with a wireline formation tester," paper SPE 77345, presented at the Annual Technical Conference and Exhibition, San Antonio, Texas, September 29-October 2, 2002.

Wu, J, Torres-Verdín, C., Sepehrnoori, K., and Proett, M.A.: "The influence of water-base mud properties and petrophysical parameters on mudcake growth, filtrate invasion, and formation pressure," *Petrophysics*, v. 46, no. 1, pp. 14-32, 2005.

Weinheber, P. and Vasques, R.: "New formation tester probe design for low-contamination sampling," paper Q, presented at the SPWLA 47th Annual Logging Symposium, Veracruz, Mexico, June 4-7, 2006.

Yan, J. and Sharma M.M.: "Wettability alteration and restoration for cores contaminated with oil-based muds," *Journal of Petroleum Science & Engineering*, v. 2, no. 2, pp. 63-76, 1989.

Zhang, G.J., Wang, G.L., and Wang, H.M.: "Application of novel basis functions in a hybrid method simulation of the response of induction logging in axisymmetrical stratified media," *Radio Science*, v. 34, no. 1, pp. 19-26, 1999.

Zeybek, M., Ramakrishnan, T.S., Al-Otaibi, S.S., Salamy, S.P., and Kuchuk, F.J.: "Estimating multiphase-flow properties from dual-packer formation tester interval tests and openhole array resistivity measurements," *SPEREE*, February, v. 7, no. 1, pp. 40-46, 2004.

# Vita

Mayank Malik was born in Lucknow, India on July 19, 1979, the son of Kanchan and Dev Raj Malik. He received a B.E. in Mechanical Engineering from Delhi College of Engineering in 2001 and M.A.Sc. in Mechanical Engineering from University of Toronto in 2004. He was a research assistant with the Department of Petroleum and Geosystems Engineering at the University of Texas at Austin between June 2004 and March 2008. He was bestowed two SPWLA Foundation scholarships, 2005-2007. In the summers of 2006 and 2007, he was a summer intern at Shell International Exploration and Production.

Permanent address: 120, A-4, Konark Apartments, Kalkaji Extension, New Delhi, Delhi, 110019, India

This dissertation was typed by the author.